Fabrication and Characterisation of SAMs for Spin Crossover and Photocleavable Surfaces

Laurynas Pukenas

Submitted in accordance with the requirements for the degree of Doctor of Philosophy

The University of Leeds
School of Physics and Astronomy

September 2016

The candidate confirms that the work submitted is his/her own, except where work which has formed part of jointly authored publications has been included. The contribution of the candidate and the other authors to this work has been explicitly indicated below. The candidate confirms that appropriate credit has been given within the thesis where reference has been made to the work of others.

Work from the following jointly authored publication is presented in ***chapters 3 and 5***:

L. Pukenas, P. Prompinit, B. Nishitha, D. J. Tate, N. D. Pradeep Singh, C. Wälti, S. D. Evans and R. J. Bushby. Soft UV Photo-patterning and Metallization of Self-Assembled Monolayers of the Lipoic Acid Ester of α-Hydroxy-1-acylpyrene: The Generality of Acid Catalysed Removal of Thiol-on-Gold SAMs using Soft UV Light. (in preparation)

Work contained within the publications that is directly attributable to me is the characterisation of fresh and UV treated (under various conditions) Self-Assembled Monolayers (SAMs) of reagent 1, ALA, DTBA, MHA, MOA and MUA by performing XPS, FTIR, ellipsometry and contact angle measurements. Although photo-patterning and metallisation work presented in this publication were performed by P. Prompinit, photo-patterning and metallisation experiments presented in ***chapter 3*** and ***chapter 5*** were performed by me.
Contributions of the other authors to the work also include the synthesis and analytical characterisation of the novel reagent 1.

Work from the following jointly authored publication is presented in ***chapter 4***:

L. Pukenas, F. Benn, E. Lovell, A. Santoro, L. J. Kershaw Cook, M. A. Halcrow and S. D. Evans. Bead-like structures and self-assembled monolayers from 2,6-dipyrazolylpyridines and their iron(ii) complexes. J. Mater. Chem. C, 3(30), 7890-7896 **(2015)**

Work contained within the publications that is directly attributable to me is the characterisation of Self-Assembled Monolayers (SAMs), drop cast films and powder samples of L^2 and L^3 ligands and their Fe(II) complexes by performing XPS, ellipsometry and contact angle measurements.
Contributions of the other authors are the synthesis of all of the ligands and

their metal complexes, and the characterisation of $[Fe(bpp)_2][BF_4]_2$ complex in drop-cast films and powders by STM and XPS.

Work from the following jointly authored publication is presented in ***chapter 5***:

F. Benz, C. Tserkezis, L. O. Herrmann, B. de Nijs, A. Sanders, D. O. Sigle, **L. Pukenas**, S. D. Evans, J. Aizpurua, and J. J. Baumberg. Nanooptics of molecular-shunted plasmonic nanojunctions. Nano Letters, 15(1), 669674 **(2015)**

Work contained within the publications that is directly attributable to me is thickness measurements of BPDT and BPT Self-Assembled Monolayers (SAMs) using ellipsometry.
Contributions of the other authors to the work are the characterisation of pure and mixed BPDT, BPT SAMs with surface enhanced Raman spectroscopy (SERS), dark-field microscopy, scattering spectroscopy, and comparison of the experimental results with the performed full electromagnetic simulation.

Work from the following jointly authored publication is presented in ***chapter 5***:

F. Benz, B. de Nijs, C. Tserkezis, R. Chikkaraddy, D. O. Sigle, **L. Pukenas**, S. D. Evans, J. Aizpurua, and J. J. Baumberg. Generalized circuit model for coupled plasmonic systems. Optics Express, 23(26), 33255-33269 **(2015)**

Work contained within the publications that is directly attributable to me is thickness measurements of C4, C5, C9, C12, and C18 Self-Assembled Monolayers (SAMs) using ellipsometry.
Contributions of the other authors to the work are the characterisation of Self-Assembled Monolayers (SAMs) of C4, C5, C9, C12, C18 using dark field spectroscopy, and development of the generalised circuit model.

Work from the following jointly authored publication is presented in ***chapter 5***:

J. Murray, D. Nowak, **L. Pukenas**, R. Azhar, M. Guillorit, C. Wälti, K. Critchley, S. Johnson and R. S. Bon. Solid phase synthesis of functionalised SAM-forming alkanethiol-oligoethyleneglycols. J. Mater. Chem. B, 2(24), 3741-3744 **(2014)**

Work contained within the publications that is directly attributable to me is characterisation of the quality of Self-Assembled Monolayers (SAMs) and mixing of 11a, 11b and 13 by performing XPS, ellipsometry and contact angle measurements.

Contributions of the other authors to the work are synthesis of the novel molecules, characterisation of Self-Assembled Monolayers (SAMs) with other techniques (e.g. Cyclic Voltammetry, Electrochemical Impedance Spectroscopy) and reactivity of the SAMs (e.g. by studying binding of anti-hCG with Surface Plasmon Resonance).

In Loving Memory of my Grandparents

'To live is to change, and to be perfect is to have changed often.'

John Henry Newman

'Nothing is more common than for men to think that because they are familiar with words, they understand the ideas they stand for.'

John Henry Newman

Acknowledgements

My deepest gratitude goes to my supervisor Prof. Steve D. Evans. As a lecturer, as a scientist and as a person, you inspired me to further pursue my interest in Physics when I was still an undergraduate student. I would like to thank you also for giving me the opportunity to work on this project, for your guidance, help, patience, and scientific and personal support, especially in the final stages of my PhD. Thank you for believing in me, even when I didn't believe in myself! Your rigorous oversight, questioning of various aspects of physical problems down to the very details, and at the same time seeing the bigger picture and spotting positivity within it, taught me not only to approach research differently but also to look at the world with a more open mind. Your personality and character have strongly influenced me for the better. Thank you to Prof. Richard J. Bushby and Prof. Malcolm A. Halcrow for your help, invaluable advice, stimulating discussions, and for providing me with the novel compounds studied in this thesis; and to the EPSRC for funding this research.

Thank you to Dr Alex S. O. Walton for shepherding me through the very basics of research in the early stages of my PhD. I remember you calling it 'a challenging project'; well, now I know the definition of 'challenging' ☺. Thank you to Dr Jonathan P. Bramble for persuading me that the investment of time into writing a programme to automate data processing, analysis, and plotting does actually pay off. Whenever I have to reluctantly use OriginPro, MS Excel, or MS Word, I remember how glad I am that you introduced me to the world of R, ggplot2, and LaTeX!

Thank you to former and current members of the Molecular and Nanoscale Physics (MNP) group for a pleasant and co-operative working environment, discussions, jokes, banters and entertaining pranks. Also for the 'MNP out of office' initiative that ranged from wild nights out to running half-marathons or attending insane circuit trainings. Thank you to all my housemates, who were a pleasure to live with in Leeds, lovely people at CathSoc, and all other friends that I was fortunate enough to meet, especially Fr Peter Kravos, who guided me during the most difficult times. I am grateful for the influence of my physics teacher Mr Albinas Ivanauskas and undergraduate tutor Dr Jim R. Henderson, who is the cleverest guy I have ever met, and will probably ever meet. Also, I would like to pay tribute to Dr James Hayton for his online seminar 'How to get through your PhD without going insane', which helped me to understand how to correctly approach a PhD – as a degree – during the critical time of my studies, and to the late Prof. Randy Pausch, whose 'Last Lecture' and following seminars inspired me and helped me to get through my PhD.

Foremost, I would like to thank my family and relatives for their unconditional love, care and support throughout all the years! I am especially grateful to my parents, Danute and Bronius, who have fostered generosity, virtue, and education, often under difficult circumstances; and provided me the opportunity to go to a university in the UK. I am thankful to my godfather Petras and uncle Algis for sparking and then stimulating my interest in technology, to my hard working godmother Stase for her always kind and encouraging words. To my sister Elena for coaching me on how to live in the real world and making our family chase after her around Europe for the last few years. Finally to my cousins, an amazing bunch of friends I can count on, who inspire me, shepherd me and make me happy, whenever I get a chance to see them. Without you this thesis would not have been born. Thank you so much!

Abstract

This thesis investigates self-assembled monolayers (SAMs) of molecules of various complexity with a special focus on fabrication of surfaces that could exhibit an intrinsic active function, more precisely a capability to switch between two stable states upon external stimuli (spin crossover phenomenon) or to expose functional groups upon irradiation with light, i.e. photocleavage of a SAM.

SAM formation of a complex novel molecule, lipoic acid ester of α-hydroxy-1-acetyl-pyrene (**reagent 1**), was studied in chapter 3. It contains i) a dithiolane headgroup capable of binding to gold surfaces via two sulfur atoms, and ii) a chromophore that makes it light sensitive (photocleavable) and leads to a deprotection of lipoic acid molecule upon exposure to soft UV (365 nm). **Reagent 1** successfully forms **SAM1**, but it interacts with the gold surface weaker than conventional thiol based SAMs, due to cross-linking of dithiolane headgroups. Nevertheless, **SAM1** is a relatively stable monolayer and exerts a higher barrier against diffusion of copper ions towards gold surface in electrochemical deposition than SAMs of similarly complex molecules but with thiol headgroups or shorter alkanethiol SAMs terminated with carboxylic acid groups (COOH). **SAM1** undergoes photolysis upon soft UV (365 nm) irradiation, but only in the acidic catalyst 100 mM HCl in isopropanol (IPA). Unexpectedly, this also leads to a removal of the resulting **lipoic acid** monolayer, thus ultimately leading to **SAM1** with lower surface coverage, and changes packing and ordering. SAMs of alkanethiols terminated with COOH and of varying chain length were investigated in order to better understand the cause for the instability of **lipoic acid** monolayer. Loss of molecules from the surfaces was found to be a common issue in the COOH SAMs, however, the severity of the loss is strongly related to the initial SAM thickness. Thin SAMs like **DTBA SAM** yield huge ($\sim$50 %) loss, while thick SAMs like **MUA SAM** show no detectable loss.

On the other hand, photo-patterned **SAM1** produces especially high selectivity of Cu deposition between UV treated and non-treated regions, which is associated to this loss of surface coverage, packing and ordering. Surprisingly, **reagent 1** also interacts with glass and silicon oxide surfaces to form hydrophobic films that exhibit green fluorescence under soft UV light. Such surfaces are photo-sensitive and can be photo-patterned in the air or in the acidic catalyst to produce non-fluorescent hydrophilic regions due to photo-bleaching of pyrene groups and photo-deprotection of lipoic acid molecules, respectively. The films and patterns stored under ambient conditions are detectable for at least 35 days. Formation of those films is associated

with an interaction of pyrene group with adsorbates on the surfaces, while film growth is attributed to the cross-linking of dithiolane headgroups.

SAM fabrication of metal complexes was explored in chapter 4. Two novel ligands $\mathbf{L_1}$ and $\mathbf{L_2}$, and their corresponding Fe(II) complexes $\mathbf{C_1}$ and $\mathbf{C_2}$, which can exhibit spin crossover (SCO) behaviour in bulk, were investigated. Both ligands successfully form SAMs. However, **SAM $\mathbf{L_1}$** does not coordinate Fe(II), while its preformed complex $\mathbf{C_1}$ is not stable on Au surface and forms **SAM $\mathbf{L_1}$** instead of **SAM $\mathbf{C_1}$**. In contrast, **SAM $\mathbf{L_2}$** coordinates Fe(II) at nearly 100 % yield, which leads to almost the same chemical composition as in a SAM of its preformed Fe(II) complex $\mathbf{C_2}$ (**SAM $\mathbf{C_2}$**). Although complex $\mathbf{C_2}$ with MeCN as the sixth exogenous ligand (SEL) exhibits low spin (LS) state in bulk at room temperature, only high spin (HS) state was detected in **SAM $\mathbf{C_2}$**. Complex $\mathbf{C_2}$ exhibits a unique property of changing its spins state in certain solvents, because a solvent molecule can easily displace the sixth exogenous ligand (SEL). However, rinsing **SAM $\mathbf{C_2}$** with such solvents did not lead to a spin transition, and LS state was never observed for the SAM. This implies that the strength of the ligand field may need to be increased or SEL with a higher affinity coordinated to complex $\mathbf{C_2}$, in order to change the spin state by rinsing or to detect SCO in **SAM $\mathbf{C_2}$**.

A long-chain alkanethiololigoethyleneglycol (LCAT-OEG) type molecule terminated with the azide group (**reagent 2**) was investigated for the facilitation of click chemistry on gold surfaces (chapter 5). **Reagent 2** forms a good quality SAM (**SAM2**), and the concentration of **reagent 2** in the SAM can be reduced in a controlled and predictable manner by the addition of **LCAT-OEG-1** or **LCAT-OEG-4** to the growth solution. QCMD measurements indicate that the whole surface of **SAM2** successfully undergoes click reaction with cycloalkyne in aqueous solution without any catalyst.

Finally, simple alkanethiol and aromatic type SAMs were investigated for use in surface-enhanced Raman spectroscopy (SERS) with nanoparticle-on-mirror configuration and for studying plasmonic systems, due to their ability to yield optimum precision over the control of thickness and dielectric function (chapter 5).

Publications

1. **L. Pukenas**, P. Prompinit, B. Nishitha, D. J. Tate, N. D. Pradeep Singh, C. Wälti, S. D. Evans and R. J. Bushby. Soft UV Photo-patterning and Metallization of Self-Assembled Monolayers of the Lipoic Acid Ester of α-Hydroxy-1-acylpyrene: The Generality of Acid Catalysed Removal of Thiol-on-Gold SAMs using Soft UV Light. (in preparation)

2. **L. Pukenas**, F. Benn, E. Lovell, A. Santoro, L. J. Kershaw Cook, M. A. Halcrow and S. D. Evans. Bead-like structures and self-assembled monolayers from 2,6-dipyrazolylpyridines and their iron(ii) complexes. J. Mater. Chem. C, 3(30), 7890-7896 **(2015)**

3. F. Benz, C. Tserkezis, L. O. Herrmann, B. de Nijs, A. Sanders, D. O. Sigle, **L. Pukenas**, S. D. Evans, J. Aizpurua, and J. J. Baumberg. Nanooptics of molecular-shunted plasmonic nanojunctions. Nano Letters, 15(1), 669-674 **(2015)**

4. F. Benz, B. de Nijs, C. Tserkezis, R. Chikkaraddy, D. O. Sigle, **L. Pukenas**, S. D. Evans, J. Aizpurua, and J. J. Baumberg. Generalized circuit model for coupled plasmonic systems. Optics Express, 23(26), 33255-33269 **(2015)**

5. J. Murray, D. Nowak, **L. Pukenas**, R. Azhar, M. Guillorit, C. Wälti, K. Critchley, S. Johnson and R. S. Bon. Solid phase synthesis of functionalised SAM-forming alkanethiol-oligoethyleneglycols. J. Mater. Chem. B, 2(24), 3741-3744 **(2014)**

Contents

List of Figures

List of Tables

Abbreviations

$\Delta_{\mathbf{o}}$ crystal field splitting.

ALA SAM SAM formed from DCM solution of **lipoic acid**.

ALA SAM+UV **ALA SAM** after exposure to soft UV.

ALA SAM+UV$_{1.5\,\mathrm{h}}$ **ALA SAM** after exposure to soft UV for 1.5 h.

ALA SAM+UV$^{HCl}_{1.5\,\mathrm{h}}$ **ALA SAM** after exposure to soft UV for 1.5 h in 100 mM HCl in IPA.

BE binding energy.

BF_4^- tetrafluoroborate anion.

BPDT Biphenyl-4,4'-dithiol.

BPDT SAM SAM formed from EtOH solution of **BPDT**.

bpp-SH complex Fe(II) complex of ligand **bpp-SH**.

BPT Biphenyl-4-thiol.

BPT SAM SAM formed from EtOH solution of **BPT**.

Br^- bromide anion.

CA contact angle.

CFT crystal field theory.

$CHCl_3$ chloroform.

Cl^- chloride anion.

ClO_4^- perchlorate anion.

CN^- cyanide anion.

CO carbon monoxide.

complex C_1 Fe(II) complex of ligand L_1.

complex C_2 Fe(II) complex of ligand L_2 with H_2O as the SEL.

DCM dichloromethane.

DTBA 4,4'-Dithiodibutyric acid.

DTBA SAM SAM formed from DCM solution of **DTBA**.

DTBA SAM+UV **DTBA SAM** after exposure to soft UV.

DTBA SAM+$UV_{1.5\,h}$ **DTBA SAM** after exposure to soft UV for 1.5 h.

DTBA SAM+$UV^{HCl}_{1.5\,h}$ **DTBA SAM** after exposure to soft UV for 1.5 h in 100 mM HCl in IPA.

ECD electrochemical deposition.

E_p peak potential.

EtOH ethanol.

FTIR Fourier Transform Infrared.

FWHM Full width at half maximum.

H_2O milliQ water.

HCl hydrochloric acid.

I^- iodide anion.

IPA isopropanol.

LCAT-OEG-1 short alkanethiol-oligoethyleneglycol, i.e. N-[2-(2-hydroxyethoxy)-ethyl]-11-sulfanylundecanamide.

LCAT-OEG-1 SAM SAM formed from EtOH solution of **LCAT-OEG-1**.

LCAT-OEG-4 alkanethiol-oligoethyleneglycol, i.e. N-(14-hydroxy-3,6,9,12-tetra-oxatetradecan-1-yl)-11-sulfanylundecanamide.

LCAT-OEG-4 SAM SAM formed from EtOH solution of **LCAT-OEG-4**.

LFT ligand field theory.

ligand bpp ligand 2,6-di[pyrazol-1-yl]pyridine.

ligand bpp-SH ligand 4-mercapto-2,6-di[pyrazol-1-yl]pyridine.

ligand L_1 ligand 4-(thiomorpholin-4-yl)-2,6-di[pyrazol-1-yl]pyridine.

ligand L_2 ligand 4-(thiomorpholin-4-yl)-2,6-di[hydroxydi(pyridin-2-yl)methyl]pyridine.

lipoic acid α-Lipoic acid, i.e. (R)-5-(1,2-Dithiolan-3-yl)pentanoic acid.

MeCN acetonitrile.

$MeNO_2$ nitromethane.

MeOH methanol.

MHA 6-Mercaptohexanoic acid.

MHA SAM SAM formed from DCM solution of **MHA**.

MHA SAM+UV **MHA SAM** after exposure to soft UV.

MHA SAM+$UV_{1.5\,h}$ **MHA SAM** after exposure to soft UV for 1.5 h.

MHA SAM+$UV^{HCl}_{1.5\,h}$ **MHA SAM** after exposure to soft UV for 1.5 h in 100 mM HCl in IPA.

MO molecular orbital theory.

MOA 8-Mercaptooctanoic acid.

MOA SAM SAM formed from DCM solution of **MOA**.

MOA SAM+UV **MOA SAM** after exposure to soft UV.

MOA SAM+$UV_{1.5\,h}$ **MOA SAM** after exposure to soft UV for 1.5 h.

MOA SAM+$UV^{HCl}_{1.5\,h}$ **MOA SAM** after exposure to soft UV for 1.5 h in 100 mM HCl in IPA.

MUA 11-Mercaptoundecanoic acid.

MUA SAM SAM formed from DCM solution of **MUA**.

MUA SAM+UV **MUA SAM** after exposure to soft UV.

MUA SAM+$UV_{1.5\,h}$ **MUA SAM** after exposure to soft UV for 1.5 h.

MUA SAM+$UV^{HCl}_{1.5\,h}$ **MUA SAM** after exposure to soft UV for 1.5 h in 100 mM HCl in IPA.

N_3^- azide.

OCP open circuit potential.

OPD over potential deposition.

P2VP poly(2-vinylpyridine).

P4VP poly(4-vinylpyridine).

P-alpha-MS poly(alpha-methylstyrene).

PAN poly(acrylonitrile).

PBAC poly(bisphenol A carbonate).

PES poly(ether sulphone).

PHMS poly(hexamethylene sulphone).

PIB Poly(isobutylene).

PMAN poly(methacrylonitrile).

PSS poly(sodium 4-styrenesulphonate).

PVA poly(vinyl alcohol).

PVME poly(vinyl methyl ether).

Py pyridine.

QCMD quartz crystal microbalance with dissipation monitoring.

reagent 1 lipoic acid ester of α-hydroxy-1-acetylpyrene, i.e. 2-oxo-2-(pyren-1-yl)-ethyl 5-[(R)-1,2-dithiolan-3-yl]pentanoate.

reagent 2 azide terminated alkanethiol-oligoethyleneglycol, i.e. N-(17-azido-3,6,9,12,15–pentaoxaheptadecan-1-yl)-11-sulfanylundecanamide.

reagent Py-SH reagent 4-mercaptopyridine.

R.S.F. relative sensitivity factor.

SAM self-assembled monolayer.

SAM bpp-SH SAM formed from solution of ligand **bpp-SH**.

SAM $\mathbf{C_1}$ SAM formed from solution of complex $\mathbf{C_1}$.

SAM $\mathbf{C_2}$ SAM formed from solution of complex $\mathbf{C_2}$.

SAM $\mathbf{C_2}$ [MeCN] SAM formed from MeCN solution of complex $\mathbf{C_2}$.

SAM $\mathbf{C_2}$ [MeOH] SAM formed from MeOH solution of complex $\mathbf{C_2}$.

SAM $\mathbf{L_1}$ SAM formed from solution of ligand $\mathbf{L_1}$.

SAM $\mathbf{L_1}$+Fe SAM $\mathbf{L_1}$ after exposure to Fe(II) solution.

SAM $\mathbf{L_1}$+Fe(1m) SAM $\mathbf{L_1}$ after exposure to Fe(II) solution for 1 minute.

SAM L_1+Fe(30m) **SAM L_1** after exposure to Fe(II) solution for 30 minutes.

SAM L_2 SAM formed from $CHCl_3$ solution of ligand **L_2**.

SAM L_2+Fe **SAM L_2** after exposure to Fe(II) solution.

SAM L_2+Fe(1m) **SAM L_2** after exposure to Fe(II) solution for 1 minute.

SAM L_2+Fe(30m) **SAM L_2** after exposure to Fe(II) solution for 30 minutes.

SAM Py-S SAM formed from solution of reagent **Py-SH**.

SAM1 SAM formed from DCM solution of **reagent 1**.

SAM1+Dark$^{HCl}_{1.5\,h}$ **SAM1** after immersion into 100 mM HCl in IPA for 1.5 h.

SAM1+UV **SAM1** after exposure to soft UV.

SAM1+UV$_{1.5\,h}$ **SAM1** after exposure to soft UV for 1.5 h.

SAM1+UV$^{HCl}_{1.5\,h}$ **SAM1** after exposure to soft UV for 1.5 h in 100 mM HCl in IPA.

SAM1+UV$^{IPA}_{1.5\,h}$ **SAM1** after exposure to soft UV for 1.5 h in IPA.

SAM1+UV$^{50\,\%IPA}_{1.5\,h}$ **SAM1** after exposure to soft UV for 1.5 h in 50% (v/v%) of IPA in H_2O.

SAM1+UV$^{50\,\%MeCN}_{1.5\,h}$ **SAM1** after exposure to soft UV for 1.5 h in 50% (v/v%) of MeCN in H_2O.

SAM1+UV$^{50\,\%MeOH}_{1.5\,h}$ **SAM1** after exposure to soft UV for 1.5 h in 50% (v/v%) of MeOH in H_2O.

SAM1+UV$_{2.5\,h}$ **SAM1** after exposure to soft UV for 2.5 h.

SAM1+UV$^{HCl}_{2.5\,h}$ **SAM1** after exposure to soft UV for 2.5 h in 100 mM HCl in IPA.

SAM1+UV$^{IPA}_{2.5\,h}$ **SAM1** after exposure to soft UV for 2.5 h in IPA.

SAM1+UV$_{5\,h}$ **SAM1** after exposure to soft UV for 5 h.

SAM1+UV$^{HCl}_{5\,h}$ **SAM1** after exposure to soft UV for 5 h in 100 mM HCl in IPA.

SAM1+UV$^{IPA}_{5\,h}$ **SAM1** after exposure to soft UV for 5 h in IPA.

SAM2 SAM formed from EtOH solution of **reagent 2**.

SAM2$^{OEG1}_{19\%}$ SAM formed from EtOH solution of 19% and 81% molar fractions of **reagent 2** and **LCAT-OEG-1**, respectively.

SAM2$^{OEG1}_{50\%}$ SAM formed from EtOH solution of 50% and 50% molar fractions of **reagent 2** and **LCAT-OEG-1**, respectively.

SAM2$^{OEG4}_{19\%}$ SAM formed from EtOH solution of 19% and 81% molar fractions of **reagent 2** and **LCAT-OEG-4**, respectively.

SAM2$^{OEG4}_{50\%}$ SAM formed from EtOH solution of 50% and 50% molar fractions of **reagent 2** and **LCAT-OEG-4**, respectively.

SCO spin crossover.

SEL sixth exogenous ligand.

SERS surface-enhanced Raman spectroscopy.

soft UV soft ultraviolet light.

UPD under potential deposition.

XPS X-ray Photoelectron Spectroscopy.

Chapter 1

Introduction

Self-assembly is a process when disordered individual building blocks form an organised structure(s) due to local interactions between themselves and without any external stimuli.[1–3] This phenomena is prevalent in nature, and spans the scale from molecules to galaxies and various types of interactions.[3]

Molecular self-assembly has drawn a lot of attention due to its direct relevance to biological systems, supramolecular chemistry and 'bottom-up' fabrication in nanotechnology.[4] In particular, 2D molecular assemblies called self-assembled monolayers (SAMs) have been adopted in many disciplines, primarily due to their spontaneous self-assembly on various substrates into highly packed, ordered and oriented monolayers, which allow easy manipulation of surface functionality via flexible modification of chemical groups in molecular chain and its terminals.[1,2] SAMs can control a number of surface properties, for example, wetting and adhesion,[5] fluorescence,[6] electron transfer,[7] bio-compatibility and cell adhession,[8] chemical resistance, molecular recognition,[9] and nano fabrication.[10] SAMs have been applied in many different fields, such as biosensors,[11] cell biology,[8] oriented nucleation of crystal,

alignment of liquid crystals, organic molecular electronics, component surface modification for nanoelectromechanical systems (NEMS), microelectromechanical systems (MEMS), and functionalisation of nanostrucutres, to name a few.[4]

The aim of this thesis is to explore SAMs of various complexity with a special focus on fabrication of surfaces that could exhibit an intrinsic active function. The complexity ranges from: (i) simple alkanethiol and aromatic type SAMs to give optimal precision for optical spectroscopy (e.g. surface-enhanced Raman spectroscopy) and to study plasmonic systems; (ii) azide terminated SAMs to facilitate click chemistry on gold surfaces; (iii) a more complex SAM of larger molecules containing chromophore that turns it into a light sensitive (more specifically photocleavable) system capable of exposing functional groups; and finally to (iv) bi-stable metal complexes (spin crossover compounds) that exhibit reversible switching between two stable states with distinctively different properties upon external stimuli, such as light irradiation, magnetic field, change in temperature or pressure. For a better understanding of this study, the outline of this thesis is presented at the end of this chapter, while the rest of the chapter provides a general background including SAM formation, SAM patterning and photolysis, electrochemical deposition of metals on SAMs, spin crossover (SCO) phenomena, and click chemistry.

1.1 Self-assembled monolayers (SAMs)

Self-assembled monolayers (SAMs) are molecular assemblies that form spontaneously upon exposure to surfactants (solution or gas phase). Initial work in this field can be traced back to the adsorption of monomolecular layer of alkyl amine on a clean platinum surface reported by Zisman in 1946;[12] however, at the time the potential of such self-assemblies was not widely recognised. A few decades later, chemical functionalisation of hydroxylated surfaces (usually silicon) using chlorosilane

derivatives gained some attention,[13–15] which eventually led to the developement of silane SAM on hydroxylated glass by Sagiv in 1980.[16]

However, silane SAMs have been reported to have reproducibility issues due to sensitivity of silanes to moisture.[17,18] In contrast, Nuzzo and Allara developed and reported SAMs formed on gold surface from dilute solutions of dialkyl disulfides in 1983,[19] which yielded high reproducibility and high degree of controlling chemical and physical properties of the surface.[19,20] Since then various SAMs have been reported on various substrates, however, alkanethiolates on gold are the most commonly adopted and studied SAMs to date.

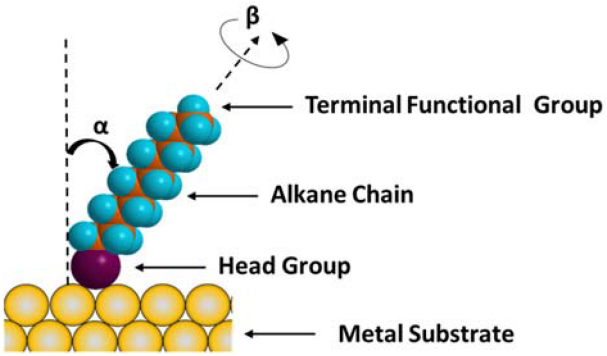

FIGURE 1.1: Structure of a surfactant molecule that forms a SAM. Tilt angle from the surface normal is indicated by α, and twist angle by β. Taken from reference[21].

In general, surfactants that form SAMs can be considered to consist of three parts: head group, (alkyl) chain and functional (or end) group, as shown in figure 1.1. Each part plays a unique role in self-assembly. The first part, head group, usually possesses a strong affinity towards a specific surface and often forms a chemical bond. Therefore, it is largely responsible for initiating and driving the self-assembly. It has been speculated[1,4] and later experimentally shown that both alkanethiols and disulfides form Au-S (40-50 kcal/mol)[1,4,22] bonds.[23–26] Alkanethiols proceed via cleavage of S-H (∼87 kcal/mol)[1] bond and formation of H_2 (∼104 kcal/mol)[1] by-product,[23–25] which is energetically more favourable by 10-30 kcal/mol (or 5-15 kcal/mol per alkanethiolate). On the other hand, disulfides undergo only cleavage of S-S (∼62 kcal/mol)[4]

bond,[23,26–28] which is energetically more favourable by 18-38 kcal/mol per disulfide molecule (or 9-24 kcal/mol per alkanethiolate). Although Au-S bond is weaker than both S-C (∼62 kcal/mol)[29] and C-C (∼83 kcal/mol)[29] bonds, it is still a relatively strong bond. The second part, chain, is usually responsible for enhancing packing, order and orientation of molecules within a SAM due to intermolecular interactions. The stability of a SAM increases by 1-2 kcal/mol per each methylene (-CH_2-) group[4,22] in the chain due to van der Waals' interaction. Because this energy scales with chain length, long chain (consisting of 10-12 or more carbons[1,30]) alkanethiol SAMs yield a higher order, closer packing and a smaller area per molecule on gold surfaces. Dominance of chain-chain interaction over molecule-substrate interaction is most evident in dialkyl monosulfide SAMs.[31,32] Incorporation of specific chemical groups into alkyl chain can exert other – more important – interactions, e.g. amide groups increase chain-chain interaction by 6 kcal/mol[22] due to hydrogen bonding. On the other hand, chain-chain interaction can be suppressed due to the presence of bulky and non-interacting chemical groups. The third and final part, functional (or end) group, predominantly determines the physical and chemical properties of the surface. Various end groups have been reported, but the most commonly used are hydroxyl (-OH),[20] carboxylic acid (-COOH), amine (-NH_2),[20] perfluorocarbon (-CF_3) and aromatic hydrocarbon.

SAMs with sulfur head groups can be formed on a number of metals like silver,[20] copper,[20] platinum, mercury, iron, to name a few. However, most of the studies or applications have been reported on gold, which does not have a stable native oxide, and thus experiments can be carried out under standard laboratory conditions. Typically SAMs are formed on thin polycrystalline gold films prepared by evaporation under high vacuum (HV). Lowest surface energy for gold is Au(111) reconstruction, which is predominately formed in the polycrystalline films.[2]

SAM adsorption time typically varies from minutes to several hours, depending on

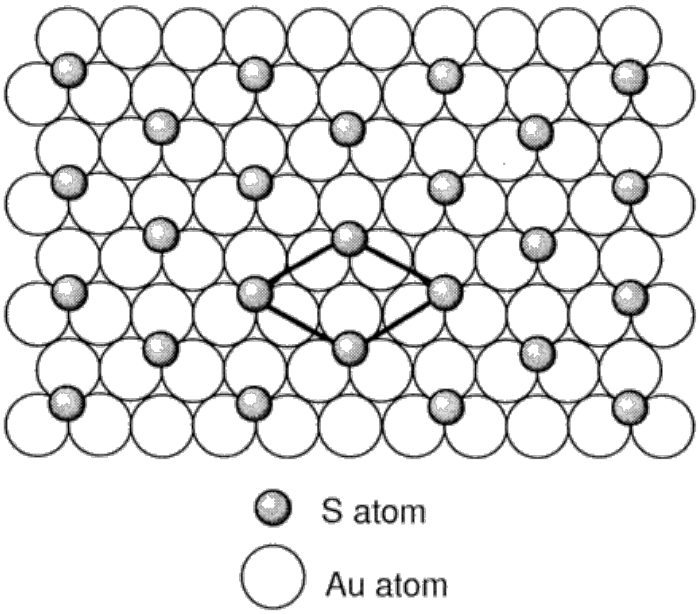

FIGURE 1.2: A schematic representation of hexagonal $(\sqrt{3} \times \sqrt{3})R30°$ structure formed by alkanethiolates on gold surfaces in a highly ordered and densely packed SAM. Taken from reference[33].

molecular structure, solution concentration (usually in the range of µM to mM) and solvent.[34] Long chain (10-12 or more carbons) alkanethiols can produce highly ordered and crystalline monolayers with sulfur atoms binding to threefold hollow sites on Au(111) lattice and arranging themselves in a hexagonal $(\sqrt{3} \times \sqrt{3})R30°$ structure,[1] as shown in figure 1.2. The spacing between sulfur atoms bound to gold is $\sim$5 Å[35] (area of 21.6 Å^2[2,36] per molecule), while the van der Waals diameter of an alkyl chain is $\sim$4.6 Å[35] (cross-section area of 18.4 Å^2.[2]) Therefore, chains are expected to tilt away from the surface normal by about 30°, in order to lower the energy, due to the van der Waals interaction between chains. Fourier Transform Infrared (FTIR) studies have shown average molecular tilt angle of 20-35°.[30,35] Later, however, studies using helium diffraction revealed a $c(4 \times 2)$ superstructure on top of $(\sqrt{3} \times \sqrt{3})R30°$ lattice, and in the last decade the standard model has been progressively more challenged,[37–39] especially for low- and medium-coverage SAMs. Based on theoretical as well as experimental work, a number of bonding motifs between thiolates and gold has been proposed, such as disulfide bonding, a complex

of gold adatom and a thiolate, a polymeric chain formed of bridging thiolates in between gold adatoms, as shown in figure 1.3.

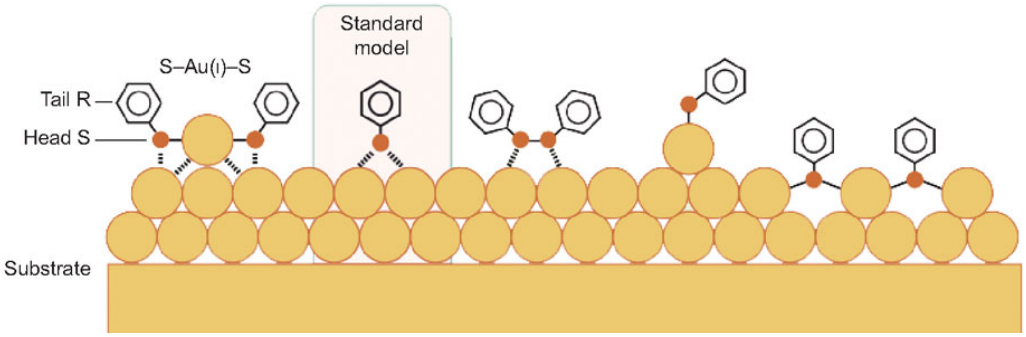

FIGURE 1.3: A schematic of various proposed bonding motifs between thiolates and gold proposed. From the standard model to the right: disulfide bonding, a complex with gold adatom and a thiolate, a polymeric chain formed of bridging thiolates in between gold adatoms. Taken from reference[37].

This section on SAMs was designed to serve as a brief introduction, for more details the reader is referred to the review papers,[1,4,34,35,37–41] which are just a few of many that have been published on various aspects of SAMs.

1.2 Photo-patterning of SAMs

Although SAMs offer a versatile and inexpensive method to tune surface chemical and physical properties by chemical substitution in surfactant molecules, this could be taken a step further by introducing patterning of SAMs. Such additional surface modification further broadens the potential for applicability.[4,34,42–50] Patterned SAMs can be used for spatially selective immobilisation of biological species or nanoparticles, directing nanoparticle assembly on the surface, to control the alignment of liquid crystals, selective biomineralisation, growth of metal nanostructures, to name a few.[4,42–50]

A variety of approaches have been developed for patterning SAMs: (i) soft lithography, for example micro-contact printing (μCP), microtransfer molding (μTM),

micromolding in capillaries (MIMIC), and microfluidics assisted patterning;[43,44,46,47,51–55] (ii) scanning probe lithography, for example nanoshaving, nanografting, and dip-pen nanolithography;[42,44,56,57] and (iii) photolithography, for example electron-beam lithography (EBL), scanning near-field photolithography (SNP), X-ray irradiation, and ultraviolet/visible light irradiation.[7,41,44,45,47,58]

Here, the use of photolithography is proposed due to its wide uptake within the semiconductor community. More specifically, ultraviolet light (UV) is used, because (i) it does not require sophisticated instrumentation, and (ii) is widely accessible in scientific research environments. Irradiation of alkanethiolate SAMs with 254 nm or shorter wavelength UV in the presence of air usually causes photo-oxidation of thiolate group into sulfonate group.[4,41] Because sulfonate group interacts weakly with the gold surface, the oxidised molecules are easily rinsed away or displaced by other thiols.[4,41] This provides the basis for the photo-patterning. On the other hand, irradiation of a SAM with UV (254 nm) under inert atmosphere does not induce any damage.[59] Furthermore, it has been shown that when alkyne groups are incorporated, molecules within a SAM undergo cross-linking; this strengthens their interaction with the gold surface.[59] Areas that have not been exposed to UV, and are thus not cross-linked, can be desorbed by electrochemical reductive stripping or other methods.[59] Both methods lead to non-selective chemical patterning, i.e. they do not expose any new surface chemical functionality upon irradiation with UV.[4,41]

On the other hand, soft UV (i.e. 365 nm) is significantly weaker and does not affect thiolate bond under most conditions. Therefore, it can be used to induce specific functional group transformations and to fabricate well-defined patterns on both gold and silica substrates.[60–64] Soft UV can be used to activate reversible photochemical switching in a SAM,[60,65] deprotect a specific functional chemical group (e.g. carboxylic acid group,[61] amine group,[62] aniline group[66]) in a SAM, or to

fabricate robust templates for reversible metallisation,[61] to name a few. Another advantage of the photocleavable SAM (as oppose to a SAM that can only be oxidised) is the ability to pattern it with a resolution higher than the wavelength of the light (if configuration of the molecule allows two-photon absorption).[61] The ability to photo-deprotect a SAM with soft UV is also advantageous for drug delivery. Light with ∼800 nm wavelength can penetrate relatively deep into biological tissue, where up-converting nanoparticles can be used to convert 960 nm light to ∼365 nm light, and thus activate photo-deprotection reaction in the SAM bound to the nanoparticle.[63,64]

Although self-assembled monolayers (SAMs) can accommodate many preparative photochemical reactions, *ortho*-nitrobenzyl derivatives have been studied the most[62,66] due to high yields in their photochemical reactions in a solution. However, reactions in a SAM environment do not necessarily proceed in the same way and do not necessarily give the same yield. SAMs containing *ortho*-nitrobenzyl derivatives, without a catalyst, give 50-80 % yield.[67,68] Consequently, alternative systems, such as photoreduction of azides,[69] photo-reaction of azides with amines,[70] CH bond insertion reactions of benzophenone derivatives,[71,72] and the photocleavage of N-alkyl picolinium (NAP) esters[73] have been investigated.

A study on SAMs of the novel molecule **reagent 1** (see figure 3.1), which is based on photo-deprotection of α-esters with 1-acetylpyrene,[74] is presented in chapter 3. Pyrene group is expected to produce a better photo-reaction yield.

1.3 Spin crossover (SCO) phenomena

Spin crossover (SCO) is an ability to switch between two stable spin states in certain metal complexes due to external stimuli, such as change in temperature or pressure, light irradiation or pulsing magnetic field, interaction with solvents or adjacent molecules.[75] Such a phase transition occurs in certain transition metal complexes due to the rearrangement of $3d$ electrons, and leads to a low spin (LS) state with a minimum number of unpaired electrons or a high spin (HS) state with a maximum number of unpaired electrons in the d orbital. This rearrangement in electronic structure yields a change in conductivity, magnetic susceptibility, colour and other properties. Thus, such intrinsic bistability is promising for developing molecular switches, data storage devices, optical displays.[76,77] Since the first SCO compound was reported by Cambi in 1931,[78] the field has expanded enormously and various compounds have been reported with abrupt spin transition, tunable transition temperature, hysteresis loop, and multiple transitions.[76,79]

1.3.1 Metal complexes

Metal complexes are chemical compounds that contains a metal ion or atom in a centre bonded to surrounding molecules or ions. Consequently, many metal containing compounds are metal complexes.[80] Molecules or ions bound to metal centre in a complex are called ligands. They bind (coordinate) to a metal centre through a dative covalent (coordination) bond, which is weaker than an ionic or covalent bond, but stronger than a hydrogen or van der Waals interaction. The basis of modern theory of coordination chemistry was developed by Alfred Werner, who was awarded the first Nobel prize award in inorganic chemistry in 1913 for proposing the octahedral configuration of transition metal complexes. All metals form complexes, but their properties depend strongly on the electronic structure. Complexes can be

neutral, cationic or anionic, which is determined by the charges of the metal ion and its ligands. A number of sites on the central ion that ligands can bind to is called coordination number. It depends on the size, charge and electronic configuration of the metal centre and the ligands. Coordination number determines the coordination geometry (see figure 1.4 for linear, tetrahedral and octahedral forms), and can vary from 2 to more than 12, but most common values are 2, 4 and 6. Metal complexation was initially of great interest to inorganic chemists. It has, however, over the years also gained the attention of organic and physical chemists, biochemists and molecular biologists. It also has been applied in photography, extraction and plating of silver and gold, softening of hard water and dissolution of scale.

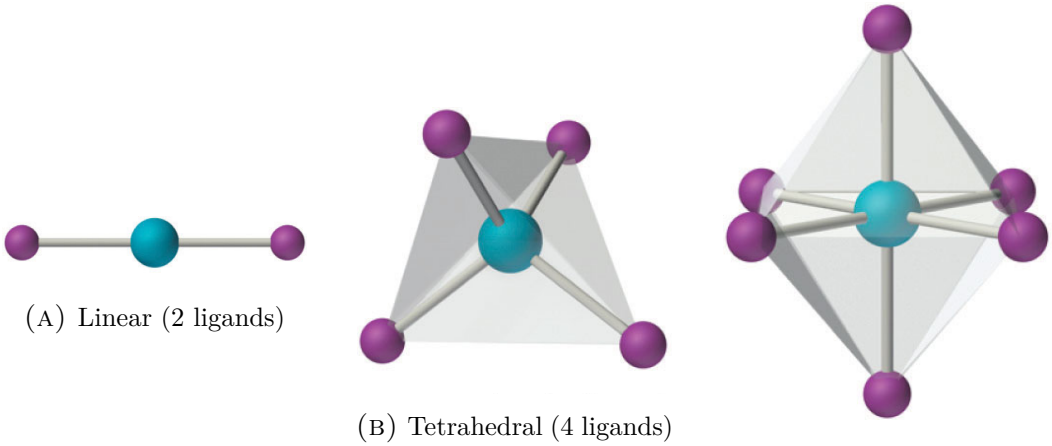

(A) Linear (2 ligands)

(B) Tetrahedral (4 ligands)

(C) Octahedral (6 ligands)

FIGURE 1.4: The most common coordination geometries in complexes of transition metals. Metal centre and ligands are represented by blue and purple spheres, respectively. Taken from reference[81].

1.3.2 Ligand and Crystal field theories

Metal complexes possess unique and interesting properties. Some of these properties, however, had not been explained until crystal field theory (CFT) and ligand field theory (LFT) were developed. CFT is a relatively simple ionic model that considers interactions between the metal centre and ligands to be purely electrostatic. Except

for the determination of how many ligands can physically fit around a metal centre, ligands are treated as point charges. Therefore CFT describes a metal complex as a distribution of negative point charges attracted to a positively charged metal ion. However, electrons in the outer layers of a metal cation and electrons in the ligand repel each other due to electrostatic repulsion of the like charges. As ligands approach a metal ion, electrons of the ligands are closer to certain d or f orbitals of the metal ion. This raises the required energy for electrons to stay in those particular orbitals (of the metal ion), and therefore leads to a splitting of their degeneracy.

The most common configuration is octahedral, where six ligands form an octahedron around metal cation (figure 1.4c). Such an arrangement in Cartesian coordinates correspond to ligands positioned along x, y and z axes. For transition metals (d-block elements), this leads to an overlap of d-orbitals (see figure 1.5b) with the ligands, more specifically $d_{x^2-y^2}$ with electrons of four ligands positioned on the x and y axes, and d_{z^2} with electrons of two ligands positioned on the z axis, while other orbitals point between the ligands. Consequently, d_{z^2} and $d_{x^2-y^2}$ orbitals (collectively called $\mathbf{e_g}$[a]) are higher in energy than d_{xy}, d_{xz} and d_{yz} (collectively called $\mathbf{t_{2g}}$[a]), as shown in figure 1.5a. Difference between the two energy levels is known as crystal field splitting (Δ_o) and its value depends on the strength of interaction between metal ion and ligands. Ligands that bind strongly lead to high overlap with $\mathbf{e_g}$ orbitals and produce high Δ_o values that are greater than electron pairing energy. Consequently it is more energetically favourable to completely fill $\mathbf{t_{2g}}$ orbitals by pairing electrons before starting to fill $\mathbf{e_g}$, which leads to low spin (LS) due to the lowest number of unpaired electrons. On the other hand, weak ligands produce low values of Δ_o that are smaller than electron pairing energy and electrons partially fill $\mathbf{e_g}$ and $\mathbf{t_{2g}}$ orbitals, before electrons start pair-up and fully fill each orbital, which leads to high spin (HS) due to the largest possible number of unpaired electrons. This explains some magnetic and structure properties of metal complexes. Also some of the colour

[a] This label is based on orbital symmetry, and does not indicate energy level on its own.

properties can be explained by electron excitation from $\mathbf{t_{2g}}$ to $\mathbf{e_g}$ orbitals following absorption of photons with the same energy as Δ_o.

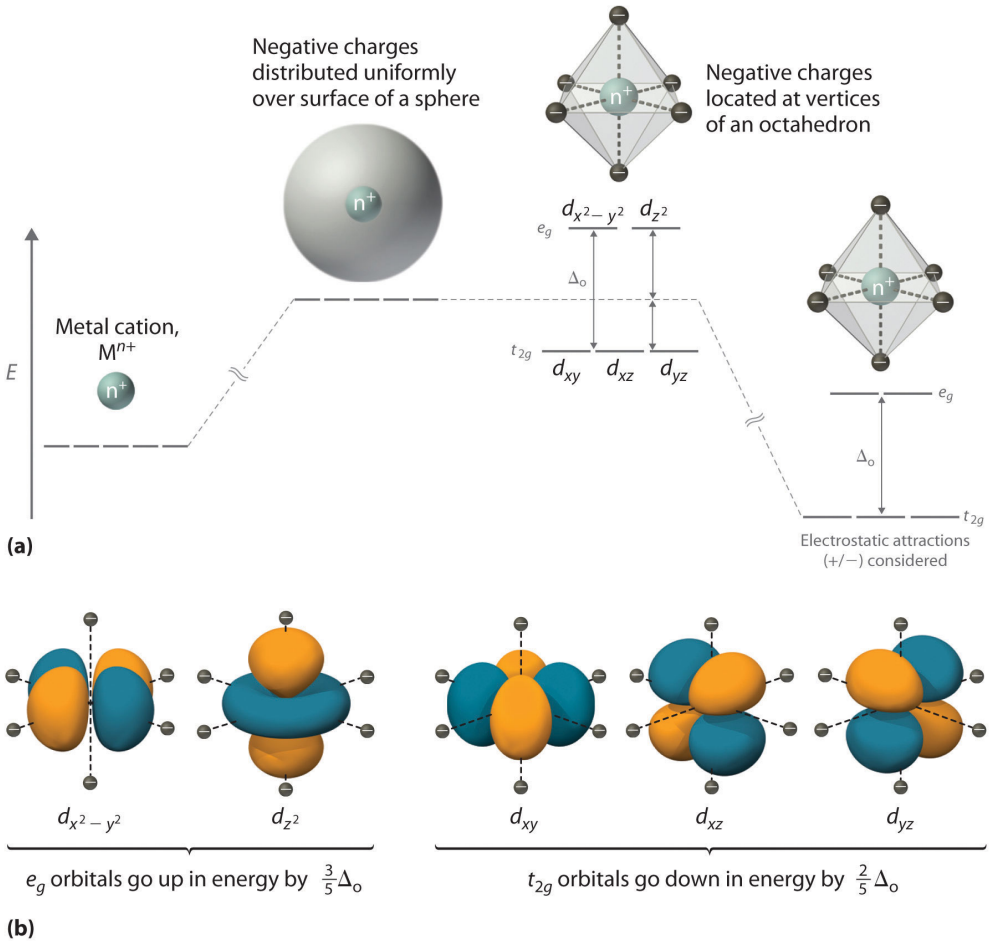

FIGURE 1.5: Diagrams of a) CFT description of *d*-orbital degeneracy splitting in octahedral complexes of transition metals caused by a spherical distribution of six charges, b) geometries of 3*d* orbitals. Taken from reference[81].

LFT is more sophisticated, but also more complex than CFT. It can be considered as an extension to CFT, because it describes complexes in the same way, but treats bonding as dative covalent (coordination) based on molecular orbital theory (MO), where each ligand donates two electrons (lone pair) per bond. Therefore, LFT can explain bonding of neutral ligands, and give a more accurate description of ligands' strength, magnetic and colour properties. In LFT description of an octahedral complex of a transition metal, ligands also approach along the x, y and z axes. The overlap of two ligand lone pairs with d_{z^2} and $d_{x^2-y^2}$ orbitals is treated as a formation

of molecular orbitals (σ-bonding), i.e. formation of bonding and anti-bonding orbitals. The other four lone pairs form bonding (and anti-bonding) molecular orbitals with $4s$ and $4p$ metal orbitals, while the d_{xy}, d_{xz} and d_{yz} orbitals remain non-bonding as shown in figure 1.6.

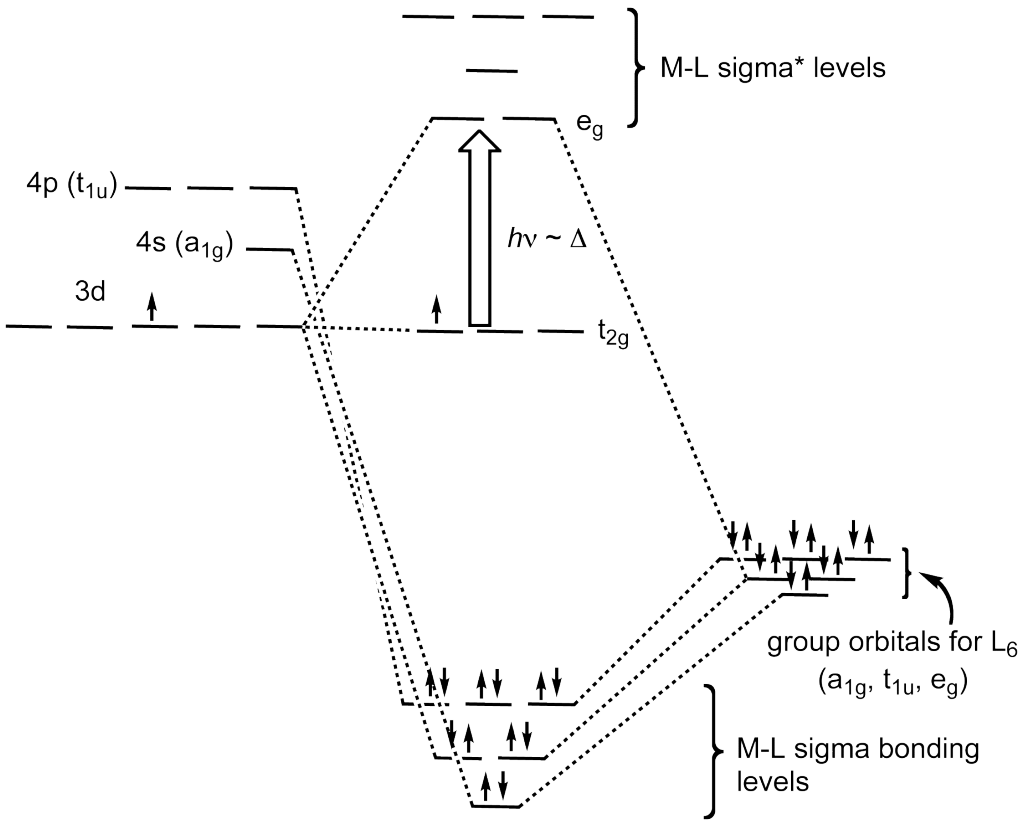

FIGURE 1.6: Diagrams of LFT description of d-orbital degeneracy splitting in octahedral complexes of transition metals that originates from formation of molecular orbitals. Taken from a public domain source.

LFT also explains more accurately than CFT the variation in coordination strength among ligands by the presence of additional π-bonding. It can occur between d_{xy}, d_{xz} and d_{yz} (otherwise non-bonding) and any of ligand's π and π^*, or p orbitals that are not involved in σ-bonding already. They can be categorised into two groups: metal-to-ligand π-bonding (π backbonding) and ligand-to-metal π-bonding. The former leads to the donation of electrons by the metal centre to the ligands (π-acceptor, such as CN^-, CO), which significantly strengthens the metal-ligand bond

and increases Δ_o, while the latter leads to the donation of electrons by the ligands (π-donors, such as I^-) to the metal centre and reduces Δ_o.

A partial list of ligands and metal ions in order of increasing Δ_o
$O_2^{2-} < I^- < Br^- < S^{2-} < SCN^- < Cl^- < NO_3^- < N_3^- < F^- < OH^- < C_2O_4^{2-} \approx H_2O <$ $NCS^- <$ MeCN $<$ pyridine $< NH_3 <$ en (ethylenediamine) $<$ bipy (2,2'-bipyridine) $<$ phen (1,10-phenanthroline) $< NO_2^- < PPh_3 < CN^- \approx$ CO
and $Mn^{2+} < Ni^{2+} < Co^{2+} < Fe^{2+} < V^{2+} < Fe^{3+} < Cr^{3+} < V^{3+} < Co^{3+} < Mn^{4+} <$ $Mo^{3+} < Rh^{3+} < Ru^{3+} < Pd^{4+} < Ir^{3+} < Pt^{4+}$.

The order of ligands is independent of the identity of the metal centre of the complex, and likewise the order of metal ions is largely independent of identity of the ligand. However, the order of increasing ligand field strength does not necessarily correlate to the order of increasing binding affinities of the ligands. Depending on a charge of metal complex, weak field anionic ligands (e.g. Cl^- or N_3^-) can exhibit much higher affinity than strong field neutral ligands (e.g. MeCN or pyridine),[82] which is attributed to a greater stabilisation energy gained from binding anionic ligand than from complex transition from LS to HS state.

In metal complexes with other coordination geometries, ligands interact with different metal centre orbitals, which can lead to various grouping and arrangement of the orbitals with more than two distinct energy levels.

1.4 Click chemistry

Click chemistry[83] is a quick, reliable, efficient, biocompatibile, highly selective and versatile method to join two molecular units together.[83–87] Therefore, it is widely used in areas such as material science,[88–90] biosciences,[88,89,91–96] and drug developement.[88,89,92,96,97] Furthermore, click chemistry and requirements for the chemical reactions performed on a surface share the same characteristics.[98] Consequently, a number of the application of click reactions in SAM environment have been reported, for example, incorporation of functional groups,[98–103] control of cell adhesion due to the ease of precise conjugation of peptides at a desired density via click chemistry on otherwise bioinert SAMs,[99] investigation of biomimetic electrocatalysis under rate limited electron transfer,[104] application in micro printing (μCP) due to fast reaction rates in click chemistry,[105,106] and use in production of SAMs with chemical gradients and patterns.[91,105]

1.5 Thesis outline

This thesis investigates fabrication of SAMs to yield surfaces with an intrinsic active function. The current chapter provides an introduction to this thesis, the aim and objectives as well as relevant background knowledge. The rest of the thesis is organised into the following chapters:

Chapter 2 describes characterisation techniques and details preparation methods for the fabrication, photolysis, and photo-patterning of SAMs on gold surfaces.

Chapter 3 characterises 1-acetylpyrene protected carboxylic acid SAMs, describes effects of its photolysis under soft ultraviolet light (365 nm) irradiation in various catalysts and the resulting monolayers. Probable pathways of the photolysis are discussed with a special focus on instability of the resulting lipoic acid monolayer under the photolysis conditions. Also, photo-patterning of the SAM and its use as a template for selective metallisation with copper (ECD) on the photolysed regions are demonstrated. Finally, a brief study on formation of fluorescent hydrophobic layers (not SAMs) on glass and silicon oxide surfaces and their photo-patterning, that produces hydrophilic non-fluorescent regions, is presented.

Chapter 4 discusses SAM fabrication of two novel ligands and their corresponding Fe(II) complexes that exhibit SCO behaviour in bulk. It demonstrates that SAM of one of the ligands does not coordinate Fe(II), and its preformed Fe(II) complex is not stable on gold surface and forms a monolayer of just the ligand. On the other hand, SAM of the other ligand successfully coordinates Fe(II), and does so at nearly 100 % yield; furthermore, its preformed Fe(II) complex also successfully forms a SAM. Finally, possible causes that might be preventing (i) SCO behaviour and (ii) change of spin state or ligand exchange in the SAM upon rinsing with appropriate solvent are discussed, and a number of solutions are proposed.

Chapter 5 consists of three parts. The first presents a study on UV and acid impact on stability of lipoic acid SAM. It also shows that the loss of molecules under soft UV irradiation in acidic conditions is a general phenomenon among conventional thiol SAMs terminated with COOH groups. It is also shown that severity of the loss is high in thin SAMs, while long chain SAMs are not affected. The possibility to use patterned short chain COOH-terminated SAM is also investigated. The second part discusses a characterisation of azide-terminated SAMs, formation of mixed SAMs with alkanethiolooligoethyleneglycols of different chain length, and demonstrates successful click reaction on the SAM surface under aqueous conditions without the need of any catalyst. Finally, the third part demonstrates that relatively simple alkyl and aryl type SAMs can give optimal precision for the studies of surface-enhanced Raman spectroscopy (SERS) in nanoparticle-on-mirror configuration.

Chapter 6 contains conclusions and suggestions for further studies in each area.

1.6 References

[1]A. Ulman, Chem. Rev. **96**, 1533–1554 (1996).

[2]F. Schreiber, Prog. Surf. Sci. **65**, 151–256 (2000).

[3]G. M. Whitesides and B. Grzybowski, Science **295**, 2418–2421 (2002).

[4]J. C. Love, L. A. Estroff, J. K. Kriebel, R. G. Nuzzo and G. M. Whitesides, Chem. Rev. **105**, 1103–1170 (2005).

[5]P. E. Laibinis, G. M. Whitesides, D. L. Allara, Y. T. Tao, A. N. Parikh and R. G. Nuzzo, J. Am. Chem. Soc. **113**, 7152–7167 (1991).

[6]S. A. Jadhav, J. Phys. Org. Chem. (2016) `10.1002/poc.3611`.

[7]T. Kondo and K. Uosaki, J. Photochem. Photobiol. C Photochem. Rev. **8**, 1–17 (2007).

[8]P. M. Mendes, Chem. Soc. Rev. **42**, 9207–9218 (2013).

[9]T. Noyhouzer and D. Mandler, Anal. Chim. Acta **684**, 1–7 (2011).

[10]D. K. Schwartz, Phys. Chem. **52**, 107–137 (2001).

[11]Y. Zhou, C. W. Chiu and H. Liang, Sensors (Switzerland) **12**, 15036–15062 (2012).

[12]W. Bigelow, D. Pickett and W. Zisman, J. Colloid Sci. **1**, 513–538 (1946).

[13]C. R. Hastings, W. A. Aue and J. M. Augl, J. Chromatogr. A **53**, 487–506 (1970).

[14]J. J. Kirkland, J. Chromatogr. Sci. **9**, 206–214 (1971).

[15]H. H. Weetall and L. S. Hersh, Biochim. Biophys. Acta - Enzymol. **206**, 54–60 (1970).

[16]J. Sagiv, J. Am. Chem. Soc. **399**, 92–98 (1980).

[17]M. E. McGovern, K. M. R. Kallury and M. Thompson, Langmuir **10**, 3607–3614 (1994).

[18]B. C. Bunker, R. W. Carpick, R. A. Assink, M. L. Thomas, M. G. Hankins, J. A. Voigt, D. Sipola, M. P. De Boer and G. L. Gulley, Langmuir **16**, 7742–7751 (2000).

[19]R. G. Nuzzo and D. L. Allara, J. Am. Chem. Soc. **105**, 4481–4483 (1983).

[20]P. E. Laibinis and G. M. Whitesides, J. Am. Chem. Soc. **114**, 1990–1995 (1992).

[21]Z. Wang, J. Chen, S. Oyola-Reynoso and M. Thuo, Coatings **5**, 1034–1055 (2015).

[22]S. A. Claridge, W.-S. Liao, J. C. Thomas, Y. Zhao, H. H. Cao, S. Cheunkar, A. C. Serino, A. M. Andrews and P. S. Weiss, Chem. Soc. Rev. **42**, 2725–45 (2013).

[23]L. Kankate, A. Turchanin and A. Gölzhäuser, Langmuir **25**, 10435–10438 (2009).

[24]S. M. Ansar, G. S. Perera, D. Jiang, R. A. Holler and D. Zhang, J. Phys. Chem. C **117**, 8793–8798 (2013).

[25]B. Varnholt, P. Oulevey, S. Luber, C. Kumara, A. Dass and T. Bürgi, J. Phys. Chem. B **118**, 9604–9611 (2014).

[26]T. Ishida, S. Yamamoto, W. Mizutani, M. Motomatsu, H. Tokumoto, H. Hokari, H. Azehara and M. Fujihira, Langmuir **13**, 3261–3265 (1997).

[27]R. G. Nuzzo, B. R. Zegarski and L. H. Dubois, J. Am. Chem. Soc. **109**, 733–740 (1987).

[28]D. G. Castner, K. Hinds and D. W. Grainger, Langmuir **12**, 5083–5086 (1996).

[29]T. J. Hummel, S. S. Zumdahl and S. A. Zumdahl, *Chemistry*, 5th ed. (Houghton Mifflin, 2000), ISBN: 0395985889.

[30]M. D. Porter, T. B. Bright, D. L. Allara and C. E. D. Chidsey, J. Am. Chem. Soc. **109**, 3559–3568 (1987).

[31]C.-J. Zhong, R. C. Brush, J. Anderegg and M. D. Porter, Langmuir **15**, 518–525 (1999).

[32]H. Takiguchi, K. Sato, T. Ishida, K. Abe, K. Yase and K. Tamada, Langmuir **16**, 1703–1710 (2000).

[33]M. Tachibana, K. Yoshizawa, A. Ogawa, H. Fujimoto and R. Hoffmann, J. Phys. Chem. B **106**, 12727–12736 (2002).

[34]A. Ulman, *Self-assembled monolayers of thiols* (Academic Press, San Diego, 1998), ISBN: 0125330243.

[35]A. Ulman, *An Introduction to Ultrathin Organic Films from Langmuir-Blodgett to Self-Assembly* (Academic Press, Boston, 1991), ISBN: 0127082301.

[36]N. Camillone, C. E. D. Chidsey, G. Liu, G. Scoles and N. C. Iii, J. Chem. Phys. **3503**, 3503–3511 (2011).

[37]R. L. Whetten and R. C. Price, Sci. 318 **318**, 407–408 (2007).

[38]H. Häkkinen, Nat. Chem. **4**, 443–455 (2012).

[39]T. Bürgi, Nanoscale **7**, 15553–15567 (2015).

[40]R. H. Tredgold, *Order in Thin Organic Films* (Cambridge University Press, New York, 1994), ISBN: 0521394848.

[41]P. M. Mendes and J. A. Preece, Curr. Opin. Colloid Interface Sci. **9**, 236–248 (2004).

[42]H. Liu, S. Hoeppener and U. S. Schubert, Adv. Eng. Mater. **18**, 890–902 (2016).

[43]F. M. Wisser, B. Schumm, G. Mondin, J. Grothe and S. Kaskel, J. Mater. Chem. C **3**, 2717–2731 (2015).

[44]W. Z. Krishnan and K. M, J. Micromechanics Microengineering **24**, 93001 (2014).

[45]M. J. Hynes and J. a. Maurer, Mol. Biosyst. **9**, 559–564 (2013).

[46]A. Carlson, A. M. Bowen, Y. Huang, R. G. Nuzzo and J. A. Rogers, Adv. Mater. **24**, 5284–5318 (2012).

[47]J. T. Koepsel and W. L. Murphy, ChemBioChem **13**, 1717–1724 (2012).

[48]S. J. Koh, Nanoscale Res. Lett. **2**, 519–545 (2007).

[49]R. Garcia, R. V. Martinez and J. Martinez, Chem.Soc.Rev. **35**, 29–38 (2005).

[50]R. K. Smith, P. A. Lewis and P. S. Weiss, Prog. Surf. Sci. **75**, 1–68 (2004).

[51]A. P. Quist, E. Pavlovic and S. Oscarsson, Anal. Bioanal. Chem. **381**, 591–600 (2005).

[52]S. Alom Ruiz and C. S. Chen, Soft Matter **3**, 168–177 (2007).

[53]X.-M. Zhao, Y. Xia and G. M. Whitesides, Adv. Mater. **8**, 837–840 (1996).

[54]E. Kim, Y. Xia and G. M. Whitesides, Nature **376**, 581–584 (1995).

[55]Y. Xia, E. Kim and G. M. Whitesides, Chem. Mater. **8**, 1558–1567 (1996).

[56]L. G. Rosa and J. Liang, J. Phys. Condens. MATTER **21**, 483001 (2009).

[57]B. Basnar and I. Willner, Small **5**, 28–44 (2009).

[58]G. J. Leggett, Chem. Soc. Rev. **35**, 1150–1161 (2006).

[59]K. C. Chan, T. Kim, J. K. Schoer and R. M. Crooks, J. Am. Chem. Soc. **117**, 5875–5876 (1995).

[60]O. Ivashenko, J. T. V. Herpt, B. L. Feringa, P. Rudolf and W. R. Browne, Langmuir **29**, 4290–4297 (2013).

[61]P. Prompinit, A. S. Achalkumar, A. S. Walton, R. J. Bushby, C. Wälti and S. D. Evans, J. Mater. Chem. C **2**, 5916 (2014).

[62]K. Critchley, J. P. Jeyadevan, H. Fukushima, M. Ishida, T. Shimoda, R. J. Bushby and S. D. Evans, Langmuir **21**, 4554–4561 (2005).

[63]Y. Yang, Q. Shao, R. Deng, C. Wang, X. Teng, K. Cheng, Z. Cheng, L. Huang, Z. Liu, X. Liu and B. Xing, Angew. Chemie - Int. Ed. **51**, 3125–3129 (2012).

[64]Y. Yang, B. Velmurugan, X. Liu and B. Xing, Small **9**, 2937–2944 (2013).

[65]C. L. Yeung, S. Charlesworth, P. Iqbal, J. Bowen, J. a. Preece and P. M. Mendes, Phys. Chem. Chem. Phys. **15**, 11014–24 (2013).

[66]M. Nakagawa and K. Ichimura, **204**, 1–7 (2002).

[67]B. Zhao, J. S. Moore and D. J. Beebe, Anal. Chem. **74**, 4259–4268 (2002).

[68]P. Prompinit, A. S. Achalkumar, X. Han, R. J. Bushby, C. Wälti and S. D. Evans, J. Phys. Chem. C **113**, 21642–21647 (2009).

[69]M. K. F. Lo, M. N. Gard, B. R. Goldsmith, M. A. Garcia-Garibay and H. G. Monbouquette, Langmuir **28**, 16156–16166 (2012).

[70]O. El Zubir, I. Barlow, E. Ul-Haq, H. A. Tajuddin, N. H. Williams and G. J. Leggett, Langmuir **29**, 1083–1092 (2013).

[71]T. A. Martin, C. T. Herman, F. T. Limpoco, M. C. Michael, G. K. Potts and R. C. Bailey, ACS Appl. Mater. Interfaces **3**, 3762–3771 (2011).

[72]S. H. Kim, H. Ohtsuka, M. C. R. Tria, K. Tanaka, R. C. Advincula and H. Usui, Thin Solid Films **554**, 78–83 (2014).

[73]Y. Yu, X. Kang, X. Yang, L. Yuan, W. Feng and S. Cui, Chem. Commun. (Camb). **49**, 3431–3 (2013).

[74]A. Jana, S. Atta, S. K. Sarkar and N. D. P. Singh, Tetrahedron **66**, 9798–9807 (2010).

[75]M. Hostettler, K. W. Törnroos, D. Chernyshov, B. Vangdal and H. B. Bürgi, Angew. Chemie - Int. Ed. **43**, 4589–4594 (2004).

[76]P. Gütlich and H. A. Goodwin, *Spin Crossover in Transition Metal Compounds I*, Spin Crossover in Transition Metal Compounds (Springer, Berlin, 2004), ISBN: 9783540403944.

[77]O. Kahn and C. Jay Martinez, Science **279**, 44–48 (1998).

[78]L. Cambi and L. Szegö, Ber. Dtsch. Chem. Ges. (A B Ser., 2591–2598 (1931).

[79]J. A. Real, A. B. Gaspar, V. Niel and M. C. Muñoz, Coord. Chem. Rev. **236**, 121–141 (2003).

[80]N. N. Greenwood and A. Earnshaw, *Chemistry of the Elements (2nd ed.)* (Butterworth-Heinemann, 1997).

[81]B. Averill and P. Eldredge, *General Chemistry: Principles, Patterns, and Applications* (Saylor Foundation, 2011), ISBN: 9781453322307.

[82]C. R. Goldsmith, R. T. Jonas, A. P. Cole and T. D. P. Stack, Inorg. Chem. **41**, 4642–4652 (2002).

[83]H. C. Kolb, M. G. Finn and K. B. Sharpless, Angew. Chemie - Int. Ed. **40**, 2004–2021 (2001).

[84]E. M. Sletten and C. R. Bertozzi, Angew. Chemie - Int. Ed. **48**, 6974–6998 (2009).

[85]M. D. Best, Biochemistry **48**, 6571–6584 (2009).

[86]J. C. Jewett and C. R. Bertozzi, Chem. Soc. Rev. **39**, 1272–9 (2010).

[87]E. Lallana, R. Riguera and E. Fernandez-Megia, Angew. Chemie - Int. Ed. **50**, 8794–8804 (2011).

[88]J. E. Moses and A. D. Moorhouse, Chem. Soc. Rev. **36**, 1249–1262 (2007).

[89]K. Nwe and M. W. Brechbiel, Cancer Biother. Radiopharm. **24**, 289–302 (2009).

[90]R. A. Evans, Aust. J. Chem. **60**, 384–395 (2007).

[91]C. Nicosia and J. Huskens, Mater. Horizons **1**, 32 (2014).

[92]C. Hein, X.-M. Liu and D. Wang, Pharm Res **25**, 2216–2230 (2009).

[93]M. Grammel and H. C. Hang, Nat Chem Biol **9**, 475–484 (2013).

[94]R. Xie, S. Hong and X. Chen, Curr. Opin. Chem. Biol. **17**, 747–752 (2013).

[95]Y. Su, J. Ge, B. Zhu, Y. G. Zheng, Q. Zhu and S. Q. Yao, Curr. Opin. Chem. Biol. **17**, 768–775 (2013).

[96]P. Thirumurugan, D. Matosiuk and K. Jozwiak, Chem. Rev. **113**, 4905–4979 (2013).

[97]D. Zeng, B. M. Zeglis, J. S. Lewis and C. J. Anderson, J. Nucl. Med. **54**, 829–32 (2013).

[98]N. K. Devaraj and J. P. Collman, QSAR Comb. Sci. **26**, 1253–1260 (2007).

[99]G. A. Hudalla and W. L. Murphy, Langmuir **25**, 5737–5746 (2009).

[100]D. Samanta and A. Sarkar, Chem. Soc. Rev. **40**, 2567–2592 (2011).

[101]R. Chelmowski, D. Kafer, S. D. Köster, T. Klasen, T. Winkler, A. Terfort, N. Metzler-Nolte and C. Wöll, Langmuir **25**, 11480–11485 (2009).

[102]I. S. Choi and Y. S. Chi, Angew. Chemie - Int. Ed. **45**, 4894–4897 (2006).

[103]M. V. Gil, M. J. Arévalo and Ó. López, Synthesis **11**, 1589–1620 (2007).

[104]R. a. Decréau, J. P. Collman and A. Hosseini, Chem. Soc. Rev. **39**, 1291–1301 (2010).

[105]J. Wang, F. Wu, M. Watkinson, J. Zhu and S. Krause, Langmuir **31**, 9646–9654 (2015).

[106]J. Mehlich and B. J. Ravoo, Org. Biomol. Chem. **9**, 4108 (2011).

Chapter 2

Experimental methods

2.1 X-ray Photoelectron Spectroscopy (XPS)

X-ray Photoelectron Spectroscopy (XPS), also known as Electron Spectroscopy for Chemical Analysis (ESCA),[1] is a powerful surface sensitive technique providing qualitative and quantitative data. This method is extremely useful to study SAMs structure, because it probes the outer ∼10 nm of a surface and provides not only elemental composition and surface coverage, but also chemical state of elements.[1]

XPS relies on photoelectric effect to identify specific atoms on a surface. If an incident photon has an energy (frequency) equal to or higher than the binding (ionisation) energy of an electron in an atom, an electron (conventionally referred to as a photoelectron) can be ejected and its kinetic energy can be described by Einstein's equation:

$$KE = h\nu - BE \tag{2.1}$$

where KE is the kinetic energy of the ejected electron, $h\nu$ is the energy of a photon and BE is the binding energy of the electron in an atom, which depends on an element, orbital and chemical state of the atom. When irradiated with a beam

of light, the number of generated photoelectrons is proportional to the number of incident photons that have sufficient energy (frequency). However, if energy (frequency) of incident photons is below the binding energy of the electrons, no electrons are ejected, regardless of beam intensity (number of photons) or irradiation time. Weakly bound outer shell (valence) electrons can be ejected with a UV light, however, probing inner shell (core) electrons requires photons of much higher energy, such as X-rays.

During XPS measurements, a sample is usually irradiated with X-rays of a known energy (typically 1.2 - 1.5 keV). A set of lenses is used to capture and direct emitted photoelectrons towards the analyser and detector, where the number of electrons is recorded as a function of their kinetic energy, in order to produce photoelectron spectra. Although soft X-rays penetrate deep into a sample, ejected (photo)electrons ($\sim$1 keV) rapidly lose their kinetic energy through inelastic scattering.[1] An average distance that an electron travels between two inelastic collision is called 'inelastic mean free path' (IMFP), often noted with a symbol λ. A number of factors influence the IMFP length, but it mostly depends on the energy of photoelectron and type of material that it travels through. Photoelectrons that do not experience inelastic collisions form peaks in XPS spectra, while the rest contribute to the background. If I_0 is the number of electrons generated at depth x below the sample surface/vacuum interface and θ is the take off angle, the number of electrons reaching the surface is given by:

$$I = I_0 e^{\frac{-x}{\lambda \sin \theta}}, \tag{2.2}$$

which closely relates to Beer-Lambert law in optics.[1] The integrated area under a curve defined by the equation above shows that 95% of all detected photoelectrons come from within a depth of $3\lambda \sin \theta$, which is defined as XPS sampling depth and

typically is of the order of 3 - 10nm. Therefore, such strong electron interaction with matter allows XPS technique to probe the outermost layers of a sample surface.

Each peak in the XPS spectra relates to the energy state that electrons were ejected from, which can be described using three principle quantum numbers: (i) energy level n = 1, 2, .. of the electron; (ii) the electron's orbital angular momentum, l, which can have any positive integer value between 0 and $n - 1$; and (iii) spin of the electron, s, which has either a value of $-1/2$ (spin down) or $+1/2$ (spin up).[1] A particular peak is labelled in the form of 'nl_j', where $j = |l + s|$ refers to total angular momentum of the electron based on j-j coupling nomenclature.[1] Typically only electrons from subshells l = 0, 1, 2 and 3 appear in XPS spectra and it is conventional to refer to them in 'nl_j' as s, p, d and f, respectively. For example, the most intense peaks of oxygen and carbon atoms are labelled as $O1s_{1/2}$ and $C1s_{1/2}$, because they are produced by electrons ejected from 's' subshell (l = 0) in the first energy level (n = 1). It is common to drop the subscript, when referring to subshell 's', which, regardless of energy level, has zero angular momentum and leads to the same total angular momentum $j = |0 \pm 1/2| = 1/2$ and energy state for both spin-up and spin-down electrons. Consequently, shortened labels, for example $O\,1s$ or $C\,1s$, are more common. In all other subshells, the electron has non-zero orbital angular momentum, which interacts with the intrinsic spin of the unpaired electron (left behind after its partner was photoejected from the orbital) and leads to spin-orbit splitting with two distinct energy levels. As a result, doublet appears instead of a single peak. For example, in XPS spectra of gold, the strongest feature is a doublet arising from photoelectrons in 'f' subshell (l = 3) in the fourth energy level (n = 4). Due to spin-orbit coupling, the total angular momentum is equal to $j = |3 - 1/2| = 5/2$ for spin-down electron and $j = |3 + 1/2| = 7/2$ for spin-up electron, which leads to two different energy states corresponding to $Au\,4f_{5/2}$ and $Au\,4f_{7/2}$ peaks in the XPS spectra. Each state has different $(2j + 1)$ degeneracy, which in turn determines the ratio of the peak areas in a doublet.

XPS data presented in this thesis were collected using two instruments. Vast majority of samples were analysed using ThermoVG ESCA-Lab 250 system with a monochromated Al $K\alpha$ (1486.7 eV) X-ray source (15 kV 150 W), with a beam spot diameter of 500 μm, and with activated magnetic lens 'Large Area XL'. Pass energy was set to 150 eV and 20 eV to acquire survey and high resolution spectra, respectively. However, some of the XPS spectra presented in chapters 3 and 5 were acquired with a Thermo Scientific K-Alpha XPS system at the National ERSRC XPS Users' Service (NEXUS) at Newcastle University. Samples were irradiated with a monochromated Al $K\alpha$ (1486.7 eV) X-ray source (12 kV 36 W), with a beam spot diameter of 400 μm, and with activated standard lens. Pass energy was set to 200 eV and 40 eV to acquire survey and high resolution spectra, respectively.

All of the spectra were obtained with an electron take-off angle of 90°. High resolution spectra were fitted using CasaXPS (version 2.3.16) peak fitting algorithms. All spectra have been referenced to alkyl/aryl C 1s peak at 284.5 eV, unless stated otherwise.

2.2 Contact Angle measurements (CA)

Surface wettability is a useful technique for studying surface disorder and composition. It is particularly useful for monitoring SAM quality, change in the hydrophobicity of SAM surface and mixing of multiple components in a SAM.[2–4]

By placing a small droplet of liquid on a flat surface, contact angle can be obtained, which provides information about surface free energy. Surface energy can be expressed as linear combination of polar (polar interaction and hydrogen bonding) and dispersive (van der Waals) parts, which can be studied individually by probing the chosen surface with polar (e.g. water) or non-polar (e.g. hexadecane) liquid.

Work of adhesion due to all interactions between solid and liquid mediums surrounded by vapour is given by:

$$W_{SLV} = \gamma_{SV} + \gamma_{LV} - \gamma_{SL}, \tag{2.3}$$

where γ is the interfacial tension (surface tension or surface free energy per unit area) between liquid-vapour γ_{LV}, solid-vapour γ_{SV} and solid-liquid γ_{SL} interfaces measured in units of N m^{-1} or J m^{-2}. Consequently, total surface energy can be written as:

$$W_{Total} = \gamma_{LV}(A_c + A_f) - W_{SLV}A_f, \tag{2.4}$$

where A_c is curved and A_f is flat areas of a droplet. If the contact line of intersection of the three interfaces is moved infinitesimally, then the equation can be rewritten as:

$$0 = \gamma_{LV}(dA_c + dA_f) - W_{SLV}dA_f, \tag{2.5}$$

which gives Young's equation after $cos\theta = \frac{dA_c}{dA_f}$ substitution and combination with equation 2.3:

$$\gamma_{LV}\cos\theta = \gamma_{SV} - \gamma_{SL}, \tag{2.6}$$

which directly relates contact angle at the edge of a liquid drop and surface tension between solid, liquid and gas phases. Contact angle can be measured on static, advancing and receding droplets. In practise, hysteresis exists between advancing and receding angles, which most often originate from pinning due to surface roughness and chemical heterogeneity.[5,6] Hysteresis of $\sim 10°$ is typical even for highly ordered SAMs.

Wetting can be used to study mixed SAMs consisting of components with different hydrophobicities. Contact angle can be predicted using Cassie equation, which averages adhesion energies of each component[7]

$$\cos\theta = \sum_n f_n \cos\theta_n \tag{2.7}$$

or Israelachvili-Gee equation, which averages molecular polarisation[8]

$$(1+\cos\theta)^2 = \sum_n f_n (1+\cos\theta_n)^2, \tag{2.8}$$

where f_n refers to the fractional area of the surface that makes contact angle θ_n. It has been shown that fitting both equations to experimental data produces small differences due to the inherent spread of data.[9]

Contact angle measurements were obtained using FTA4000 (First Ten Angstrom, USA) goniometer. Typically advancing and receding angles were measured to determine SAM characteristics and qualitatively describe surface composition or presence of possible functional groups.

2.3 Ellipsometry

Ellipsometry is an established technique for determining the thickness and/or refractive index of thin films. It measures the change in polarisation of light upon specular reflection from (or transmission through) the sample of interest by acquiring ellipsometric angles Ψ and Δ related to change in amplitudes and phase respectively. Using various models, Ψ and Δ can be related to a number of properties, for example optical constants (complex refractive index or dielectric function) and thickness of films, interface roughness and mixing. Due to high sensitivity of

Δ in sub-10nm regime, ellipsometry is ideal for studying SAMs thickness. Measurements can be obtained at a single wavelength and angle of incidence, however, usually multiple wavelengths and/or angles are used to extract more information and at the higher precision, especially for complex multilayer samples.

2.3.1 Polarisation states

Polarisation is the direction (axis) that the electric field component of an electromagnetic wave is oscillating along. If the direction of the oscillation is constantly changing, then the polarisation state can be defined by tracing the tip of the electric field vector over one oscillation cycle. Polarised light can be considered to be a superposition of two light waves (components) in orthogonal (for example Cartesian x and y) planes. If both components oscillate in phase, than linearly polarised light is produced in the $x - y$ plane and ratio of the amplitudes determines the angle between the x (or y) axis and direction of polarisation (e.g. 45° when both components have equal amplitudes). If both components have the same amplitude, but there is a 90° phase shift in oscillation between the two waves, then circular polarisation is obtained. In all the other cases, elliptically polarised light is produced. Any polarisation state can be fully characterised with two parameters Ψ and Δ, which will be discussed in following sections.

2.3.2 Light interaction with interface: Fresnel coefficients

For studies of light interaction with surfaces and interfaces, it is convenient to consider light as a superposition of the p-component, which lies in the plane of incidence, and the s-component, which lies in the perpendicular plane. Depending on an experimental set up and a sample (e.g. angle of incidence, refractive index of medium

on each side of the interface, roughness of the interfaces etc.), molecules interact differently with s- and p- components and usually refract (transmit) and reflect them with different amplitudes and/or phases. If incident light is linearly polarised, then reflection from an interface between two transparent media leads to a different linear polarisation state, while reflection from an interface where at least one medium is absorbing produces elliptical polarisation. In this case, the strength of ellipticity depends on angle of incidence and absorption coefficient of the medium.

Complex Fresnel coefficients determine the amplitudes of reflected and transmitted light. They can be derived by (i) considering a ratio of complex amplitudes of reflected (or transmitted) and incident light for both s- and p- components, and then (ii) matching tangential electric **E** and magnetic **H** fields across an interface

$$r_{p01} = \frac{E_p^r}{E_p^i} = \frac{N_1 \cos\theta_0 - N_0 \cos\theta_1}{N_1 \cos\theta_0 + N_0 \cos\theta_1} = \frac{\tan(\theta_0 - \theta_1)}{\tan(\theta_0 + \theta_1)} \tag{2.9}$$

$$r_{s01} = \frac{E_s^r}{E_s^i} = \frac{N_0 \cos\theta_0 - N_1 \cos\theta_1}{N_0 \cos\theta_0 + N_1 \cos\theta_1} = \frac{-\sin(\theta_0 - \theta_1)}{\sin(\theta_0 + \theta_1)} \tag{2.10}$$

$$t_{p01} = \frac{E_p^t}{E_p^i} = \frac{2N_0 \cos\theta_0}{N_1 \cos\theta_0 + N_0 \cos\theta_1} = \frac{2\sin\theta_1 \cos\theta_0}{\sin(\theta_0 + \theta_1)\cos(\theta_0 - \theta_1)} \tag{2.11}$$

$$t_{s01} = \frac{E_s^t}{E_s^i} = \frac{2N_0 \cos\theta_0}{N_0 \cos\theta_0 + N_1 \cos\theta_1} = \frac{2\sin\theta_1 \cos\theta_0}{\sin(\theta_0 + \theta_1)} \tag{2.12}$$

where r_{p01} refers to the complex Fresnel coefficient for p-polarised light propagating through medium 0 and reflected by the interface with medium 1; superscripts i, r and t refer to incident, reflected and transmitted lights, N_0 and N_1 correspond to the complex refractive index of medium 0 and 1, θ_0 and θ_1 denote incident and refracted angles, respectively. Similarly, r_{s01} coefficient refers to s-polarised light, while t_{p01} and t_{s01} coefficients correspond to transmitted light.

It is useful to note that if the direction of propagation of refracted wave in medium 1 is reversed, i.e. light propagates through medium 1 before it interacts with the same interface at angle θ_1 (which is equal to the refracted angle in the previous set up), then Fresnel coefficients r_{10} and t_{10} are related to r_{01} and t_{01} by

$$r_{10} = -r_{01} \tag{2.13}$$

$$t_{10} = \frac{1 - r_{01}^2}{t_{01}} \tag{2.14}$$

Equations above apply to both p and s polarisations, thus the subscripts are dropped.

2.3.3 Relating Ψ and Δ to measured complex reflection ratio ρ

In order to determine the polarisation state, the ellipsometer obtains Ψ and Δ by measuring complex reflectance ratio ρ given by

$$\rho = \frac{R_p}{R_s} = \tan(\Psi) e^{i\Delta} \tag{2.15}$$

where R_p and R_s refer to overall complex-amplitude reflection coefficients (equal to individual or a combination of complex Fresnel coefficients) for p- and s- components, respectively. They also correspond to the ratio of total reflected wave (after interaction with all interfaces and media present in the sample) and total incident wave for each component, as shown by the following equations

$$R_p = \frac{E_p^r}{E_p^i} = \frac{|E_p^r| e^{i\delta_p^r}}{|E_p^i| e^{i\delta_p^i}} = \frac{|E_p^r|}{|E_p^i|} e^{i(\delta_p^r - \delta_p^i)} \tag{2.16}$$

$$R_s = \frac{E_s^r}{E_s^i} = \frac{|E_s^r| e^{i\delta_s^r}}{|E_s^i| e^{i\delta_s^i}} = \frac{|E_s^r|}{|E_s^i|} e^{i(\delta_s^r - \delta_s^i)}, \tag{2.17}$$

where E is the electric field amplitude, δ is the phase offset, i and r superscripts refer to incident and reflected waves, p and s subscripts correspond to p and s components, i preceding δ or parenthesis denotes the imaginary unit. By combining equations 2.15, 2.16 and 2.17, it can be shown that Ψ is related to the ratio of (normalised to the initial values) reflected amplitudes of p and s components

$$\tan \Psi = \frac{|E_p^r|/|E_p^i|}{|E_s^r|/|E_s^i|} \tag{2.18}$$

and Δ describes the difference between the phase shifts in each component

$$\Delta = (\delta_p^r - \delta_p^i) - (\delta_s^r - \delta_s^i) \tag{2.19}$$

Various information, such as optical constants and thickness of each medium, surface roughness, interfacial mixing etc. can be extracted from Ψ and Δ using appropriate models.

2.3.4 Relating Ψ and Δ to physical properties of two- and three-layer models

Light interaction with a sample can be modelled in various ways depending on its complexity. The simplest approach is a two-layer model consisting of semi-infinite ambient and sample of interest media, as illustrated in figure 2.1. Light incident onto the interface of the media is reflected and transmitted with amplitudes defined by complex Fresnel coefficients 2.9-2.10 and 2.11-2.12, respectively. Because the sample is treated as a semi-infinite medium, refracted light, which probes the thickness of the medium, is not reflected back towards the interface and consequently cannot be detected when the ellipsometer is operated in reflection mode. Thus,

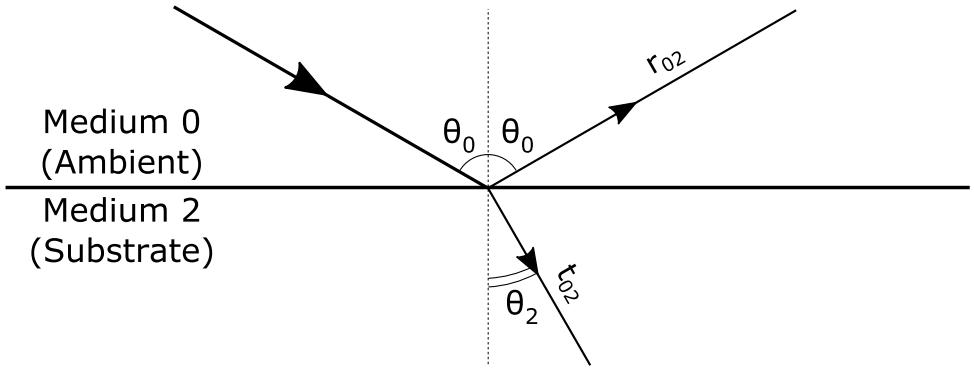

FIGURE 2.1: Oblique reflection and transmission of light by a two-layer optical system, where θ_0 and θ_2 correspond to angles of incidence (reflection) and refraction, respectively. The substrate is denoted as medium 2, in order to keep the consistent numbering with figure 2.2. One semi-infinite medium usually represents ambient and another the sample of interest, which can be just a clean substrate of a complex sample. Although thickness cannot be obtained of either of the media, due to very definition of such models, complex refractive index can be determined. Both transmitted and reflected light consist of only one wave with relative amplitudes $(r_{02}, t_{02})E_i$ defined by Fresnel coefficients. The second medium is denoted as 'Medium 2 (Substrate)' for easier comparison with the three-layer model that will be discussed later.

thickness of the sample cannot be obtained, due to the very definition of the two-layer model. However, other properties, for example complex refractive index, can still be determined. Because total reflected light consists of only one wave, which is reflected from only one interface, overall complex-amplitude and Fresnel coefficients are equal ($R_p = r_p$, $R_s = r_s$), thus Ψ and Δ can be related to the complex refractive index by combining equations 2.15, 2.9 and 2.10 into the following expression

$$\begin{aligned}\tan(\Psi)e^{i\Delta} = \frac{R_p}{R_s} = \frac{r_{p01}}{r_{s01}} &= \frac{N_1\cos\theta_0 - N_0\cos\theta_1}{N_1\cos\theta_0 + N_0\cos\theta_1} \cdot \frac{N_0\cos\theta_0 + N_1\cos\theta_1}{N_0\cos\theta_0 - N_1\cos\theta_1} \\ &= -\frac{\cos(\theta_0+\theta_1)}{\cos(\theta_0-\theta_1)}\end{aligned} \tag{2.20}$$

Often samples are more complex and require more sophisticated methods, that can accurately model them as well as extract more information from the acquired data.

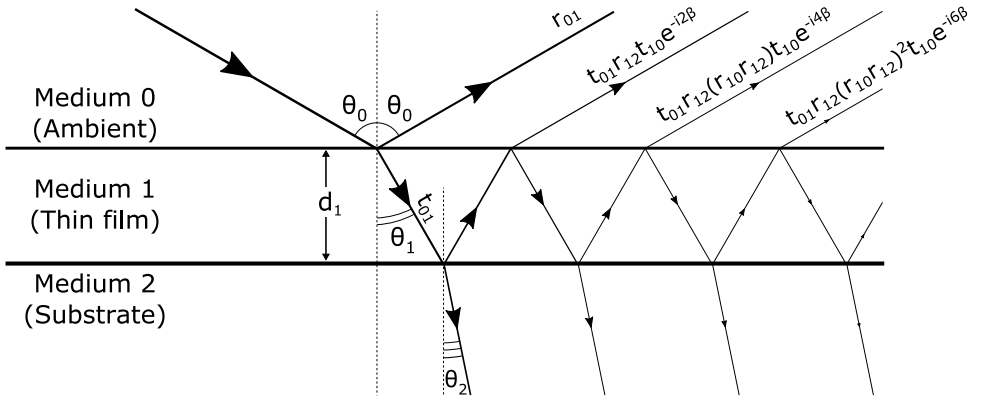

FIGURE 2.2: Oblique reflection and transmission of light by a three-layer optical system. Two semi-infinite media usually represent ambient and substrate, while medium of finite thickness d_1 correspond to the film of interest. Symbols θ_0, θ_1 and θ_2 denote angles of incidence in the ambient, refraction in the film and in the substrate, respectively. Reflected light consists of multiple waves with various relative magnitudes (r_{01}, $t_{01}r_{12}t_{10}e^{-i2\beta}$, $t_{01}r_{12}(r_{10}r_{12})t_{10}e^{-i4\beta}$, ...)$E_i$, which are defined by Fresnel coefficients (equations 2.9-2.12) and film thickness phase β (equation 2.21). Such a three layer model assumes smooth and parallel interfaces.

This can be achieved by considering a three-layer model, which can easily be expanded for multilayer samples. It consists of a finite thickness medium (e.g. film) sandwiched between semi-infinite ambient and substrate media. In contrast to the two-layer model, refracted light wave (t_{01}) into the medium 1 by the first interface (medium 0 - medium 1) does interact with the second interface (medium 1 - medium 2). Although the part of the wave that is refracted into medium 2 cannot be recorded, another part is reflected back towards the first interface, where fraction of it is transmitted into medium 0 and can be detected. This detectable wave ($t_{01}r_{12}t_{10}$) now has a phase difference of $e^{-i2\beta}$ relative to the non-refracted wave (r_{01}). Symbol β corresponds to the phase change in radians as wave propagates once between two interfaces

$$\beta = 2\pi\frac{d_1}{\lambda}N_1\sin(\theta_1) \tag{2.21}$$

where λ is the wavelength of light (in vacuum), θ_1 is the angle of refraction in medium 1, d_1 and N_1 refers to the thickness and complex refractive index of the medium 1, respectively.

As shown in the figure 2.2, when light refracts into medium 1 (t_{01}), it then reflects multiple times from each interface, but with subsequently smaller amplitude, because on each interaction a fraction of it refracts into medium 0 or medium 2. Therefore total reflected and total transmitted light by the three-layer system correspond to multiple waves with varying amplitudes. If the complex amplitude of incident light is set to unity, then reflected and transmitted waves have the same magnitude as the overall complex-amplitude coefficients

$$R = r_{01} + t_{01}r_{12}t_{10}e^{-i2\beta} + t_{01}r_{12}(r_{10}r_{12})t_{10}e^{-i4\beta} + t_{01}r_{12}(r_{10}r_{12}t_{10})^2e^{-i6\beta} + ... \quad (2.22)$$

$$T = t_{01}t_{12}e^{-i\beta} + t_{01}(r_{12}r_{10})t_{12}e^{-i3\beta} + t_{01}(r_{12}r_{10})^2t_{12}e^{-i5\beta} + ... \quad (2.23)$$

which are infinite geometric series and can be re-written as

$$R = r_{01} + \frac{t_{01}r_{12}t_{10}e^{-i2\beta}}{1 - r_{10}r_{12}e^{-i2\beta}} \quad (2.24)$$

$$T = \frac{t_{01}t_{12}e^{-i\beta}}{1 - r_{10}r_{12}e^{-i2\beta}} \quad (2.25)$$

and simplified further by substitution of equations 2.13-2.14

$$R = \frac{r_{01} + r_{12}e^{-i2\beta}}{1 + r_{01}r_{12}e^{-i2\beta}} \quad (2.26)$$

$$T = \frac{t_{01}t_{12}e^{-i2\beta}}{1 + r_{01}r_{12}e^{-i2\beta}} \quad (2.27)$$

Subscripts p and s are dropped again, because those expressions are generic and valid for light in both polarisations.

Substitution of 2.26 into 2.15 gives ρ or Ψ and Δ as functions of complex Fresnel coefficients and film thickness phase β

$$\rho = \tan(\Psi)e^{i\Delta} = \frac{R_p}{R_s} = \frac{r_{p01} + r_{p12}e^{-i2\beta}}{1 + r_{p01}r_{p12}e^{-i2\beta}} \cdot \frac{1 + r_{s01}r_{s12}e^{-i2\beta}}{r_{s01} + r_{s12}e^{-i2\beta}} \quad (2.28)$$

Additionally, the above relationship can be expressed as a function of complex indices, film thickness, angle of incidence and wavelength $\rho = f(N_0, N_1, N_2, d_1, \theta_0, \lambda)$, when substituted with equations 2.9, 2.10 and 2.21.

The function defined by the equation 2.28 has two important aspects. Firstly, by plugging-in complex Fresnel coefficients 2.9-2.10, it can be shown that when $d_1 = 0$ the expression simplifies to a two-layer model defined by equation 2.20. Thus, it allows one to use a two-layer model as a base for a three-layer system, which is particularly beneficial when working with ultra thin layers (i.e. thickness is equal to a fraction of probing wavelength). Various substrate imperfections, which have a significant contribution in the determination of film thickness, can be taken into account by performing ellipsometry measurements on a clean substrate and applying a two-layer model to extract effective optical constants for the use in a three-layer model.

Secondly, if the thin film (medium 1) is non-absorbing, i.e. refractive index N_1 is real, then function ρ, described by the equation 2.28, is periodic w.r.t. the film thickness. In other words, identical data is obtained, when ellipsometry is performed under the same conditions on two samples that are indistinguishable, except that one of them has film thickness d, while the other one has thickness $d + \frac{m\beta}{2\pi}$, where m is a positive integer. If measurements are performed at angle of incidence $\theta_0 = 70°$ in air (i.e. $N_0 = 1$) on thin films with refractive index $N_1 = 1.45$ at wavelengths 400 nm $< \lambda <$ 800 nm, then the minimum periodic thickness is $\sim$180 nm $< \frac{\beta}{2\pi} <$ $\sim$360 nm. Nevertheless, performing measurements at multiple wavelengths and/or angles of incidence increases substantially the magnitude of the period $\frac{\beta}{2\pi}$. If the film (medium 1) is absorbing, then periodicity diminishes and ρ values represent a spiral curve (in polar coordinates) connecting two discrete points corresponding to a two-layer model, where the first layer is always a semi-infinite ambient (medium

0), and the second layer is either a semi-infinite substrate (medium 2) $\rho_{02} = \frac{r_{p02}}{r_{s02}}$ or a semi-infinite film (medium 1) $\rho_{01} = \frac{r_{p01}}{r_{s01}}$.

2.3.5 Simplified film thickness calculations using linear approximation

If thickness of the film in a three-layer model changes by an increment (small fraction of the wavelength of probing light), reasonably accurate results can be produced by a linear approximation of equation 2.20 given by

$$\frac{\delta\rho}{\rho} = K\delta d_1 \tag{2.29}$$

where

$$K = -i\frac{4\pi}{\lambda}\sqrt{N_1^2 - N_0^2\sin^2(\theta_0)}[\frac{r_{p12}}{r_{p01}+r_{p12}} - \frac{r_{p01}r_{p12}}{1+r_{p01}r_{p12}} - \frac{r_{s12}}{r_{s01}+r_{s12}} + \frac{r_{s01}r_{s12}}{1+r_{s01}r_{s12}}] \tag{2.30}$$

and δd_1 is an increment in film thickness. This approach is extremely applicable, because it works for arbitrary values of d_1, including when $d_1 = 0$. Equation 2.29 can also be rearranged for $\delta\Psi$ or $\delta\Delta$

$$\delta\Psi = \frac{1}{2}\sin(2\Psi)Re(\frac{\delta\rho}{\rho}) \tag{2.31}$$

$$\delta\Delta = Im(\frac{\delta\rho}{\rho}) \tag{2.32}$$

Therefore, it can be used with effective optical constants of a substrates measured with ellipsometry and determined with a two-layer model. On the other hand, it is necessary to know an approximate complex refractive index of the film.

2.3.6 Experimental details

A Jobin-Yvon UVISEL phase modulated spectroscopic ellipsometer was used for the SAMs studies. A polariser, that is placed between the light source and a sample, produces linearly polarised light. Interaction with a surface produces elliptically polarised light, which is then modulated at 50kHz frequency, as it passes through a photoelastic modulator. Before the light is detected, it passes through another polariser (usually called the analyser), which produces linearly polarised light again. A single wavelength is extracted using the monochromator placed between the analyser and the detector. Unless stated otherwise, data were obtained at 70° angle of incidence and at wavelengths between 300 - 800 nm in 5 nm steps in both configuration II and III.

DeltaPsi2 software was used for data acquisition and fitting. SAMs on gold were treated as three-layer systems, where substrate was modelled using ellipsometry data obtained from freshly piranha cleaned gold (also referred as a 'reference') and refractive index of the film was assumed to be transparent (non-absorbing) and modelled with Cauchy's dispersion

$$n(\lambda) = n_{inf} + \frac{A}{\lambda^2} + \frac{B}{\lambda^4} \tag{2.33}$$

$$k(\lambda) = 0 \tag{2.34}$$

which describes real $n(\lambda)$ and imaginary $k(\lambda)$ parts of refractive index as functions of wavelength λ, where A, B and n_{inf} are coefficients determined by fitting. The latter was constrained tightly around $n_{inf} = 1.5$, which is commonly observed for hydrocarbons. Values of thickness were obtained using both tightly constrained around 70°and fixed at 70°angle of incidence.

Typically ellipsometry measurements were obtained from three areas on each sample (including references). At least two samples were used per each type of SAM. Reference gold samples were always taken from the same evaporation batch and at least three reference samples were used. References were cleaned for 2-3 minutes in piranha solution and rinse with copious amounts of milli-Q water immediately prior to ellipsometer measurements. Additionally C18 (1-Octadecanethiol) SAMs were prepared and measured as an additional control.

2.4 Fourier Transform Infrared Reflection Absorption Spectroscopy (FT-IRRAS)

FT-IR is a widely used technique for probing molecular structure of compounds in gaseous, liquid and solid forms. Due to strong sensitivity and certain selection rules, it is also a powerful method to study molecular orientation in SAMs.[10,11]

It is based on excitation of vibrational states in intra-molecular bonds by absorption of infrared light (IR). Unique bond and molecular vibrational energies produce fingerprints in IR region, which can be used to identify certain molecules, functional groups, bonds, molecular conformations, intra- and intermolecular interactions. Absorbed light is usually expressed in wavenumber $\tilde{\nu}$, which is related to wavelength λ_{photon} and frequency ν_{photon} by the following expression, where c is speed of light in vacuum

$$\tilde{\nu} = \frac{1}{\lambda_{photon}} = \frac{\nu_{photon}}{c} \tag{2.35}$$

Any molecular vibration can be described by a superposition of fundamental vibrations. The number of those vibrations in a molecule depends on its degrees of freedom and structural symmetry. A molecules that consists of N atoms has 3N

degrees of freedom, three of which are translational, two or three (for linear or non-linear molecules, respectively) are rotational and the rest are vibrational. Therefore, linear molecules have 3N-5, while non-linear molecules have 3N-6 fundamental vibrations, which can be categorised into two modes: (i) stretching (high in energy) - continuous change in distance between atoms at a fixed bond angle; and (ii) bending (low in energy) - change in bond angle between individual or groups of atoms. The modes can be specified further, stretching into symmetric and antisymmetric, and bending into scissoring, rocking, wagging and twisting.

However, not all types of bond vibrations can be detected. A set of so called selection rules determines, if a particular vibration is IR active (i.e. absorbs IR light). Let's consider bonds as quantum harmonic oscillator (QHO) with energy levels given by:

$$E_v = (v + \frac{1}{2})h\nu_{vib}, \tag{2.36}$$

where the vibrational quantum number $v = 0, 1, 2, \ldots$, defines the vibrational energy state and h is Planck's constant. Frequency ν_{vib} of a dipole oscillation (modelled as a spring that obeys Hooke's law) is defined as:

$$\nu_{vib} = \frac{1}{2\pi}\sqrt{\frac{k}{m}}, \tag{2.37}$$

where k is a force (spring) constant and m is reduced mass of the dipole bond. Therefore, the energy difference between two vibrational levels is equal to

$$\Delta E = \Delta v h\nu_{vib}, \tag{2.38}$$

where positive integers of Δv correspond to an excitation of vibrational state due to photon absorption, and negative integers correspond to a relaxation of vibrational state by photon emission.

Quantum harmonic oscillator imposes two rules. The first (often called coarse) selection rule only allows transitions that lead to a change in dipole moment, and the greater the change the more easily radiation is absorbed. That is, the probability of excitation is proportional to the square of the transition dipole moment. For example, diatomic molecules that are composed of the same chemical element, such as N=N, have no dipole moment. On the other hand, $C0_2$ has a dipole moment, which changes during the bending or the asymmetric stretching (therefore are IR active and can be detected), however, the symmetric stretching creates zero dipole moment and does not change it (and therefore is IR inactive).

The second (also referred to as specific) selection rule only allows transitions between adjacent energy levels, which leads to $\Delta v = \pm 1$ and energy difference of $\pm h\nu_{vib}$ for the allowed transitions. Therefore, frequencies of the absorbed IR light directly correspond to frequencies of fundamental vibrations ($\nu_{photon} = \nu_{vib}$) of the bonds present in a sample. However, this is not a strict rule, because it is very specific to the harmonicity of oscillations. Molecular bonds posses anharmonic character, due to asymmetric potential felt by atoms, possibility of bond dissociation, vibrational and rotational interactions, effects of molecular environment etc. Therefore, a better representation is given by QHO with added anharmonicity using perturbation theory or Morse oscillator, which is less commonly used in spectroscopy. On one hand, both anharmonic methods, in agreement to experimental observations, account for (i) smaller gaps between higher energy levels (i.e. $\Delta E_{n\leftrightarrow n-1} > \Delta E_{n-1\leftrightarrow n-2}$) and (ii) overtone transitions (i.e. when $|\Delta v| > 1$) and combination bands, but with small probabilities. On the other hand, both approaches are more complex, while at low ν_{vib} produce energy levels similar to those predicted by QHO. At room temperature most molecules are in ground vibrational state, thus almost exclusively fundamental (i.e. from ground state $v = 0$ to first excited state $v = 1$) transitions take place. Therefore, anharmonic oscillators determine correct selection rules, while

QHO provides a quick and easy method to calculate usually accurate enough energies for fundamental transitions.

IR spectra is acquired by measuring transmittance as a function of IR wavelength (wavenumber or frequency). The spectra can be built-up a piece at a time by measuring transmittance over a set of narrow ranges of wavelengths using a monochromator, however, it is a slow process, especially, when high resolution is desired. Fourier transform infrared spectroscopy (FT-IR) is a technique that simultaneously collects data over a wide spectral range. It uses Michelson interferometer[12] to periodically create different modulation of multiple wavelengths, which interact with a sample at the same time. Then, it uses Fourier transform to decode light intensity at each modulation into intensity at each wavelength.

Typically IR or FT-IR spectroscopy on bulk materials is performed in transmission. However, such a configuration faces a number of limitation, when it comes to characterisation of thin films, especially when they are placed on a non-transparent (to IR) substrates. IR or FT-IR reflection absorption spectroscopy (IRRAS or FT-IRRAS) allows one to study as thin as single molecular layer films on metal surfaces and determine molecular orientation due to angle and surface selection rules. Light can only be absorbed, if dipole transition has a component parallel to the axis of electric field oscillation in the electromagnetic wave. Typically, this has no effect in bulk samples, because molecules tend to have varying, usually random, orientation and inevitably, for each unique vibration there is always a fraction of molecules that are aligned appropriately with the electric field component of the electromagnetic wave. On the other hand, molecules have a particular orientation with respect to surface in ordered thin films, such as SAMs (e.g. highly packed alkanethiol SAMs on gold have a tilt angle of $\sim 30^\circ$ from the surface normal). Therefore, changing light polarisation allows for the probing of bond vibrations of chosen angles. A molecule with dipole moments adsorbed onto a surface induces the image of opposite charges

in the substrate. Consequently, the charge image reinforces dipole moments that are perpendicular to the surface, but cancels out those that are parallel. Thus, only those vibrations stay IR active that have a component of dipole transition in the former orientation, and the larger the component (or the smaller the angle between dipole transition and surface normal) the higher the enhancement. Comparison of IR absorption intensities can reveal the angle of vibrations or bonds.[10,11] For SAMs on metal surfaces, it is convenient to choose p-polarised light, because it consists almost entirely of component perpendicular to the surface when incident at grazing angles.

FT-IR and FT-IRRAS spectra were acquired using a Bruker IFS 66v/S spectrometer operated with liquid nitrogen cooled MCT detector, and evacuated optics and sample chambers. Unless stated otherwise, 1000 scans at 2 cm^{-1} resolution were recorded for each spectrum. Bulk materials were studied in transmission using KBr pellets that contained uniformly dispersed 0.1-1.0% (w/w) of the corresponding compound, and reference spectra were obtained from pure KBr pellets. Pellets were formed by compressing 100-200 mg of the powder between two polished stainless steel pellets (13 mm in diameter) under 8-10 tons for 3-5 minutes. SAMs were probed in reflection configuration (FT-IRRAS) using p-polarised light incident on the samples at 80° angle from the surface normal; reference spectra were obtained from piranha cleaned gold surface.

2.5 Sample preparation

2.5.1 Substrate cleaning

Microscope glass slides were cleaned by ultrasonication in 10% Decon90 solution in Milli-Q for 15 min, rinsed 10 times with Milli-Q, ultrasonicated in isopropyl

alcohol for 15 min, dried under nitrogen stream, ultrasonicated in dichloromethane (DCM) for 15 min and dried under stream of nitrogen again. Immediately before evaporation of gold, the slides were cleaned in piranha solution (70:30 of H_2SO_4 : H_2O_2, by volume) for 10 min, rinsed with Milli-Q 10 times and dried with nitrogen stream. The same procedure was performed for pieces of silicon wafer, but cleaned in piranha for 2 min, in order to minimise surface roughening.

2.5.2 Gold deposition

Piranha cleaned microscope glass slides or pieces of silicon wafer were loaded into an Edwards Auto 306 thermal evaporator. Adhesion layer of 5 nm of chromium and then 150nm of gold were evaporated at 0.1-0.2 nm/s rate at a base pressure of 10^{-6} mbar.

2.5.3 SAM formation

Immediately before using, gold coated substrates were cleaned in piranha solution for 2 minutes, then rinsed with Milli-Q 10 times and dried under nitrogen stream. Unless stated otherwise, gold coated substrates were then immersed into 0.5-1.0 mM solution of corresponding reagent in DCM overnight at room temperature. Finally, samples were taken out and rinsed with DCM, dried with nitrogen, rinsed with Milli-Q and dried with a stream of nitrogen again. Aluminium foil was used to wrap glassware containing light sensitive solutions.

2.5.4 UV irradiation

Samples were irradiated with soft UV (365 nm) light using either (i) Blak-Ray B100AP lamp with nominal power of 4.0-4.2 mW/cm^2 at the sample or (ii) fluorescence microscope with x4 objective producing ∼35 W/cm^2. In both cases, UV filters were used to only pass a narrow range of wavelengths centred around 365 nm. The Blak-Ray lamp allowed for the illumination of large areas (of the order of cm^2), while the microscope offered ∼10 times short irradiation time over a beam spot of 6 mm in diameter. The output power was regularly checked and exposure time altered, in order to reproduce the consistent input of energy per area.

2.6 References

[1]D. Briggs and M. P. Seah, *Practical Surface Analysis, Auger and X-ray Photoelectron Spectroscopy*, Practical Surface Analysis (Wiley, 1990), ISBN: 9780471920816.

[2]C. D. Bain, E. B. Troughton, Y. T. Tao, J. Evall, G. M. Whitesides and R. G. Nuzzo, J. Am. Chem. Soc. **111**, 321–335 (1989).

[3]L. H. Dubois, B. R. Zegarski and R. G. Nuzzo, J. Am. Chem. Soc. **112**, 570–579 (1990).

[4]K. Critchley, J. P. Jeyadevan, H. Fukushima, M. Ishida, T. Shimoda, R. J. Bushby and S. D. Evans, Langmuir **21**, 4554–4561 (2005).

[5]L. Gao and T. J. McCarthy, Langmuir **22**, 6234–6237 (2006).

[6]D. Gennes, **57** (1985).

[7]A. B. D. Cassie, Discuss. Faraday Soc. **3**, 11–16 (1948).

[8]J. N. Israelachvili and M. L. Gee, Langmuir **5**, 288–289 (1989).

[9]P. E. Laibinis and G. M. Whitesides, J. Am. Chem. Soc. **114**, 1990–1995 (1992).

[10]D. L. Allara and J. D. Swalen, J. Phys. Chem. **86**, 2700–2704 (1982).

[11]D. L. Allara and R. G. Nuzzo, Langmuir **1**, 52–66 (1985).

[12]A. A. Michelson, Philos. Mag. Ser. 5 **31**, 256–259 (1891).

Chapter 3

Characterisation of Photocleavage of Acetylpyrene SAM

Some of the data presented in this chapter on the photo-cleavage and photo-patterning of Lipoic Acid Ester of α-Hydroxy-1-acylpyrene SAMs with soft UV are included in the publication (in preparation):

L. Pukenas, P. Prompinit, B. Nishitha, D. J. Tate, N. D. Pradeep Singh, C. Wälti, S. D. Evans and R. J. Bushby. Soft UV Photo-patterning and Metallization of Self-Assembled Monolayers of the Lipoic Acid Ester of α-Hydroxy-1-acylpyrene: The Generality of Acid Catalysed Removal of Thiol-on-Gold SAMs using Soft UV Light. (in preparation)

This chapter investigates the formation, photocleavage, photo-patterning and potential application of a novel self-assembled monolayer (SAM) of lipoic acid ester of α-hydroxy-1-acetylpyrene (**reagent 1**). **Reagent 1** contains 1-acetylpyrene as a photo-protecting group, which can be removed under soft UV (365 nm) irradiation in solution,[1] thus exposure of its SAM to UV light should lead to a monolayer

terminated with carboxylic acid group. The main objectives of this study were as follows:

- Characterise a novel SAM of **reagent 1** (figure 3.1).
- Characterise photolysis of **SAM1** (figure 3.2a).
- Investigate catalytic effects of solvents, their aqueous mixtures and presence of protons on the photo-deprotection in **SAM1**.
- Demonstrate application of photo-patterned **SAM1** for selective metallisation by electrochemical deposition (ECD) of copper on UV treated regions.

The study presented in this chapter has revealed that UV (365 nm) treatment of **SAM1** does not produce a monolayer terminated with carboxylic acid group (figure 3.2a), but leads to a less dense **SAM1** (figure 3.2b). Although it could not be shown directly in this study, the unexpected outcome of the UV treatment has been attributed to the successful photo-deprotection of a fraction of **SAM1** and the removal of the resulting **lipoic acid** molecules due to their instability under the photolysis conditions (**Scheme B**, figure 3.12).

An unusual effect of **reagent 1** film (not SAM) formation on glass (figure 3.19) and silicon oxide (figure 3.22) surfaces was observed. **Reagent 1** does not interact chemically with the surfaces, nevertheless, relatively strong adsorption and fluorescence of the films have drawn attention and a brief photo-patterning study was performed to investigate:

- Pattern formation of non-fluorescent hydrophilic regions.
- Stability of the patterns under ambient conditions over a period of days.
- Stability of the patterns under typical cleaning procedures.

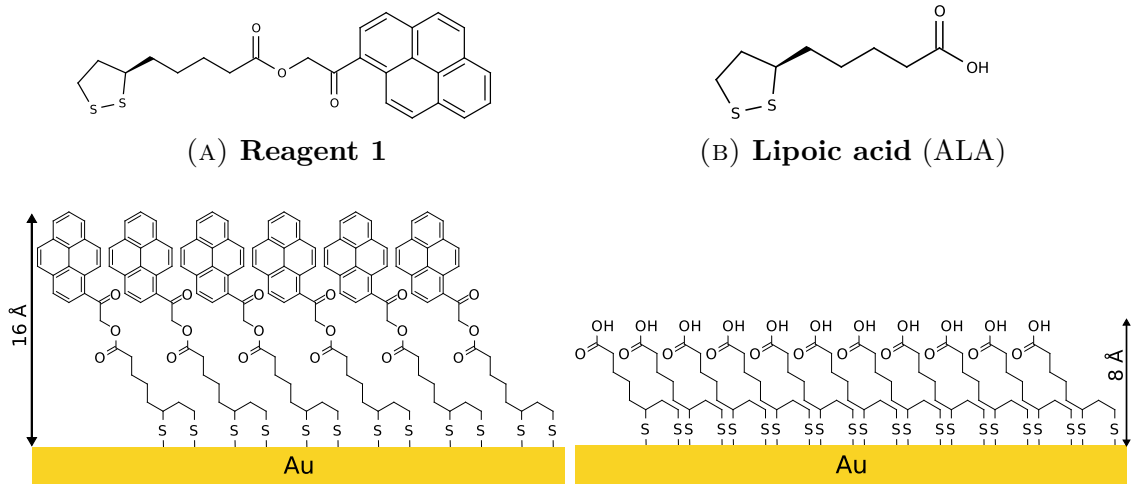

(A) **Reagent 1** (B) **Lipoic acid** (ALA)

(C) **SAM1** (D) **ALA SAM**

FIGURE 3.1: Molecular structures of a) **reagent 1** and product after its photolysis b) **lipoic acid** (ALA), and schematics of their corresponding SAMs c) **SAM1** and d) **ALA SAM**.

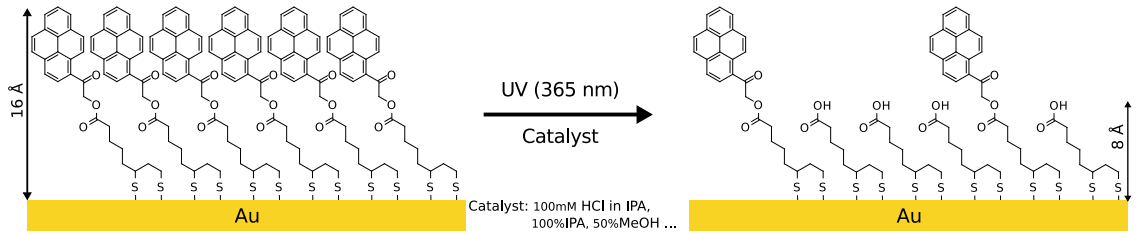

(A) Expected outcome

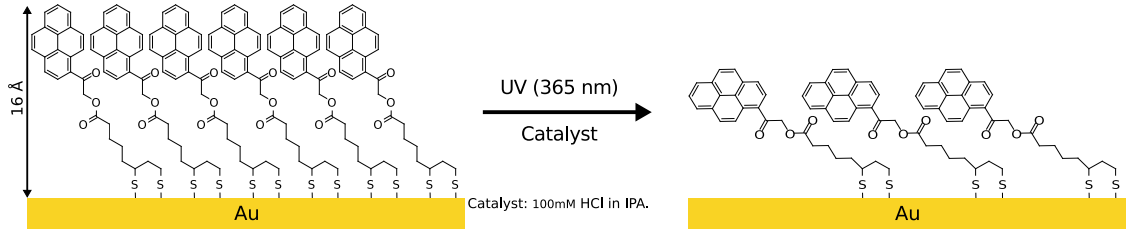

(B) Observed outcome

FIGURE 3.2: Schematics of the a) expected and b) observed outcomes of **SAM1** photolysis .

3.1 Introduction

As discussed in the 'Introduction' chapter, self-assembled monolayers (SAMs) can accommodate many preparative photochemical reactions, however, most of photochemistry work has been carried out on *ortho*-nitrobenzyl derivatives,[2,3] due to their

high yields in photo-chemical reactions, in dilute solutions. Nevertheless, photo-reactions in a SAM environment do not necessarily have the same yields, and, for SAMs containing *ortho*-nitrobenzyl derivatives, drop in yield to 50-80 % has been observed, unless catalysed.[4,5] This poor yield inspired investigation of alternative systems, such as photo-reduction of azides,[6] photo-reaction of azides with amines,[7] CH bond insertion reactions of benzophenone derivatives,[8,9] and the photocleavage of N-alkyl picolinium (NAP) esters.[10] **Reagent 1**[a] (figure 3.1) is based on photo-deprotection of α-esters with 1-acetylpyrene,[1] where photo-reaction takes place by invoking heterolysis of the α-carbon-to-oxygen bond.[1,11] This design was chosen for **reagent 1**[a] in order to produce a better selectivity of metallisation than that reported for photo-patterned SAM containing *ortho*-nitrobenzyl group.[12] Better selectivity might be anticipated if the pyrene group acts as a stronger barrier against diffusion of metal (copper) ions towards the gold surface, and lower packing of molecules in the resulting SAM upon removal of bulkier pyrene groups with soft UV.

3.2 Characterisation and study of photo-reaction in SAM1

This section discusses characterisation of fresh **SAM1** and **lipoic acid (ALA) SAM** formed from dilute (1 mM) dichloromethane (DCM) solutions over night at room temperature. Also this section presents a study of photolysis in **SAM1**, which successfully occurs upon irradiation with soft UV under the acidic catalyst (100 mM HCl in IPA). Fresh and treated samples were characterised with ellipsometry, wetting, Fourier Transform Infrared (FTIR) and X-ray Photoelectron Spectroscopy (XPS) measurements.

[a] Synthesised by Prof. R. J. Bushby (School of Chemistry, University of Leeds, UK) based on the procedure described in the reference[1].

3.2.1 Ellipsometry and Wetting measurements

Wettability data and thickness obtained from ellipsometry measurements of **SAM1** before and after exposure to soft UV (365 nm, 4 mW cm^{-2}) under various conditions are shown in table 3.1. Ellipsometric thicknesses of fresh **SAM1** (16 ± 1) Å and **ALA SAM** (9 ± 2) Å are in a good agreement with the expected values of 15.8 Å[b] and 7.9 Å,[b] respectively. The advancing water contact angle of $(88 \pm 2)°$ on fresh **SAM1** is comparable to the reported value for pyrene-terminated silane SAMs $(85 \pm 1)°$,[13] while fresh **ALA SAM** is hydrophilic in character with advancing and receding contact angles $(30 \pm 2)°$ and $(7 \pm 2)°$, which are typical for other COOH-terminated SAMs discussed in this thesis. The cause for the higher advancing contact angles for COOH SAMs presented in this thesis than reported in the literature for such acids is attributed to slightly different conditions of SAMs formation, namely SAMs were formed from a solution without addition of any acid and using pure DCM rather than ethanol (EtOH) as a solvent, in order to keep experimental parameters consistent with those used for **SAM1** formation. It has been reported that quality of COOH-terminated SAMs highly depends on preparation conditions,[14–20] however, slightly disordered COOH-terminated SAMs were useful in providing more accurate control samples for **SAM1**, which would be expected to produce slightly disordered **lipoic acid** monolayer due to removal of the bulky pyrene group.

Upon exposure to soft UV (365 nm, 4 mW cm^{-2}) for 1.5 h in the presence of the acidic catalyst (100 mM HCl in IPA), **SAM1** thickness decreases to (4 ± 2) Å. That is ∼4 Å thinner than expected or measured thickness for fresh **ALA SAM**. Prolonged exposures of up to 5 h does not yield any further significant change in the SAM thickness. Immersion of fresh **SAM1** into the acidic catalyst in the dark for 1.5 h

[b] Based on conventional 30° tilt angle from the surface normal and molecule's chain length calculated with HyperChem package (semi-empirical AM1).

TABLE 3.1: Ellipsometric thickness and contact angles of fresh **SAM1**, **SAM1** treated under various conditions, fresh **ALA SAM** and **C18 SAM**.

SAM	Ellipsometric thickness (Å)		Water contact angles (°)		
	Measured	Expected[b]	Advancing	Receding	Hysteresis
C18 SAM	22 ± 2	22	111 ± 1	103 ± 2	8
SAM1	16 ± 1	16	88 ± 2	62 ± 6	26
SAM1+Dark$^{HCl}_{1.5\,h}$	17 ± 1	16			
SAM1+UV$^{HCl}_{1.5\,h}$	4 ± 2	8	89 ± 2	44 ± 7	45
SAM1+UV$^{HCl}_{2.5\,h}$	4 ± 1	8	89 ± 1	58 ± 4	31
SAM1+UV$^{HCl}_{5\,h}$	5 ± 1	8	92 ± 2	61 ± 1	31
SAM1+UV$^{IPA}_{1.5\,h}$	16 ± 1	8	87 ± 2	51 ± 3	36
SAM1+UV$^{IPA}_{2.5\,h}$	15 ± 1	8	88 ± 1	48 ± 4	40
SAM1+UV$^{IPA}_{5\,h}$	15 ± 1	8	89 ± 2	46 ± 3	43
SAM1+UV$^{50\,\%IPA}_{1.5\,h}$	16 ± 1	8			
SAM1+UV$^{50\,\%MeOH}_{1.5\,h}$	16 ± 1	8			
SAM1+UV$^{50\,\%MeCN}_{1.5\,h}$	14 ± 1	8			
ALA SAM	9 ± 2	8	30 ± 2	7 ± 2	23

- UV refers to soft UV (365 nm, 4 mW cm^{-2}).
- HCl (superscript) refers to acid catalyst 100 mM HCl in IPA.
- Ellipsometric thickness was obtained using refractive index of 1.45 in Cauchy's equation.
- Uncertainties refer to whichever is the larger (i) standard deviation of sample-to-sample values or (ii) average of standard deviations from each sample (originating from variation in a single measurement or measurement-to-measurement).

does not affect its thickness. Ellipsometry also shows no change in **SAM1** thickness when exposed to soft UV (365 nm, 4 mW cm^{-2}) in pure isopropanol (IPA) for 1.5 h, while longer exposures of 2.5 h and 5 h reduce its thickness only by 1 Å, which is within the experimental error of the fresh **SAM1** thickness. Furthermore, despite reported considerably faster rates of photo-deprotection in a closely related molecule in aqueous mixtures (50:50) of solvents (i.e. IPA, MeOH or MeCN) rather than pure solvents,[1] UV treatment (365 nm, 4 mW cm^{-2}, 1.5 h) of **SAM1** in the above mentioned mixtures does not yield any significant change in the thickness.

All treated samples of **SAM1** show effectively the same advancing contact angle

as a fresh **SAM1** monolayer. Taking into account the ellipsometry measurements discussed above, this is not surprising, except for the UV treated **SAM1** in the acidic catalyst, which is expected to have an advancing angle close to that of the fresh **ALA SAM**. Although some of the treated **SAM1** samples do show a decrease in the receding contact angle, it is still 6-7 times higher compared to fresh **ALA SAM**. The increase in CA hysteresis, could indicate higher surface roughness due to increased physical or chemical disorder in the SAM, or chemical heterogeneity in the SAM.

3.2.2 FT-IRRAS

Effects of UV treatment and role of the catalysts were investigated by studying chemical information and structure of the monolayers using Fourier Transform Infrared (FTIR) spectroscopy in reflectance and transmission configurations on fresh and treated SAMs, as well as their corresponding reagent molecules dispersed in KBr pellets.

3.2.2.1 Fresh SAM1 and ALA SAM

IR spectra of **SAM1** and **reagent 1** dispersed in KBr matrix (figure 3.3a and 3.3b respectively) show very similar characteristics, with some peaks absent in **SAM1** due to the surface selection rule. Strong peaks at 1740 cm^{-1} and 1685 cm^{-1} in the spectrum of the KBr pellet correspond to the stretching mode of the C=O bond in the ester[1,15,16,21] and aryl ketone[1,22] groups, respectively. Equal intensit-

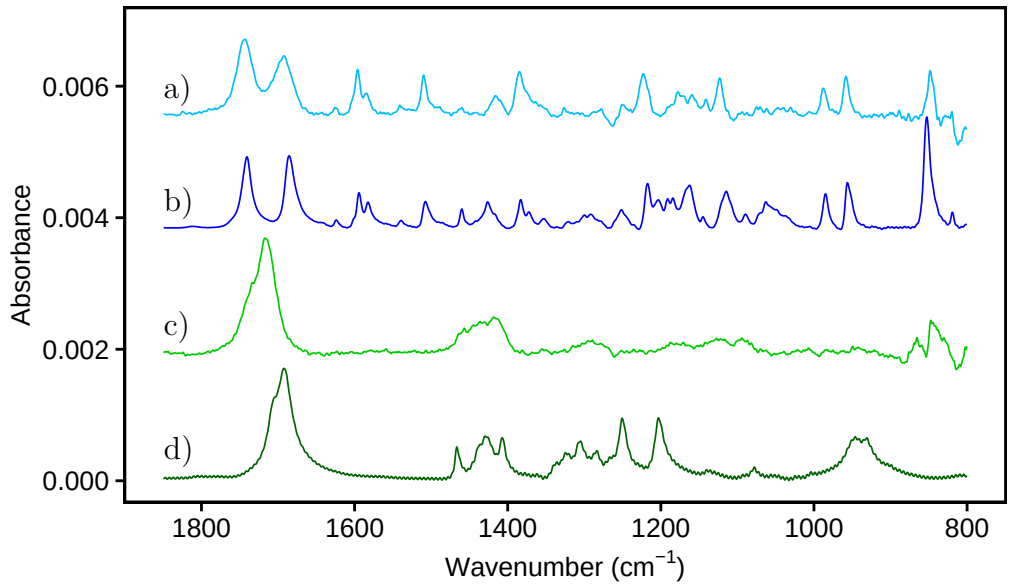

FIGURE 3.3: Infrared spectra of a) fresh **SAM1**, b) **reagent 1** dispersed in KBr matrix, c) fresh **ALA SAM**, and d) **lipoic acid** dispersed in KBr matrix.

ies, in the KBr, indicate similar amounts of both groups, which is in agreement

with molecular structure of **reagent 1** shown in figure 3.1a. In **SAM1** spectrum, these peaks are shifted to slightly higher wavenumbers at 1744 cm^{-1} and 1695 cm^{-1} with the latter being ~20 % weaker in intensity than the former. This could indicate some loss in the aryl ketone group in fresh **SAM1**, or more likely could reflect orientational differences. In both spectra, other peaks are assigned to C=C stretching (1630–1380 cm^{-1}) and C-C deformations, C-H stretching, C-H bending (1325–850 cm^{-1}) in aromatic pyrene group.[14,23–25] However, some peaks in 1400–1100 cm^{-1} region might arise from C-O stretching in ester group.[14–16,25]

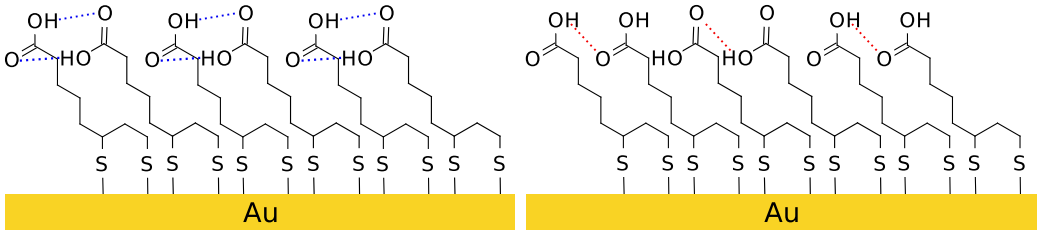

(A) Cyclic dimeric form of hydrogen bonding ($\nu_{C=O}$ = ~1680 cm^{-1})

(B) Acyclic dimeric form of hydrogen bonding ($\nu_{C=O}$ = ~1716 cm^{-1})

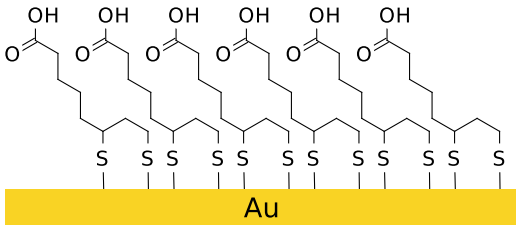

(C) Monomeric (no hydrogen bonding) form ($\nu_{C=O}$ = ~1745 cm^{-1})

FIGURE 3.4: Schematics showing different interactions between lipoic acid molecules in **ALA SAM** induced by molecular arrangement and hydrogen bonding or its absence.

IR spectra of **ALA SAM** and **lipoic acid** molecules dispersed in KBr pellet (figure 3.3c and 3.3d, respectively) have similar characteristics. Strong C=O peak is located at ~1717 cm^{-1} rather than ~1740 cm^{-1} in **ALA SAM** spectrum, which implies presence of acyclic[14,18,25] dimers (figure 3.4b), due to hydrogen bonding in carboxylic acid groups. Nevertheless, shoulder on the left-side could be assigned to a peak at ~1735 cm^{-1} suggesting that fraction of molecules in the SAM have

carboxylic acid groups in monomeric form (figure 3.4c).[14,15,18,25–27] The main peak in the spectra of **lipoic acid** compound in KBr matrix is a convolution of peaks located at $\sim$1705 cm^{-1} and $\sim$1692 cm^{-1} indicating that carboxylic acid groups are predominantly in a form of cyclic[14,18] dimers (figure 3.4a), but a noticeable fraction of molecules could be in a different state or in a form of acyclic dimers.[14,18,25]

3.2.2.2 Effects of UV treatment on SAM1

After exposure of **SAM1** to soft UV (365 nm, 4 mW cm^{-2}, 1.5 h) in the acidic catalyst (100 mM HCl in IPA) most of the peaks disappear (see figure 3.5d), but weak C=O peaks at 1744 cm^{-1} and 1695 cm^{-1} are still detectable. The shape of those peaks does not change, i.e. their relative intensities suggest similar ratio of ester and aryl ketone groups as in fresh **SAM1**. Furthermore, broad peak present in the range of 1400–1475 cm^{-1} in both IR spectra of **lipoic acid** (figure 3.3c and 3.3d) was not detected in the treated **SAM1**. The diminishing of peaks corresponding to vibrations in aromatic rings (pyrene group) could be caused by a loss of molecules from the surface.

No significant changes appear in IR absorption of **SAM1** after it was kept in the dark in the acidic catalyst (100 mM HCl in IPA) for 1.5 h (figure 3.5c). Also, no effects are noticeable in IR spectra of **SAM1** due to UV irradiation in pure IPA (figure 3.5b) or aqueous mixtures (50:50) of IPA, MeOH or MeCN solvents (figure 3.6b, 3.6c and 3.6d, respectively).

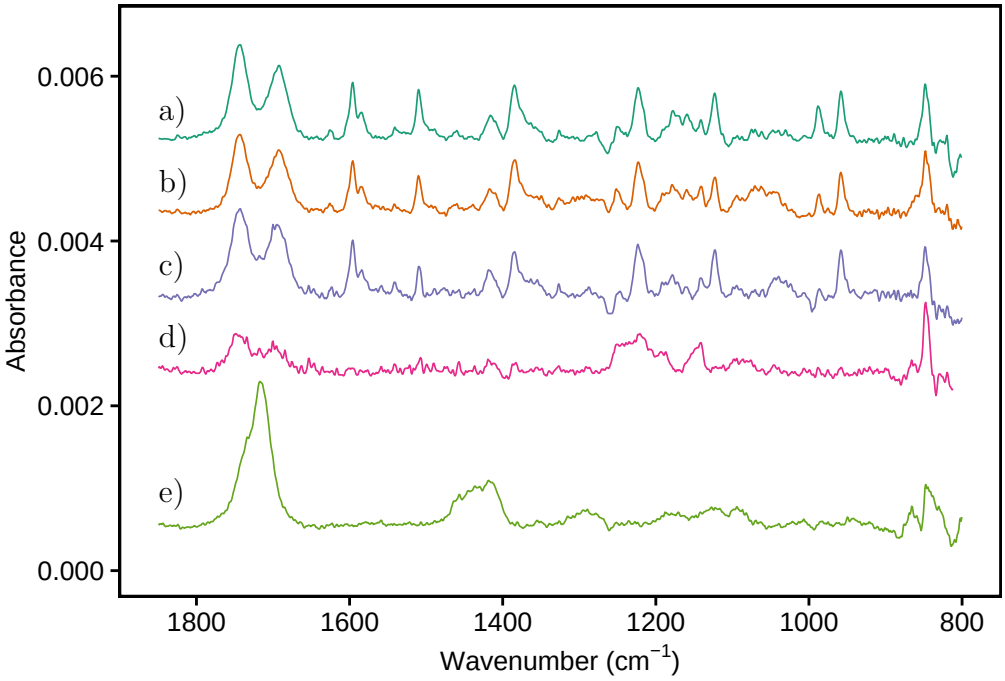

FIGURE 3.5: Infrared spectra of a) fresh **SAM1**, b) **SAM1** after UV irradiation for 1.5 h in IPA, c) **SAM1** kept for 1.5 h in 100 mM HCl in IPA in dark, d) **SAM1** after UV irradiation for 1.5 h in 100 mM HCl in IPA, and e) fresh **ALA SAM**. Exposure to UV light for 1.5 h is equivalent to 22 J cm^{-2} (4 mW cm^{-2}, 365 nm).

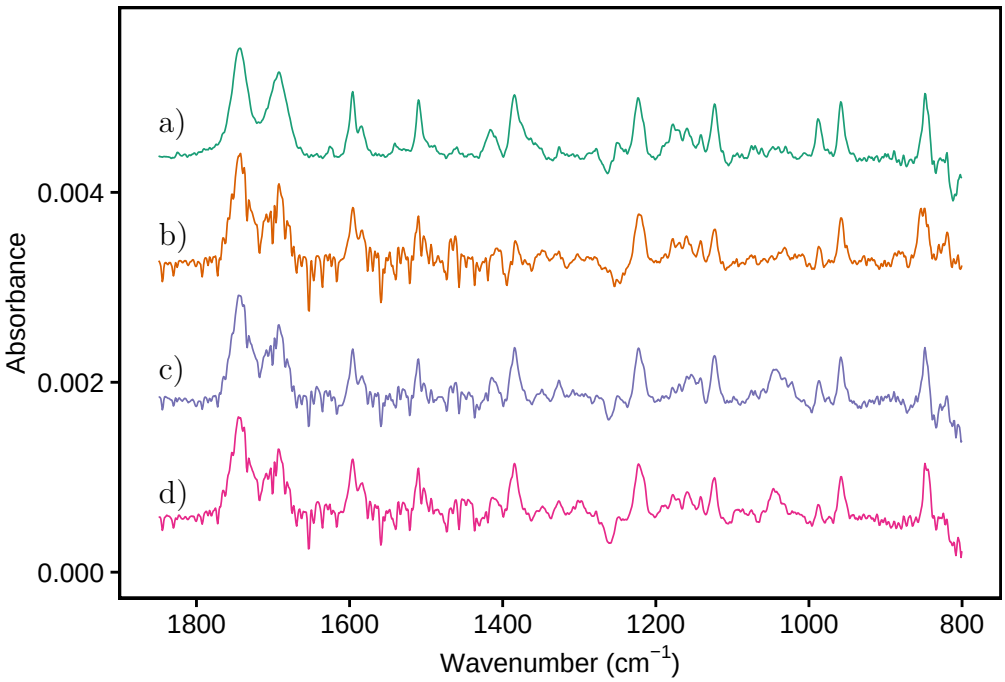

FIGURE 3.6: Infrared spectra of a) fresh **SAM1**, b) **SAM1** after UV irradiation for 1.5 h in 50 % IPA, c) **SAM1** after UV irradiation for 1.5 h in 50 % MeOH, and d) **SAM1** after UV irradiation for 1.5 h in 50 % MeCN. Exposure to UV light for 1.5 h is equivalent to 22 J cm^{-2} (4 mW cm^{-2}, 365 nm).

3.2.3 XPS

X-ray Photoelectron Spectroscopy (XPS) measurements were carried out to obtain additional chemical information of fresh and treated SAMs, and to quantify changes in chemical composition, especially in UV treated samples under acidic conditions. Unless stated otherwise, binding energies are referenced to alkyl carbon in C 1s at 284.5 eV and spectra are scaled so that intensity of Au $4f_{7/2}$ peak in each set of measurements would reach the same (arbitrary chosen[c]) value.

3.2.3.1 Photoreaction in SAM1 in 100 mM HCl in IPA

This section quantitatively discusses the effect of UV irradiation under acidic catalyst based on differences in binding energies, relative ratios of carbon, oxygen, sulphur and gold, and their chemical species in fresh **SAM1**, treated **SAM1** (365 nm, 4 mW cm^{-2}, 1.5 h) in 100 mM HCl in IPA, and fresh **ALA SAM**.

Fitted peaks in the carbon C 1s spectra of fresh **SAM1** and **ALA SAM** (figure 3.7a and 3.7c, respectively) represent carbon species in their corresponding reagent molecules (see figures 3.1a and 3.1b for the structures). The peak located at 284.5 eV is commonly attributed to alkyl/aryl (C-C/C=C) carbon,[28–32] the peak at 286.3 eV is associated with C-S carbon,[31,32] and the peak at 288.6 eV is usually assigned to carbon in carbonyl groups (C=O).[25,27,31,33–36] The latter shows higher binding energy (288.9 eV) in fresh **ALA SAM**, due to slight differences between ester and carboxylic acid chemical environments. Both fresh and treated **SAM1** show an additional peak at 287.2 eV that is attributed to ether carbon (C-O)[25,32,36,37] in the ester group. Similar binding energies of alkyl/aryl (C-C/C=C) and C-S carbon lead to a severe overlap of the peaks, but only the former can be fitted accurately, due to its much stronger intensity. That in turn reduces accuracy of the position

[c]The arbitrary value, in fact, corresponds to initial Au $4f_{7/2}$ peak intensity in one of the samples.

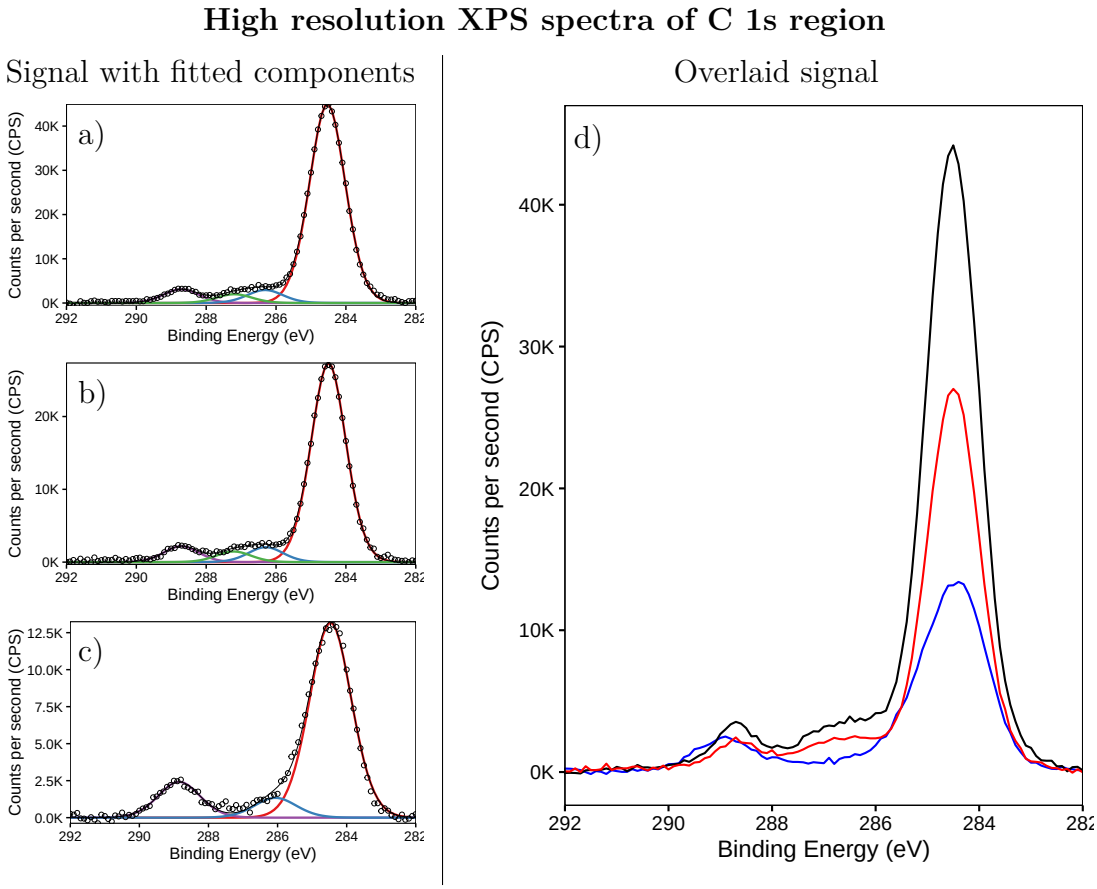

FIGURE 3.7: XPS C 1s spectra with fitted components of a) fresh **SAM1**, b) **SAM1** irradiated with UV for 1.5 h in 100 mM HCl in IPA and c) fresh **ALA SAM**. Figure d) shows overlaid spectra (without fitted components) from a), b) and c) figures in black, red and blue respectively.

and intensity of the C-S component. Fitted peaks in treated **SAM1** spectra have practically identical binding energies as in fresh **SAM1** spectra, suggesting presence of the same chemical species.

The overlaid C 1s spectra (figure 3.7d) of the SAMs show the differences in chemical composition of carbon between fresh **SAM1**, treated **SAM1** and fresh **ALA SAM**. Although the carbonyl (C=O), ether (C-O) and alkyl/aryl (C-C/C=C) carbon peaks drop in intensity following the UV treatment of **SAM1** in the acidic catalyst, quantitative analysis of integrated peak areas presented in table 3.2 reveals that relative to carbonyl carbon (C=O), there is no change in ether carbon (C-O) and carbon bonded to sulfur (C-S), while 7 % drop in total carbon falls within

experimental uncertainty. That contrasts with the expected drop of 100 % in ether carbon and ∼50 % in total carbon for the photo-deprotection with 100 % yield. Furthermore, carbonyl (C=O) carbon peak does not shift to higher binding energy upon UV exposure. It should also be noted that table 3.2 shows only ∼40 % more carbonyl (C=O) carbon than ether (C-O) carbon in fresh **SAM1**, despite the expected 2:1 ratio, respectively.

Table 3.2: Relative ratios of carbon chemical species (based on peak areas) in fresh **SAM1**, treated **SAM1** and fresh **ALA SAM**.

SAM	Carbonyl carbon (C=O)	Ether carbon (C-O)	Carbon (C-S)	Total carbon
SAM1	1.0	0.7	0.9	16.7
SAM1+UV$^{HCl}_{1.5\,h}$	1.0	0.7	0.9	15.6
ALA SAM	1.0	-	0.5	7.3

UV refers to soft UV (365 nm, 4 mW cm^{-2}).
HCl (superscript) refers to acid catalyst 100 mM HCl in IPA.

XPS spectra of the oxygen (O 1s) region in figures 3.8a-c can be fitted with two components - ether (C-O) and carbonyl (C=O) oxygen, which again is in agreement with the molecular structures (figures 3.1a and 3.1b). While the former peak is observed at 533.3 eV[25,32,37,38] for all the SAMs, the latter is found at 531.7 eV[25,32,37,38] for fresh and treated **SAM1**, but at 531.9 eV for **ALA SAM**. The subtle increase in the binding energy is associated with differences in ester and carboxylic acid chemical environments.

Table 3.3: Relative ratios of oxygen chemical species (based on peak areas) in fresh **SAM1**, treated **SAM1** and fresh **ALA SAM**.

SAM	Carbonyl oxygen (C=O)	Ether oxygen (C-O)	Total oxygen
SAM1	1.4	1.0	2.5
SAM1+UV$^{HCl}_{1.5\,h}$	1.6	1.0	2.6
ALA SAM	1.2	1.0	2.2

UV refers to soft UV (365 nm, 4 mW cm^{-2}).
HCl (superscript) refers to acid catalyst 100 mM HCl in IPA.

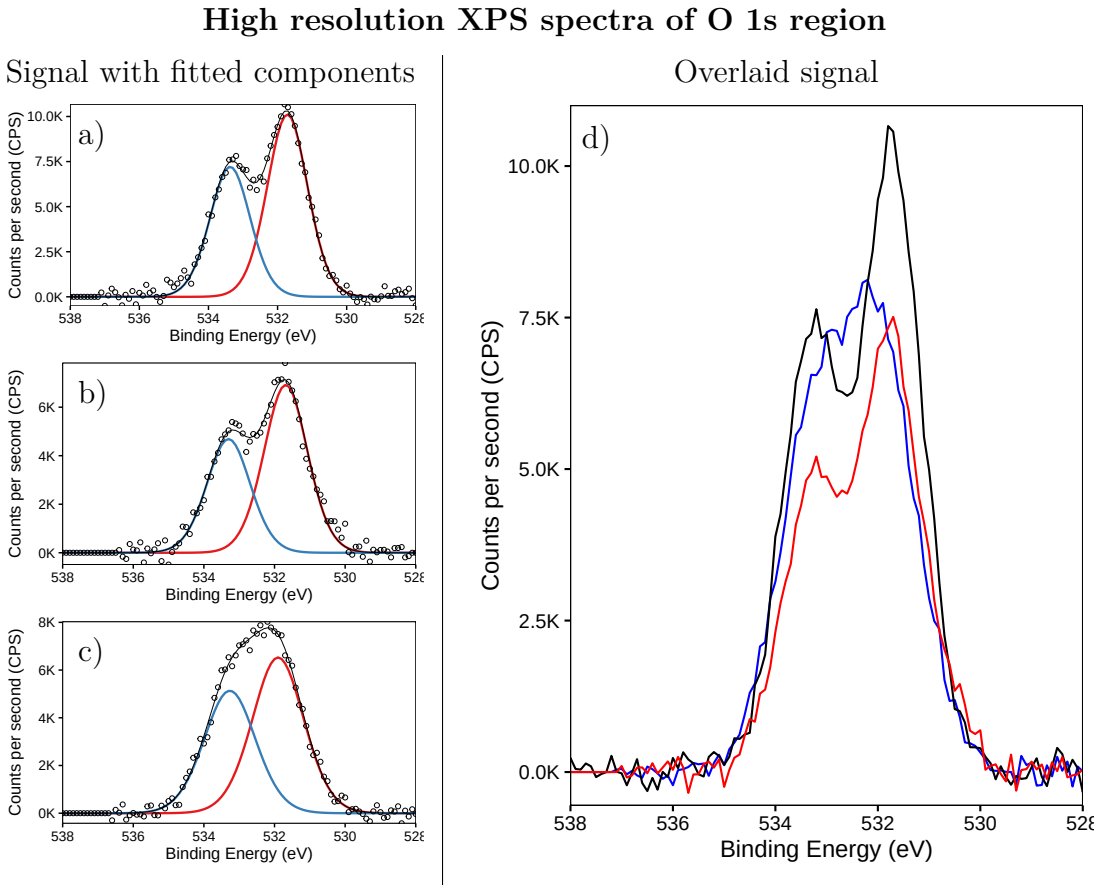

FIGURE 3.8: XPS O 1s spectra with fitted components of a) fresh **SAM1**, b) **SAM1** irradiated with UV for (365 nm, 4 mW cm^{-2}, 1.5 h) in 100 mM HCl in IPA, and c) fresh **ALA SAM**. Figure d) shows overlaid spectra (without fitted components) from a), b) and c) figures in black, red and blue respectively.

The overlaid O 1s spectra of the three SAMs (figure 3.8d) indicate that a similar amount of ether (C-O) oxygen, but higher levels of carbonyl (C=O) oxygen are present in fresh **SAM1** than in fresh **ALA SAM**, which reflect differences in the molecular structures (see figure 3.1a and 3.1b). Nevertheless, table 3.3 indicates only ∼40 % more carbonyl (C=O) oxygen than ether (C-O) oxygen in fresh **SAM1**, despite the expected 2:1 ratio, respectively. In case of photo-deprotection of carboxylic acid group in **SAM1**, only the second (C=O) component is expected to decrease, however, treated **SAM1** shows a drop in both peaks and by a similar fraction. Also, binding energy (BE) of carbonyl (C=O) oxygen does not change. The XPS data suggest that **SAM1** treated with UV in the acid catalyst is less densely packed than either fresh **SAM1** or **ALA SAM**.

All of the SAMs show a double peak in S 2p region with a shoulder at higher binding energy (figures 3.9a-c). The spectra can be fitted with two spin-orbit doublets, one at S $2p_{3/2} = (161.8 \pm 0.1)$ eV and S $2p_{1/2} = (163.0 \pm 0.1)$ eV is assigned to thiolates (R-S-Au),[21,28,39,40] while the other one at S $2p_{3/2} = (163.3 \pm 0.2)$ eV and S $2p_{1/2} = (164.5 \pm 0.2)$ eV is commonly attributed to unbound thiols/disulfides (R-S-H/R-S-S-R).[21,41–44] Although presence of the strong second doublet (i.e. component corresponding to unbound thiols/sulfides) is not common in alkanethiol-based SAMs,[21,28,39,40,44] it is reported in **lipoic acid** SAMs.[33,45]

Based on integrated peak areas (table 3.4), proportion of the second doublet is ∼46 % in **ALA SAM**, ∼34 % in **SAM1** and ∼24 % in the treated **SAM1**. This

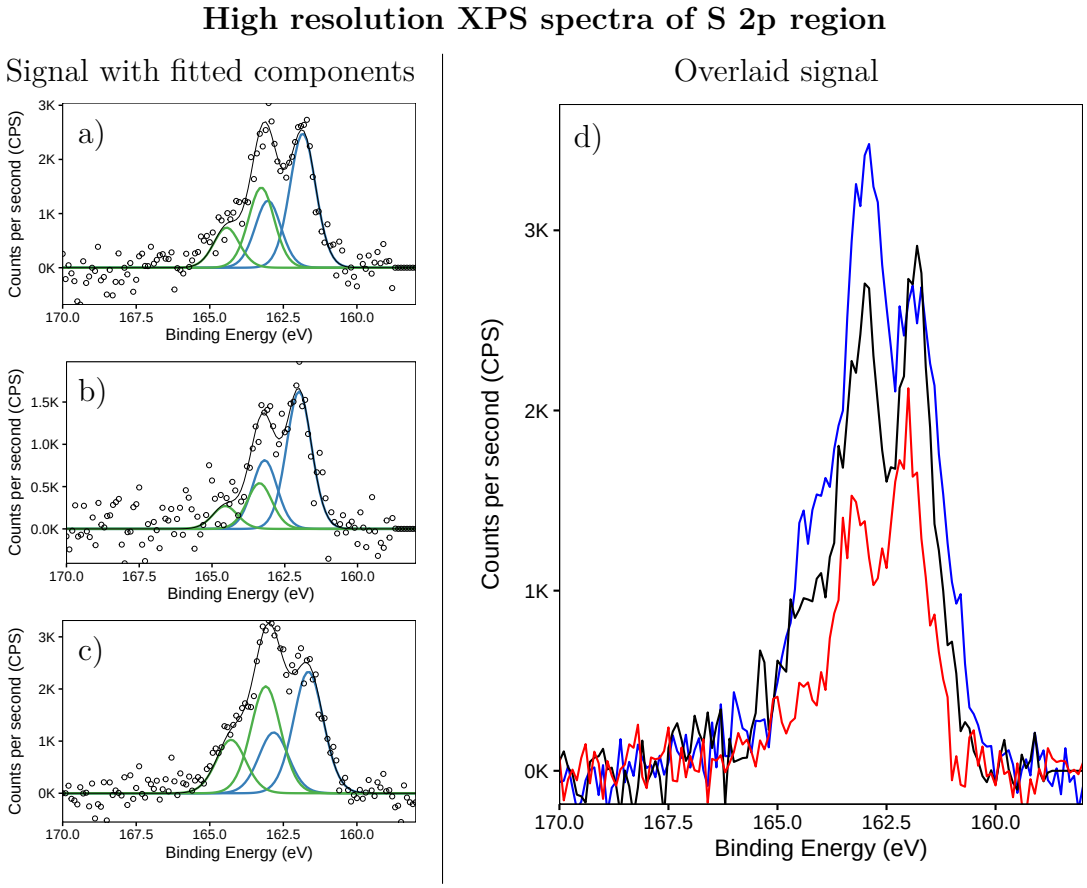

FIGURE 3.9: XPS S 2p spectra with fitted components of a) fresh **SAM1**, b) **SAM1** irradiated with UV for (365 nm, 4 mW cm^{-2}, 1.5 h) in 100 mM HCl in IPA and c) fresh **ALA SAM**. Figure d) shows overlaid spectra (without fitted components) from a), b) and c) figures in black, red and blue respectively.

TABLE 3.4: Relative ratios of sulfur chemical species (based on peak areas) in fresh **SAM1**, treated **SAM1** and fresh **ALA SAM**.

SAM	Thiolates (R-S-Au)	Unbound thiols/disulfides (R-S-Au/R-S-S-R)	Total sulfur
SAM1	0.61	0.34	1.00
SAM1+UV$^{HCl}_{1.5\,\mathrm{h}}$	0.72	0.24	1.00
ALA SAM	0.51	0.46	1.00

UV refers to soft UV (365 nm, 4 mW cm^{-2}).
HCl (superscript) refers to acid catalyst 100 mM HCl in IPA.

is attributed to cross-linking of dithiolane groups and discussed in detail in section 3.2.4.

The overlaid S 2p spectra in figure 3.9d reveal higher amounts of sulphur in fresh **ALA SAM** than in fresh **SAM1**, which is expected and originates from a combination of lower signal attenuation (due to lower thickness of **ALA SAM**) and suspected higher packing compared to **SAM1**. Therefore, the signal in S 2p region (at least the component corresponding to bound sulphur) is also expected to increase in treated **SAM1** (in case of photo-deprotection), however, intensity of both doublets drops, which is a typical sign of loss of material from the gold surface.

Based on C 1s, O 1s, S 2p and Au 4f regions, relative ratios (w.r.t. total sulfur) of chemical elements and their species in **SAM1** and **ALA SAM** are in a reasonable agreement with the calculated ratios from their corresponding molecular structures (table 3.5). There are distinct differences in relative ratios of carbon and oxygen species between **SAM1** and **ALA SAM**. Nevertheless, only small fractional changes in relative ratios are observed after **SAM1** is treated with UV light under the acidic conditions. Furthermore, most ratios change in the opposite direction than expected, i.e. carbonyl, ether and total carbon, in addition to carbonyl and total oxygen, increase w.r.t. sulfur, but their amounts should decrease, in case

TABLE 3.5: Relative ratios of chemical elements and their species (based on peak areas) in fresh **SAM1**, treated **SAM1** and fresh **ALA SAM**.

	Carbon				Oxygen			Gold	Sulfur
SAM	C=O	C-O	C-S	Total	C=O	C-O	Total		
Expected (**SAM1**)	2	1	2	26	2	1	3	n/a	2
SAM1	1.8	1.2	1.7	29.9	1.8	1.3	3.2	27	2.0
SAM1+UV$^{HCl}_{1.5\,h}$	2.1	1.4	2.0	32.3	2.4	1.5	3.9	46	2.0
ALA SAM	1.3	-	0.7	9.3	1.2	1.0	2.1	21	2.0
Expected (**ALA SAM**)	1	-	2	8	1	1	2	n/a	2

UV refers to soft UV (365 nm, 4 mW cm^{-2}).
HCl (superscript) refers to acid catalyst 100 mM HCl in IPA.

of photo-deprotection. An increase of the gold peak relative to that of sulfur corresponds to a less dense organic film (composed of fewer molecules) rather than thinner SAM (composed of shorter molecules). Despite the slight increase in the relative chemical ratios, which for most elements and their species is around 17 %, the chemical composition is much closer to **reagent 1** than **lipoic acid** molecule.

3.2.4 Discussion

Contact angle, ellipsometry, FTIR and XPS data indicate that **reagent 1** and **lipoic acid** successfully form SAMs. However, XPS reveals an unusual feature – a high amount (30-50 %) of sulfur – that is usually attributed to unbound thiol/disulfide (R-S-H/R-S-S-R) groups,[21,41–44] in **SAM1** and **ALA SAM** (table 3.4). There is a number of explanations for this:

(i) a fraction of molecules are bound to gold surfaces via the carboxylic acid (in **ALA SAM**) or the pyrene (in **SAM1**) groups, which results in a fraction of dithiolane head groups being exposed to SAM-air interface;

(ii) an additional layer is formed on top of the SAMs (due to interactions between functional groups, i.e. carboxylic acid for **ALA SAM** and pyrene for **SAM1**, or a simple physisorption of molecules on top of the SAMs) that results in dithiolane head groups of the second layer not exposed to the gold surface;

(iii) intermolecular interactions dominate over the head group-substrate interaction – as reported in some dialkyl monosulfide SAMs[44] – which lead to trapping ca. 35-45 % of the molecules in such a way, that prevents their dithiolane head groups from interacting with the gold surface and forming Au-S bonds;

(iv) most of the molecules are bound to the gold surface via only one of the two sulfur atoms;

(v) molecules (dithiolane head groups, to be more precise) are cross-linked.

The first explanation is unlikely to be correct, because thiolate bonds (Au-S) are reported to dominate over gold interaction with both the carboxylic acid group[46–50] and pyrene group.[51,52] Therefore, this could not lead to such a large fraction of molecules bound to gold surfaces via their functional group. Furthermore, the second S

2p doublet has a low intensity in XPS spectra of **DTBA SAM**, **MHA SAM**, **MOA SAM** and **MUA SAM** (see section 5.1.3), all of which have the same carboxylic acid functional group, all of which were formed in the same way as **ALA SAM**, and all of which show equivalent characteristics in contact angle and ellipsometry data (see section 5.1.1).

The second explanation is also unlikely to be correct. In addition to the previous argument, there are two other reasons: (i) the second S 2p doublet does not decrease after rinsing with copious amounts of organic solvents, but drops after UV treatment, (ii) there is little difference between the obtained (with ellipsometry) and the expected thickness for **ALA SAM** and for **SAM1** (see table 3.1).

The third explanation is also not likely. Even though the strength of intermolecular attraction is increased by van der Waals' interaction of 1-2 kcal/mol per each methylene (-CH_2-) group[53,54] in the alkyl chain, and hydrogen bonding of up to ∼7 kcal/mol[55,56] between carboxylic acid groups in **ALA SAM**, this is not enough to overcome Au-S (40-50 kcal/mol)[53,54,57] bond (in contrast to some dialkyl monosulfide SAMs[44]). This is concluded because no evidence of such trapping of molecules have been observed in similarly thick **MOA SAM** and significantly thicker **MUA SAM** (see section 5.1.3), even though both SAMs should exhibit stronger intermolecular interaction than **ALA SAM**. Although **SAM1** is considerably thicker than **ALA SAM**, that is mostly due to the addition of pyrene group. If pyrene functional groups would exert strong enough π-π interaction[d] in **SAM1**, then this would also lead to formation of the double layer, which is not the case as discussed earlier.

The fourth explanation is possible, but it describes only an intermediate state. Once the molecule is bound to a gold surface via only one sulfur, the other sulfur atom

[d] Based on reported studies, the strength of π-π interactions between pyrene groups are most likely to be in the range of 2-10 kcal/mol, but could be as high as ∼20 kcal/mol[58–62]

becomes a radical, and either binds to the gold surface to form thiolate group (Au-S), abstracts a hydrogen atom from the environment to form thiol group (S-H), or forms a disulfide bond (S-S) with another molecule.

The fifth and final explanation, i.e. a cross-linking of the dithiolane head groups, is thought to be the most probable case. This is due to the fact that other explanations contradict the acquired data, the fact that numerous reports have been published that lipoic acid and its derivatives undergo polymerisation and form linear polydisulfides,[63–74] and the fact that polymerisation has been an issue in the synthesis of **reagent 1**. The presence of the ring strain in dithiolane head group reduces the energy of a typical S-S bond ($\sim$62 kcal/mol)[53] by 15-25 kcal/mol.[66,75] This favours reversible reduction of lipoic acid to dihydrolipoic acid, and ring-opening disulfide exchange polymerisation. Such polymerisation can be induced thermally,[63] chemically,[64,65] photochemically[66,67] or electrochemically[68] in a solution. Also, dithiolane groups incorporated into large molecules were used to fabricate multilayer films on solid substrates using self-organising surface-initiated polymerisation (SOSIP) method.[69–74] Based on the literature, cross-linking of dithiolane groups in **ALA SAM** and **SAM1** could lead to formation of long polymers anchored to the gold surfaces (see figure 3.10). However, disulfide bonds in a close vicinity to gold surface will energetically favour breakage and formation of two Au-S bonds instead. Furthermore, the second S 2p doublet corresponds to half, or less, of the total sulfur in **ALA SAM** and **SAM1** (see table 3.4), which indicates that on average there is one or more thiolate (Au-S) bonds per molecule and would suggest mainly formation of dimers on the gold surfaces. Formation of dimers is not surprising, if **lipoic acid** molecules are considered to bind to gold surfaces in **MOA** (as opposed to **MHA**) configuration, because it prevents the second sulfur atom from binding to the gold surface due to steric hindrance. Consequently, in the vicinity of another **lipoic acid** molecule bound to gold surfaces in **MOA** configuration, both molecules can form intermolecular disulfide bond. A possible explanation, in

terms of SAM stability, is the fact that this configuration could increase the density of molecules on the surface (i.e. a number of molecules per sulfur bonding site), which would strengthen intermolecular interactions and compensate the unfavourable formation of S-S (∼62 kcal/mol)[53] bonds instead of twice as many Au-S (40-50 kcal/mol)[53,54,57] bonds. Nevertheless, cross-linking could also lead to a small fraction of trimers and maybe even longer oligomers on the surface. Relative reduction of the second S 2p doublet after the UV treatment in the acidic catalyst could be explained by a loss of intermediate segments in trimers and longer oligomers due to breakage of disulfide (S-S) bonds. Also, it could be explained by a weakening of intermolecular interactions (due to loss of molecules from the gold surface) leading to an energetically more favourable state, in which a fraction of molecules are bound to gold surfaces via both sulfur atoms. The same explanation could be applied to **SAM1**. Furthermore, growth of the fluorescent **reagent 1** films on silicon oxide and glass surfaces is assigned to the cross-linking of **reagent 1** molecules (discussed in section 3.3.2). Proposal of such a configuration in **ALA SAM** and **SAM1** could be studied in detail by investigating SAMs of dihydrolipoic acid and **lipoic acid** derivatives (for example, molecules with shorter alkyl chains, different functional groups, or with one sulfur atom per molecule). This is, however, beyond the scope of this study.

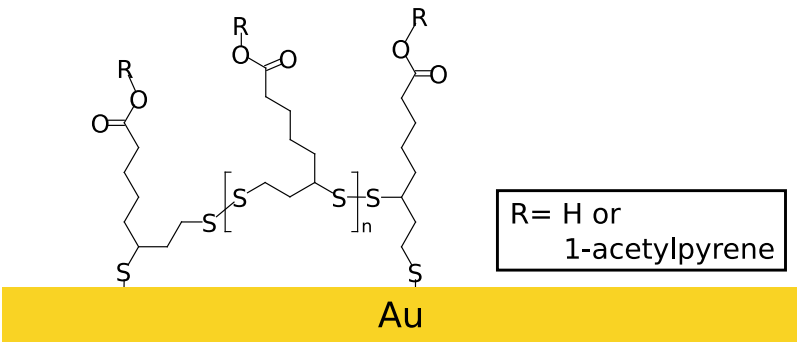

FIGURE 3.10: An example of polymerised **reagent 1** and **lipoic acid** on gold surface due to opening of dithiolane rings and formation of disulfide bonds between neighbouring molecules. However, the most likely configuration is a cross-linking of only few molecules that leads mostly to dimers ($n = 0$) and perhaps a small fraction of trimers ($n = 1$) or longer oligomers.

Additionally, XPS spectroscopy of **SAM1** samples consistently show lack of carbonyl (C=O) carbon and oxygen w.r.t. to ether (C-O) carbon and oxygen (this analysis is independent of normalisation of spectra intensities), as shown in tables 3.2 and 3.3. The discrepancy between relative ratios of species of chemical elements (this analysis is affected by the choice of reference for normalisation of spectra intensities) and molecular structure becomes evident, when spectra are normalised to ethyl oxygen (more appropriate for analysis of molecular structure), rather than gold (more appropriate for studying change in surface coverage), and suggest presence of ~ 1.4 instead of 2.0 carbonyl oxygen per molecule (see section A.1 for further details). On the other hand, IR spectroscopy shows near equal amount of aryl ketone (C=O) and ester (C=O) bonds in **SAM1** and **reagent 1** in KBr pellet (figure 3.3), which agrees with the molecular structure (figure 3.1a) and suggests that discrepancy in XPS data might be due to damage induced during XPS measurements. One of the possibilities is a partial reduction of aryl ketone C=O to CHOH in the same way that aryl nitro is reduced to aryl amine group by the exposure to X-rays. Cyclic voltammetry measurements indicate that aryl ketone reduces at $\sim$0.255 V more negative potential than aryl nitro (1.386 V vs $Ag/AgNO_3$), but still requires less energy than reduction of aliphatic ketone.

UV treatment of **SAM1** (365 nm, 4 mW cm^{-2}) for 1.5 h in the presence of acidic catalyst (100 mM HCl in IPA) reduces ellipsometric thickness to 4 Å, which is $\sim$4 Å thinner than expected or measured thickness for fresh **ALA SAM**, as shown in table 3.1. That is not entirely unexpected, bulky pyrene group in **reagent 1** prevents high density packing in the SAM, and the resulting photo-deprotected lipoic acid monolayer inherits this level of density, which is, of course, lower than that of **ALA SAM** formed from solution of **lipoic acid** molecules. Surprisingly though, contact angle (CA) data (table 3.1) suggest no change to the surface chemistry, despite the expected decrease of $\sim$50-80° in receding and advancing angles. That could be explained by a decrease in surface coverage, but no chemical change in

the molecules. Prolonged exposure for up to 5 h does not yield further change in thickness or advancing angle, but an increase in receding angle by ∼15° (table 3.1); this could be indicative of a severe removal of the monolayer, because the resulting surface characteristics are common to freshly cleaned gold surfaces covered with adventitious hydrocarbons due to short exposure to ambient conditions. Decrease in intensity of FTIR and XPS spectra after the treatment for 1.5 h in the acidic conditions also suggest partial loss of the SAM. The shape and relative intensities of the peaks, corresponding to C=O bond in ester and ketone environments, in IR spectra do not change, and no other changes appear in this region that would be indicative of the ester deprotection (figure 3.5). Although peaks corresponding to vibrations in aromatic rings (pyrene group) diminishes, that is attributed to (i) a decrease in intensity due to the decrease in surface coverage and (ii) greater impact of the surface selection rule following an increase in angle between axes of vibrations and the surface normal caused by higher disorder in the SAM. After the UV treatment of **SAM1**, intensity in all of the XPS spectra drops, but relative ratios of chemical elements hardly change, and any subtle changes show the opposite trend then expected for the photo-deprotection of lipoic acid (table 3.5). This confirms that no significant changes occur in the chemical composition. Nevertheless, intensity of Au 4f spectra increase, which is an exception, but also an indication of loss of molecules from the surface, in agreement with the indications from the other techniques.

Further investigations revealed that the process described above is a photo-chemical reaction. Both treatment of **SAM1** for up to 5 h with the soft UV light in IPA without HCl acid, and incubation of **SAM1** in the acidic catalyst in the dark for 1.5 h does not affect the characteristics of **SAM1**. Despite the reported study of higher photo-deprotection rates in aqueous solvent mixtures,[1] no important changes were detected due to exposure to UV for 1.5 h under such conditions (table 3.1 and figure 3.6).

TABLE 3.6: Fraction of chemical elements and their species left in **SAM1** and **ALA SAM** after the soft UV treatment in the acidic catalyst. *Analysis is based on XPS spectra normalised to have equal Au $4f_{7/2}$ peak areas before and after the treatment, therefore, amount of gold stays at 100 %.*

	Carbon				Oxygen			Gold	Sulfur		
SAM	C=O	C-O	C-C C=C	Total	C=O	C-O	Total	Total	S-S S-H	S-Au	Total
SAM1+ UV$^{HCl}_{1.5\,h}$	66%	68%	60%	62%	74%	67%	71%	100%	40%	67%	57%
ALA SAM+ UV$^{HCl}_{1.5\,h}$	63%	-	66%	68%	72%	64%	69%	100%	32%	75%	58%

UV refers to soft UV (365 nm, 4 mW cm^{-2}).
HCl (superscript) refers to acid catalyst 100 mM HCl in IPA.

Photolysis of **SAM1** can take a number of possible pathways. Exposure to the soft UV in the acid might lead to (i) breakage of disulfide bonds between cross-linked **reagent 1** molecules and thus removal of cross-linked molecules that are not bound to gold (**Scheme A**, figure 3.12), (ii) photo-deprotection followed by breakage of S-Au bond of the resulting **lipoic acid** molecules (**Scheme B**, figure 3.12), or (iii) breakage of S-Au bond of **reagent 1** (**Scheme C**, figure 3.12). The first pathway is likely to contribute, because a larger fraction the disulfide-like sulfur than thiolate-like sulfur is lost due to the treatment, however, that is not the only or main pathway, given that **SAM1** still contains a significant amount of unbound thiols after the treatment (table 3.4). In order to gain a better understanding of the photolysis mechanism, stability of **ALA SAM** was investigated under the same photocleavage conditions. XPS, FTIR, CA and ellipsometry data suggest a limited stability of **ALA SAM** (see chapter 5). XPS provides the most quantitative data, but also the most suitable for cross-comparison. As summarised in table 3.6, **ALA SAM** and **SAM1** show a surprisingly similar fractional drop of chemical elements and their species due to the treatment. However, this does not identify the pathway of the photolysis in either of the SAMs. In order to understand if the instability

of the **ALA SAM** arises from its unique head group or its short chain length, the stability of **DTBA SAM**, **MHA SAM**, **MOA SAM** and **MUA SAM** under the same conditions was investigated, because these SAMs have the same carboxylic acid end group, but a conventional thiol head group and varying chain lengths centred around the chain length of **lipoic acid**. Full study on stability of these SAMs and **ALA SAM** are presented in chapter 5, however, figure 3.11 summarises their XPS data. The figure clearly shows that fractional loss of molecules from gold surface is related the chain length, which strongly suggests that loss of molecules is due to breakage of S-Au bond in short chain SAMs, while long chain SAMs are practically unaffected. Short chain SAMs lead to thin film thickness that allows penetration of the catalyst to the gold-SAM interface, where S-Au bond is likely to be broken in presence of soft UV. Longer SAMs not only have greater thickness, but also stronger van der Waals interactions between the chains, which lead to higher packing and creates additional barrier for the catalyst to penetrate to the gold surface; also strong van der Waals interactions help to keep SAMs together, even if a small fraction of S-Au bonds are affected, which could be the case in **MOA SAM** (see chapter 5).

Because average of fractional loss in **ALA SAM** fits almost perfectly into the middle between average fractional loss in **MHA SAM** and **MOA SAM**, which represent the two possible arrangements for **lipoic acid** molecule to bound to gold through one sulfur atom, the instability of **lipoic acid** is highly likely to be be predominantly caused by its short chain length and not by its unique head group.

It is most likely that photolysis in **SAM1** proceed via photo-deprotection of **SAM1** to **ALA SAM**, which is then removed by the breakage of Au-S bond(**Scheme B**, figure 3.12), because figure 3.11 shows almost identical fractional loss in **SAM1** and **ALA SAM**, but also suggests that SAM's stability depends on its thickness (and packing), while cyclic voltammetry (presented in section 3.3.1.1) and ellipsometry (table 3.1) measurements suggest that **SAM1** has higher packing and thickness,

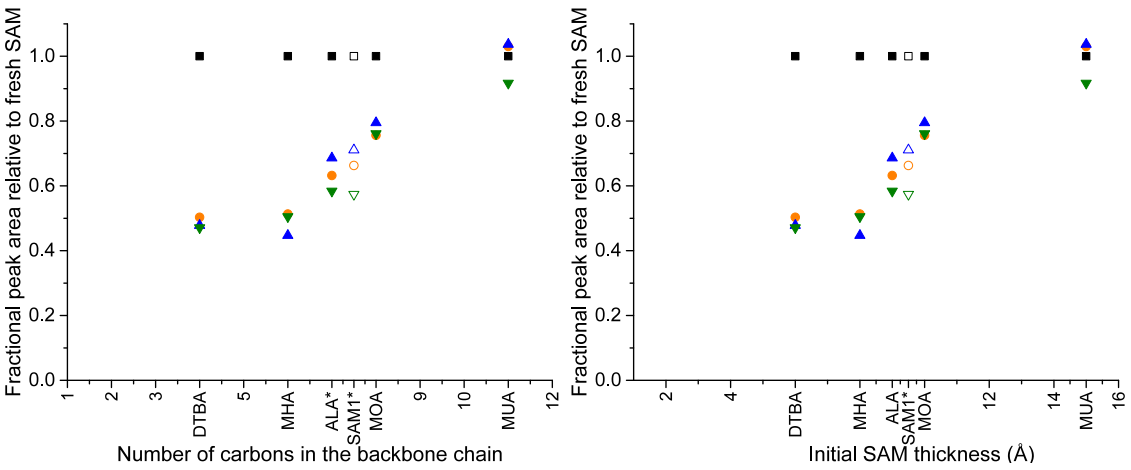

(A) Based on number of carbons (B) Based on initial SAM thickness

FIGURE 3.11: Fractions of carbonyl (C=O) carbon (yellow circles), total oxygen (blue triangles pointing up) and total sulfur (green triangles pointing down) left in **SAM1**, **ALA SAM**, **DTBA SAM**, **MHA SAM**, **MOA SAM**, and **MUA SAM** after exposure to soft UV (365 nm, 4 mW cm^{-2}, 1.5 h) in the acidic catalyst (100 mM HCl in IPA) are plotted against a) number of carbons in the chain and b) initial SAM thickness. ALA is assigned an average chain length of 7 carbons, while **SAM1** is plotted next to ALA for comparative purposes only. Analysis is based on XPS spectra normalised to have equal Au $4f_{7/2}$ peak areas before and after the treatment, therefore, amount of gold (black squares) stays at 100 %, which also visually indicates the expected level of chemical elements and their species for the SAMs that do not exhibit loss of surface coverage.

respectively, than **ALA SAM**. The fact that photolysis of **reagent 1** films does lead to deprotection of **lipoic acid** (at least when not in a close proximity to a gold surface) is supported by the fact that physisorbed films on silicon oxide or glass are transformed from hydrophobic to hydrophilic upon irradiation with soft UV in air or in acid, as discussed in section 3.3.2.

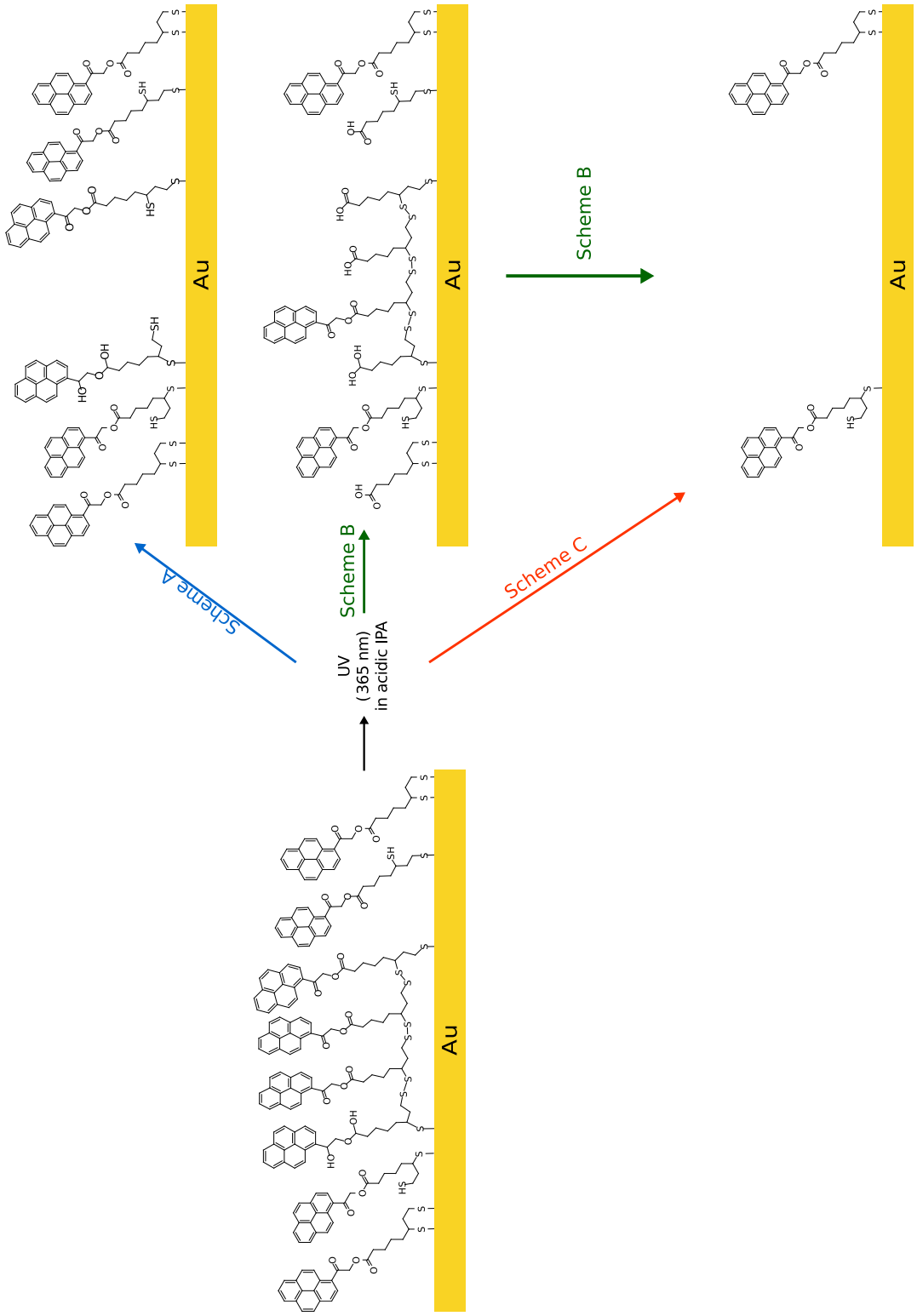

FIGURE 3.12: Three possible pathways for photolysis to take place in **SAM1**. **Scheme A** - breakage of disulfide (S-S) bonds between the cross-linked molecules, and therefore removal of cross-linked segments only. **Scheme B** - photo-deprotection that yields **lipoic acid** monolayer, which is not stable under the UV treatment conditions and consequently is removed from gold surface. **Scheme C** - breakage of S-Au bond in **SAM1** without the photo-deprotection reaction.

3.3 Photo-patterning

Following the photo-deprotection study, suitability of **SAM1** on gold and **reagent 1** films formed on silicon oxide and glass surfaces were investigated for photo-patterning purposes. All samples were photo-patterned through a chromium mask under an optical microscope with soft UV (365 nm, 22 J cm^{-2}, 36 mW cm^{-2}, 10 min), unless stated otherwise. A chromium mask was separated from the sample using organic spacers with thicknesses varying from a few to tens of microns, in order to prevent mechanical damage and to accommodate the acidic catalyst (100 mM HCl in IPA). Some **reagent 1** films on silicon oxide and glass were successfully photo-patterned in air.

3.3.1 Selective copper deposition on photo-patterned SAM1

The following sections present a study of electrochemical deposition (ECD) of copper on photo-patterned **SAM1**. High selectivity of metallisation is expected due difference in order and packing between UV treated and non-treated regions under the acid. It was advantageous to use specially designed samples that had the evaporated gold film limited to a circle of 6mm in diameter. This way, the size of the gold film is similar to that of a focussed light beam produced by an optical microscope. This allows one to control the fraction of the total area that is exposed to UV and subsequently metalised with copper. Cyclic voltammetry of fresh, uniformly photolysed and photo-pattered **SAM1**, as well as fresh **ALA SAM**, was conducted in 10 mM $CuSO_4$ in 10 mM H_2SO_4 electrolyte, in order to identify a range of most suitable potentials for the copper deposition. Copper films were deposited at a number of potentials within the determined range using both constant potential and sweeping

potential methods. Quality of copper films and selectively of depositions were studied with an optical microscope. Stability and reversibility of copper deposition and oxidation were also investigated.

3.3.1.1 Cyclic Voltammetry (CVs)

First of all, cyclic voltammetry on a clean gold electrode (figure 3.13) in 10 mM $CuSO_4$ in 10 mM H_2SO_4 electrolyte was performed at 10 mV s^{-1} scan rate and used as a reference within the potential range of −0.30 V to 0.40 V. Copper electrodeposition can be achieved by reducing Cu^{2+} ions at a more negative potential than open circuit potential (OCP).[76] In this study, OCP was observed at +0.02 V and peak potential (E_p) for the highest reduction rate was found at −0.07 V for this system. Figure 3.13 shows hardly any changes over nine consecutive cycles, which indicates stability of the system and reversibility of copper reduction onto and oxidation from the gold surface. The same values were repeatedly obtained across multiple samples of clean gold electrodes, and therefore were used as controls for comparison of different sample batches. For the investigated conditions, under potential deposition (UPD) of copper was not observed on any of the samples.[76]

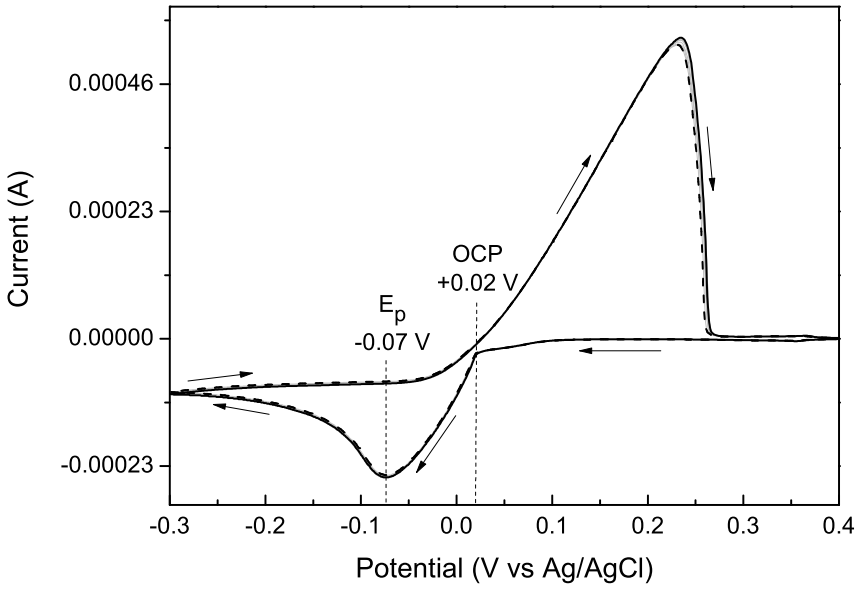

FIGURE 3.13: Cyclic voltammograms (CVs) of 10 mM $CuSO_4$ in 10 mM H_2SO_4 solution on a clean gold electrode. Ten cycles were performed at 10 mV s^{-1} scan rate. The first cycle is omitted, the black solid line represents the second cycle, light grey solid lines represent the 3rd-9th cycles, and the black dashed line represents the tenth cycle.

Figure 3.14 shows CVs performed under the same conditions, but on electrodes with fresh **SAM1**, soft UV (365 nm, 22 J cm^{-2}, 36 mW cm^{-2}, 10 min) treated and patterned **SAM1** under acidic conditions (100 mM HCl in IPA), and fresh **ALA SAM**. CVs of all of the SAM-modified electrodes show significantly lower E_p potential (i.e. 2-3 times compared to clean gold electrode), which is assigned to the barrier-like behaviour of the SAMs. On clean gold electrode, Cu^{2+} ions can reduce directly onto the gold surface at potentials slightly more negative than OCP and initiate nucleation. However, when gold electrode is covered with a SAM, copper deposition most likely takes place either by a charge (electron) transfer from gold surface to SAM-electrolyte interface, or by penetration of Cu^{2+} ions towards the gold surface through defects in the SAM.[76,77] In either case, energy barrier increases, as reflected by the more negative E_p potentials and the fact that over potential deposition (OPD) values are significantly more negative than OCP. The order of E_p values is the inverse to that of ellipsometric thicknesses:

fresh **SAM1** (−0.24 V) < **ALA SAM** (−0.22 V) < UV treated **SAM1** (−0.21 V)

fresh **SAM1** (16 Å) > **ALA SAM** (9 Å) > UV treated **SAM1** (4 Å)

with an exception of UV patterned **SAM1** that shows the lowest E_p of −0.18 V, but expected to have ellipsometric thickness equal to the average of fresh and fully treated **SAM1**. As discussed in section 3.2.4, a decrease in thickness of **SAM1** upon exposure to UV light is associated to the decrease in surface coverage rather than the decrease in chain length of the molecules. The same is expected for the UV treated regions in patterned **SAM1**, however, that still does not account for the lowest E_p value.

Similarly to bare gold, electrode modified with fresh **SAM1** shows hardly any change over nine consecutive cycles (figure 3.14a) indicating stability of the SAM on the gold surface and reversible copper deposition.

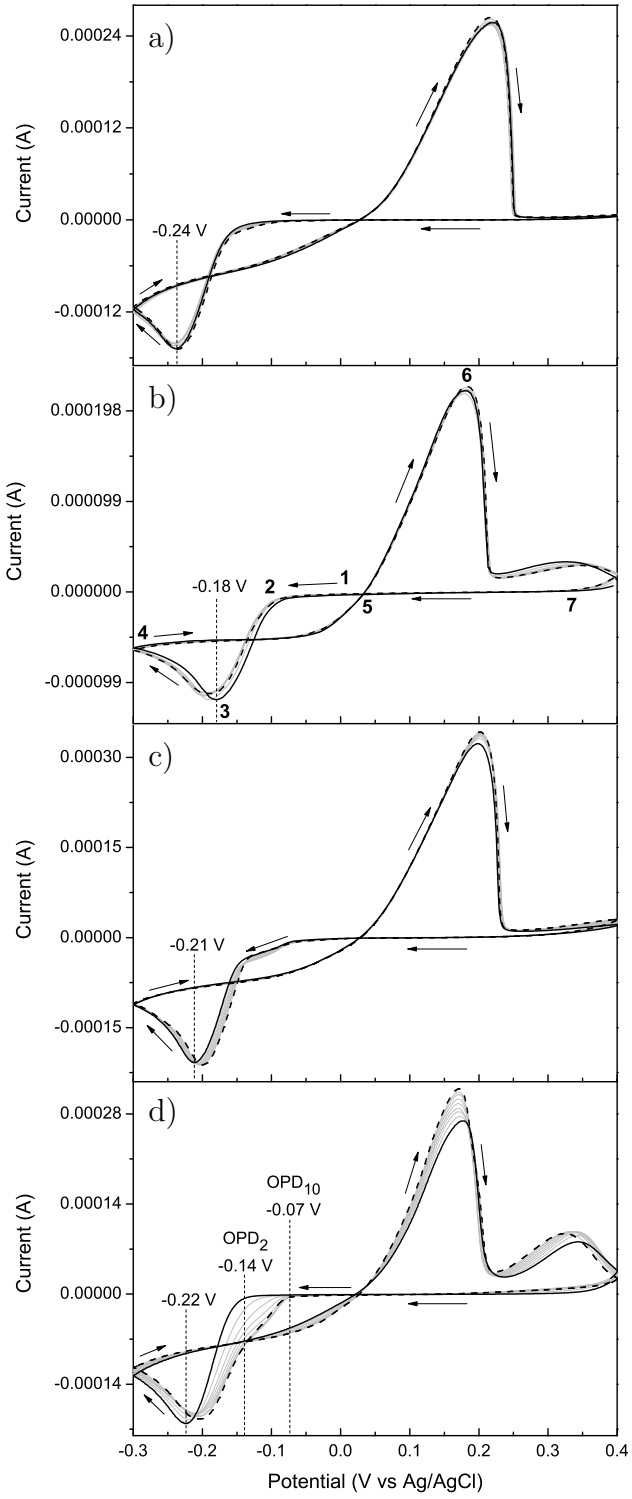

FIGURE 3.14: Cyclic voltammograms (CVs) of 10 mM $CuSO_4$ in 10 mM H_2SO_4 solution on a) fresh **SAM1**, b) patterned (50 µm x 50 µm stripes) **SAM1** with UV in acid, c) **SAM1** treated with UV in acid, d) fresh **ALA SAM**. Ten cycles were performed at 10 mV s^{-1} scan rate on each sample. First cycle is omitted, black solid line represents the second cycle, light grey solid lines represent 3-9 cycles and black dashed line represents the tenth cycle. Acid refers to 100 mM HCl in IPA, UV refers to exposure of 22 J cm^{-2} (36 mW cm^{-2}, 365 nm).

In contrast, CVs in figure 3.14d reveal considerably lower stability of **ALA SAM** on the electrode upon reversible copper deposition. Most notably, the E_p shifts by 0.02 V to a less negative potential and OPD changes from −0.14 V to −0.07 V. On one hand, this could originate from distortion of the SAM during cyclic copper deposition leading to an increase of permanent defects in the monolayer. On the other hand, ligand replacement in COR and COOR terminated SAMs by Cu^{2+} ions has been reported,[78,79] which could result in formation of unidentate Cu-O complex and eventually lead to copper nucleation sites that are not completely removed during oxidation phase. CVs shown in figures 3.14b and 3.14c indicate slight instability in both UV patterned and uniformly treated **SAM1**. This could be indicative of higher number of defects in the SAMs due to UV induced decrease in surface coverage, or due to presence of small fraction of deprotected lipoic acid molecules within the SAMs.

Double peak has been reported in CVs of photo-patterned SAMs,[12,80] where each peak corresponds to maximum reduction rate of copper on each region. However, this is not evident in CVs of photo-patterned **SAM1** (figure 3.14b). Because total areas of both UV treated and non-treated regions are equal, and because separation between E_p potentials (for each region in patterned **SAM1**) is similar to the separation in the reported photo-patterned SAM,[12,80] the absence of the double peak is attributed to suppression of electrodeposition rate on non-treated region due to (i) radial diffusion of Cu^{2+} ions in electrolyte near electrode caused by close proximity of regions with high and low E_p potentials, and (ii) additional gradient towards UV-treated region due to stronger barrier against penetration of Cu^{2+} ions exerted by polycyclic pyrene than CF_3 groups. Indeed the latter is evident after the first half of a CV cycle is performed (i.e. voltage sweep from stage 1 to 5 in figure 3.14b), when copper is mainly deposited on UV-treated regions, in contrast to the small difference between the amounts of deposited copper on treated and non-treated regions in the reported patterned SAM.[80]

3.3.1.2 Electrochemical deposition of Cu - constant potential

A number of **SAM1** samples were patterned and subsequently metallised with copper using electrochemical deposition (ECD) at various potentials around the E_p value of $-0.18\,V$ determined from the cyclic voltammetry studies shown in figure 3.14b and discussed in the previous section. ECD was performed for 20 s at various constant potentials in the same electrolyte (10 mM $CuSO_4$ in 10 mM H_2SO_4) that was used for cyclic voltammetry.

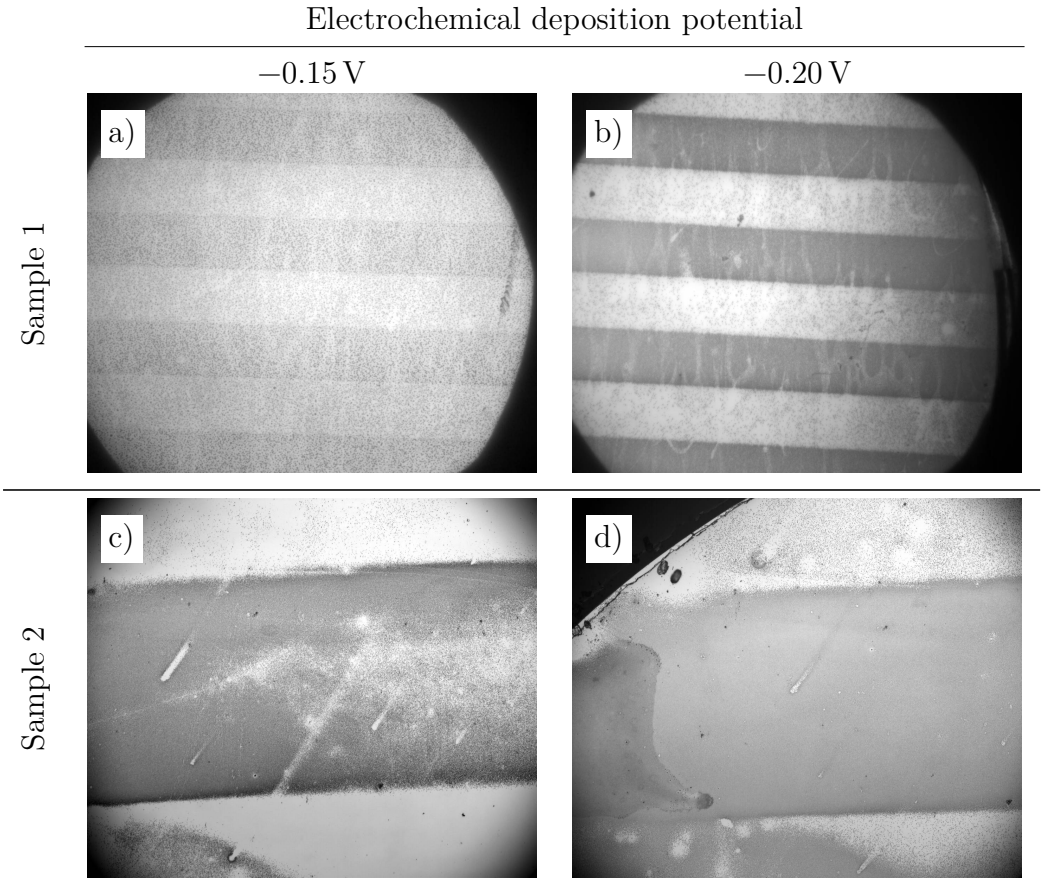

FIGURE 3.15: High magnification optical images of photo-patterned **SAM1** (365 nm, 22 J cm^{-2}, 36 mW cm^{-2}, 10 min) after electrochemical deposition of copper for 20 s in 10 mM $CuSO_4$ in 10 mM H_2SO_4 electrolyte at a constant potential of a) $-0.15\,V$, b) $-0.20\,V$, c) $-0.15\,V$, and d) $-0.20\,V$. Figure a) and b) correspond to one sample, and figure c) and d) correspond to another sample. Darker areas correspond to UV-treated regions and higher quantities of reduced copper.

Generally reduction of Cu^{2+} ions at $-0.10\,V$ or less negative potentials does not produce significant amount of copper across the whole area of interest. On the other

hand, reduction at −0.25 V or more negative potentials leads to large amounts of reduced copper, but poor selectivity between UV treated and non-treated regions. ECD performed in the range of −0.15 V to −0.20 V produces selective copper deposition on the UV treated samples, however, the level of selectivity varies from sample to sample. Figures 3.15a and 3.15c present optical images of two samples prepared in identical way (copper reduced at −0.15 V), but the latter shows much greater selectivity. Similarly, figures 3.15b and 3.15d show optical images of the same samples after copper reduction at −0.20 V), but this time the former shows better selectivity.

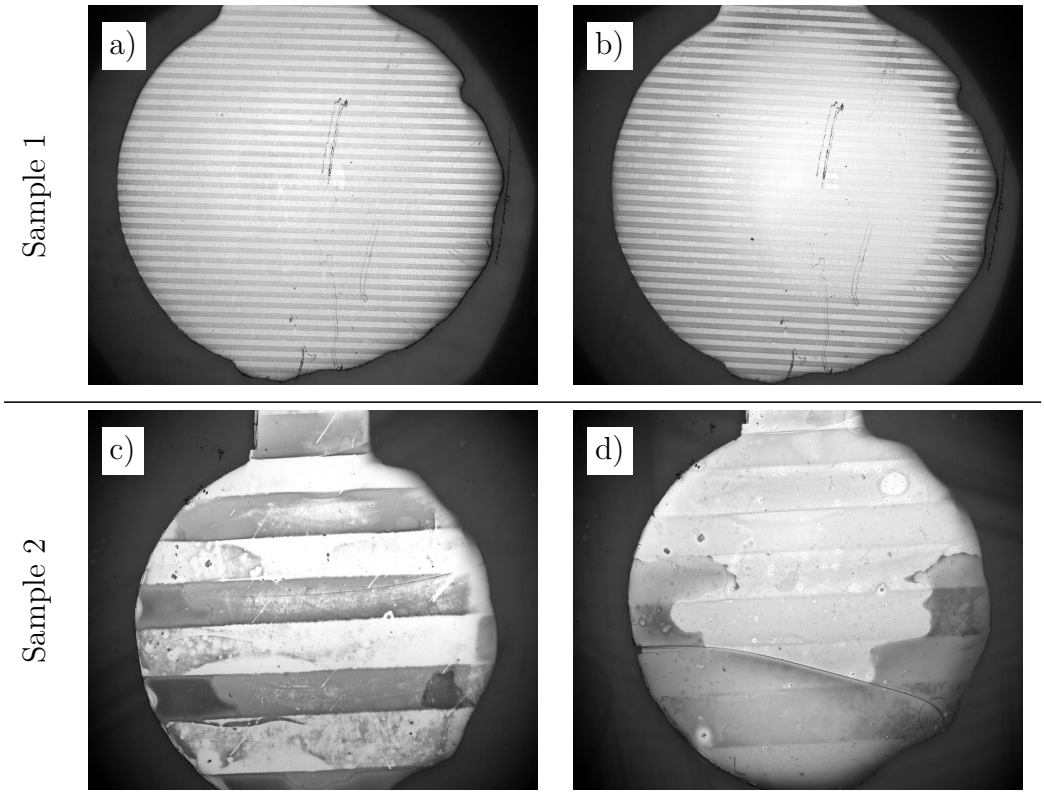

FIGURE 3.16: Optical images of photo-patterned **SAM1** (365 nm, 22 J cm^{-2}, 36 mW cm^{-2}, 10 min) after electrochemical deposition of copper for 20 s in 10 mM $CuSO_4$ in 10 mM H_2SO_4 electrolyte. Figures a) and b) show difference between consecutive (but after oxidation phase in between) copper reductions, while figure b) also shows variation within macroscopic area of the sample. Likewise, figures c) and d) show differences within macroscopic areas and between the copper reductions. Darker areas correspond to UV-treated regions and higher quantities of reduced copper.

Furthermore, copper reduction is not uniform on macroscopic level and between different electrodepositions on the same samples (see figure 3.16), even though copper is oxidised between the depositions. This is attributed to effects of sudden initialisation of nucleation sites on the sample surface upon sudden application of electric field across the electrochemical cell. Improved deposition results obtained using sweeping potential deposition are discussed in the following section.

3.3.1.3 Electrochemical deposition of Cu - sweeping potential

ECD produces better and more consistent results, when performed using sweeping potential (at $10\,\mathrm{mV\,s^{-1}}$ scan rate) between $0.00\,\mathrm{V}$ and various negative potentials. First of all, this method yields a uniform copper deposition on macro scale and between the samples (figure 3.17), which is attributed to a gradual initiation of nucleation sites and their growth on the surface.

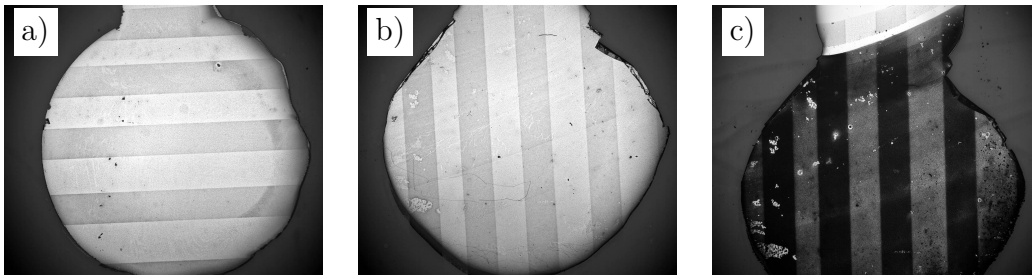

FIGURE 3.17: Optical images of photo-patterned **SAM1** (365 nm, $22\,\mathrm{J\,cm^{-2}}$, $36\,\mathrm{mW\,cm^{-2}}$, 10 min) after electrochemical deposition of copper by sweeping potential (at $10\,\mathrm{mV\,s^{-1}}$ scan rate) from $0.00\,\mathrm{V}$ to $-0.30\,\mathrm{V}$ for one cycle on a) sample 1, b) sample 2, and sweeping for ten cycles on c) sample 2. Figure b) shows deposited copper on relative fresh sample 2 (only three cyclic voltammograms were recorded beforehand), while optical image shown in figure c) was taken of deposited copper after over 80 cycles of copper reduction at various potentials and seven oxidations were performed beforehand. Darker areas correspond to UV-treated regions and higher quantities of reduced copper.

Furthermore, sweeping potential between $0.00\,\mathrm{V}$ and $-0.30\,\mathrm{V}$ for one cycle produces a more selective copper deposition on the surface (figures 3.17a, 3.17b and 3.18a) than a reduction at a constant potential of $-0.25\,\mathrm{V}$ for 20 s. Moreover, even after 10

such cycles, the pattern was still clearly evident (figure 3.17c and 3.18b), which were performed after more than 80 reduction cycles and seven oxidations. Nevertheless, a significant amount of copper was present on non-treated regions. Highest selectivity of copper deposition is achieved by sweeping potential between 0.00 V and −0.18 V (which is the determined E_p value for patterned **SAM1** from CVs in figure 3.14b). Figure 3.18c shows optical image of the patterned SAM after 10 such cycles

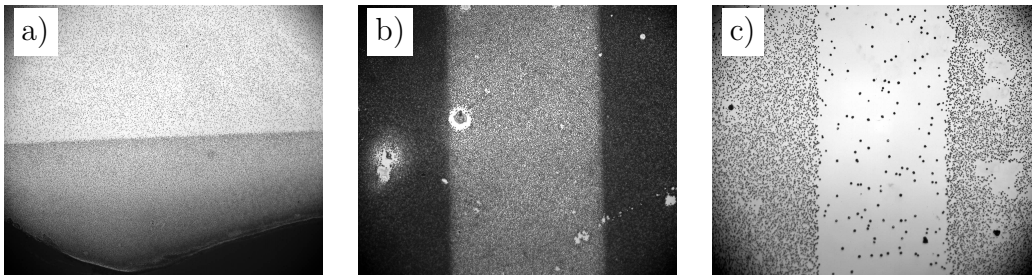

FIGURE 3.18: High magnification optical images of photo-patterned **SAM1** (365 nm, 22 J cm^{-2}, 36 mW cm^{-2}, 10 min) after electrochemical deposition of copper by sweeping potential (at 10 mV s^{-1} scan rate) from 0.00 V to −0.30 V for a) one cycle, b) ten cycles, and c) sweeping potential from 0.00 V to −0.18 V for ten cycles. Figure a) shows deposited copper on relative fresh sample 2 (only three cyclic voltammograms were recorded beforehand), while optical image shown in figure b) was taken of deposited copper after over 80 cycles of copper reduction at various potentials and seven oxidations were performed beforehand. Darker areas correspond to UV-treated regions and higher quantities of reduced copper.

3.3.2 Fluorescent and hydrophilic/hydrophobic patterns

It has been observed that prolonged **SAM1** formation (over 24 h) on evaporated gold electrodes on microscope slides leads to green fluorescence (upon exposure to soft UV, i.e. 365 nm) of the glass surface that is not covered with gold, as shown in the figure 3.19a. Fluorescence itself is not surprising, because pyrene is the functional group in **reagent 1**, and pyrene's derivatives are valuable molecular probes in fluorescence spectroscopy due to high quantum yield and lifetime. However, it was unexpected to discover that fluorescence does not disappear or distinctly decrease upon extensive rinsing and ultrasonication for up to 30 min in pure DCM, the solvent that is used to prepare **reagent 1** solution for SAM formation. It was also discovered that glassware used for SAM formation also becomes fluorescent and could not be cleaned with DCM rinse or ultrasonication. A brief study is presented in the following sections on **reagent 1** films on glass and silicon oxide surfaces, and their photo-patterning to produce patterns of non-fluorescent hydrophilic regions.

3.3.2.1 Reagent 1 film on glass

Green fluorescence only appears on glass substrates, partly covered with evaporated gold electrode, used to form **SAM1** (figure 3.19a), but not on the such substrates used to form **ALA SAM** (figure 3.19c). Fluorescence disappears after exposure to soft UV (365 nm, 22 J cm^{-2}, 36 mW cm^{-2}, 10 min), as shown in the optical image (figure 3.19b) around the top part of gold electrode, and fluorescence disappears on both sides of glass substrates, i.e. on the top side in contact to acidic catalyst (100 mM HCl in IPA) and the back side that is exposed to air. Similarly, photo-patterning of **SAM1** on gold electrodes leads to a pattern of non-fluorescent regions on glass around the electrode. Figure 3.21a-d compares white and dark field optical images of two representative samples. Dark field optical images were acquired by illuminating sample with 365 nm light, but light illuminated and reflected by the

sample, in addition to background light, was not filtered before capturing with black and white camera. Thus, patterns on gold electrode in dark field images (figure 3.21) are attributed to reflections of background and fluorescent light by the electrode rather than fluorescence of **SAM1** on gold surface. Fluorescence, and therefore patterns of non-fluorescent regions, are observable for at least 35 days of storage under ambient conditions, as shown in the figures 3.21e-f.

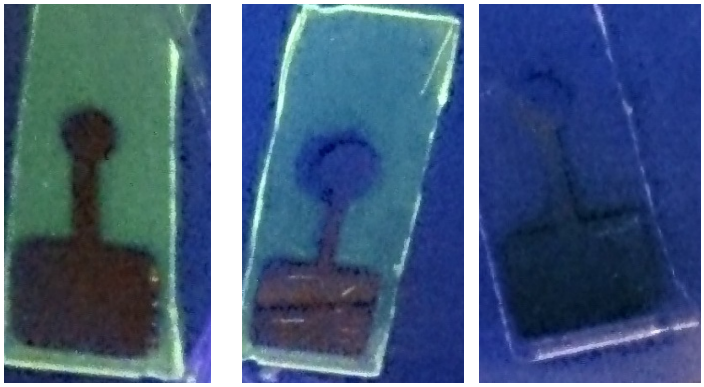

(A) **SAM1** (B) **SAM1** + UV (C) **ALA SAM**

FIGURE 3.19: Photos taken with an ordinary camera of a) glass substrate fluorescent in green after formation of **SAM1** on gold electrode, b) loss of the fluorescence after exposure to UV (365 nm, 22 J cm^{-2}, 36 mW cm^{-2}, 10 min), and c) non-fluorescent glass substrate after formation of **ALA SAM** on gold electrode.

The non-fluorescent regions show hydrophilic character, thus rinsing UV treated samples with water produces a pattern of confined water features on both sides of glass (figure 3.20). Quality of the patterns improves after rinsing surfaces with DCM.

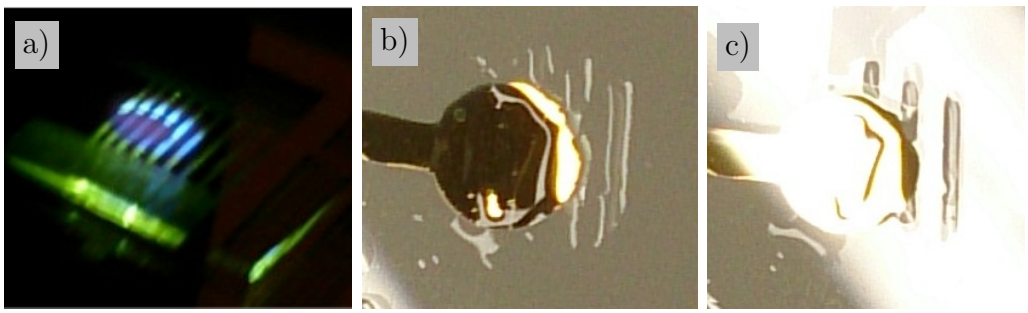

FIGURE 3.20: Photos taken with an ordinary camera of a) photo-patterning **SAM1** on gold electrode on glass substrate, followed by formation of b)-c) pattern of confined water features upon rinsing with water.

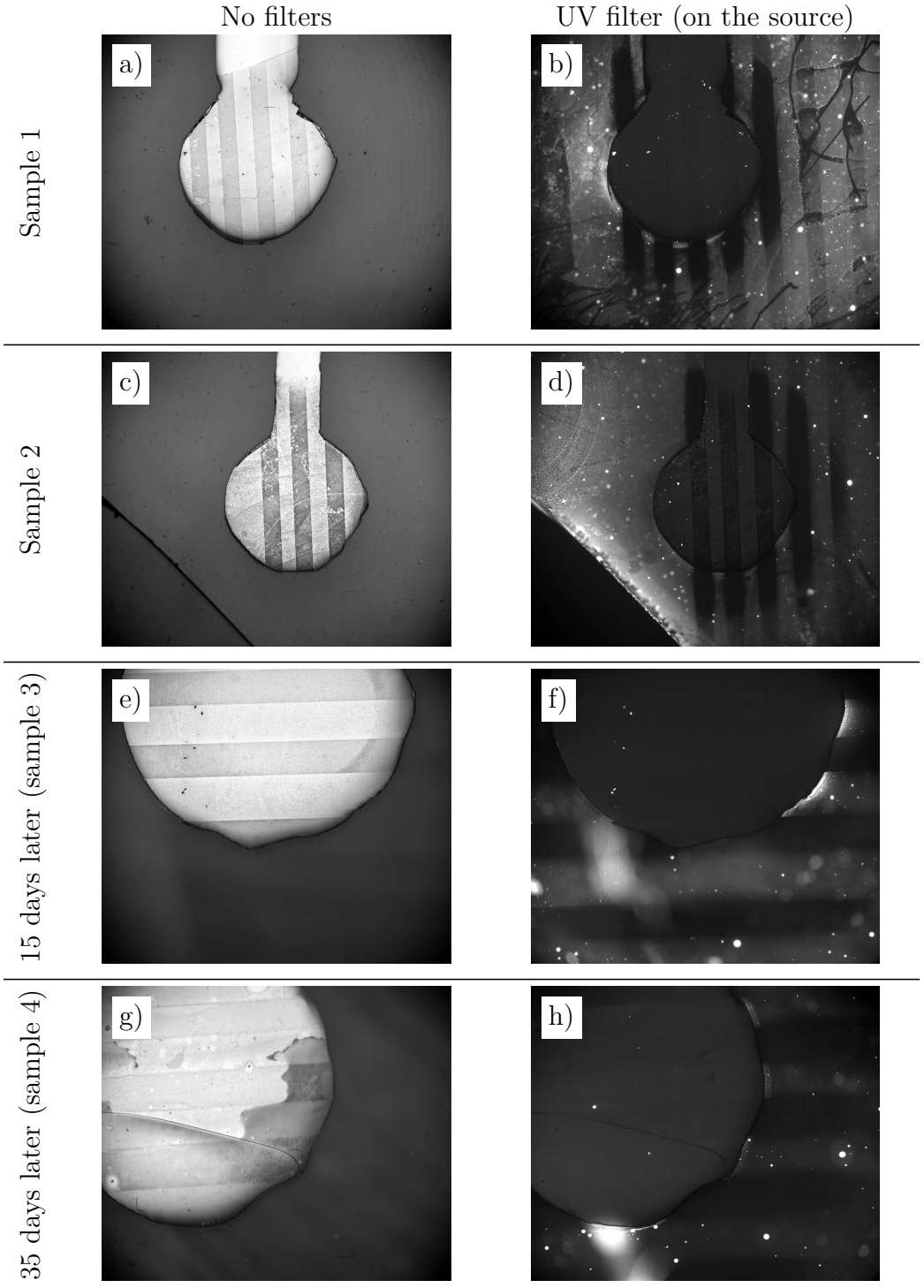

FIGURE 3.21: Optical images acquired on a fluorescence microscope of photopatterned **SAM1** (365 nm, 22 J cm^{-2}, 36 mW cm^{-2}, 10 min) with deposited copper. Fresh a)-b) sample 1 and c)-d) sample 2, e)-f) sample 3 after 15 days, and g)-h) sample 4 after 35 days. No filters were used to capture light form the samples, but images on the left and on the right were acquired when samples were illuminated with white and UV (365 nm) light, respectively. Darker areas correspond to higher amounts of deposited copper on UV-treated regions in images on the left, but lack of green fluorescence in images on the right.

3.3.2.2 Reagent 1 film on silicon oxide

Formation of **reagent 1** layers and their photo-patterning were also investigated on silicon wafer. Reflectivity of silicon in visible region allows to qualitatively study structure of **reagent 1** films and structural changes induced by soft UV photo-patterning and rinsing with chemicals (e.g. solvents and detergents) on micro scale.

Silicon's reflectivity also enhances green fluorescence of **reagent 1** films (figure 3.19 vs 3.22), but patterns of non-fluorescent (figure 3.22a) and hydrophilic (figure 3.22b and 3.22c) regions are formed in the same way as on glass substrates. The latter can also be observed after rinsing with DCM, because that leads to condensation of water micro-droplets from moisture in the air. Water repeatedly formed better quality hydrophilic patterns after a rinse with DCM.

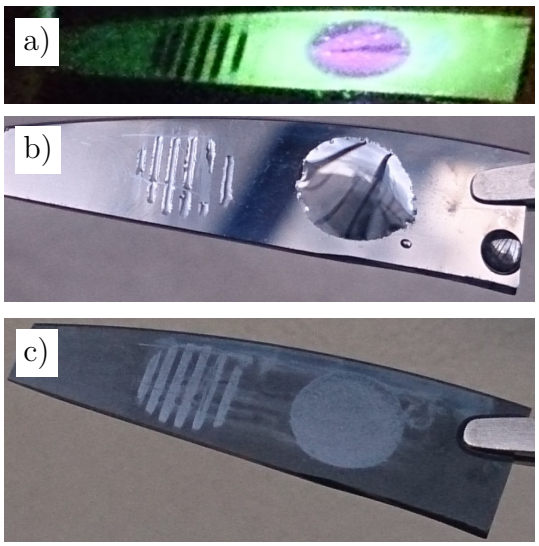

FIGURE 3.22: Photos taken with an ordinary camera of a) photo-patterned **reagent 1** film on a piece of silicon wafer with UV (365 nm) showing the loss of green fluorescence, and the formation of hydrophilic pattern of water droplets upon the rinse with b) water, or c) DCM.

Features observed with optical microscope on a smooth and mirror-like silicon surface can be unambiguously assigned to **reagent 1** film, in contrast to transparent and relatively uneven microscope glass slides that give rise to various back-reflections and scattered light.

Figures 3.23a, 3.24a and 3.24e indicate that uniformity of the films is comparable to that of drop-cast films rather those obtained by self-assembly, spin coating, thermal evaporation etc. Also, the fact that various features can be observed in optical microscopy indicate that the films have greater thickness than **SAM1** by orders of magnitude.

Figures 3.23b, 3.24b and 3.24f show optical images captured when photo-patterned samples were illuminated with soft UV light. Images were acquired with black and white camera, thus bright and dark regions mainly correspond to green fluorescence (as shown in figure 3.22a) and its absence, respectively. Despite the evident patterns in the images, there are no sign of them in ordinary optical images (samples illuminated with white light) presented in figures 3.23a, 3.24a and 3.24e. Furthermore, images in figures 3.23c, 3.23e and 3.23g indicate that structure of the film at micro scale is not affected with a rinse of water, unless it is rinsed with DCM first; in which case **reagent 1** molecules are washed away from both UV treated and non-treated regions, because initially stripes have the same intensity of fluorescence as the surrounding region, but it drops in the the former upon rinsing with DCM. Further rinse with water enhances the pattern in ordinary images and cause visible deterioration of the film in UV treated areas (figure 3.23g).

Finally, images in figure 3.24 indicate that **reagent 1** films are removed from regions not exposed to UV, mostly removed from the regions exposed to UV for 10 min and hardly removed from the regions exposed to UV for 40 min by a rinse with 10 % Decon90 solution. Additionally, it was observed that formation of the film was most pronounced on substrates, that were piranha cleaned days after ultrasonication in 10 % Decon90 for 15 min (following by appropriate rinsing and drying and the ultrasonication in a solvent, such as DCM), and severely suppressed when the procedure was performed immediately before the piranha etching. That is indicative that **reagent 1** is potentially interacting strongly with adventitious species adsorbed onto

glass and silicon oxide surfaces rather than the substrates themselves; also it suggest that piranha etching (at least during the first 2-5 min) does not remove those specific species from the surfaces.

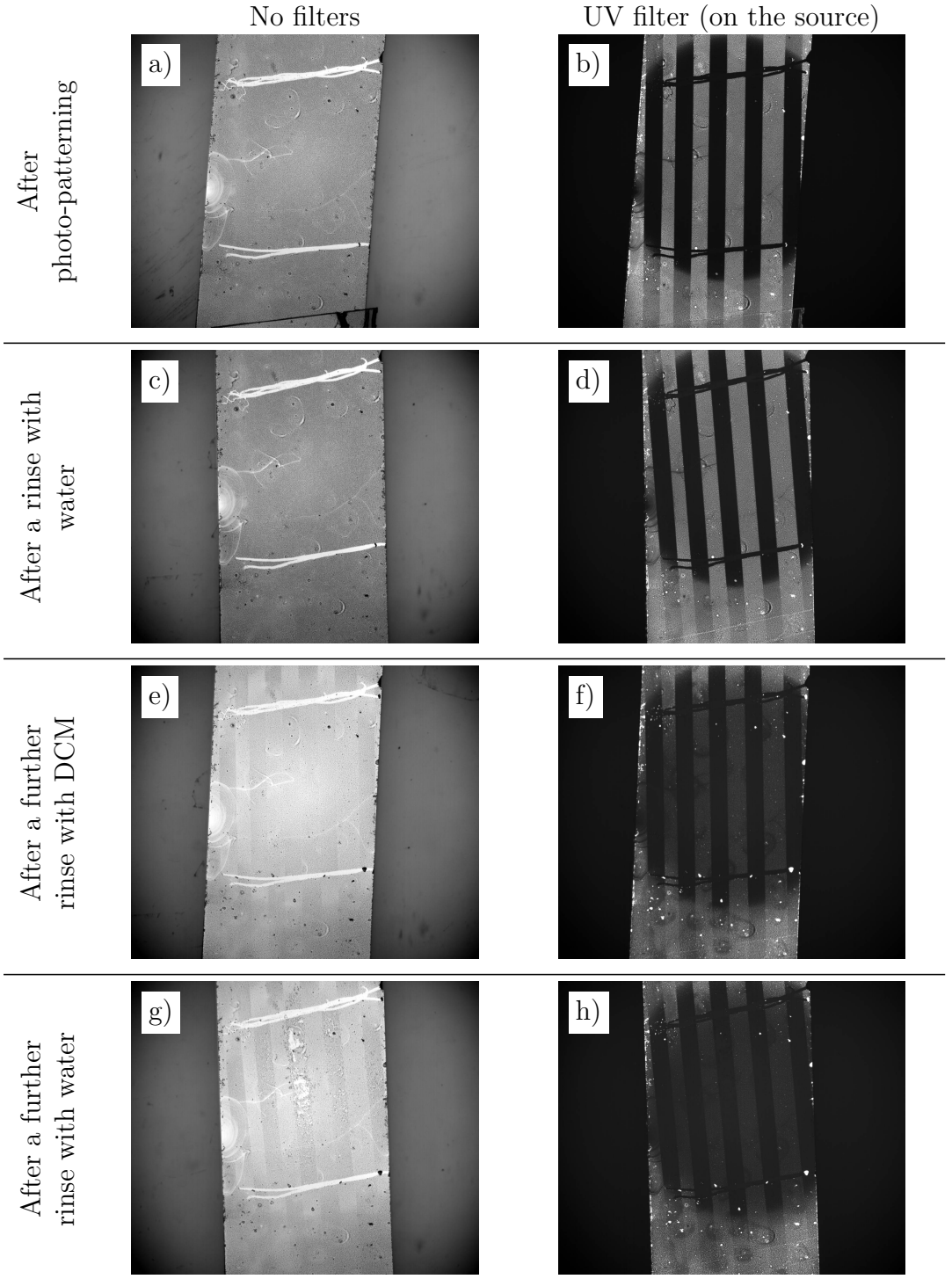

FIGURE 3.23: Optical images acquired on a fluorescence microscope of **reagent 1** layers on a silicon wafer a)-b) after photo-patterning (365 nm, 22 J cm^{-2}, 36 mW cm^{-2}, 10 min), followed by c)-d) a rinse with water, then e)-f) a further rinse with DCM, and g)-h) a rinse with water again. No filters were used to capture light form the sample, but images on the left and on the right were acquired when the sample was illuminated with white and UV (365 nm) light, respectively. Darker areas in images on the right correspond to a lack of green fluorescence and scratch marks (in white in images on the left) identifying region of interest.

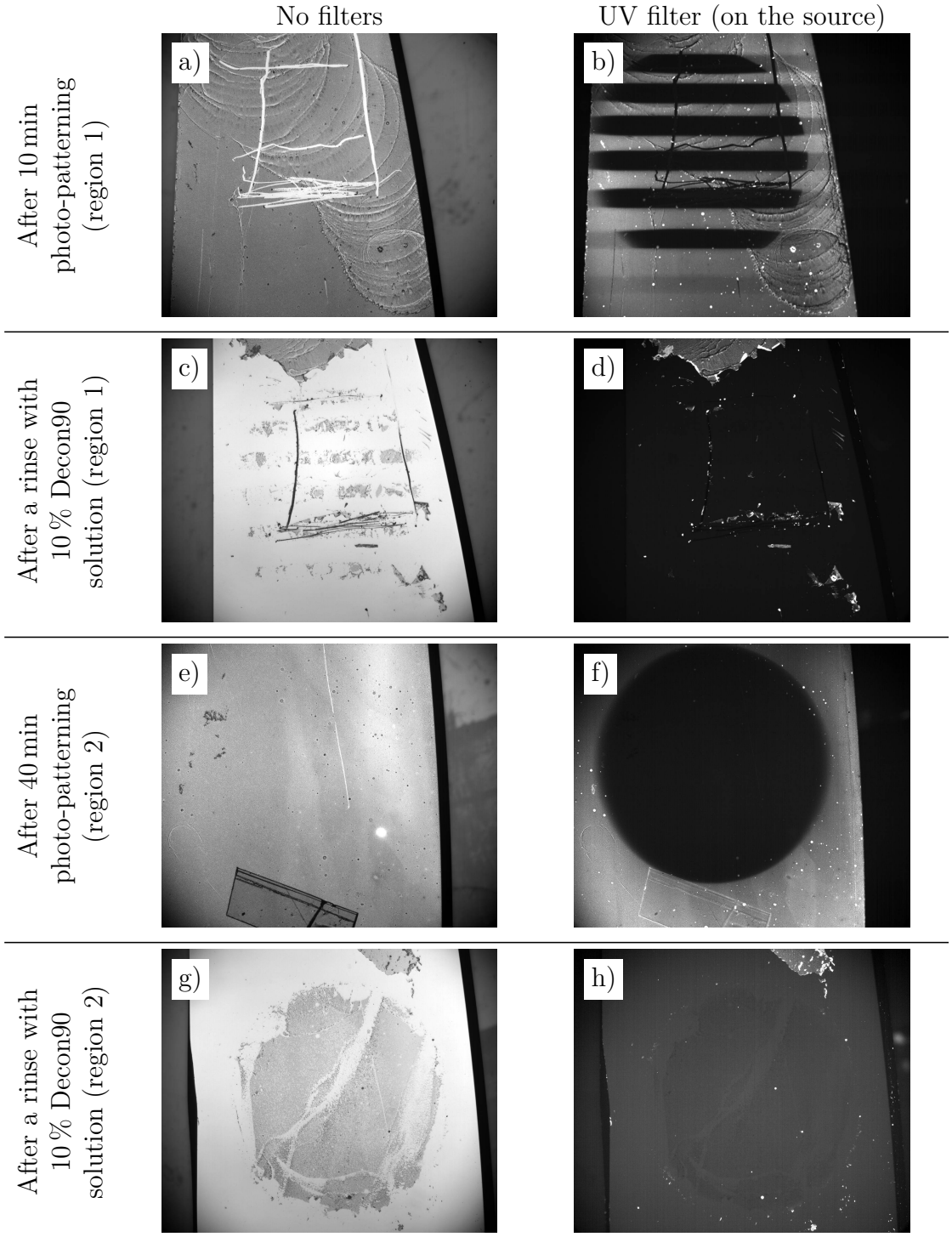

FIGURE 3.24: Optical images acquired on a fluorescence microscope of **reagent 1** layers on a silicon wafer after photo-patterning (365 nm, 36 mW cm^{-2}) a)-b) region 1 for 10 min and e)-f) region 2 for 40 min and effects of rinsing the sample with 10 % Decon90 solution on c)-d) region 1 and g)-h) region 2. No filters were used to capture light form the sample, but images on the left and on the right were acquired when the sample was illuminated with white and UV (365 nm) light, respectively. Darker areas in images on the right correspond to a lack of green fluorescence and scratch marks (in white in images on the left) in region 1.

3.3.3 Discussion

Cyclic voltammetry of **SAM1** modified electrodes in 10 mM $CuSO_4$ in 10 mM H_2SO_4 shows considerably higher E_p potential (0.07 V more negative) than reported for photo-patternable system based on *ortho*-nitrobenzyl and perfluoro groups.[12,80] It indicates that **SAM1** acts as a stronger barrier against diffusion of Cu^{2+} ions towards gold surface, which most likely originates from both chemical properties of pyrene group and higher packing in the SAM. The latter is likely to play an important role, as **ALA SAM** also yields a higher E_p value than any of the SAMs (some of which with higher thickness) in the reported study.[12,80] Furthermore, the fact that UV treated **SAM1** yields lower E_p value than fresh **ALA SAM**, can also be explained by the fact that UV treatment reduces packing in **SAM1**. The instability of CVs performed on electrodes modified with **ALA SAM** in the acidic electrolyte (10 mM $CuSO_4$ in 10 mM H_2SO_4) might be related to the instability observed under acidic (100 mM HCl in IPA) UV treatment conditions (section 3.2.4), but could also correspond to a chemical interaction of copper with carboxylic acid group or permanent disruption of the SAM by formation and growth of copper nucleation sites. Reasons mentioned above are believed to be the cause for relatively little metallisation on non-treated regions, even after first half of a CV cycle is performed (i.e. voltage sweep from stage 1 to 5 in figure 3.14b), which is in contrast to the reported system, which exhibits a severe metallisation at this stage.[80]

The weaker E_p potential of photo-patterned SAMs (−0.18 V) than uniformly treated (with UV in the acid catalyst) **SAM1** (−0.21 V), and the shift of the potential towards a more negative value (−0.20 V) in consecutive CV cycles in the former SAM are perplexing. Nevertheless, it was found that the highest selectivity of copper occurs around potential of −0.18 V, whether electrochemical deposition is performed at constant or sweeping potential. The former method gave lower reproducibility rate and poor uniformity on micro scale, both of which are attributed to a phase of

quick and spontaneous initialisation of nucleation sites that is immediately followed by a phase of rapid growth of the sites, due to sudden activation of the potential across the electrochemical cell. On the other hand, sweeping potential method led to a much higher reproducibility and a better uniformity on micro scale, attributed to a prolonged phase of initialisation of nucleation sites, followed by a smooth transition into the phase of growth of nucleation site.

Non-fluorescence of **SAM1** illustrates the quenching effect - a well known property of gold that also occurs in gold thin films. However, **reagent 1** films (not SAMs) on silicon oxide or glass substrates exhibit green fluorescence due to absence of gold. It is thought that films are formed due to strong interaction between **reagent 1** and adventitious species that are not removed by piranha etching (during the first 2-5 min), as layers cannot be rinsed away with DCM, which is the solvent used to dissolve the molecules in the first place, but a brief rinse with 10 % Decon90 solution almost completely removes the films. Also, the films only form effectively on samples that were not immediate cleaned with 10 % Decon90 solution before etching with piranha solution. More specifically, the pyrene end group in **reagent 1** is associated with the interaction, because no formation of **lipoic acid**, **DTBA**, **MHA**, **MOA** or **MUA** layers have been observed. Nevertheless, it is thought that the growth of the layers might result from the cross-linking of dithiolane head groups in **reagent 1**, as is the case in **SAM1**. This could explain the lack of uniformity and considerable thickness of the layers. However, it is not understood whether prolonged exposure to soft UV induces any chemical reactions between (i) **reagent 1** and the surfaces or (ii) the cross-linked molecules in the layer, that could prevent removal of molecules when the surface is rinsed with 10 % Decon90 solution.

Loss of fluorescence upon prolonged exposure to soft UV (365 nm in air or in acidic catalyst 100 mM HCl in IPA) could be attribute to the effect of photo-bleaching, because no structural changes appear in the film on the micro scale. However,

exposure to the UV also turns hydrophobic regions into hydrophilic, which could only be explained by appearance of polar groups on the surface; a process that is not natural under ambient conditions. Given that **reagent 1** undoubtedly photocleaves in dilute solutions to release lipoic acid,[1] it is likely that the same process takes place in these films. That would explain why patterns also appears in ordinary optical images and why quality of hydrophilic patterns of water improve after a rinse with DCM. It cannot be excluded that exposure to UV also breaks up disulfide bonds in the cross-linked film and, therefore, a rinse with DCM also removes chunks of cross-linked **lipoic acid** and cross-linked **reagent 1** molecules. Surprisingly, samples stay fluorescence, and patterns stay hydrophilic for at least 35 days under ambient conditions, which indicates high stability of the formed layers.

3.4 Conclusions

A novel molecule containing functional carboxylic acid group protected with 1-acetylpyrene was used to form self-assembled monolayers (**SAM1**) on gold surfaces. Photo-deprotection of carboxylic acid group in **SAM1** was investigated by treating it with soft UV (365 nm, 4 mW cm^{-2}) light for various time periods and in various catalysts. It was found that irradiation under pure IPA or aqueous mixtures (50:50) of IPA, MeOH and MeCN for 1.5 h (and in some cases up to 5 h) has no significant impact on **SAM1** thickness, contact angles, IR absorption or chemical composition. On the other hand, exposure of the SAM to soft UV in 100 mM HCl in IPA for 1.5 h leads to a severe decrease in thickness (4 times), however, it does not change the contact angles, which are distinctively different from the angles usually observed on surfaces containing carboxylic acid groups. Furthermore, despite the drop in absorption, IR spectra does not change in shape, suggesting that total amount of material decreases, but relative ratio of ester and aryl ketone groups stays the same, thus indicating no emergence of deprotected carboxylic acid groups on the gold surface. Finally, XPS spectra and quantitative analysis do not show any change in relative amounts of chemical elements or their species, except a significant increase of gold signal w.r.t. all other elements. However, such treatment performed in the dark does not yield any significant changes. Therefore, the acquired data suggest that photo-reaction takes place under the acidic conditions, but ultimately it leads to a loss of **reagent 1** molecules from the surface, rather than a monolayer terminated with carboxylic acid group.

Three possible pathways for the photolysis in **SAM1** are proposed (figure 3.12): (i) **Scheme A** - loss of cross-linked molecules from the surface, due to breakage of S-S bond; (ii) **Scheme B** - photo-deprotection that yields **lipoic acid** molecules, which are unstable under the UV treatment conditions and consequently removed from the gold surface; (iii) **Scheme C** - removal of **reagent 1** molecules from the surface,

due to breakage of S-Au interaction. Taken into account investigations of (i) cyclic voltammetry on **SAM1** and **ALA SAM**, (ii) **reagent 1** film formation on silicon oxide and glass surfaces, and their photo-patterning, and (iii) the stability of **DTBA SAM**, **MHA SAM**, **MOA SAM** and **MUA SAM** (see chapter 5 for details), **Scheme B** is likely to be dominating and **Scheme A** partially contributing, while **Scheme C** is unlikely, but can not be fully excluded from the photolysis in **SAM1**. This unexpected outcome of **SAM1** treatment triggered investigation of stability of **ALA SAM** and SAMs of conventional thiolates of various chain lengths with carboxylic acid end group, which is presented in chapter 5.

Although UV treatment of **SAM1** under such conditions does not lead to a monolayer terminated with carboxylic acid group, the induced disorder and lower packing of **reagent 1** molecules proved to be more beneficial in highly selective metallisation Copper can be successfully and reversibly deposited (ECD) multiple times on the treated regions on photo-patterned **SAM1** samples, which could possibly be used for selective fabrication of nanostructures of metals or alloys.[81–83] Furthermore, little copper is found on non-treated regions even when ECD is performed at more negative than usual potentials, and at the end of the reduction phase in CV sweeps, which contrasts with reported photo-patternable SAM based on *ortho*-nitrobenzyl and perfluoro groups.[12,80]

Although **SAM1** does not fluoresce due to quenching by gold, it was discovered that **reagent 1** molecules form fluorescent (in green) films on silicon oxide and glass surfaces. Films can not be removed with a thorough rinse or prolonged ultrasonication in DCM, even though it is used to dissolve **reagent 1** molecules in the first place. On the other hand, films are easily rinsed away with 10 % Decon90 solution, which indicates that films physisorb rather than chemisorb onto the surfaces. Furthermore, it was noticed that while all of the substrates were etched with piranha immediately before immersion into **reagent 1** solution in DCM, layers were effectively formed

only on the substrates that were cleaned with 10 % Decon90 solution not immediately before piranha etching. Thus, film formation is assigned to interaction of **reagent 1**, more precisely pyrene group, with the adventitious contamination on silicon oxide and glass surface that is not removed by piranha etching (at least during the first 2-5 min). The films yield high thickness, and the growth of the thickness is attributed to cross-linking of the molecules via disulfide bonds after opening of the dithiolane rings, a phenomena that has been observed in **reagent 1** synthesis, **SAM1**, and **ALA SAM**. Photo-patterning in the air or in the acid leads to the creation of non-fluorescent hydrophilic regions attributed to photo-bleaching and photo-deprotection of lipoic acid molecules in the films. Such patterns are stable for at least 35 days under ambient conditions.

3.5 References

[1]A. Jana, S. Atta, S. K. Sarkar and N. D. P. Singh, Tetrahedron **66**, 9798–9807 (2010).

[2]M. Nakagawa and K. Ichimura, **204**, 1–7 (2002).

[3]K. Critchley, J. P. Jeyadevan, H. Fukushima, M. Ishida, T. Shimoda, R. J. Bushby and S. D. Evans, Langmuir **21**, 4554–4561 (2005).

[4]B. Zhao, J. S. Moore and D. J. Beebe, Anal. Chem. **74**, 4259–4268 (2002).

[5]P. Prompinit, A. S. Achalkumar, X. Han, R. J. Bushby, C. Wälti and S. D. Evans, J. Phys. Chem. C **113**, 21642–21647 (2009).

[6]M. K. F. Lo, M. N. Gard, B. R. Goldsmith, M. A. Garcia-Garibay and H. G. Monbouquette, Langmuir **28**, 16156–16166 (2012).

[7]O. El Zubir, I. Barlow, E. Ul-Haq, H. A. Tajuddin, N. H. Williams and G. J. Leggett, Langmuir **29**, 1083–1092 (2013).

[8]T. A. Martin, C. T. Herman, F. T. Limpoco, M. C. Michael, G. K. Potts and R. C. Bailey, ACS Appl. Mater. Interfaces **3**, 3762–3771 (2011).

[9]S. H. Kim, H. Ohtsuka, M. C. R. Tria, K. Tanaka, R. C. Advincula and H. Usui, Thin Solid Films **554**, 78–83 (2014).

[10]Y. Yu, X. Kang, X. Yang, L. Yuan, W. Feng and S. Cui, Chem. Commun. (Camb). **49**, 3431–3 (2013).

[11]P. Klan, T. Solomek, C. G. Bochet, R. Givens, M. Rubina, V. Popik, A. Kostikov and J. Wirz, Chem. Rev. **113**, 119–191 (2012).

[12]P. Prompinit, A. S. Achalkumar, A. S. Walton, R. J. Bushby, C. Wälti and S. D. Evans, J. Mater. Chem. C **2**, 5916 (2014).

[13]F. Lü, Y. Fang and G. Blanchard, Spectrochim. Acta Part A Mol. Biomol. Spectrosc. **74**, 991–999 (2009).

[14]R. Arnold, W. Azzam, A. Terfort and C. Wöll, Langmuir **18**, 3980–3992 (2002).

[15]A. Myrskog, H. Anderson, T. Aastrup, B. Ingemarsson and B. Liedberg, Langmuir **26**, 821–829 (2010).

[16]R. G. Nuzzo, L. H. Dubois and D. L. Allara, J. Am. Chem. Soc. **112**, 558–569 (1990).

[17]J. Li, K. S. Liang, G. Scoles and A. Ulman, Langmuir **11**, 4418–4427 (1995).

[18]E. L. Smith, C. a. Alves, J. W. Anderegg and M. D. Porter, Langmuir **8**, 2707–2714 (1992).

[19]O. Dannenberger, K. Weiss, H. J. Himmel, B. Jäger, M. Buck and C. Wöll, Thin Solid Films **307**, 183–191 (1997).

[20]H. J. Himmel, K. Weiss, B. Jäger, O. Dannenberger, M. Grunze and C. Wöll, Langmuir **13**, 4943–4947 (1997).

[21]F. Sun, D. G. Castner and D. W. Grainger, Langmuir **9**, 3200–3207 (1993).

[22]R. S. Rasmussen, D. D. Tunnicliff and R. R. Brattain, J. Am. Chem. Soc. **71**, 1068–1072 (1949).

[23]H. Toriumi, H. Sugisawa and H. Watanabe, Jpn. J. Appl. Phys. **27**, L935–L937 (1988).

[24]A. A. Jbarah, K. Döring, H. Lang and R. Holze, Vib. Spectrosc. **49**, 162–173 (2009).

[25]M. Wells, D. L. Dermody, H. C. Yang, T. Kim, R. M. Crooks and a. J. Ricco, Langmuir **12**, 1989–1996 (1996).

[26]S. E. Creager and C. M. Steiger, Langmuir **11**, 1852–1854 (1995).

[27]E. B. Troughton, C. D. Bain, G. M. Whitesides, R. G. Nuzzo, D. L. Allara and M. D. Porter, Langmuir **4**, 365–385 (1988).

[28]P. E. Laibinis, G. M. Whitesides, D. L. Allara, Y. T. Tao, A. N. Parikh and R. G. Nuzzo, J. Am. Chem. Soc. **113**, 7152–7167 (1991).

[29]J. M. Tour, L. Jones, D. L. Pearson, J. J. S. Lamba, T. P. Burgin, G. M. Whitesides, D. L. Allara, A. N. Parikh and S. Atre, J. Am. Chem. Soc. **117**, 9529–9534 (1995).

[30]K. Heister, M. Zharnikov, M. Grunze and L. S. O. Johansson, J. Phys. Chem. B **105**, 4058–4061 (2001).

[31]S. D. Techane, L. J. Gamble and D. G. Castner, J. Phys. Chem. C **115**, 9432–9441 (2011).

[32]G. Beamson and D. Briggs, *High Resolution XPS of Organic Polymers: The Scienta ESCA300 Database* (Wiley, 1992), ISBN: 9780471935926.

[33]T. M. Willey, A. L. Vance, C. Bostedt, T. van Buuren, R. W. Meulenberg, L. J. Terminello and C. S. Fadley, Langmuir **20**, 4939–4944 (2004).

[34]S.-J. Xiao, S. Brunner and M. Wieland, J. Phys. Chem. B **108**, 16508–16517 (2004).

[35]R. V. Duevel and R. M. Corn, Anal. Chem. **64**, 337–342 (1992).

[36]A. C. Gouget-Laemmel, J. Yang, M. A. Lodhi, A. Siriwardena, D. Aureau, R. Boukherroub, J. N. Chazalviel, F. Ozanam and S. Szunerits, J. Phys. Chem. C **117**, 368–375 (2013).

[37]S. Engin, V. Trouillet, C. M. Franz, A. Welle, M. Bruns and D. Wedlich, Langmuir ACS J. Surfaces Colloids **26**, 6097–6101 (2010).

[38]E. W. Wollman, D. Kang, C. D. Frisbie, I. M. Lorkovic and M. S. Wrighton, J. Am. Chem. Soc. **116**, 4395–4404 (1994).

[39]C. D. Bain, E. B. Troughton, Y. T. Tao, J. Evall, G. M. Whitesides and R. G. Nuzzo, J. Am. Chem. Soc. **111**, 321–335 (1989).

[40]P. Gupta, A. Ulman, S. Fanfan, A. Korniakov and K. Loos, J. Am. Chem. Soc. **127**, 4–5 (2005).

[41]C. D. Bain, H. A. Biebuyck and G. M. Whitesides, Langmuir **5**, 723–727 (1989).

[42]Y. Tai, M. Buck, M. Grunze, M. Zharnikov, A. Shaporenko, H.-T. Rong and W. Eck, J. Phys. Chem. B **108**, 16806–16810 (2004).

[43]T. Ishida, N. Choi, W. Mizutani, H. Tokumoto, I. Kojima, H. Azehara, H. Hokari, U. Akiba and M. Fujihira, Langmuir **15**, 6799–6806 (1999).

[44]H. Takiguchi, K. Sato, T. Ishida, K. Abe, K. Yase and K. Tamada, Langmuir **16**, 1703–1710 (2000).

[45]A. Vokert, V. Subramaniam, M. Ivanov, A. Goodman and A. Haes, ACS Nano **5**, 25–41 (2011).

[46]J. Dote and R. Mowery, J. Phys. Chem. **92**, 1571–1575 (1988).

[47]A. Ulman, *An Introduction to Ultrathin Organic Films from Langmuir-Blodgett to Self-Assembly* (Academic Press, Boston, 1991), ISBN: 0127082301.

[48]W. K. Paik, S. Han, W. Shin and Y. Kim, Langmuir **19**, 4211–4216 (2003).

[49]K. Bandyopadhyay, V. Patil, K. Vijayamohanan and M. Sastry, Langmuir **13**, 5244–5248 (1997).

[50]Z. Zhang and T. Imae, Nano Lett. **1**, 241–243 (2001).

[51]G. Battistini, P. G. Cozzi, J.-P. Jalkanen, M. Montalti, L. Prodi, N. Zaccheroni and F. Zerbetto, ACS Nano **2**, 77–84 (2008).

[52]B. I. Ipe and K. G. Thomas, J. Phys. Chem. B **108**, 13265–13272 (2004).

[53]J. C. Love, L. A. Estroff, J. K. Kriebel, R. G. Nuzzo and G. M. Whitesides, Chem. Rev. **105**, 1103–1170 (2005).

[54]S. A. Claridge, W.-S. Liao, J. C. Thomas, Y. Zhao, H. H. Cao, S. Cheunkar, A. C. Serino, A. M. Andrews and P. S. Weiss, Chem. Soc. Rev. **42**, 2725–45 (2013).

[55]R. C. Thomas, J. E. Houston, R. M. Crooks, T. Kim and T. A. Michalske, J. Am. Chem. Soc. **117**, 3830–3834 (1995).

[56]T. Steiner, Angew. Chem. Int. Ed. **41**, 48–76 (2002).

[57]A. Ulman, Chem. Rev. **96**, 1533–1554 (1996).

[58]H. Yuasa, N. Miyagawa, T. Izumi, M. Nakatani, M. Izumi and H. Hashimoto, Org. Lett. **6**, 1489–1492 (2004).

[59]Y. Zhang, S. Yuan, W. Zhou, J. Xu and Y. Li, J. Nanosci. Nanotechnol. **7**, 1–10 (2007).

[60]R. Nandy, M. Subramoni, B. Varghese and S. Sankararaman, J. Org. Chem. **72**, 938–944 (2007).

[61]J. M. Sanders, J. Phys. Chem. A **114**, 9205–9211 (2010).

[62]T. Sato, T. Tsuneda and K. Hirao, J. Chem. Phys. **123**, 104307 (2005).

[63]A. KISANUKI, Y. KIMPARA, Y. OIKADO, N. KADO, M. MATSUMOTO and K. ENDO, J Polym Sci Part A Polym Chem **48**, 5247–5253 (2010).

[64]E.-k. Bang, G. Gasparini, G. Molinard, A. Roux, N. Sakai and S. Matile, J. Am. Chem. Soc. **135**, 2088–2091 (2013).

[65]E.-K. Bang, S. Ward, G. Gasparini, N. Sakai and S. Matile, Polym. Chem. **5**, 2433 (2014).

[66]J. Barltrop, P. Hayes and M. Calvin, J. Am. Chem. Soc. **76**, 4348–4367 (1954).

[67]P. R. BROWN and J. O. EDWAR, **34**, 3131–3135 (1969).

[68]C. Krishnan and M. Garnett, Int. J. Electrochem. Sci **6**, 3607–3630 (2011).

[69]E. Orentas, M. Lista, N.-T. Lin, N. Sakai and S. Matile, Nat. Chem. **4**, 746–750 (2012).

[70]N. Sakai, M. Lista, O. Kel, S.-i. Sakurai, D. Emery, J. Mareda, E. Vauthey and S. Matile, J. Am. Chem. Soc., 15224–15227 (2011).

[71]M. Lista, J. Areephong, N. Sakai and S. Matile, J. Am. Chem. Soc. **133**, 15228–15231 (2011).

[72]N. Sakai and S. Matile, J. Am. Chem. Soc. **133**, 18542–18545 (2011).

[73]J. Areephong, E. Orentas, N. Sakai and S. Matile, Chem. Commun. **48**, 10618 (2012).

[74]P. Charbonnaz, N. Sakai and S. Matile, Chem. Sci. **3**, 1492 (2012).

[75]L. Teuber, Sulfur reports **9**, 257–333 (1990).

[76]J. A. M. Sondag-Huethorst and L. G. J. Fokkink, Langmuir **11**, 4823–4831 (1995).

[77]E. D. Eliadis, R. C. Nuzzo, A. A. Gewirth and R. C. Alkire, J. Electrochem. Soc. **144**, 96–105 (1997).

[78]G. C. Herdt, D. R. Jung and A. W. Czanderna, Prog. Surf. Sci. **50**, 103–129 (1995).

[79]D. R. Jung, A. W. Czanderna and G. C. Herdt, J. Vac. Sci. Technol. A **14**, 1779–1787 (1996).

[80]P. Prompinit, *Formation and Application of Photo-patterned SAMs* (University of Leeds (School of Physics and Astronomy), 2011).

[81]L. P. Bicelli, B. Bozzini, C. Mele and L. D. Urzo, Int. J. Electrochem. Sci. **3**, 356–408 (2008).

[82]Switzer, Shumsky and Bohannan, Science **284**, 293–6 (1999).

[83]F. Yang, K. Liu, K. Hong, D. Reich, P. Searson and C. Chien, Science **284**, 1335–1337 (1999).

Chapter 4

SAMs for spin crossover (SCO) surfaces

Some of the data presented in this chapter on the study of SAM formation of ligand $\mathbf{L_1}$ and its Fe(II) complex have been included in the publication L. Pukenas et al., J. Mater. Chem. C **3**, 7890–7896 (2015).

This chapter investigates the formation of novel self-assembled monolayers (SAMs) that could have a potential to exhibit spin crossover (SCO) behaviour. New derivatives $\mathbf{L_1}$ and $\mathbf{L_2}$ of ligands **bpp** and $\mathbf{Py_5}$, respectively, contain thiomorpholine head group that facilitates self-assembly on gold surface. The main objectives of this study are as follows:

- to form SAMs of ligands only, i.e. **SAM** $\mathbf{L_1}$ and **SAM** $\mathbf{L_2}$ (figure 4.1).
- to coordinate Fe(II) to **SAM** $\mathbf{L_1}$ and **SAM** $\mathbf{L_2}$ (figure 4.2).
- to form SAMs of Fe(II) complexes, i.e. **SAM** $\mathbf{C_1}$ and **SAM** $\mathbf{C_2}$ (figure 4.3).

- to perform ligand exchange at the sixth exogenous ligand (SEL) positions in **SAM C_2** by rinsing with solvents, in order to change spin state of the iron centres (figure 4.4).

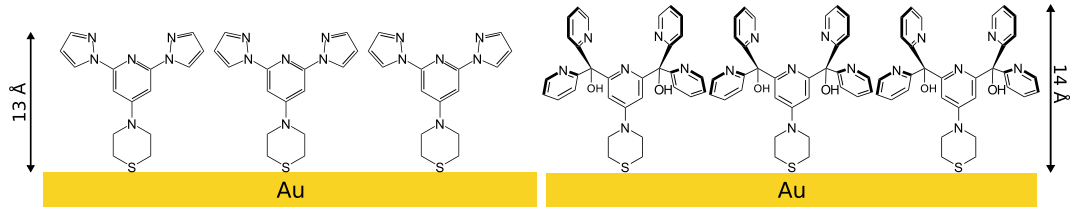

(A) **SAM L_1** (B) **SAM L_2**

FIGURE 4.1: Schematic model of the novel SAMs.

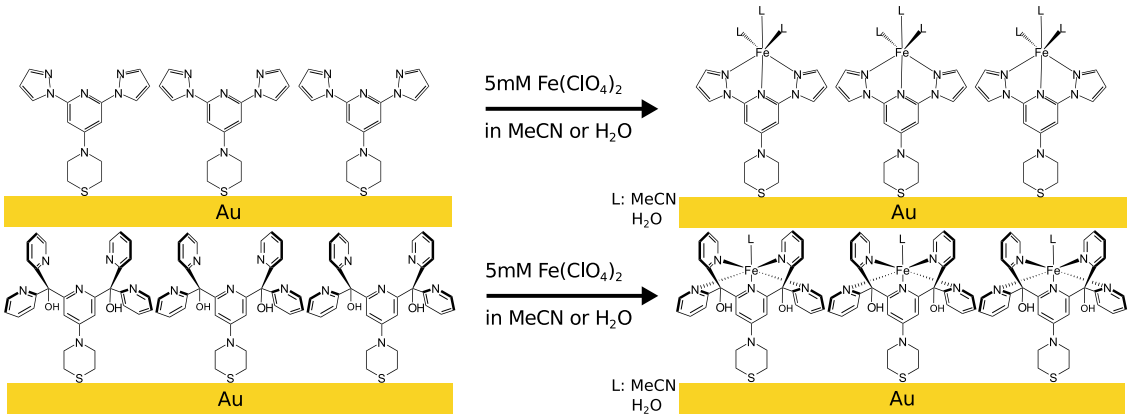

FIGURE 4.2: Schematic detailing Fe coordination to **SAM L_1** and **SAM L_2** in MeCN or H_2O.

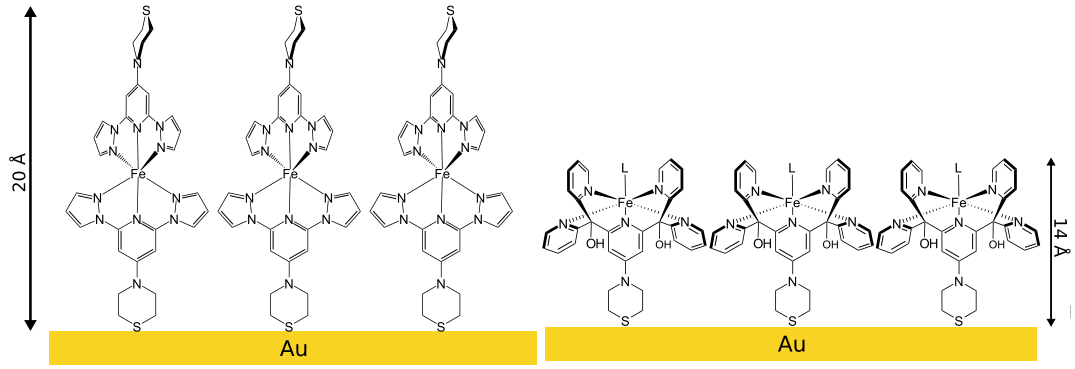

(A) **SAM C_1** (B) **SAM C_2** with exogenous ligand L

FIGURE 4.3: Schematic model of the novel SAMs.

The study presented in this chapter has revealed that both ligand **L_1** and **L_2** successfully form SAMs, however, **SAM L_2** does not show any signs of Fe(II) coordination.

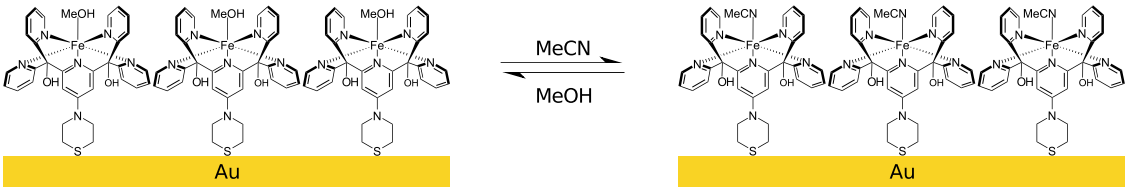

FIGURE 4.4: Schematic detailing reversible ligand exchange by rinsing **SAM C_2** with MeCN and MeOH.

Also, instead of forming **SAM C_1**, complex **C_1** produces **SAM L_1** indicating demetallisation during SAM formation. Complex **C_2** successfully forms **SAM C_2** in MeOH and MeCN solutions, and shows the same characteristics as **SAM L_2** after Fe(II) coordination. However, successful ligand exchange and therefore change in spin state was not detected and SCO behaviour was not 'unlocked' in **SAM C_2**.

4.1 Introduction

Since the first observation of the SCO phenomena nearly a century ago,[2] the field has expanded and a wide range of ligands have been synthesised to form complexes of transition metals with desired and fine tuned SCO properties. Recently, attention has shifted towards studies of SCO in nanoscale materials,[3–6] that not only opened opportunities for new applications, but also led to enhancement of some SCO properties.[7,8] However, the majority of work has been undertaken on coordination polymers,[9,10] and less so on molecular SCO compounds. Most of the fabricated structures include continuous films,[3–5] but other structures, such as patterned films[3] or nanoparticles,[3,4,11] have also been developed. Spin coating and thermal vacuum deposition have attracted attention for production of homogeneous films. The latter is of particular interest, as it provides fine control over film thickness, and allows for the study of SCO behaviour across a wide range - from multilayer stacking of hundreds of nanometres down to isolated molecules at sub-monolayer level.[3–5,12–21] It has been discovered that while complexes in thin films still exhibit

SCO behaviour,[13–15,19–21] the substrate can alter the SCO properties[15,17,19,22] and often leads to 'pinned' states[13,15,17,22,23] in sub-monolayers, monolayers and the first few layers within multilayer films. These effects originate from direct contact with solid surfaces[17,19] that react chemically with ligands and induce conformational changes in the complex (e.g. changing coordiantion number and geometry[15]), or cause packing constraints in the adjacent layers.[18,19] It is possible that such issues could be overcome using self-assembled monolayers (SAMs), that offer a fine control over monolayer properties, for example, molecular orientation, packing, interaction with substrate, and intermolecular interactions. However, despite reported 2D self-assembly of SCO nanoparticles,[7] SAMs of ligands,[23,24] metal complexes[25,26] and different type molecular spin state switches,[27,28] SAMs of SCO complexes have not been reported yet. In this chapter the potential of ligand $\mathbf{L_1}$ and $\mathbf{L_2}$ to be used for SAMs of SCO complexes is investigated.

4.2 SAMs of bpp-type tridentate ligand L_1 and its Fe(II) complex C_1

The study of iron(II) complexes of tridentate ligand **bpp** (figure 4.5a), its derivatives and their magnetic properties in bulk was pioneered by M. Halcrow and coworkers.[29,30] Various reported substitution patterns highlight the flexibility of **bpp** to accommodate a variety of substituents, while preserving SCO behaviour of the complex.[30–32] Furthermore, surface nanostructures[33–36] and single-molecule junctions[37,38] have been successfully fabricated using derivatives of Fe(II) complex of **bpp**.

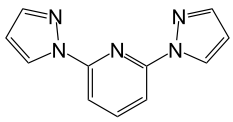

(A) Ligand **bpp**

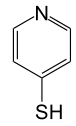

(B) Reagent **Py-SH**

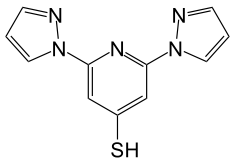

(C) Ligand **bpp-SH**

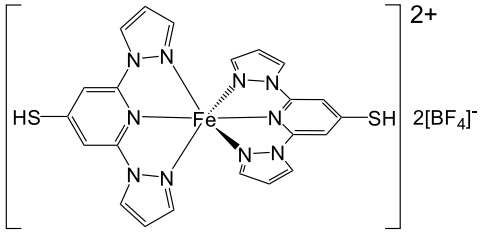

(D) Tetrafluoroborate salt of **bpp-SH** complex

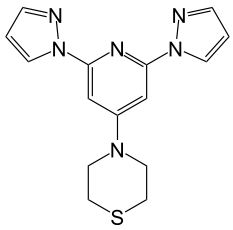

(E) Ligand $\mathbf{L_1}$

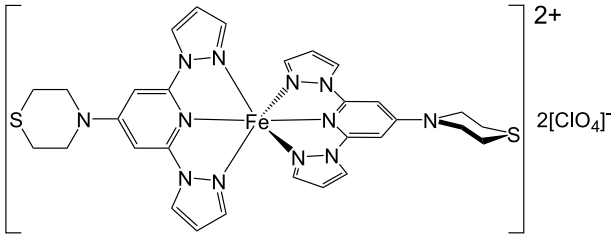

(F) Perchlorate salt of complex $\mathbf{C_1}$

FIGURE 4.5: Molecular structures of ligand ligand **bpp**, reagent **Py-SH**, ligand **bpp-SH**[a] and its **bpp-SH** complex,[a] ligand $\mathbf{L_1}$[b] and its complex $\mathbf{C_1}$.[b] Complexes **bpp-SH** and $\mathbf{C_1}$ contain BF_4^- and ClO_4^- counter ions, respectively, in their crystalline form.

In order to form a SAM of **bpp** and ultimately of its complex exhibiting SCO behaviour, a new ligand 4-mercapto-2,6-di[pyrazol-1-yl]pyridine (ligand **bpp-SH**) was

synthesised.[a] As shown in figure 4.5c, it is a derivative of ligand **bpp** containing a thiol group attached to the pyridine ring. However, X-ray Photoelectron Spectroscopy (XPS) spectra clearly indicate a severe decomposition of the molecule on the gold surface. SAMs formed from a solution of preformed Fe(II) complex of **bpp-SH** (figure 4.5d) yield the same signs of the decomposition, despite showing presence of iron on the surface. The instability of ligand **bpp-SH** is attributed to desulfurisation that leads to formation of atomic sulfur on gold surface, that has been reported for reagent **Py-SH**[40,41] (figure 4.5b), which is the 'backbone' of ligand **bpp-SH**. Desulfurisation in **SAM Py-S** on gold is rapid (within 10 min) in ethanolic solution,[40] but much slower (within hours) in aqueous solution.[40] Indeed, a similar trend was observed in **SAM bpp-SH** formed for varying amount of time in 1 mM **bpp-SH** in aqueous 0.1 M NaOH. Nevertheless, immersion into the solution even as short as 10 s led to profound decomposition of ligand **bpp-SH** on the surface. Data on the study of SAM formation of ligand **bpp-SH** and its Fe(II) complex are not presented in this thesis, but have been published.[1]

In the light of these results, a new ligand 4-(thiomorpholin-4-yl)-2,6-di[pyrazol-1–yl]pyridine (ligand $\mathbf{L_1}$)[b] with a more remotely bound sulfur (figure 4.5e) and its complex $\mathbf{C_1}$[b] (figure 4.5f) were investigated for the purpose of SAM formation. The following sections will discuss the formation and characterisation of **SAM** $\mathbf{L_1}$, **SAM** $\mathbf{C_1}$ and Fe(II) coordination to **SAM** $\mathbf{L_1}$.

[a] Synthesised by L. J. Kershaw Cook at Prof. M. A. Halcrow research group, School of Chemistry, University of Leeds, UK. Procedure described in the references[1,39].

[b] Synthesised by A. Santoro at Prof. M. A. Halcrow research group, School of Chemistry, University of Leeds, UK. Procedure described in the reference[1].

4.2.1 Ellipsometry and Wetting measurements

Wettability data and ellipsometric thickness of **SAM L_1**, **SAM L_1+Fe(1m)**, **SAM L_1+Fe(30m)** and **SAM C_1** are summarised in table 4.1. Fresh **SAM L_1** yields thickness of 9 Å,[c] which is considerably lower than the expected value of 13 Å[d] corresponding to crystallographic length of extended ligand $\mathbf{L_2}$. This indicates that molecules are tilted at an angle of 46° from the surface normal or surface coverage of 69 %.

TABLE 4.1: Thickness and contact angles of **SAM L_1**, **SAM L_1+Fe(1m)**, **SAM L_1+Fe(30m)** and **SAM C_1**

	Ellipsometric thickness (Å)		Contact Angles (°)	
SAM	Experimental[c]	Expected	Advancing	Receding
SAM L_1	9 ± 1	13[d]	84 ± 2	57 ± 7
SAM L_1+Fe(1m)	8 ± 1	14[e]	82 ± 3	53 ± 5
SAM L_1+Fe(30m)	6 ± 1	14[e]	87 ± 4	51 ± 9
SAM C_1	8 ± 1	20[d]	78 ± 3	50 ± 13

SAM L_1 exposure to ∼5 mM $Fe(ClO_4)_2$ in MeCN for 1 min does not show expected increase in thickness, while prolonged (30 min) exposure of the SAM noticeably reduces its thickness. Furthermore, **SAM C_1** yields the same thickness as **SAM L_1** within the experimental uncertainty, despite the fact that extended length of complex $\mathbf{C_1}$ is nearly two times larger. Due to the molecular structure of complex $\mathbf{C_1}$, it is unlikely that the complex binds to gold surface through both thiomorpholine rings, or that the tilt angle from the surface normal increases much beyond the level calculated in **SAM L_2**. Wettability data reveal slight spread of the contact angles, however, due to variation in the acquired values and similar width of hysteresis loops, significant difference in surface energy is not evident between **SAM L_1**, **SAM**

[c] Given the nature of the molecular structures it is quite possible that the refractive index (1.45) used in the experimental modelling underestimates the molecular thickness. Refractive index of 1.45 is for condensed alkanes, the ligands and complexes here are of lower density and may lead to lower refractive indices.

[d] Based on X-ray crystallography performed by A. Santoro at Prof. M. A. Halcrow research group, School of Chemistry, University of Leeds, UK.

[e] Estimation based on crystallographic length of ligand $\mathbf{L_1}$.

L_1+Fe(1m), **SAM L_1+Fe(30m)** and **SAM C_1**. Overall, the data suggest fairly similar thickness and surface chemistry in all of the SAMs.

4.2.2 XPS

4.2.2.1 SAM L_1 and SAM C_1

Figure 4.6 presents the XPS spectra of the regions corresponding to chemical elements in ligand **L_1** and additionally includes spectra of oxygen 1s region, in order to investigate the quality of **SAM L_1** and stability of ligand **L_1** when in direct contact with gold surface.

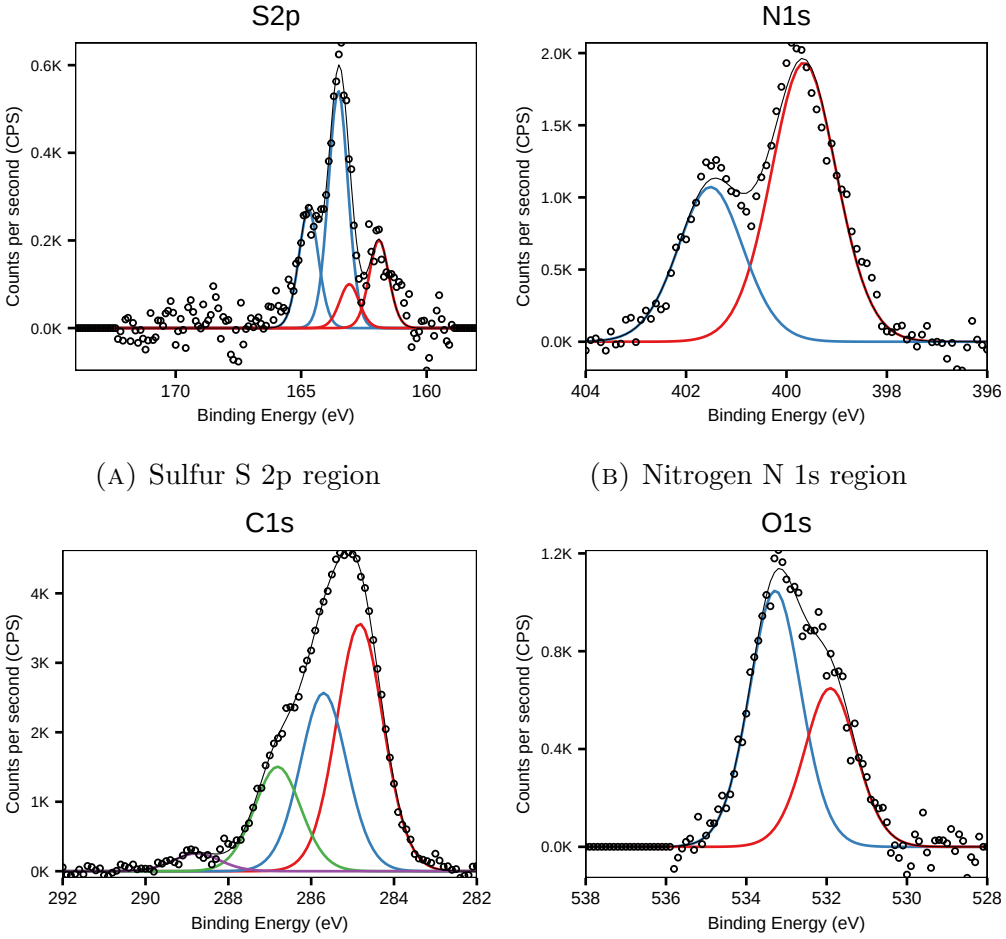

(A) Sulfur S 2p region

(B) Nitrogen N 1s region

(C) Carbon C 1s region

(D) Oxygen O 1s region

FIGURE 4.6: High resolution XPS spectra of **SAM L_1**.

The spectrum of S 2p region in figure 4.6a shows three peaks resulting from two spin-orbit doublets. The first at S $2p_{3/2}$ = 161.8 eV and the second at S $2p_{3/2}$ = 163.5 eV are commonly assigned to bound and unbound thiols,[42–44] respectively. On the other hand, presence of those spin-orbit doublets has been reported in SAMs with thiomorpholine, thiomorpholine-like and dialkyl monosulfide head groups,[45–50] and were attributed to different sulfur interactions with gold, rather than an indication of molecules bound to gold surface in an unexpected manner (i.e. through their functional group).

TABLE 4.2: Integrated (normalised using R.S.F.) and fractional XPS peak areas of N 1s region and fitted components in **SAM L_1** and **SAM C_1**.

	Peak area (x 1000 CPS eV) [Fraction of the region (%)] N 1s		
	Region	Component	
		A	B
BE (eV)	-	399.6	401.4
BE std. dev. (eV)	-	0.1	0.1
SAM L_1	4.3 [100]	2.8 [64]	1.5 [36]
SAM C_1	3.2 [100]	2.1 [64]	1.2 [38]

1) Components were constrained to have the same FWHM within each spectrum. Across the samples FWHM varied within 1.4-1.6 eV.
2) Binding energies are associated as follows:[24]
- Component A: nitrogen in pyridine, thiomorpholine and N2 position in pyrazole.
- Component B: nitrogen in N1 position in pyrazole.

The spectrum of N 1s region shows two clearly resolved peaks at 399.6 eV and 401.4 eV (see figure 4.6b and table 4.2) assigned to nitrogens in (i) pyridine, thiomorpholine and N2 position in pyrazole, and (ii) N1 position in pyrazole, respectively.[24] The peak with lower BE has nearly a two times larger area than the other peak, which agrees with the molecular structure shown in figure 4.5e.

The C 1s region shows a peak with a shoulder, which can be fitted with four components (see figure 4.6c and table 4.3), three of which have BE comparable to reported values: component A to carbon in meta-positions of pyridine, pyrazole C3 and C4; component B to carbon in para-position of pyridine, pyrazole C5; and component

C to carbon in ortho-positions of pyridine.[24] Availability of literature on SAMs containing thiomorpholine head group is limited, especially those containing XPS studies. The carbons in thiomorpholine are expected to show similar binding energies to the corresponding carbon atoms in pyridine. Table 4.3 presents the fractional percentage of each component, in addition to peak areas of the whole region and fitted components. The approximate ratio of fitted components is 5:3:2:0.3, respectively, however, due to strong overlap of the peaks, even a slight change in the peak shape strongly affects the mathematical fitting and consequently the relative amounts of the chemical species. This limits accuracy of the peak positions and integrated areas of the fitted components, which are consequently used for indicative purposes only.

TABLE 4.3: Integrated (normalised using R.S.F.) and fractional XPS peak areas of C 1s region and fitted components in **SAM L_1** and **SAM C_1**. *Due to low confidence in accuracy, presented values are for indicative purposes only.*

Peak area (x 1000 CPS eV) [Fraction of the region (%)] C 1s					
	Region	Component			
		A	B	C	D
BE (eV)	-	284.8	285.7	286.9	288.7
BE std. dev. (eV)	-	0.1	0.2	0.1	0.3
SAM L_1	18.6 [100]	8.3 [45]	6.0 [32]	3.5 [19]	0.6 [3]
SAM C_1	14.7 [100]	8.5 [58]	3.8 [26]	1.8 [12]	0.5 [4]

1) Components were constrained to have the same FWHM within each spectrum. Across the samples FWHM varied within 1.2-1.4 eV.
2) Binding energies are associated as follows:[24]
- Component A: carbon in meta-positions of pyridine, pyrazole C3 and C4.
- Component B: carbon in para-position of pyridine, pyrazole C5.
- Component C: carbon in ortho-positions of pyridine.

The presence of oxygen is attributed to the underlying hydrocarbon contamination, as it has been reported, that even freshly cleaned gold surface under ambient conditions contains a few angstroms thick layer of adventitious hydrocarbons,[43,51] which is displaced efficiently, only if the head group has a strong affinity towards gold[43,51,52] and head groups can pack effectively.[53]

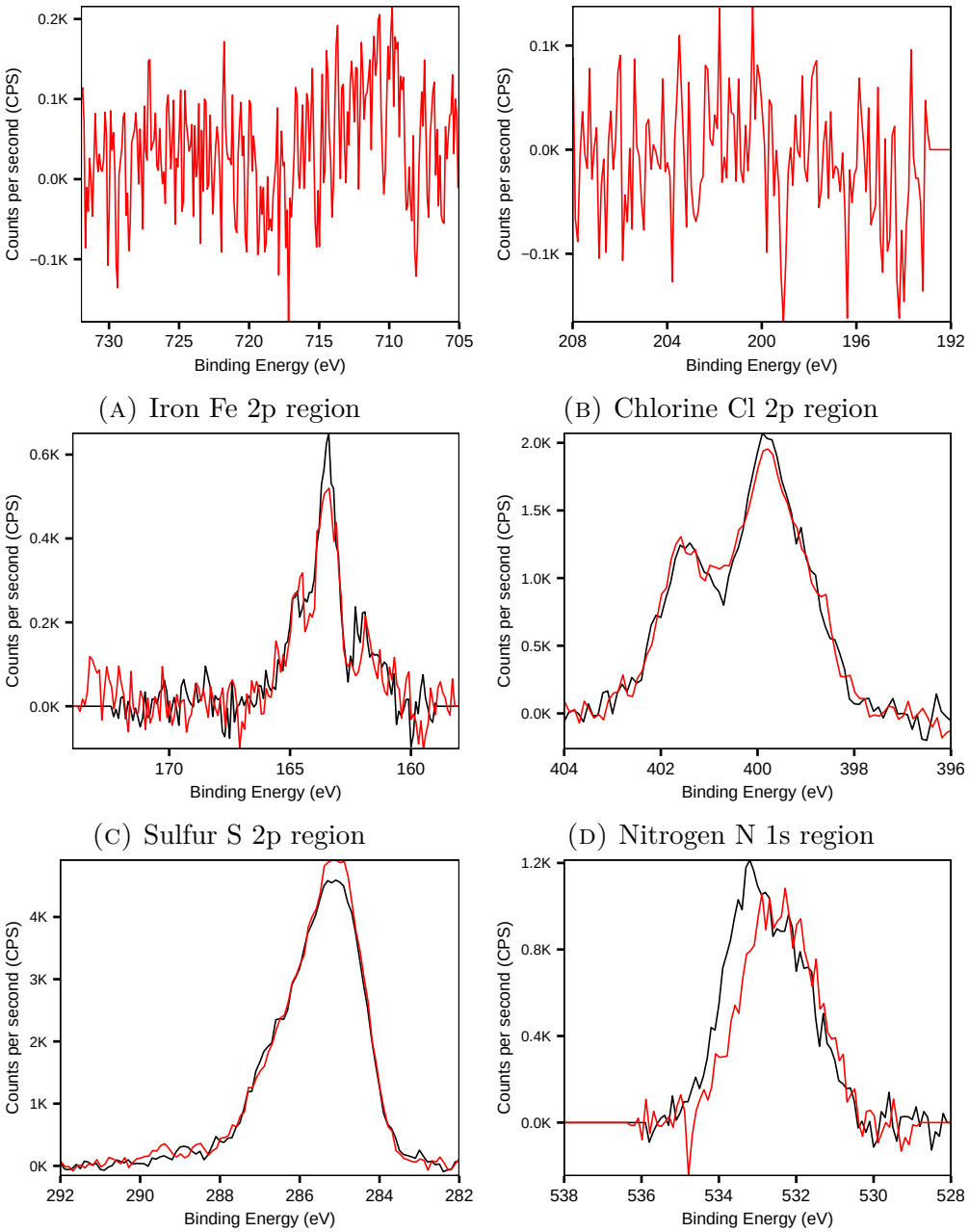

(A) Iron Fe 2p region

(B) Chlorine Cl 2p region

(C) Sulfur S 2p region

(D) Nitrogen N 1s region

(E) Carbon C 1s region

(F) Oxygen O 1s region

FIGURE 4.7: High resolution XPS spectra of **SAM L_1** (in black) and **SAM C_1** (in red).

Figure 4.7 compares the XPS spectra of **SAM L_1** and **SAM C_1**, where the most important result is Fe 2p spectrum in figure 4.7a shows little if any presence of iron. Although two bumps could be resolved at 710 eV and 725 eV, the signal intensity is too low for any meaningful interpretation. In fact, this perturbation in the background is of a similar intensity to spectrum of Fe 2p acquired on gold, that was

exposed to ∼5 mM $Fe(ClO_4)_2$ in MeCN solution for 30 min. Furthermore, figure 4.7b shows no peaks that would indicate presence of the ClO_4^- counter ions. Finally, the N 1s region yields the same spectra (figure 4.7d), while differences in the S 2p and C 1s regions are minute between the SAMs. Overall, XPS spectra suggest rather similar chemical composition in both SAMs.

4.2.2.2 Fe(II) coordination to SAM L_1

Figure 4.8 compares the XPS spectra of **SAM L_1** and **SAM L_1** exposed to ∼5 mM $Fe(ClO_4)_2$ in MeCN for 1 min and 30 min. Exposure to the Fe(II) solution for 1 min yields the same spectra in all the regions, except S 2p, where a slight increase in intensity is assigned to an artefact caused by baseline correction, due to weak and noisy signals in the region. On the other hand, immersion of **SAM L_1** into the Fe(II) solution for 30 min leads to a weak peak in Fe 2p region, however, its intensity is too low for any meaningful analysis, while the N 1s spectrum suggests partial loss of nitrogen atoms and change in their chemical state. Spectra of the Cl 2p regions does not indicate any presence of the ClO_4^- counter ion in any of the SAMs, suggesting that either it is readily removed during washing or that it was not present at all.

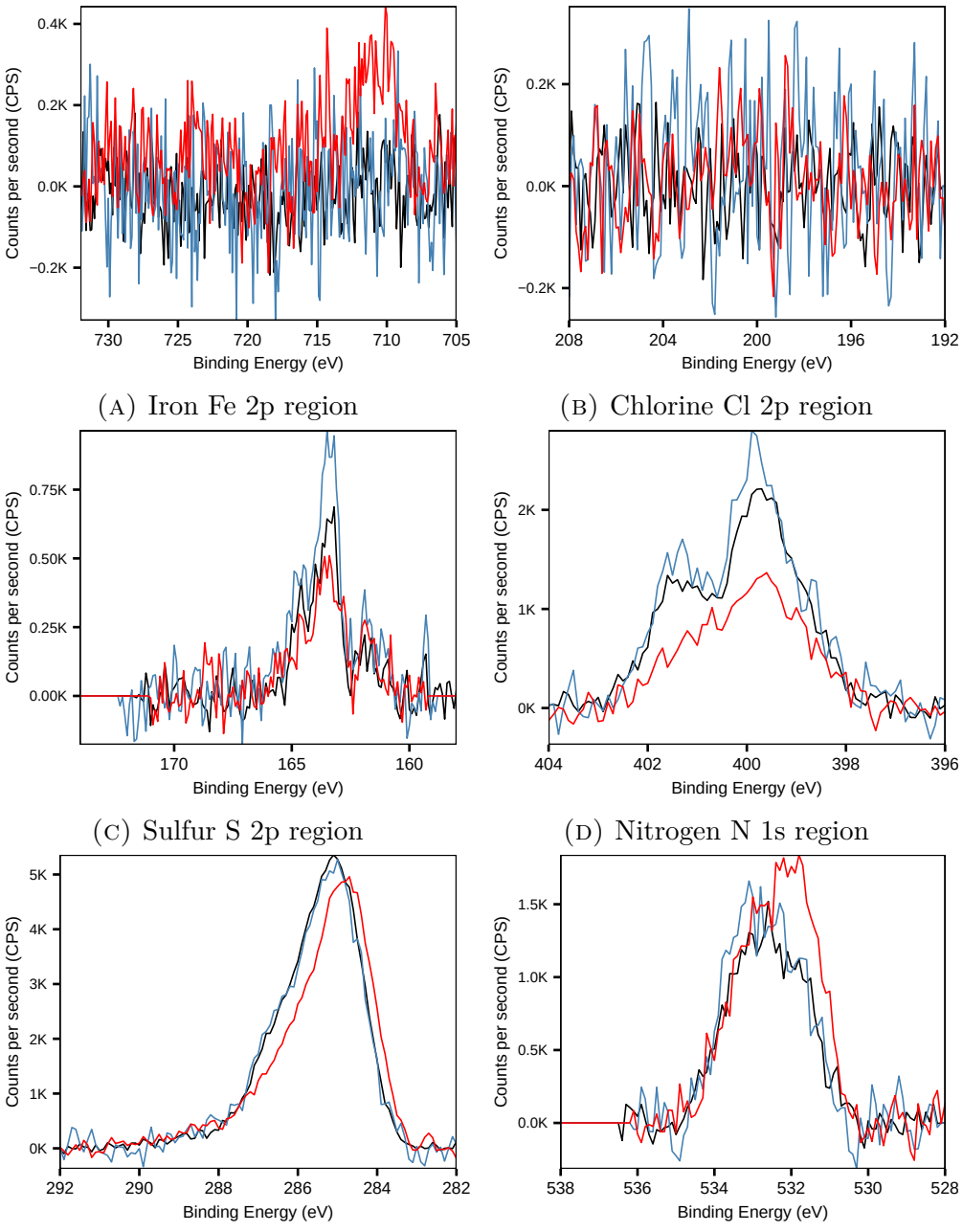

(A) Iron Fe 2p region

(B) Chlorine Cl 2p region

(C) Sulfur S 2p region

(D) Nitrogen N 1s region

(E) Carbon C 1s region

(F) Oxygen O 1s region

FIGURE 4.8: High resolution XPS spectra of **SAM L_1** (in black), **SAM L_1+Fe(1m)** (in blue) and **SAM L_1+Fe(30m)**(in red) exposed to ∼5 mM $Fe(ClO_4)_2$ in MeCN for 0 min, 1 min and 30 min, respectively.

4.2.3 Discussion

XPS spectra of **SAM $\mathbf{L_1}$** show presence of sulfur, carbon and nitrogen, in agreement with the molecular structure (figure 4.5e), but yield S:C:N relative ratio of 1:17:4 instead of 1:15:6, respectively. The slight excess of carbon is expected due to adventitious contamination, however, lower average amount of nitrogen per sulfur is attributed to traces of thiomorpholine and 4-(thiomorpholin-4-yl)-2,6-difluoro-pyridine from final steps of ligand $\mathbf{L_1}$ synthesis. Relative ratio of the nitrogen species is close to 1:2, in agreement to the amounts of assigned nitrogen atoms discussed in section 4.2.2.1.

The S 2p region (figure 4.6a) shows presence of bound and unbound thiols to gold. Although, such a large proportion of unbound thiols in a conventional alkanethiol SAM would indicate serious issues with SAM quality, those doublets are commonly observed in SAMs with thiomorpholine, thiomorpholine-like and dialkyl monosulfide head groups.[45–50] Nevertheless, low surface coverage is indicated by the weak XPS signal, especially in S 2p region (compared to SAMs of molecules with similar length) and detected oxygen, which could originate from hydrocarbons, that have been reported to reversibly adsorb onto gold surface prior formation of a well packed SAM.[43,51–53] Low surface coverage could be assigned to weak affinity of the head group and bulky structure of the molecules preventing close packing. Such observation is in agreement with the ellipsometry measurements, which indicate that **SAM $\mathbf{L_1}$** thickness is 9 Å, while X-ray crystallography data[f] indicate that the length of ligand $\mathbf{L_1}$ is 13 Å; such a difference between the ellipsometric thickness and the length of individual molecules could indicate that (i) molecules in the SAM are tilted at an angle of ∼46° from the surface normal, (ii) cover ∼70 % of the gold surface, or (iii) a combination of both.

[f] See footnote [d] on page 113.

Ellipsometry and XPS data do not show any significant differences between **SAM $\mathbf{L_1}$** and **SAM $\mathbf{C_1}$**, suggesting demetallisation in complex $\mathbf{C_1}$ during SAM formation. Similarly, there is little difference between **SAM $\mathbf{L_1}$** and **SAM $\mathbf{L_1}$+Fe(1m)** indicating no Fe(II) coordination to immobilised ligand $\mathbf{L_1}$ on gold surface. On the other hand, a peak is present in Fe 2p spectra in **SAM $\mathbf{L_1}$+Fe(30m)** (figure 4.8a), but the intensity is too weak for a meaningful interpretation, while N 1s region (figure 4.8d) shows a decrease in intensity and a change in shape suggesting decomposition of ligand $\mathbf{L_1}$ in the SAM. Also, **SAM $\mathbf{L_1}$+Fe(30m)** shows decrease in ellipsometric thickness.

Finally, the SAMs yield slightly different contact angles, however, due to the spread in the values, CA data do not indicate a significant difference in the surface energy among the SAMs.

Overall, ligand $\mathbf{L_1}$ is stable on gold surface and successfully forms a SAM. Whilst the low surface coverage for **SAM $\mathbf{L_1}$** indicates it is not well packed. Short exposure to $\sim$5 mM $Fe(ClO_4)_2$ in MeCN does not lead to Fe(II) coordination, while prolonged exposure suggests decomposition of ligand $\mathbf{L_1}$ on the surface. Complex $\mathbf{C_1}$ also forms a SAM, but all the characteristics suggest that it is **SAM $\mathbf{L_1}$** and not **SAM $\mathbf{C_1}$**, which is attribute to demetallisation complex $\mathbf{C_1}$ during SAM formation.

4.3 SAMs of caged pentadentate ligand L_2 and its Fe(II) complex C_2

The caged pentadentate ligand **Py$_5$** displayed in figure 4.9a was initially synthesised for biomimetic purposes.[54–56] It is designed to simulate specific attributes of the Lewis acidic iron site in mammalian lipoxygenases (LOs) and successfully reproduces many similar structural and spectroscopic properties, which allow to study mechanism of catalysed dioxygenation of fatty acids in lipids containing a cis,cis-1,4-pentadiene structure.[54–56] However, new applications of **Py$_5$** have emerged since. Its Fe(II) complex (figure 4.9b) with MeCN as the SEL has been reported as a potential alternative to clinically used drugs cisplatin and bleomycin in killing cancer cells,[57,58] and its Co(II) complex with bromide anion (Br^-) or chloride anion (Cl^-) as the SEL have been reported to show promising properties for water splitting into oxygen and hydrogen.[59–61]

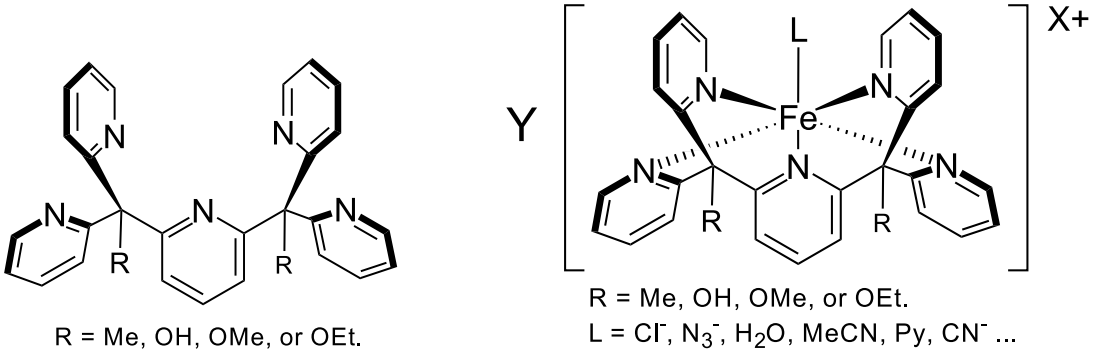

(A) Ligand **Py$_5$** (B) Fe(II) complex of **Py$_5$**

FIGURE 4.9: Molecular structures of **Py$_5$** and its Fe(II) complex. The later has a charge (X), which depends on a sixth exogenous ligand (L), and therefore forms a salt accompanied by a counter ion (Y). A number of **Py$_5$** derivatives have been reported with different group (R) attached to the tertiary carbon atoms.

Ligand **Py$_5$** also exhibits a number of desirable properties for studying SCO in SAMs. Firstly, its caged structure, containing five coordination sites, yields a stronger chelation to a metal centre than the tridentate ligand **L$_1$**, which formed a SAM, but did not coordinate to Fe(II), while its preformed complex demetallised

during SAM formation, as discussed in section 4.2. Secondly, $\mathbf{Py_5}$ metal complex can accommodate a labile SEL, which allows to easily change not only how the metal complex reacts with other molecules,[56,57] but also its spin state[54–57,62,63] and SCO behaviour.[56,62] $\mathbf{Py_5}$ complex of Fe(II) in crystaline form exhibits abrupt spin transition at ∼90 K with strong hysteresis with MeOH[56,63] as the SEL, gradual spin transition at ∼155 K with minor hysteresis with azide (N_3^-)[63] as the SEL, but HS state with Cl^-[62,63] or weaker SELs[62,63] and LS state with MeCN[54,56,57,62,63] or stronger SELs[62,63] in the temperature range 5-295 K. Ability to chose a stable spin state over a wide range of temperature is beneficial for obtaining reference data. For example, XPS spectra in Fe 2p region have been shown to vary significantly between different compounds of Fe(II) HS, Fe(III) LS or Fe(III) HS species, which can make qualitative or at least quantitative differentiation of certain iron oxidation and spin states challenging in unknown or mixed samples without reference spectra.[64–70] Weak SELs in Fe(II) complex of $\mathbf{Py_5}$ should yield a set of very similar Fe 2p spectra corresponding to HS state, and likewise strong SELs in the complex should yield another set of practically identical Fe 2p spectra corresponding to LS state. Therefore, those two types of spectra could be used as accurate references to follow SCO transition in the complex containing SELs of intermediate strength (e.g. MeOH). The same method could be applied in following SCO in $\mathbf{Py_5}$ complex of Fe(III), however, it has been reported as unstable under ambient conditions.[55,56] Thirdly, bidentate or polydentate ligands could be used as SEL to create homogeneous or heterogeneous bilayers or multilayers structures in a controlled manner. Finally, SEL in Fe(II) complex of $\mathbf{Py_5}$ can be easily replaced by dissolving in a solution containing a large excess of a desired ligand (with cyanide anion (CN^-) being an exception).[56,62] This should allow easy and reversible replacement of SELs in immobilised complexes on a surface, i.e. in a SAM, simply by rinsing with appropriate solutions, that could 'unlock' their multifunctionality, given that properties of such complexes do not change in close proximity to the surface.

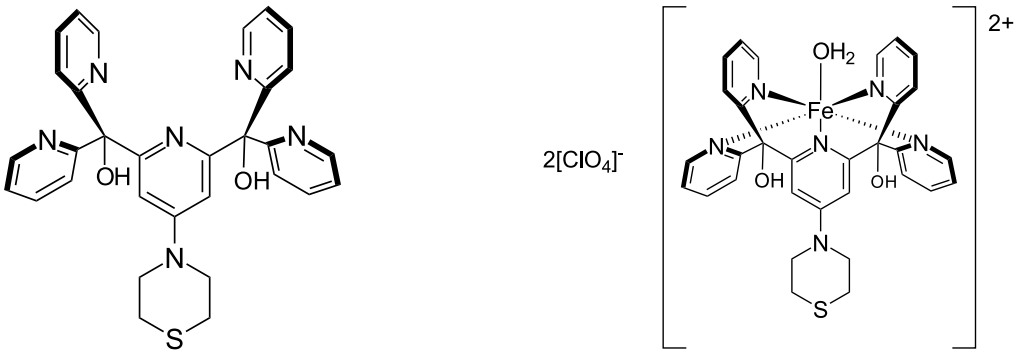

(A) Ligand $\mathbf{L_2}$ (B) Perchlorate salt of complex $\mathbf{C_2}$

FIGURE 4.10: Molecular structures of ligand $\mathbf{L_2}$[g] and its complex $\mathbf{C_2}$[g]. The later contains H_2O as the SEL and ClO_4^- counter ion in a crystalline form.

New ligand 4-(thiomorpholin-4-yl)-2,6-di[hydroxydi(pyridin-2-yl)methyl]pyridine (ligand $\mathbf{L_2}$) shown in figure 4.10a was synthesised,[g] as a derivative of $\mathbf{Py_5}$ with thiomorpholine head group that should form self-assembled monolayer on gold surface. Fe(II) complex of ligand $\mathbf{L_2}$ with H_2O as the SEL (complex $\mathbf{C_2}$) shown in figure 4.10b was also synthesised[g] and crystalised, which, in a similar manner to Fe(II) complex of $\mathbf{Py_5}$, exhibits LS or HS state depending on the SEL. The following sections will discuss the formation and characterisation of **SAM $\mathbf{L_2}$**, **SAM $\mathbf{C_2}$**, SEL exchange in **SAM $\mathbf{C_2}$** by rinsing, and Fe(II) coordination to **SAM $\mathbf{L_2}$**.

4.3.1 SAM $\mathbf{L_2}$ and SAM $\mathbf{C_2}$

SAMs of just ligand $\mathbf{L_2}$ and of the pre-formed complex $\mathbf{C_2}$ were formed as depicted in figures 4.11a and 4.11b, accordingly. XPS, contact angle and ellipsometry measurements were performed to characterise SAM formed from $CHCl_3$ solution of ligand $\mathbf{L_2}$ (**SAM $\mathbf{L_2}$**), SAM formed from MeOH solution of complex $\mathbf{C_2}$ (**SAM $\mathbf{C_2}$ [MeOH]**), and SAM formed from MeCN solution of complex $\mathbf{C_2}$ (**SAM $\mathbf{C_2}$ [MeCN]**).

[g] Synthesised by A. Santoro at Prof. M. A. Halcrow research group, School of Chemistry, University of Leeds, UK.

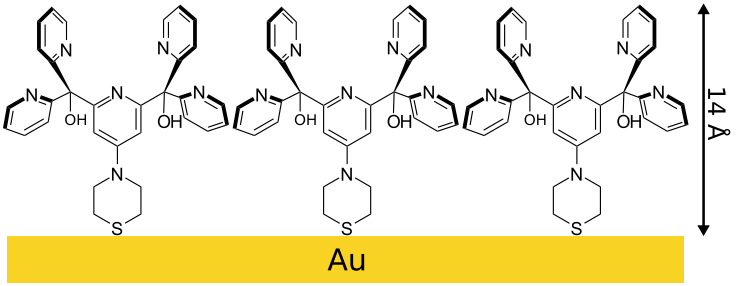

(A) **SAM L_2**

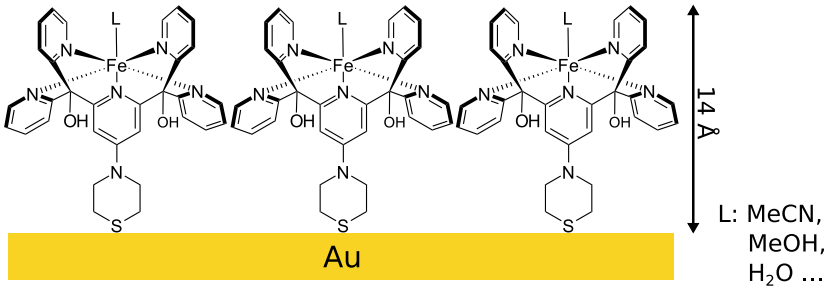

(B) **SAM C_2**

FIGURE 4.11: **SAM L_2** is neutral, however **SAM C_2** is expected to be positively charged, because perchlorate counter ion has been detected in dropcast and in powder samples of complex **C_2** salt, but not in the SAM. Three types of SEL - H_2O, MeOH and MeCN (denoted as (L) in **SAM C_2**) were studied.

Formation of **SAM L_2** was also attempted in other solvents (e.g. MeOH, nitromethane ($MeNO_2$)), but the SAMs suffered either from strongly enhanced reactivity of impurities towards gold surface or partial decomposition of ligand **L_2**. MeOH and MeCN solutions were used to form **SAM C_2**, because in solution complex **C_2** coordinates solvent molecule as SEL, and obtains HS and LS state at room temperature, respectively. Consequently, **SAM C_2** is expected to be in the corresponding states.

Different SELs lead to changes in composition of chemical elements and their species. However, expected differences between H_2O and MeOH coordinated to complex **C_2** are small[q], and correspond to HS in both cases. Furthermore, there is a significant probability that thin water film is formed on top of **SAM C_2** and MeOH is replaced by H_2O, when samples are exposed to ambient conditions. Therefore, both states are treated as one, while the SEL is denoted as $MeOH/H_2O$.

4.3.1.1 XPS

XPS spectra show some variation in O 1s and C 1s regions across the samples of **SAM C_2 [MeOH]** and **SAM C_2 [MeCN]**. Consequently two sets of spectra for each of those SAMs, but only one representative set of spectra for **SAM L_2** are presented and discussed in this section.

All of the SAMs show a single peak in N 1s region (figure 4.12a) corresponding to a single component[h] with ∼1.5 eV FWHM (see table 4.7, and figures B.1b and B.2b in the appendix) indicating that nitrogen atoms in the molecules of the formed SAMs have very similar chemical environments. Equal intensity and the same binding energy of the peak in N 1s region among spectra of all the SAMs are simply a direct consequence of using this peak to normalise intensities[i] and binding energies (referenced to 399.7 eV, which is comparable to reported values for nitrogen in pyridine[j][24,41,72,73]) for XPS spectra of the mentioned SAMs above, and **SAM L_2+Fe(1m)** and **SAM L_2+Fe(30m)** discussed in the following sections.

The presence of iron in the spectra of **SAM C_2** in figure 4.12b reflects the main difference between ligand **L_2** and complex **C_2** (figures 4.10a and 4.10b, respectively). Due to weak signal and often complex background in Fe 2p region, baseline corrected spectra are subject to a significant variation limiting precision and accuracy of the analysis. Nevertheless, the baseline corrected spectra of Fe 2p region in figure 4.12b show surprisingly good agreement across the SAMs and their samples (when intensities[i] and binding energies[m] are normalised to N 1s region). Consequently,

[h] A shoulder at 398.3 eV in **SAM L_2** spectrum is most likely an artefact, as it was not evident in other samples of **SAM L_2**.

[i] All of the spectra in this set were normalised to have equal integrated area of N 1s region, and, for convenience, it was set to a value of six, which is the number of nitrogen atoms in ligand **L_2**. Expected changes in the amount of nitrogen atoms per molecule in **SAM C_2** due to different SELs are described in footnote [k] and discussed in the section 4.3.1.2.

[j] Based on poly(2-vinylpyridine) (P2VP) and poly(4-vinylpyridine) (P4VP) in reference[71].

[k] Number of nitrogen atoms per complex depends on the sixth exogenous ligand (L), as shown in figure 4.11b. For L = H_2O or L = MeOH there are 6 nitrogen atoms, but for L = MeCN there are 7 nitrogen atoms per complex.

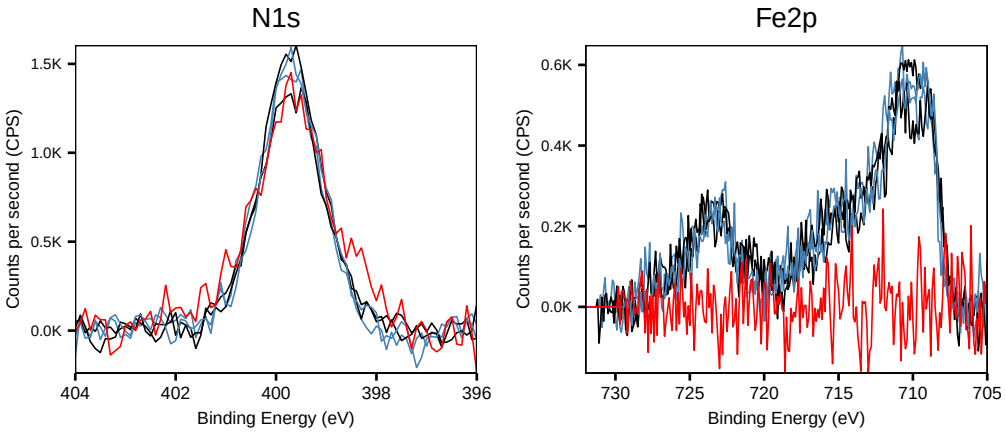

(A) Nitrogen N 1s region (B) Iron Fe 2p region

FIGURE 4.12: High resolution XPS spectra (normalised and referenced to N 1s region) of **SAM L_2** (**in red**), **SAM C_2 [MeOH]** (**in black**) and **SAM C_2 [MeCN]** (**in blue**).

TABLE 4.4: Integrated and normalised (using R.S.F.) XPS peak areas in N 1s and Fe 2p regions and their relative ratios in **SAM L_2**, **SAM C_2 [MeCN]** and **SAM C_2 [MeOH]**.

SAM	Peak area (x 1000 CPS eV) [relative to N 1s region][i] Region	
	N 1s[i]	Fe 2p
SAM L_2 expected	[6.0]	[-]
SAM C_2 expected	[6.0[k]]	[1.0]
SAM L_2	1.1[6.0]	- [-]
SAM C_2 [MeOH]	1.7[6.0]	0.3[1.0]
	2.0[6.0]	0.4[1.2]
SAM C_2 [MeCN]	1.4[6.0]	0.3[1.2]
	2.0[6.0]	0.3[1.0]

SAM C_2 formed from MeOH and MeCN have the same average ratio of nitrogen to iron, as shown in table 4.4. Furthermore, average N:Fe ratio is 6.0:1.1, respectively, in **SAM C_2 [MeOH]** and in **SAM C_2 [MeCN]**, which is almost equal to the expected ratio 6.0:1.0 for complex **C_2** with SELs that do not contain nitrogen. Broad Fe $2p_{3/2}$ peak (∼3 eV FWHM) and presence of the Fe $2p_{3/2}$ satellite have been reported to originate from unpaired 3d electrons.[74,75] Their respective

positions at 710.1 eV and 714.4 eV, and Fe $2p_{1/2}$ at 723.5 eV (see table 4.5) have been observed in both Fe(II) (in HS state) and Fe(III) (in both HS and LS states) compounds.[64–70,75–77] Therefore, precise state of Fe centre in **SAM C_2** could be determined only by comparison to a set of Fe 2p reference spectra of complex **C_2** or closely related compound containing iron of a known oxidation and spin sates. Although the state of the SAMs at this stage could not be conclusively assigned, almost identical[l] suggest the same spin and oxidation state in both cases.

TABLE 4.5: Binding energies (BEs) of fitted components in N 1s and Fe 2p region of XPS spectra of **SAM C_2 [MeOH]** and **SAM C_2 [MeCN]**.

	Component			
	N 1s	Fe 2p		
	A	3/2		1/2
		Main peak	Satellite	Main peak
BE (eV)	399.7[m]	710.1	714.4	723.5
BE std. dev. (eV)	n/a	0.2	0.4	0.2

1) Across the samples FWHM of component A in N 1s varied within 1.4-1.9 eV.
2) Component A in N 1s is attributed to nitrogen in pyridine and thiomorpholine rings.[j][24,41,72,73]

XPS spectra of O 1s region (figure 4.13a) show consistent amounts of oxygen in **SAM C_2 [MeCN]**, but a noticeable difference in **SAM C_2 [MeOH]** samples. On the other hand, the amount of oxygen in the former is similar to the average in the later, and oxygen levels in **SAM L_2** are similar to the lower limit in **SAM C_2 [MeOH]**. Analysis of quantitative peak areas (presented in table 4.6) shows a severe excess of oxygen, i.e. 2-5 times more relative to nitrogen/iron than expected, which corresponds to extra 5-9 atoms per molecule. It has been reported, that even freshly cleaned gold surface under ambient conditions contain a few angstroms thick

[l] The difference between two Fe 2p spectra of **SAM C_2 [MeOH]** (in black in figure 4.12b) is believed to be an artefact of low signal to noise ratio, because (i) both samples were prepared in the same way, (ii) the sharp peak at $\sim$ 708 eV could only be associated with LS state in a fraction of Fe(II) centres, which would lead to a decrease in intensity of Fe $2p_{3/2}$ satellite peak and a slight change in intensity and position of Fe $2p_{1/2}$ peak, but none of the two are evident in the spectra, and (iii) similar features do appear only in some consecutively acquired spectra on the same sample (e.g. figures B.5a and B.5b; B.6b, B.6c and B.6c; B.8b, B.8c and B.8d)

[m] All the spectra were referenced to 399.7 eV, therefore it does not have any deviation.

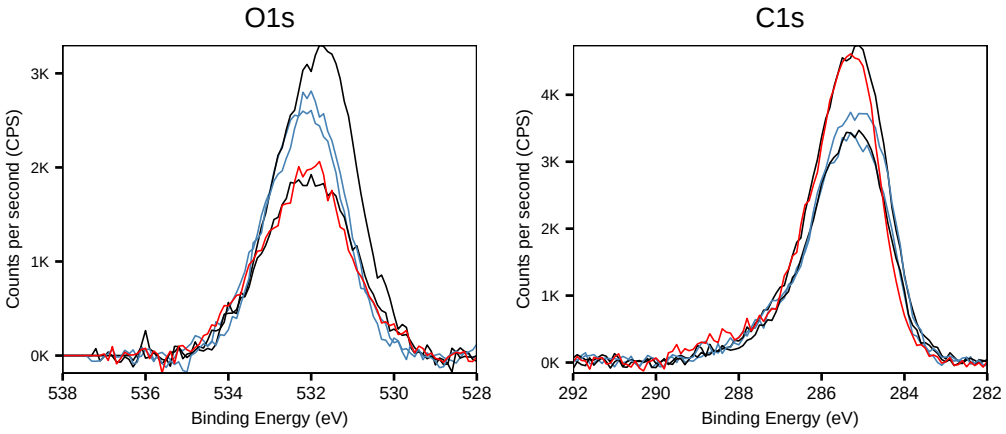

(A) Oxygen O 1s region (B) Carbon C 1s region

FIGURE 4.13: High resolution XPS spectra of **SAM L_2** (**in red**), **SAM C_2 [MeOH]** (**in black**) and **SAM C_2 [MeCN]** (**in blue**).

layer of adventitious hydrocarbons,[43,51] which is displaced efficiently, only if head group has a strong affinity towards gold[43,51,52] and head groups are able to pack effectively.[53] However, **SAM C_2 [MeOH]** and **SAM C_2 [MeCN]** yield more oxygen than **SAM L_2** on average by 1.9 and 1.3 atoms per molecule, respectively. Under ideal conditions, increase in all the other elements, except iron and gold, should correspond only to the change of SEL.

Based on mathematical fitting, the spectra of O 1s region consist of at least two components located at 531.7 eV and 532.9 eV (see table 4.7, and figures B.1d and B.2d in the appendix). The later is assigned to originate from O-H oxygen bound to tertiary carbon[71] (which is present in ligand **L_2** and complex **C_2**), but also has been reported for oxygen in O-H (bound to secondary or primary carbon),[71,78] C-O-C[71,78] and water,[72,79] that could originate from adventitious hydrocarbon contamination or moisture, due to sample exposure to ambient conditions. The former component has a BE, which is comparable to the reported values of oxygen in Fe hydroxides,[64,66,79] oxidised sulfur (e.g. sulfone)[n] and ClO_4^- counter ion[80] (but presence of ClO_4^- is excluded, the detected signal of Cl, presented in figure B.13 in the

[n] Based on poly(hexamethylene sulphone) (PHMS), poly(ether sulphone) (PES) and poly(sodium 4-styrenesulphonate) (PSS) in reference[71].

appendix, suggests much lower levels of Cl impurities, while BE indicates that Cl is not in a form of ClO_4^-).[80] Finally, XPS spectra of freshly cleaned Au show presence of oxygen and can be fitted with the same two components, and they grow upon immersion to Fe solution. However, as this does not lead to detectable peaks of Fe or Cl on treated gold surface, this is attributed to an increase of hydrocarbon contamination on the surface due to extended exposure to ambient conditions.

TABLE 4.6: Integrated and normalised (using R.S.F.) XPS peak areas in N 1s, O 1s and C 1s regions and their relative ratios in **SAM L_2**, **SAM C_2 [MeOH]** and **SAM C_2 [MeCN]**.

SAM	Peak area (x 1000 CPS eV) [relative to N 1s region][o]		
	Ref.[o]	Region	
	N 1s Region	O 1s	C 1s
SAM L_2 expected	[6.0]	[2.0]	[31.0]
SAM C_2 expected	[6.0[p]]	[3.0[q]]	[31.0[q]]
SAM L_2	1.1[6.0]	1.4 [7.9]	8.9[49.7]
SAM C_2 [MeOH]	1.7[6.0]	2.2 [7.6]	11.7[41.1]
	2.0[6.0]	4.0[11.9]	18.2[54.7]
SAM C_2 [MeCN]	1.4[6.0]	2.1 [9.3]	9.5[41.0]
	2.0[6.0]	3.0 [9.1]	15.7[46.8]

Weak intensity, subtle features indicating presence of a shoulder or a double peak in the spectra, low signal-to-noise ratio and large FWHM of the fitted components lead to relatively large variation in peak positions, that in turn gives low confidence in accuracy of the peak areas of the fitted components. Therefore, values presented in the table 4.7 are for indicative purposes only rather than for a detailed analysis

[o] See footnote[i] on page 126.

[p] See footnote[k] on page 126.

[q] Number of oxygen and carbon atoms per complex depends on the sixth exogenous ligand (L), as shown in figure 4.11b. For L = H_2O there are 3 oxygen and 31 carbon atoms, for L = MeOH there are 3 oxygen and 32 carbon atoms, for L = MeCN there are 2 oxygen and 33 carbon atoms per complex. However, due to large number of carbon atoms in ligand $\mathbf{L_2}$, fractional change in carbon is 3 % or 6 %, and even less, when adventitious carbon is treated as a baseline. Such small changes are challenging to detect accurately given noisy XPS spectra, signal attenuation and adventitious carbon.

of relative amounts of the oxygen species. Also, large excess of total oxygen limits accuracy of assignment of the actual oxygen species present in the samples.

TABLE 4.7: Binding energies (BEs) and relative peak areas (normalised using R.S.F.) of fitted components in XPS spectra of N 1s, O 1s and C 1s regions of **SAM L_2**, **SAM C_2 [MeOH]** and **SAM C_2 [MeCN]**. *Due to low confidence in accuracy, presented values are for indicative purposes only.*

	relative to N 1s region[r]							
	Ref.[r]	Component						
	N 1s	N 1s	O 1s		C 1s			
	Region	A	A	B	A	B	C	D
BE (eV)	-	399.7[s]	531.7	532.9	284.9	285.8	287.1	288.5
BE std. dev. (eV)	-	n/a	0.2	0.2	0.1	0.2	0.2	0.3
SAM L_2	6.0	6.0	1.8	6.0	31.2	13.0	3.0	2.3
SAM C_2 [MeOH]	6.0	5.7	3.4	4.3	19.7	15.8	3.8	1.0
	6.0	6.2	3.9	8.0	28.4	19.2	4.8	1.1
SAM C_2 [MeCN]	6.0	5.9	2.7	6.5	17.1	16.5	4.8	1.9
	6.0	5.9	3.2	6.0	20.9	18.3	5.3	1.3

1) Components were constrained to have the same FWHM within each spectrum of each region. Across the samples FWHM in N 1s, O 1s and C 1s varied within 1.4-1.9 eV, 1.5-2.0 eV and 1.3-1.7 eV, respectively.
2) Component A in N 1s is attributed to nitrogen in pyridine and thiomorpholine rings.[j][24,41,72,73]
3) For assignment of components in O 1s and C 1s regions, please see the text.

Figure 4.13b shows little fluctuation in carbon in **SAM C_2 [MeCN]**, but significant variation in **SAM C_2 [MeOH]**, nevertheless the higher level of carbon in **SAM C_2 [MeOH]** is practically the same as in **SAM L_2**. Although fractional excess of carbon (20-60 % relative to nitrogen/iron) is considerably smaller compared to oxygen, however, that is equal to 6-19 atoms of carbon per complex, which is up to two times larger than excess in oxygen (5-9 atoms per complex).

C 1s region can be fitted with at least four components at locations 284.9 eV, 285.8 eV, 287.1 eV and 288.5 eV (see table 4.7, and figures B.1c and B.2c in the appendix). Subtle features, such as shoulders, severely affect the mathematical fittings. Therefore, the outcome of the fitted components is highly sensitive even to

[r] See footnote[i] on page 126.
[s] See footnote[m] on page 128.

smallest changes of signal in the peak. Consequently, that leads to a relatively significant variation in their position and affects accuracy of the integrated peak areas. Furthermore, due to significant excess of carbon, there is a high possibility that more than four species with unique BE are present in the samples, which in turn could dramatically affect the peak positions and therefore the peak areas of all or at least of some components. Overall, accurate assignment of carbon species and their relative amounts is rather challenging. As in the case of oxygen, values presented in the table 4.7 are for indicative purposes only. Nevertheless, majority of carbons are in pyridine and thiomorpholine rings not neighbouring nitrogen atoms, which are assigned to component A at 284.9 eV,[j] while carbons next to nitrogen atoms are associated to component B at 285.8 eV.[j] Binding energies of tertiary carbon[t] and carbon atoms in exogenous MeCN[u] or MeOH[71] ligand are similar, and lies in the region coinciding with the components B and C, i.e. in the range of 285.8-287.1 eV.

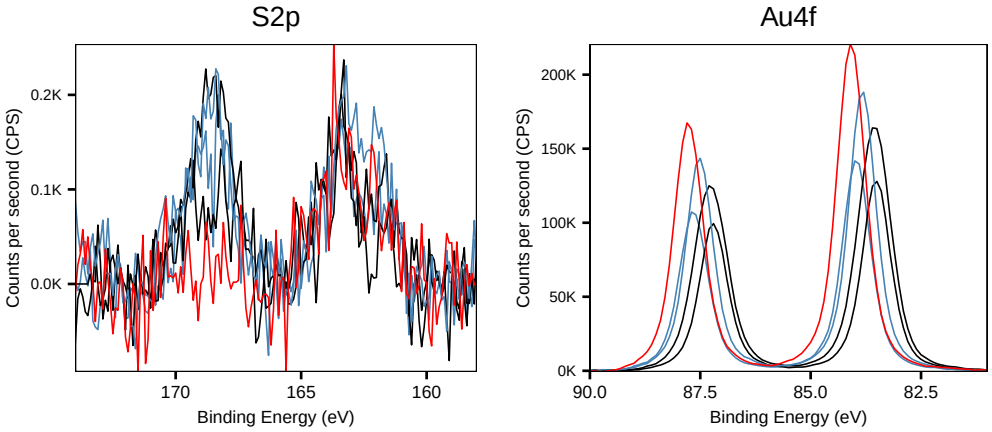

(A) Sulfur S 2p region (B) Gold Au 4f region

FIGURE 4.14: High resolution XPS spectra of **SAM L_2** (**in red**), **SAM C_2 [MeOH]** (**in black**) and **SAM C_2 [MeCN]** (**in blue**).

Weak and noisy signal in S 2p region (figure 4.14a) is usually associated with low amount of sulfur on gold surface,[42,81] or signal attenuation in thick SAMs (i.e. two

[t] Based on poly(vinyl alcohol) (PVA), poly(vinyl methyl ether) (PVME), poly(bisphenol A carbonate) (PBAC), poly(alpha-methylstyrene) (P-alpha-MS), Poly(isobutylene) (PIB), P2VP and P4VP in reference[71].

[u] Based on poly(acrylonitrile) (PAN) and poly(methacrylonitrile) (PMAN) in reference[71].

or more times thicker than **SAM L_2** or **SAM C_2**).[42] However, in contrast to O 1s and C 1s, the spectra of S 2p region, which exhibit two non-overlapping broad asymmetric peaks, are almost identical in all **SAM C_2** samples, irrespectively of SAM formation conditions. Furthermore, the lower BE peak (161-164 eV) in **SAM C_2** and **SAM L_2** overlay almost perfectly, and lie in the regions where spin-orbit doublets are usually assigned to bound and unbound thiols.[42–44] As mentioned earlier in the characterisation of **SAM L_1**, that does not necessarily indicate presence of molecules bound to gold surface in an unexpected manner (e.g. bound to gold through pyridine rings or lying sideways on the surface), because presence of those spin-orbit doublets has been reported in SAMs with thiomorpholine, thiomorpholine-like and dialkyl monosulfide head groups.[45–50] Both **SAM L_2** and **SAM C_2** yield the same ratio of nitrogen/iron to thiomorpholine-like sulfur (161-164 eV), independently of SAM formation conditions. The higher BE peak at 167-170 eV is in the region of spin-orbit doublets often attributed to oxidised sulfur (e.g. sulfone, sulfonate).[v] Although unexpected, it is only present in **SAM C_2** and in complex **C_2** powders, and in both cases peaks of oxidised and thiomorpholine-like sulfur are more or less equal.

Although, great care was taken in sample preparation, acquisition optimisation and baseline correction of XPS spectra, signal quality in S 2p region is low and data analysis is prone to erroneous interpretation, and especially with respect to the fitting of spin-orbit doublets corresponding to the sulfur species presented in table 4.9 and figures B.1a and B.2a (in the appendix).

XPS spectra of Au 4f region in figure 4.14b show varying levels of detected gold, but average values are similar in **SAM C_2 [MeOH]** and in **SAM C_2 [MeCN]**, which are ∼30 % lower than in **SAM L_2**, and is associated with the fact that these SAMs are less densely packed or thinner.[42,81] On the other hand, the weaker Au 4f signal

[v] See footnote[n] on page 129.
[w] See footnote[i] on page 126.
[x] See footnote[k] on page 126.

TABLE 4.8: Integrated and normalised (using R.S.F.) XPS peak areas in N 1s, S 2p and Au 4f regions, and their relative ratios in **SAM L_2**, **SAM C_2 [MeOH]** and **SAM C_2 [MeCN]**.

SAM	Peak area (x 1000 CPS eV) [relative to N 1s region][w]				
	Ref.[w]	S 2p region			Au 4f
	N 1s Region	Total	161 to 164 eV	167 to 170 eV	Region
SAM L_2 expected	[6.0]	[1.0]	[1.0]	[-]	[-]
SAM C_2 expected	[6.0[x]]	[1.0]	[1.0]	[-]	[-]
SAM L_2	1.1[6.0]	0.2[1.1]	0.2[1.2]	0.0[0.0]	20.0[112.1]
SAM C_2 [MeOH]	1.7[6.0]	0.6[2.0]	0.4[1.3]	0.2[0.8]	18.6 [65.3]
	2.0[6.0]	0.8[2.4]	0.3[0.9]	0.4[1.3]	31.2 [94.1]
SAM C_2 [MeCN]	1.4[6.0]	0.5[2.0]	0.3[1.1]	0.2[1.0]	16.6 [71.7]
	2.0[6.0]	1.1[3.1]	0.5[1.5]	0.5[1.3]	30.8 [91.8]

in **SAM C_2** than in **SAM L_2** could originate from the addition of coordinated Fe(II) with SEL.

It is normal practice to use the Au 4f (or C 1s) peak to reference the spectral positions, however, for the spectra presented in this section, that leads to inconsistent shifts in other regions. On the other hand, referencing to pyridine peak in N 1s shows reasonably consistent BE in most of the regions (as shown in the figures in this section), but evident shifts in Au 4f region, which most likely indicates partial coverage and charging.

Overall, XPS spectra of N 1s, Fe 2p and S 2p (thiomorpholine-like) show good agreement in binding energies and relative peak areas across **SAM L_2**, **SAM C_2 [MeOH]** and **SAM C_2 [MeCN]** samples.

[y] See footnote[m] on page 128.

TABLE 4.9: Binding energies (BEs) of fitted components in N 1s and Fe 2p regions of XPS spectra of **SAM C_2 [MeOH]** and **SAM C_2 [MeCN]**. *Due to low confidence in accuracy, presented peak positions are for indicative purposes only.*

	Component						
	Ref.[y]	S 2p				Au 4f	
	N 1s	3/2				7/2	5/2
	A	A	B	C	D	A	A
BE (eV)	399.7[y]	161.8	163.4	167.7	168.9	83.8	87.5
BE std. dev. (eV)	n/a	0.1	0.1	0.5	0.4	0.2	0.2

1) Components were constrained to have the same FWHM within each spectrum of each region. Across the samples FWHM in N 1s, S 2p and Au 4f varied within 1.4-1.9 eV, 0.9-1.4 eV and 0.8-1.0 eV, respectively.
2) Component A in N 1s is attributed to nitrogen in pyridine and thiomorpholine rings.[j,24,41,72,73]
3) Component A in Au 4f is assigned to atomic gold.
4) Binding energies in S 2p are associated as follows:
- Component A and B: thiomorpholine-like sulfur.[45–50]
- Component C and D: oxidised sulfur (e.g. sulfone, sulfonate).[v]

4.3.1.2 Discussion

The three most important aspects of the data presented in the previous section are: (i) detected iron in **SAM $\mathbf{C_2}$** (figure 4.12b); (ii) as in the case of **SAM $\mathbf{L_1}$**, presence of S 2p spin-orbit doublets, that have been reported in SAMs with thiomorpholine and thiomorpholine-like head groups, which are assigned to originate from slightly different interaction of sulfur atom with gold surface in thiomorpholine compared to conventional thiol; and (iii) consistent ratios of N:Fe:S (thiomorpholine-like) in the samples (tables 4.4 and 4.8), which are also close to the expected ratios of 6:0:1 and 6:1:1 for **SAM $\mathbf{L_2}$** and **SAM $\mathbf{C_2}$ [MeOH]**, respectively. That indicates that not only ligand $\mathbf{L_2}$, but also the SCO complex $\mathbf{C_2}$ is stable on gold surface, which is in contrast to complex $\mathbf{C_1}$ discussed in section 4.2.2.1. Furthermore, S 2p region suggests that SAMs are formed in a similar way to **SAM $\mathbf{L_1}$**, while the broad Fe $2p_{3/2}$ peak and presence of its satellite peak in Fe 2p region reveal that 3d electrons are unpaired in both **SAM $\mathbf{C_2}$ [MeOH]** and **SAM $\mathbf{C_2}$ [MeCN]**, which are only common to HS states.

The single component in the N 1s region in all of the samples[h] indicates that nitrogen atoms in thiomorpholine and in pyridine rings have similar environments and supports previously discussed (section 4.2.2.1) assignment of nitrogen atoms in spectra of **SAM $\mathbf{L_1}$** (figure 4.6b). Moreover, binding energy of nitrogen in pyridine does not change significantly, due to coordination of Fe, because the spectra are referenced to pyridine nitrogen at 399.7, but there is little or no variation in peak positions in O 1s, C 1s and S 2p regions.

If complex $\mathbf{C_2}$ is dissolved in MeOH, then SEL H_2O is replaced by MeOH. Consequently, MeOH is expected to be the SEL in **SAM $\mathbf{C_2}$ [MeOH]**. However, it is challenging to detect the difference in chemical composition with XPS, because it changes only by one carbon atom, which is equivalent to $\sim$3 %. Moreover, there is a

possibility, that once SAMs are exposed to ambient conditions during sample transfer or characterisation, H_2O from moisture displaces MeOH as the SEL. Therefore, both states are treated as one with SEL denoted as MeOH/H_2O.

If complex **C_2** is dissolved in MeCN, SEL H_2O is replaced by MeCN. Similarly to the previous case, MeCN is expected to be the SEL in **SAM C_2 [MeCN]**. However, XPS data suggest that it is not the case, because the BE of nitrogen in MeCN (i.e. nitrile group) is expected to be within or around the peak observed in N 1s region,[z] but integrated regions (tables 4.4 and 4.8) suggest similar ratio of S:N for **SAM L_2** and **SAM C_2**, and S:N:Fe for **SAM C_2 [MeOH]** and **SAM C_2 [MeCN]**, and those ratios correspond to six nitrogens per molecule. Furthermore, complex **C_2** is in LS state, when SEL is MeCN, but, as discussed earlier, Fe 2p spectra indicate that both **SAM C_2 [MeOH]** and **SAM C_2 [MeCN]** are in the same state and that it is HS state. Most likely explanation for this case would be replacement of SEL MeCN with H_2O from moisture upon exposure to ambient conditions.

Nevertheless, it cannot be ruled out that MeCN stays coordinated to the complex (at least in a fraction of the molecules). Firstly, in case the seventh nitrogen is present in the complex, expected[aa] drop in **SAM C_2 [MeCN]** is 14 % in S 2p and Fe 2p regions, which could be comparable to variation introduced from baseline correction, due to weak and noisy signal in S 2p and Fe 2p regions, and complex background in the latter. Secondly, there is a possibility that Fe(II) is oxidised to Fe(III). Although, Fe(III) complex of closely related ligand **Py_5** has been reported to be unstable under ambient conditions,[55,56] close proximity to gold surface could affect electronic configuration in complex **C_2**. In case **SAM C_2** contains Fe(III)

[z] Peak position is expected within the range 398-400 eV, based on reported BE of nitrogen in condensed MeCN[82], in polymers containing nitrile group - PAN and PMAN[71], and in thiocyanate anion[68–70].

[aa] The replacement of MeOH/H_2O with MeCN as the SEL and vice versa changes the amount of nitrogen, but does not affect the levels of sulfur or iron. However, that does change XPS spectra in S 2p, Fe 2p and other regions, because all of the spectra are normalised to have equal integrated area in N 1s region. Expected quantitative changes in XPS spectra, due to replacement of SEL, are calculated and discussed in section B.1.

centres, switching between LS and HS states would lead to subtle changes in XPS spectra of Fe 2p region,[67] which, of course, would be challenging to differentiate. Finally, it has been reported that direct contact of complexes with gold surfaces can cause unexpected effects, such as change in coordination number and geometry of a complex, suppressed transition, reduced ligand field strength.[23]

Neither the O 1s, nor the C 1s regions provide important quantitative information about the SAMs, because there is a significant variation in the signal in some samples, and potential for confounding signals from contamination. While binding energies of the fitted components are comparable to the reported values of the expected species, most of the peaks are in the region that is also associated with oxygen and carbon in adventitious hydrocarbon contamination. Such contamination is small in well packed conventional thiol SAMs, such as **C18 SAM**. Therefore, observed high excess of carbon and oxygen could indicate poorly packed and disordered SAM originating from ineffective displacement of hydrocarbons reversibly adsorbed to gold surface (naturally occurring when handling even freshly cleaned gold surfaces under ambient conditions[43,51]) during SAM formation, due to a combination of weak head group affinity towards gold[43,51,52] and bulky shape of the molecules preventing close packing of head groups.[53] In addition to a possibility of non-displaced natural contamination, signal in Cl 2p (not from ClO_4^-[80]), F 1s and Br 3p were detected by XPS (figure B.13 in the appendix), which could indicate presence of chloride, fluoride and bromide traces from synthesis of the compounds and could contain varying amounts of oxygen and carbon. Finally, higher levels of impurities could be attracted to **SAM C_2** by the unscreened Fe ions (ClO_4^- counter ions are detected in powder and drop-cast samples of reagent complex **C_2**, but not in **SAM C_2**).

Oxidation of sulfur is associated with synthesis of complex **C_2** or its storage, but not the process of **SAM C_2** formation, because almost equal amounts of oxidised

and thiomorpholine-like sulfur are present in powder, dropcast and SAM samples of complex $\mathbf{C_2}$, but not in analogous samples of ligand $\mathbf{L_2}$. Therefore, higher quality **SAM $\mathbf{C_2}$** could potentially be achieved by coordinating Fe(II) to **SAM $\mathbf{L_2}$**, which will be characterised in section 4.3.3.

One of the main concerns, low signal quality in the XPS spectra, could be improved by performing area scans, that would allow to average scans acquired over multiple spots on the sample without inducing damage due to prolonged exposure to the incident X-rays. However, other important issues, such as excess of carbon, oxygen and presence of impurities could originate from low surface coverage, which is indicated by large ratios of underlying gold atoms per molecule (70:1 to 120:1) compared to a well packed alkanethiol SAM (20:1). Perhaps the best improvement would be an alternative head group, for example a thiol, to lead to better quality SAMs.

4.3.2 Ligand exchange in SAM C_2 by rinsing

As mentioned above, molecules of certain solvents (used to dissolve complex **C_2**) can replace the SEL, which in turn affect the spin state. For molecules immobilised on a surface, i.e. SAMs, ligand exchange should take place simply by rinsing with appropriate solvent, as depicted in diagram in figure 4.15. This section presents XPS data of fresh **SAM C_2 [MeOH]** and **SAM C_2 [MeCN]**, and rinsed with MeCN and MeOH, respectively.

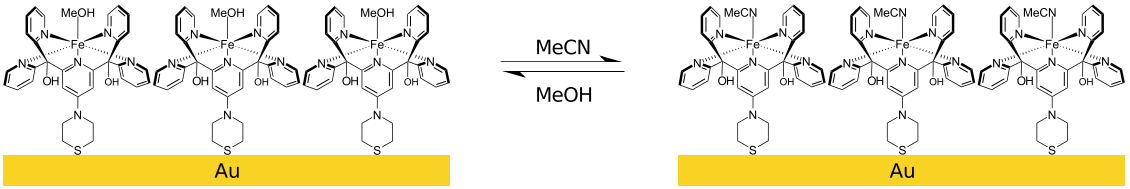

FIGURE 4.15: Schematic detailing reversible ligand exchange by rinsing **SAM C_2** with MeCN and MeOH.

XPS spectra of **SAM C_2 [MeOH]** and **SAM C_2 [MeCN]** presented in the previous section did not show significant enough changes in N 1s and Fe 2p regions to clearly indicate the change of Fe spin state or of the SEL. The uncertainty was partly attributed to variation in signal, but further complications arose from the excess signal in O 1s and C 1s regions, that are associated with underlying contamination. Data presented in this section has been acquired on the same samples before and after rinsing, this way contributions from the underlying contamination and impurities were eliminated, so changes in the data presented in this section should closely represent change of the SEL. Samples were rinsed with a corresponding pure solvent using a glass pipette for 1 min at room temperature.

4.3.2.1 SAM C_2 [MeOH] - rinsing with MeCN

Figure 4.16 compares spectra of **SAM C_2 [MeOH]** before and after the rinse with MeCN. Figure 4.16a shows no significant change in N 1s region, because it was used

to normalised spectra just like in section 4.3.1.1, but figure 4.16b shows no evident change in Fe 2p region either. In order to enhance XPS signal, Fe 2p region was also acquired with higher pass energy (i.e. PE=30 eV and PE=40 eV), but the spectra in figure B.4 (in the appendix) still show no change in the shape, while variation in intensity is attributed to baseline correction of the complex background.

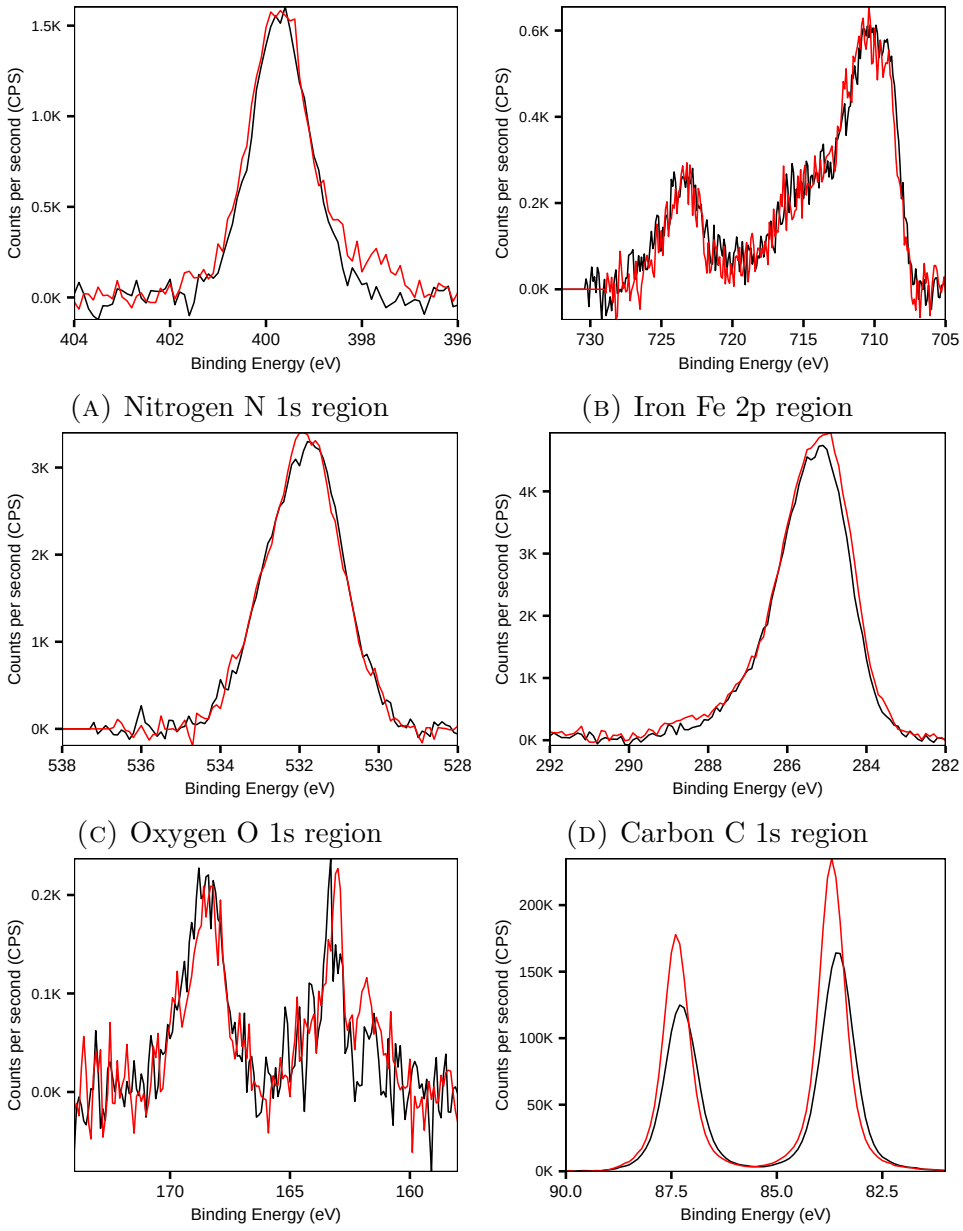

(A) Nitrogen N 1s region

(B) Iron Fe 2p region

(C) Oxygen O 1s region

(D) Carbon C 1s region

(E) Sulfur S 2p region

(F) Gold Au 4f region

FIGURE 4.16: High resolution XPS spectra of **SAM C_2 [MeOH]** before (**in black**) and after (**in red**) rinsing with MeCN. Complexes in the SAM are expected to switch from HS to LS state, however, there are no significant changes in N 1s, Fe 2p, S 2p, O 1s and C 1s regions.

Similarly there are no significant differences in O 1s and C 1s regions (figures 4.16c and 4.16d). Although S 2p signal is weak, figure 4.16e indicates almost identical composition and quantity of sulfur species. However, the Au 4f spectra are quite different. The change of 0.1 eV in BE is within instrument's resolution, but the peak area is about 40 % higher after the rinse.

As a control, a second sample of **SAM C_2 [MeOH]** was prepared, taken out of the growth solution, rinsed with pure MeOH, dried under stream of nitrogen and immediately rinsed with MeCN. Comparison of XPS spectra of this sample and the first sample (**SAM C_2 [MeOH]** before it was rinsed with MeCN) is presented in figures B.6 and B.7 (in the appendix), and again show no important differences. A further rinse of the second sample with MeCN did not yield any changes either, except a small drop in oxidised sulfur and tiny increase in Au 4f signal (figures B.8 and B.9 in the appendix).

4.3.2.2 SAM C_2 [MeCN] - rinsing with MeOH

Although, MeCN coordinates to transition metals stronger than H_2O or MeOH, a reverse ligand exchange has been reported in Fe(II) complex of closely related ligand **Py_5**.[56,62] Figure 4.17 compares spectra of **SAM C_2 [MeCN]** before and after rinsing with MeOH. It also contains reference spectra of samples discussed in the previous section, i.e. sample 1 (**SAM C_2 [MeOH]** before rinsing with MeCN) and sample 2 (**SAM C_2 [MeOH]** rinsed with MeCN immediately after SAM formation). Once again, the spectra are normalised using N 1s region. Fresh and rinsed **SAM C_2 [MeCN]** yield similar spectra in N 1s, Fe 2p and S 2p regions. Spectra of Fe 2p region in figure B.5 (in the appendix) were acquired at higher pass energies (i.e. PE=30 eV and PE=40 eV), however, there are no noticeable changes in the shape of the spectra, either. Amounts of oxygen and carbon slightly increase and reach

levels comparable to the reference spectra, while peak area in Au 4f region increases by 65 % after the rinse.

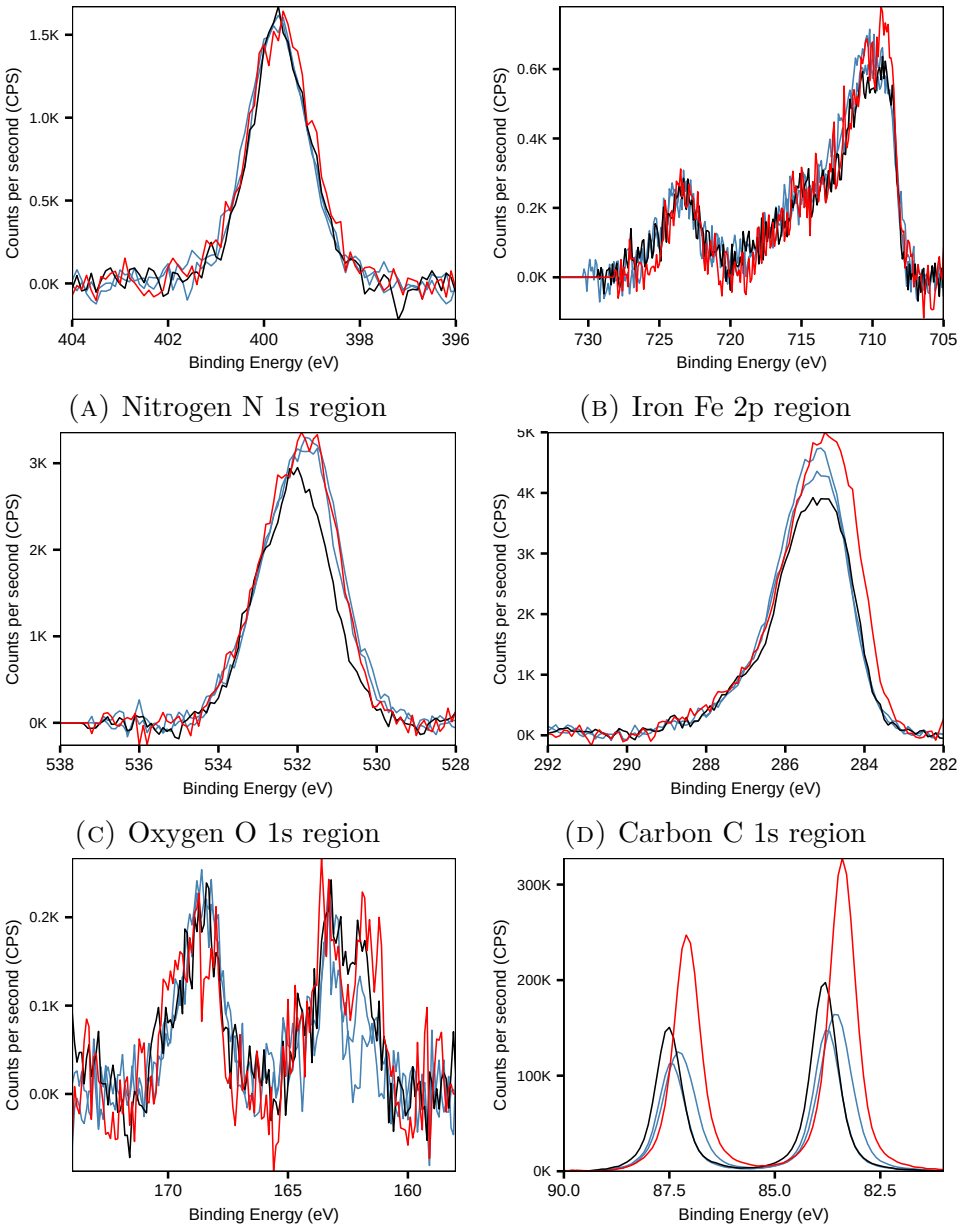

(A) Nitrogen N 1s region

(B) Iron Fe 2p region

(C) Oxygen O 1s region

(D) Carbon C 1s region

(E) Sulfur S 2p region

(F) Gold Au 4f region

FIGURE 4.17: High resolution XPS spectra of **SAM C_2 [MeCN]** before (**in black**) and after (**in red**) rinsing with MeOH. For the comparison purposes, spectra of the first sample (**SAM C_2 [MeOH]** before the rinse with MeCN) and the second sample (**SAM C_2 [MeOH]** rinsed with MeCN immediately after SAM formation) are added (**in blue**).

4.3.2.3 Discussion

Successful replacement of H_2O with MeCN at SEL position in **SAM C_2 [MeOH]** would lead to an increase in nitrogen, however, because all of the spectra are normalised to have equal integrated areas in N 1s region, this would lead to an apparent drop in peak areas of 14 % in S 2p and Fe 2p, 12 % in C 1s and 22 % in O 1s region, as explained in section B.1. No such drops are evident in XPS data (figure 4.16) of rinsed **SAM C_2 [MeOH]**. In fact, the differences between spectra of fresh and rinsed **SAM C_2 [MeOH]** are effectively negligible and indicate that relative ratio of N, Fe, S, C and O chemical elements and their species do not change upon rinsing with MeCN, which leads to a conclusion that ligand exchange does not take place. The second sample of **SAM C_2 [MeOH]**, which was rinsed immediately after SAM formation, gives the same outcome, and further rinse with MeCN had no effect either.

The same – but positive – changes in the peak areas are expected in case of successful replacement of MeCN with MeOH at the SEL position in **SAM C_2 [MeCN]** upon rinsing with MeOH. Once again, no such changes can be seen in Fe 2p and S 2p regions (figure 4.17 and B.8). Although, there is an increase in O 1s and C 1s regions after the rinse, the increase is relative. Absolute quantities of all elements other than gold decrease, therefore relative growth of O 1s and C 1s, but not S 2p and Fe 2p, is likely to originate from the higher loss of complex **C_2** molecules from the surface than the underlying contamination during the rinsing step. Again, this leads to the same conclusion that ligand exchange does not take place.

Furthermore, there is little difference between fresh **SAM C_2 [MeOH]** and **SAM C_2 [MeCN]** (figure 4.17). This suggests presence of the same SEL in **SAM C_2** under all investigated conditions so far, in agreement with the discussion of data in section 4.3.1.1. This also explains, why the shape of spectra in Fe 2p region does not change and always corresponds to the same state. **SAM C_2 [MeOH]** samples

were prepared using complex **C_2** powder without exposure to MeCN, therefore those molecule cannot contain MeCN at the SEL position and should have only six nitrogen atoms, which is supported by the quantitative analysis of peak areas in tables 4.4 and 4.8. Likewise, **SAM C_2 [MeCN]** samples were prepared using complex **C_2** without exposure to MeOH and cannot contain it at the SEL position. Because solvent molecules coordinate to the SEL position in complex **C_2** in solution, the most likely explanation is that **SAM C_2** contains MeOH or MeCN depending on the solvent of the growth solution, however, upon exposure to ambient conditions, H_2O from moisture coordinates to the SEL position. Such coordination pathway also explains why spectra of Fe 2p region always indicate HS state.

Finally, it is important to highlight that upon rinsing **SAM C_2** with the same type of solvent that was used in growth solution, intensity of signal in Au 4f region increased slightly. However, when **SAM C_2** is rinsed with a different solvent (e.g. **SAM C_2 [MeOH]** is rinsed with MeCN), intensity increases 40-65 %, which indicates loss of complex **C_2** from the surface and suggests weak affinity of thiomorpholine head group towards gold surface.

4.3.3 Fe coordination to SAM L_2

As in the case of **SAM L_1**, coordination of Fe(II) was attempted on **SAM L_2**, in order to construct SCO complex on the surface. **SAM L_2** was formed from chloroform ($CHCl_3$) solution and then immersed into ∼5 mM $Fe(ClO_4)_2$ in MeCN or in H_2O for 1 min and for 30 min, in order to coordinate Fe(II) to ligand **L_2** in **SAM L_2**, as depicted in figure 4.18.

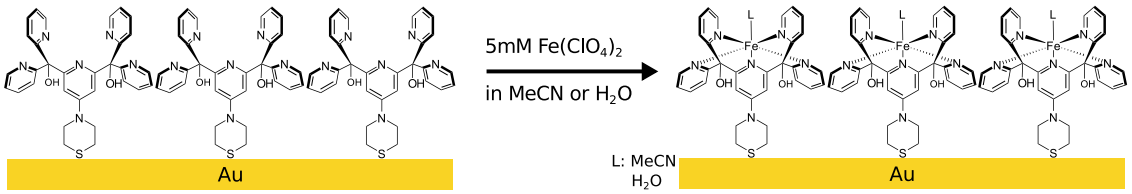

FIGURE 4.18: Schematic detailing Fe coordination to **SAM L_2** in MeCN or H_2O.

4.3.3.1 Fe(II) coordination in MeCN solution

Figure 4.19 compares XPS spectra of fresh **SAM L_2**, **SAM L_2** after immersion into ∼5 mM $Fe(ClO_4)_2$ in MeCN for 1 min and for 30 min, and fresh **SAM C_2**. Figure 4.19b shows no iron in fresh **SAM L_2**, but, in contrast to **SAM L_1**, presence of Fe even after 1 min of coordination. There are significantly (2-2.5 times) more iron in **SAM L_2** after 1 min than after 30 min of immersion time, however, it is the latter, that shows the same signal strength and shape in Fe 2p region as **SAM C_2**, which indicates the same N:Fe ratio in both SAMs.

Similar trend appears in O 1s region - fresh **SAM L_2**, **SAM L_2** exposed to ∼5 mM $Fe(ClO_4)_2$ in MeCN for 30 min, and fresh **SAM C_2** shows similar peak shapes and intensities, but after just 1 min of coordination to **SAM L_2** the main oxygen peak almost doubles in intensity and a distinct shoulder appears at 530.3 eV (figure B.3d in the appendix), which falls within the region reported for oxygen in iron oxides.[64,66,79]

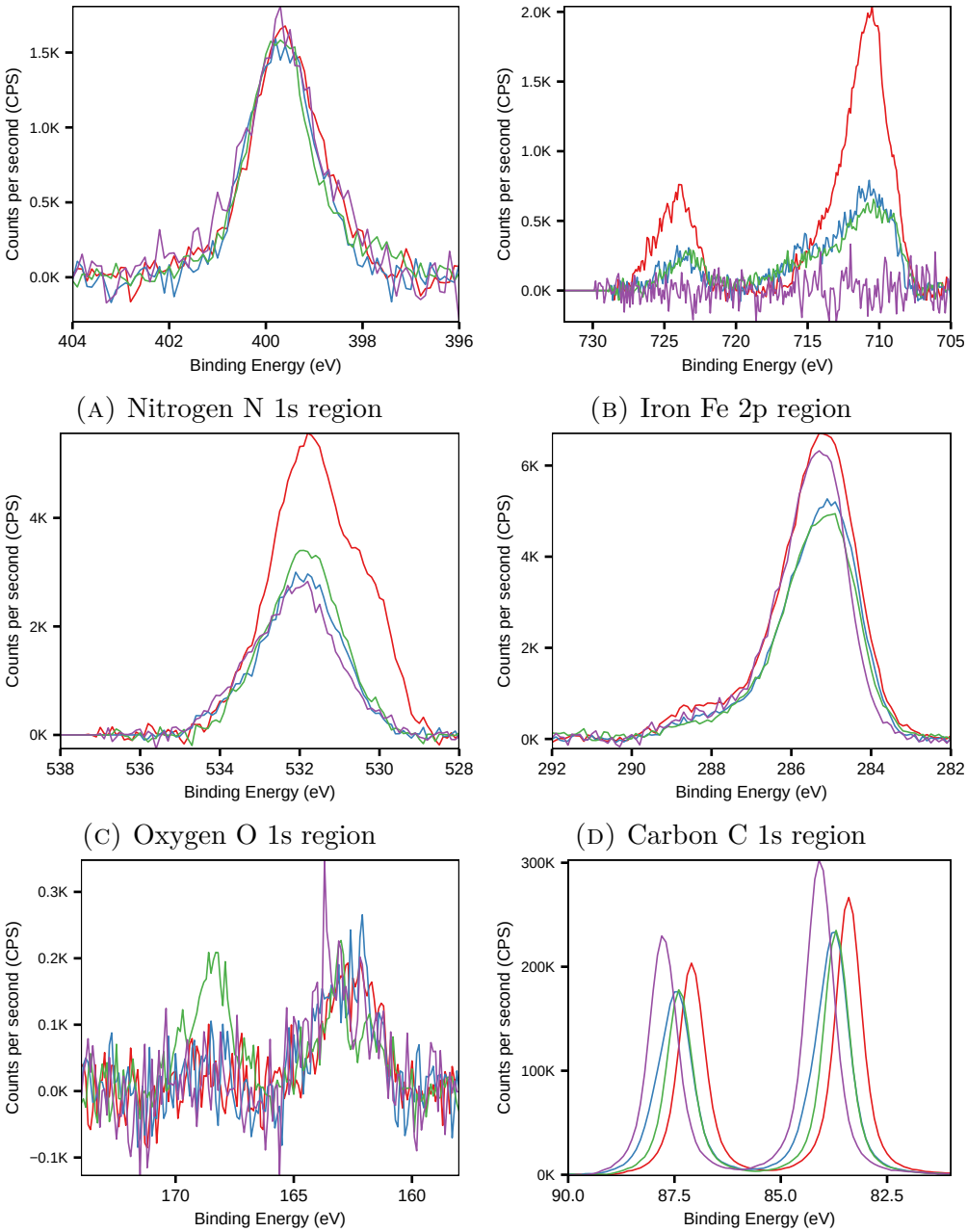

(A) Nitrogen N 1s region

(B) Iron Fe 2p region

(C) Oxygen O 1s region

(D) Carbon C 1s region

(E) Sulfur S 2p region

(F) Gold Au 4f region

FIGURE 4.19: High resolution XPS spectra of **SAM L_2** (**in purple**), **SAM L_2+Fe(1m)** and **SAM L_2+Fe(30m)** exposed to ∼5 mM $Fe(ClO_4)_2$ in MeCN (in **red** and **blue**, respectively), and **SAM C_2** (**in green**).

There are similar amounts of thiomorpholine-like sulfur in all of the SAMs, while oxidised sulfur appears only in fresh **SAM C_2** (figure 4.19e). **SAM L_2+Fe(30m)** and **SAM C_2** show almost equivalent levels and species of carbon and gold, while amount of carbon is noticeably higher in **SAM L_2** and **SAM L_2+Fe(1m)**.

The gold signal is strongest in **SAM L_2**, which is in agreement with the increase of signal in other regions in other SAMs, however, the stronger signal in **SAM L_2+Fe(1m)** than in **SAM L_2+Fe(30m)** does not correlate with higher levels of Fe, which are expected to additionally attenuate signal from gold surface. **SAM L_2+Fe(1m)** with highest levels of iron yield lowest BE in Au 4f, **SAM C_2** and **SAM L_2+Fe(30m)** show very similar intermediate BE, and **SAM L_2** containing no iron at all show the highest BE in Au 4f.

Overall, **SAM C_2** and **SAM L_2+Fe(30m)** yield fairly similar spectra. In fact, all of the SAMs, except **SAM L_2+Fe(1m)**, yield similar S:N:O:Fe ratios.[bb] Comparable fractional increase of iron and oxygen in **SAM L_2+Fe(1m)** suggests that excess iron is in a form of Fe-OR.

4.3.3.2 Fe(II) coordination in aqueous solution

Figure 4.20 compares spectra of **SAM L_2+Fe(1m)** and **SAM L_2+Fe(30m)** prepared by immersion into the Fe(II) solution in H_2O and in MeCN. Intensity of Fe $2p_{3/2}$ peak in both SAMs exposed to Fe(II) solution in H_2O is even stronger than recorded for **SAM L_2+Fe(1m)** exposed to the solution in MeCN. However, due to similar intensities of Fe $2p_{1/2}$ peaks, variation in Fe $2p_{3/2}$ might originate from the background correction. These SAMs also yield rather similar spectra in O 1s region, and all SAMs show similar spectra in S 2p region. On the other hand, both SAMs exposed to the Fe(II) solution in H_2O yield equivalent spectra in C 1s, and show noticeably stronger peak at ∼285 eV compared to **SAM L_2+Fe(1m)** treated in Fe(II) solution in MeCN. Finally, the intensity in Au 4f region is different for all the SAMs, but, SAMs exposed to aqueos solution of Fe(II) show weaker signal, which correlates with presence of higher carbon (and possibly iron) levels in those

[bb] Similar S:N:O ratio in **SAM L_2**, because there is no iron.

SAMs. On the other hand, the BEs in these SAMs do not follow the same trend as in the data discussed in section 4.3.3.1.

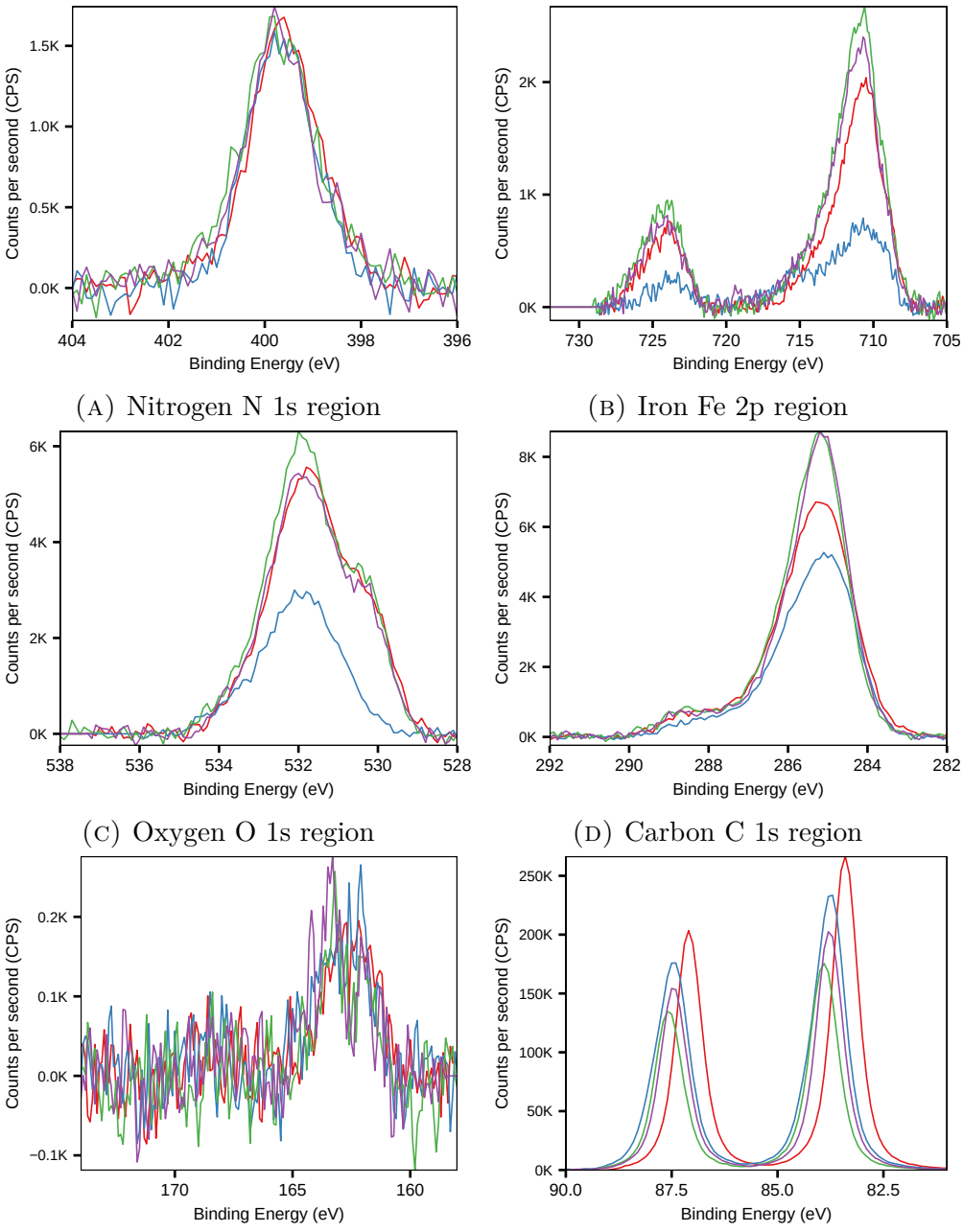

(A) Nitrogen N 1s region

(B) Iron Fe 2p region

(C) Oxygen O 1s region

(D) Carbon C 1s region

(E) Sulfur S 2p region

(F) Gold Au 4f region

FIGURE 4.20: High resolution XPS spectra of **SAM L_2+Fe(1m)** and **SAM L_2+Fe(30m)** exposed to ~5 mM $Fe(ClO_4)_2$ in MeCN (in **red** and **blue**, respectively), and **SAM L_2+Fe(1m)** and **SAM L_2+Fe(30m)** exposed to ~5 mM $Fe(ClO_4)_2$ in H_2O (in **green** and **purple**, respectively).

Overall, **SAM L_2+Fe(1m)** and **SAM L_2+Fe(30m)** produced by exposing to the Fe(II) solution in H_2O, and **SAM L_2+Fe(1m)** produced by exposing to the MeCN

solution yield similar or almost identical relative amounts and species of N, O, S, and Fe. Lower peak intensity of Au 4f in **SAM L_2+Fe(1m)** and **SAM L_2+Fe(30m)** produced by exposing to the Fe(II) solution in H_2O does correlate to the higher levels or carbon, however, the shift of the peak positions to higher BE does not follow the trend observed in the data discussed in section 4.3.3.1. Rinsing **SAM L_2+Fe(1m)** and **SAM L_2+Fe(30m)** (produced by exposing to the aqueous Fe(II) solution) with MeCN did not yield any important changes in the spectra (see figures B.10, B.11 and B.12 in the appendix).

4.3.3.3 Discussion

SAM L_2, just like **SAM L_1**, is composed of a ligand molecules, i.e. Fe(II) centres are absent. However, unlike in **SAM L_1**, immersion into ~5 mM $Fe(ClO_4)_2$ in MeCN or in H_2O yields evident iron coordination. Different immersion times (i.e. 1 min and 30 min) into the Fe(II) solution in H_2O yield practically identical spectra in N 1s, S 2p, C 1s regions, and only slightly different spectra in Fe 2p, O 1s and Au 4f regions, which suggest effectively the same chemical composition in the resulting SAMs (see figure 4.20).

Short immersion time (i.e. 1 min) into the Fe(II) solution in MeCN has similar effect on **SAM L_2** as immersion into the H_2O solution discussed above[cc]. On the other hand, longer immersion time (i.e. 30 min) into the Fe(II) solution in MeCN does lead to unexpectedly different XPS spectra compared to the shorter immersion time, i.e. severe drop in peak areas in Fe 2p, O 1s and C 1s regions. Surprisingly, such spectra are practically identical to that of **SAM C_2**[dd] (see figure 4.19), which suggest successful formation of complex **C_2** by coordination of Fe(II) to ligand **L_2** immobilised on the gold surface, this is effectively a conversion of **SAM L_2** into **SAM C_2**, but without introduction of the oxidised sulfur.

Furthermore, **SAM L_2+Fe(30m)** from the Fe(II) solution in MeCN and fresh **SAM L_2** show more or less identical spectra, except the latter yields slightly higher levels of carbon (assigned to adventitious contamination), obviously no iron peaks, and therefore stronger signal in Au 4f region. Therefore, abnormally high levels of Fe, in addition to significant increase of oxygen and carbon, in the other SAMs are attributed to excess iron, which is 2.5-3.0 times higher than expected. It most likely originates from a rapid coordination of multiple Fe(II) ions to each ligand **L_2**, due

[cc] Compared to **SAM L_2** immersed into ~5 mM $Fe(ClO_4)_2$ in MeCN, **SAM L_2** exposed to the analogous solution in H_2O for 1 min show very similar spectra in N 1s, S 2p, O 1s regions, small drop in Fe 2p and more significant drop in C 1s regions, which in turn leads to increase in Au 4f peak. Such spectra similarities suggest similar chemical composition.

[dd] Except the peak associated with oxidised sulfur in S 2p spectrum of **SAM C_2**.

to high concentration (5 mM) of Fe(II) ions in the solutions. However, over time (30 min) a more energetically favourable state is reached, where there is only one iron molecule per ligand $\mathbf{L_2}$, as pyridine coordinate stronger than H_2O or MeCN. Absence of significant increase in N 1s regions implies that H_2O molecules coordinate to available sites on Fe(II) ions.

4.4 Conclusions

SAMs of two new ligands tridentate $\mathbf{L_1}$ and pentadentate $\mathbf{L_2}$, which are promising in designing SCO complexes, were successfully formed and characterised. Both ligands facilitate their self-assembly on gold through the thiomorpholine head group, however, their coordination properties are rather different, which became evident in early stages of this study. Neither coordination of Fe(II) to **SAM $\mathbf{L_1}$**, nor SAM formation of its preformed complex $\mathbf{C_1}$ has been achieved. In fact, XPS characterisation revealed that **SAM $\mathbf{L_1}$** is hardly different from SAM formed in solution of complex $\mathbf{C_1}$, implying demetallisation in complex $\mathbf{C_2}$ during SAM formation. On the other hand, **SAM $\mathbf{L_2}$** successfully coordinates Fe ions (with ∼100 % yield) and its preformed complex $\mathbf{C_2}$ successfully forms SAMs. Indeed, XPS spectra of the former and the latter are more or less identical, except the presence of oxidised sulfur in **SAM $\mathbf{C_2}$**.

It was observed that in presence of high concentration of Fe ions coordination takes place in two stages. In the first stage, iron ions rapidly (within less than a minute) coordinate to pyridine rings, that results in multiple iron ions per ligand $\mathbf{L_2}$ molecule. In the second stage, system slowly (less than 30 min in MeCN, but longer in H_2O) approaches its minimum energy, where pyridine displaces H_2O or MeCN ligands, to leave a single iron ion per ligand $\mathbf{L_2}$.

Due to pentadentate nature of ligand $\mathbf{L_2}$, complex $\mathbf{C_2}$ can accommodate a labile sixth exogenous ligand (SEL), that determines if complex exhibits SCO behaviour or stays 'locked' in HS or LS state. Although, MeOH and MeCN leads to HS (at RT) and LS state in solution, respectively, Fe 2p region indicates HS state in both types of SAM. While there is a number of potential complications (direct contact with gold can suppress SCO behaviour and weaken ligand coordination,[23] vacuum can lead to loss of coordinated MeCN,[56] Fe(II) could oxidise to Fe(III), XPS measurements

themselves could induce damage to name a few), it is unclear if ligand substitution does take place at all. However, comparison of **SAM C_2**, formed under different conditions, rinsed with different solvents or having Fe(II) coordinated in different solvents, suggests that H_2O from moisture replaces an existing SEL upon sample exposure to ambient conditions.

A significantly higher level of carbon and oxygen than expected for adventitious contamination, especially in **SAM L_2** and **SAM C_2**, presence of impurities, weaker XPS signal in S 2p region than in other SAMs of comparable thickness, increasing intensity in Au 4f upon rinsing samples with different solvent have been attributed to weak interaction between thiomorpholine and gold surface.

4.5 References

[1]L. Pukenas, F. Benn, E. Lovell, A. Santoro, L. J. Kershaw Cook, M. A. Halcrow and S. D. Evans, J. Mater. Chem. C **3**, 7890–7896 (2015).

[2]L. Cambi and L. Szegö, Ber. Dtsch. Chem. Ges. (A B Ser., 2591–2598 (1931).

[3]M. Cavallini, Phys. Chem. Chem. Phys. **14**, 11867 (2012).

[4]H. J. Shepherd, G. Molnar, W. Nicolazzi, L. Salmon and A. Bousseksou, Eur. J. Inorg. Chem., 653–661 (2013).

[5]G. Molnar, L. Salmon, W. Nicolazzi, F. Terki and A. Bousseksou, J. Mater. Chem. C **2**, 1360–1366 (2014).

[6]M. A. Halcrow, *Spin-Crossover Materials: Properties and Applications* (Wiley, 2013), ISBN: 9781118519318.

[7]J. Dugay, M. Gimenez-Marques, T. Kozlova, H. W. Zandbergen, E. Coronado and H. S. J. Van Der Zant, Adv. Mater. **27**, 1288–1293 (2015).

[8]E. Ludwig, H. Naggert, M. Kallane, S. Rohlf, E. Kroger, A. Bannwarth, A. Quer, K. Rossnagel, L. Kipp and F. Tuczek, Angew. Chemie - Int. Ed. **53**, 3019–3023 (2014).

[9]M. C. Muñoz and J. A. Real, Coord. Chem. Rev. **255**, 2068–2093 (2011).

[10]O. Roubeau, Chem. - A Eur. J. **18**, 15230–15244 (2012).

[11]H. Peng, S. Tricard, G. Felix, G. Molnar, W. Nicolazzi, L. Salmon and A. Bousseksou, Angew. Chemie - Int. Ed. **53**, 10894–10898 (2014).

[12]T. Miyamachi, M. Gruber, V. Davesne, M. Bowen, S. Boukari, L. Joly, F. Scheurer, G. Rogez, T. K. Yamada, P. Ohresser, E. Beaurepaire and W. Wulfhekel, Nat. Commun. **3**, 936–938 (2012).

[13]T. G. Gopakumar, F. Matino, H. Naggert, A. Bannwarth, F. Tuczek and R. Berndt, Angew. Chemie - Int. Ed. **51**, 6262–6266 (2012).

[14]H. Naggert, A. Bannwarth, S. Chemnitz, T. von Hofe, E. Quandt and F. Tuczek, Dalton Trans. **40**, 6364–6366 (2011).

[15]T. G. Gopakumar, M. Bernien, H. Naggert, F. Matino, C. F. Hermanns, A. Bannwarth, S. Mühlenberend, A. Krüger, D. Krüger, F. Nickel, W. Walter, R. Berndt, W. Kuch and F. Tuczek, Chem. - A Eur. J. **19**, 15702–15709 (2013).

[16]T. Palamarciuc, J. C. Oberg, F. El Hallak, C. F. Hirjibehedin, M. Serri, S. Heutz, J.-F. Létard and P. Rosa, J. Mater. Chem. **22**, 9690–9695 (2012).

[17]B. Warner, J. C. Oberg, T. G. Gill, F. El Hallak, C. F. Hirjibehedin, M. Serri, S. Heutz, M. A. Arrio, P. Sainctavit, M. Mannini, G. Poneti, R. Sessoli and P. Rosa, J. Phys. Chem. Lett. **4**, 1546–1552 (2013).

[18]A. Pronschinske, Y. Chen, F. Lewis, D. A. Shultz, A. Calzolari, M. B. Nardelli and D. B. Dougherty, Nano Lett. **13**, 1429 (2013).

[19]A. Pronschinske, R. C. Bruce, G. Lewis, Y. Chen, A. Calzolari, M. Buongiorno-Nardelli, D. A. Shultz, W. You and D. B. Dougherty, Chem. Commun. **49**, 10446–10452 (2013).

[20]M. Bernien, D. Wiedemann, C. F. Hermanns, A. Kruüger, D. Rolf, W. Kroener, P. Muüller, A. Grohmann and W. Kuch, J. Phys. Chem. Lett. **3**, 3431–3434 (2012).

[21]M. Bernien, H. Naggert, L. M. Arruda, L. Kipgen, F. Nickel, J. Miguel, C. F. Hermanns, A. Krüger, D. Krüger, E. Schierle, E. Weschke, F. Tuczek and W. Kuch, ACS Nano **9**, 8960–8966 (2015).

[22]S. Beniwal, X. Zhang, S. Mu, A. Naim, P. Rosa, G. Chastanet, J.-F. Létard, J. Liu, G. E. Sterbinsky, D. A. Arena, P. A. Dowben and A. Enders, J. Phys. Condens. Matter **28**, 206002 (2016).

[23]M. Bernien, 'X-Ray Absorption Spectroscopy of Fe Complexes on Surfaces : Electronic Interactions and Tailoring of the Magnetic Coupling (Thesis)', PhD thesis (2009).

[24]C. Shen, M. Haryono, A. Grohmann, M. Buck, T. Weidner, N. Ballav and M. Zharnikov, Langmuir **24**, 12883–12891 (2008).

[25]S. Liatard, J. Chauvin, D. Jouvenot, F. Loiseau and A. Deronzier, J. Phys. Chem. C **117**, 20431–20439 (2013).

[26]R. Sakamoto, K.-H. Wu, R. Matsuoka, H. Maeda and H. Nishihara, Chem. Soc. Rev. **44**, 7698–714 (2015).

[27]S. Bin-Salamon, S. Brewer, S. Franzen, D. L. Feldheim, S. Lappi and D. A. Shultz, J. Am. Chem. Soc. **127**, 5328–5329 (2005).

[28]G. Poneti, L. Poggini, M. Mannini, B. Cortigiani, L. Sorace, E. Otero, P. Sainctavit, A. Magnani, R. Sessoli and A. Dei, Chem. Sci. **6**, 2268–2274 (2015).

[29]M. A. Halcrow, Polyhedron **26**, 3523–3576 (2007).

[30]M. A. Halcrow, Coord. Chem. Rev. **253**, 2493–2514 (2009).

[31]M. a. Halcrow, New J. Chem. **38**, 1868 (2014).

[32]L. J. Kershaw Cook, R. Mohammed, G. Sherborne, T. D. Roberts, S. Alvarez and M. A. Halcrow, Coord. Chem. Rev. **289-290**, 2–12 (2015).

[33]M. Matsuda and H. Tajima, Chem. Lett. **36**, 700–701 (2007).

[34]M. S. Alam, M. Stocker, K. Gieb, P. Müller, M. Haryono, K. Student and A. Grohmann, Angew. Chemie - Int. Ed. **49**, 1159–1163 (2010).

[35]M. Cavallini, I. Bergenti, S. Milita, J. C. Kengne, D. Gentili, G. Ruani, I. Salitros, V. Meded and M. Ruben, Langmuir **27**, 4076–4081 (2011).

[36]S. Basak, P. Hui and R. Chandrasekar, Chem. Mater. **25**, 3408–3413 (2013).

[37]D. Secker, S. Wagner, S. Ballmann, R. Härtle, M. Thoss and H. B. Weber, Phys. Rev. Lett. **106**, 3–6 (2011).

[38]V. Meded, A. Bagrets, K. Fink, R. Chandrasekar, M. Ruben, F. Evers, A. Bernand-Mantel, J. S. Seldenthuis, A. Beukman and H. S. J. Van Der Zant, Phys. Rev. B - Condens. Matter Mater. Phys. **83**, 1–13 (2011).

[39]L. J. Kershaw Cook, J. Fisher, L. P. Harding and M. A. Halcrow, Dalt. Trans. **44**, 9417–9425 (2015).

[40]E. A. Ramírez, E. Cortés, A. A. Rubert, P. Carro, G. Benítez, M. E. Vela and R. C. Salvarezza, Langmuir **28**, 6839–6847 (2012).

[41]B. D. Lamp, D. Hobara, M. D. Porter, K. Niki and T. M. Cotton, Langmuir **13**, 736–741 (1997).

[42]P. E. Laibinis, G. M. Whitesides, D. L. Allara, Y. T. Tao, A. N. Parikh and R. G. Nuzzo, J. Am. Chem. Soc. **113**, 7152–7167 (1991).

[43]C. D. Bain, E. B. Troughton, Y. T. Tao, J. Evall, G. M. Whitesides and R. G. Nuzzo, J. Am. Chem. Soc. **111**, 321–335 (1989).

[44]P. Gupta, A. Ulman, S. Fanfan, A. Korniakov and K. Loos, J. Am. Chem. Soc. **127**, 4–5 (2005).

[45]M. C. Lennartz, M. Baumert, S. Karthäuser, M. Albrecht and R. Waser, Langmuir **27**, 10312–10318 (2011).

[46]J. Noh, Y. Jeong, E. Ito and M. Hara, J. Phys. Chem. C **111**, 2691–2695 (2007).

[47]T. Ishida, N. Choi, W. Mizutani, H. Tokumoto, I. Kojima, H. Azehara, H. Hokari, U. Akiba and M. Fujihira, Langmuir **15**, 6799–6806 (1999).

[48]J. M. Tour, L. Jones, D. L. Pearson, J. J. S. Lamba, T. P. Burgin, G. M. Whitesides, D. L. Allara, A. N. Parikh and S. Atre, J. Am. Chem. Soc. **117**, 9529–9534 (1995).

[49]H. Takiguchi, K. Sato, T. Ishida, K. Abe, K. Yase and K. Tamada, Langmuir **16**, 1703–1710 (2000).

[50]C.-J. Zhong, R. C. Brush, J. Anderegg and M. D. Porter, Langmuir **15**, 518–525 (1999).

[51]E. B. Troughton, C. D. Bain, G. M. Whitesides, R. G. Nuzzo, D. L. Allara and M. D. Porter, Langmuir **4**, 365–385 (1988).

[52]C. D. Bain, H. A. Biebuyck and G. M. Whitesides, Langmuir **5**, 723–727 (1989).

[53]T. Ishida, S. Tsuneda, N. Nishida, M. Hara, H. Sasabe and W. Knoll, Langmuir **13**, 4638–4643 (1997).

[54]M. E. de Vries, R. M. La Crois, G. Roelfes, H. Kooijman, A. L. Spek, R. Hage and B. L. Feringa, Chem. Commun., 1549–1550 (1997).

[55]R. T. Jonas, T. D. P. Stack and V, J. Am. Chem. Soc. **119**, 8566–8567 (1997).

[56]Christian R. Goldsmith, Robert T. Jonas and T. D. P. Stack, J. Am. Chem. Soc. **124**, 83–96 (2002).

[57]W.-L. Kwong, C.-N. Lok, C.-W. Tse, E. L.-M. Wong and C.-M. Che, Chem. Eur. J. **21**, 3062–3072 (2015).

[58]E. L.-M. Wong, G.-S. Fang, C.-M. Che and N. Zhu, Chem. Commun., 4578–80 (2005).

[59]C. Bachmann, M. Guttentag, B. Spingler and R. Alberto, Inorg. Chem. **52**, 6055–6061 (2013).

[60]J. R. Long, C. J. Chang and Y. Sun, **2**, 9212–9215 (2013).

[61]B. Das, A. Orthaber, S. Ott and A. Thapper, Chem. Commun. **51**, 13074–13077 (2015).

[62]C. R. Goldsmith, R. T. Jonas, A. P. Cole and T. D. P. Stack, Inorg. Chem. **41**, 4642–4652 (2002).

[63]D. J. Rudd, C. R. Goldsmith, A. P. Cole, T. D. P. Stack, K. O. Hodgson and B. Hedman, Inorg. Chem. **44**, 1221–1229 (2005).

[64]A. P. Grosvenor, B. A. Kobe, M. C. Biesinger and N. S. McIntyre, Surf. Interface Anal. **36**, 1564–1574 (2004).

[65]T. Yamashita and P. Hayes, Appl. Surf. Sci. **254**, 2441–2449 (2008).

[66]N. S. McIntyre and D. G. Zetaruk, Anal. Chem. (1977).

[67]Y. B. M.S. Ioffe, I.N. Ivleva, Chem. Phys. Lett. **59**, 549–553 (1978).

[68]K. Burger, C. Furlani and G. Mattogno, J. Electron Spectros. Relat. Phenomena **21**, 249–256 (1980).

[69]K. Burger and H. Ebel, Inorganica Chim. Acta **53**, L105–L107 (1981).

[70]P. Brant and R. D. Feltham, J.Electron Spectrosc. Relat. Phenom. **32**, 205–221 (1983).

[71]G. Beamson and D. Briggs, *High Resolution XPS of Organic Polymers: The Scienta ESCA300 Database* (Wiley, 1992), ISBN: 9780471935926.

[72]Y. Zubavichus, M. Zharnikov, Y. J. Yang, O. Fuchs, E. Umbach, C. Heske, A. Ulman and M. Grunze, Langmuir **20**, 11022–11029 (2004).

[73]J. Liu, B. Schupbach, A. Bashir, O. Shekhah, A. Nefedov, M. Kind, A. Terfort and C. Woll, Phys. Chem. Chem. Phys. **12**, 4459–4472 (2010).

[74]R. P. Gupta and S. K. Sen, Phys. Rev. B **10**, 71 (1974).

[75]R. Gupta and S. Sen, Phys. Rev. B **12**, 15–19 (1975).

[76]X. Zhang, T. Palamarciuc, P. Rosa, J. F. Létard, B. Doudin, Z. Zhang, J. Wang and P. a. Dowben, J. Phys. Chem. C **116**, 23291–23296 (2012).

[77]H. Jacob, K. Kathirvel, F. Petersen, T. Strunskus, A. Bannwarth, S. Meyer and F. Tuczek, Langmuir **29**, 8534–8543 (2013).

[78]G. P. Lopez, D. G. Castner and B. D. Ratner, Surf. Interface Anal. **17**, 267–272 (1991).

[79]M. C. Biesinger, B. P. Payne, A. P. Grosvenor, L. W. M. Lau, A. R. Gerson and R. S. S. Smart, Appl. Surf. Sci. **257**, 2717–2730 (2011).

[80]J. Xie, C. Li, Z. Cui and X. Guo, Adv. Funct. Mater. **25**, 6519–6526 (2015).

[81]T. Ishida, M. Hara, I. Kojima, S. Tsuneda, N. Nishida, H. Sasabe and W. Knoll, Langmuir **14**, 2092–2096 (1998).

[82]K. Kishi, Y. Okino and Y. Fujimoto, Surf. Sci. **176**, 23–31 (1986).

Chapter 5

Characterisation of simple ω-alkanethiol, aromatic, COOH- and azide-terminated SAMs

Some of the data presented in this chapter on the stability of COOH-terminated SAMs under soft UV in acidic conditions are included in the publication (in preparation):

L. Pukenas, P. Prompinit, B. Nishitha, D. J. Tate, N. D. Pradeep Singh, C. Wälti, S. D. Evans and R. J. Bushby. Soft UV Photo-patterning and Metallization of Self-Assembled Monolayers of the Lipoic Acid Ester of α-Hydroxy-1-acylpyrene: The Generality of Acid Catalysed Removal of Thiol-on-Gold SAMs using Soft UV Light. (in preparation)

Some of the data presented in this chapter on the study of SAM formation of azide terminated and other long-chain alkanethiololigoethyleneglycols (LCAT-OEG), their mixing and facilitation of click chemistry on the surface are included in the publication:

J. Murray, D. Nowak, **L. Pukenas**, R. Azhar, M. Guillorit, C. Wälti, K. Critchley, S. Johnson and R. S. Bon. Solid phase synthesis of functionalised SAM-forming alkanethiol-oligoethyleneglycols. J. Mater. Chem. B, 2(24), 3741-3744 **(2014)**

Data of ellipsometry measurements of **BPDT SAM** and **BPT SAM**, and of **C4 SAM**, **C5 SAM**, **C9 SAM**, **C12 SAM** and **C18 SAM** for surface enhanced Raman spectroscopy and plasmonic systems are included in the following publications:

F. Benz, C. Tserkezis, L. O. Herrmann, B. de Nijs, A. Sanders, D. O. Sigle, **L. Pukenas**, S. D. Evans, J. Aizpurua, and J. J. Baumberg. Nanooptics of molecular-shunted plasmonic nanojunctions. Nano Letters, 15(1), 669-674 **(2015)**

F. Benz, B. de Nijs, C. Tserkezis, R. Chikkaraddy, D. O. Sigle, **L. Pukenas**, S. D. Evans, J. Aizpurua, and J. J. Baumberg. Generalized circuit model for coupled plasmonic systems. Optics Express, 23(26), 33255-33269 **(2015)**

This chapter is split into three parts. The first part presents the characterisation of self-assembled monolayers (SAMs) terminated with carboxylic acid (COOH) group and their stability under irradiation with soft UV (365 nm, 4 mW cm^{-2}) for 1.5 h in the acidic catalyst (100 mM HCl in IPA) using ellipsometry, wetting measurements, XPS and FTIR spectroscopy. SAMs based on dithiolane head group (**ALA SAM**) and conventional thiol head group (**DTBA SAM**, **MHA SAM**, **MOA SAM** and **MUA SAM**) were investigated. The main objectives of this study were as follows:

- to investigate the stability of COOH SAM based on dithiolane head group (**lipoic acid** SAM), which is the protected group in **SAM1**.

- to investigate the stability of COOH SAMs based on conventional thiol head group (**DTBA SAM**, **MHA SAM**, **MOA SAM** and **MUA SAM**).
- to determine if the instability of **ALA SAM** originates from its low thickness or unconventional dithiolane head group that is prone to cross-linking.
- to investigate the suitability of the SAMs for photo-patterning and selective copper electrochemical deposition.

The second part presents the characterisation of SAM formation using azide terminated long-chain alkanethiololigoethyleneglycol (LCAT-OEG) and its ability to facilitate click chemistry on the surface. The main objectives of this study were as follows:

- to determine the quality of azide terminated SAM (**SAM2**) and alcohol terminated LCAT-OEG SAMs (**LCAT-OEG-4 SAM**, **LCAT-OEG-1 SAM**) (see figure 5.9).
- to investigate the mixing of **reagent 2** with **LCAT-OEG-4** or **LCAT-OEG-1** in a SAM environment (see figure 5.10b).
- to investigate click chemistry of **SAM2** surface using **strained cyclooctyne** under catalyst-free aqueous conditions (see figure 5.10c).

Finally, the third part discusses the use of **BPDT SAM** and **BPT SAM** to study how molecular conductivity affects a surrounding plasmonic junction, and the use of simple alkanethiol SAMs to evaluate a generalised circuit model for coupled plasmonic systems.

5.1 Stability of COOH-terminated SAMs under soft UV in acidic conditions

The study on photolysis of **SAM1**, presented in chapter 3, produced some unexpected results (figure 3.2). It was found that the photo-reaction in **SAM1** only takes place upon UV irradiation in the acidic catalyst (100 mM HCl in IPA), however, it leads to a loss of molecules instead of the expected deprotection of carboxylic acid (COOH) monolayer. Three photolysis pathways were proposed (figure 3.12), however, the most likely pathway (**Scheme B** in figure 3.12) is associated with the instability of **lipoic acid**. In the light of such results and to confirm the proposal, this chapter presents a study on the stability of **ALA SAM** under the photolysis conditions. For a better understanding of whether the possible instability could be related to thin SAM thickness or the unconventional dithiolane head group prone to cross-linking (figure 3.10), this chapter also includes an investigation of other COOH-terminated SAMs of similar thickness, but with thiolate rather than dithiolane head group, i.e. **DTBA SAM**, **MHA SAM**, **MOA SAM** and **MUA SAM**.

5.1.1 Ellipsometry and Wetting measurements

Wettability data and thickness obtained from ellipsometry measurements of **DTBA SAM**, **MHA SAM**, **ALA SAM**, **MOA SAM** and **MUA SAM** before and after exposure to soft UV (365 nm, 4 mW cm^{-2}) for 1.5 h in the acidic catalyst (100 mM HCl in IPA) are shown in table 5.1. Fresh SAMs yield ellipsometric thicknesses in a good agreement with the expected values.[a] The UV treatment does not affect the thickness of **MOA SAM** and **MUA SAM**, but significantly reduces (to 2-3 Å) the thickness of **DTBA SAM**, **MHA SAM** and **ALA SAM**. Nevertheless the thicknesses of the latter three SAMs fall into the region, where accuracy is low due to the contamination layer of hydrocarbons few angstroms thick always being present on clean gold (which is used as a reference), that has been briefly exposed to ambient conditions (even if it was piranha cleaned immediately beforehand),[1,2] in addition to the usual instrumental error and sample-to-sample variation of at least 1-2 Å. Consequently, treated **DTBA SAM** might have an actual thickness lower than 3 Å, while **MHA SAM** has a thickness higher than 2 Å and **ALA SAM** higher than 3 Å. Furthermore, additional hydrocarbon contamination will arise in disordered SAMs, which again will have a greater fractional impact on the thickness in SAMs with poor surface coverage and lower initial thickness.

All SAMs (except **MOA SAM**) show wetting (<10°) receding contact angle, which is typical for SAMs terminated with carboxylic acid group. High advancing angle (45°) on **DTBA SAM**, and in turn large hysteresis (40°), indicates high chemical or physical surface roughness, which usually is indicative of disordered SAM. Other SAMs (except **MOA SAM**) show lower advancing angles (∼30°), but they are still higher than reported wetting angles for carboxylic acid terminated SAMs, which is attributed to lower packing, ordering and a possibility that a small fraction of the surfaces are covered with a double layer. It has been reported that the quality

[a] Based on conventional 30° tilt angle from the surface normal and molecule's chain length calculated with HyperChem package (semi-empirical AM1).

TABLE 5.1: Ellipsometric thickness and contact angles of fresh and UV treated under acidic conditions **DTBA SAM**, **MHA SAM**, **ALA SAM**, **MOA SAM** and **MUA SAM**.

SAM	Ellipsometric thickness (Å)		Water contact angles (°)		
	Measured	Expected[a]	Advancing	Receding	Hysteresis
C18 SAM	22 ± 2	22	111 ± 1	103 ± 2	8
DTBA SAM	6 ± 2	6	45 ± 2	5 ± 1	40
DTBA SAM+UV$^{HCl}_{1.5\,h}$	3 ± 2	6	94 ± 4	51 ± 4	43
MHA SAM	8 ± 1	8	32 ± 9	6 ± 2	26
MHA SAM+UV$^{HCl}_{1.5\,h}$	2 ± 2	8	79 ± 8	49 ± 6	30
ALA SAM	9 ± 2	8	30 ± 2	7 ± 2	23
ALA SAM+UV$^{HCl}_{1.5\,h}$	3 ± 2	8	70 ± 2	18 ± 4	52
MOA SAM	10 ± 1	10	39 ± 4	19 ± 2	20
MOA SAM+UV$^{HCl}_{1.5\,h}$	10 ± 1	10	63 ± 2	26 ± 1	37
MUA SAM	15 ± 1	14	29 ± 12	5 ± 1	24
MUA SAM+UV$^{HCl}_{1.5\,h}$	14 ± 1	14	67 ± 4	22 ± 6	45

- UV refers to soft UV (365 nm, 4 mW cm^{-2}).

- HCl (superscript) refers to acid catalyst 100 mM HCl in IPA.

- Ellipsometric thickness was obtained using refractive index of 1.45 in Cauchy's equation.

- Uncertainties refer to whichever is the larger (i) standard deviation of sample-to-sample values or (ii) average of standard deviations from each sample (originating from variation in a single measurement or measurement-to-measurement).

- Higher receding angle on **MOA SAM** than **MHA SAM**, **ALA SAM** and **MUA SAM** most likely originates from adventitious hydrocarbon contamination, that COOH SAMs are prone to. Indeed, reproducibility of COOH SAMs with appropriate contact angles and ellipsometric thicknesses was low, and a number of samples were excluded as unreliable. Limited number of samples or measurements resulted in unusually small or large uncertainties for certain SAMs.

of COOH-terminated SAMs is sensitive to their preparation conditions[3–9] with optimum results achieved in ethanolic solutions containing a small amount of additional acid. SAMs presented in this chapter were formed from DCM solutions and did not contain any additional acid, in order to keep consistent formation conditions to those of **SAM1**. It was difficult to achieve high reproducibility of samples (of the SAMs presented in this chapter) that would yield low contact angles. The fact that **MOA SAM** yields substantially higher receding angle than all other SAMs and slightly

higher advancing angle than **MHA SAM**, **ALA SAM** and **MOA SAM**, shows how prone to the adventitious surface contamination COOH-terminated SAMs can be.

Following the UV treatment, the contact angles drastically increase for both **DTBA SAM** and **MHA SAM**. The advancing angle reaches ∼87° and the receding angle increases to ∼50°, which indicate that a small amount of COOH groups are exposed to the surface for the water droplet to interact with, and are usually observed for adventitious hydrocarbons film on clean gold surface. Treated **ALA SAM**, **MOA SAM** and **MUA SAM** yield similar contact angles, however, compared to the fresh SAMs, advancing angles increase to ∼67°, while receding angle increase to ∼22°, but the latter is hardly different from that of fresh **MOA SAM**. Those angles, especially the receding, are significantly smaller than that of **DTBA SAM** and **MHA SAM**. While the increase in the angles for **ALA SAM** could originate from a loss of molecules, for **MOA SAM** and **MUA SAM**, this is likely a result of partial surface esterification, which has been reported to take place on comparable time-scale.[3,4]

Fresh SAMs (except **DTBA SAM**) show somewhat typical hysteresis of ∼20° for SAMs on thermally evaporated (relatively rough) gold thin films. High hysteresis (∼40°) loop in both fresh and UV treated **DTBA SAM** is attributed to disorder. Similar hysteresis in fresh and treated **MHA SAM** is associated with uniform surface chemistry in fresh (COOH groups) and treated (CH_2 or CH_3 groups) state, while large hysteresis (∼45°) in the treated **ALA SAM**, **MOA SAM** and **MUA SAM** might be indicative of chemically heterogeneous surfaces consisting of a small quantity of CH_3 groups (due to esterification[3,4]) that leads to high advancing angles, but there are still COOH groups present which leads to rather hydrophilic surface.

5.1.2 FTIR

The effects of acid concentration and UV irradiation on the stability of **ALA SAM**, as well as the stability of **DTBA SAM**, **MHA SAM** and **MOA SAM** under UV in 100 mM HCl in IPA, were investigated by studying the chemical information and structure of the monolayers using FTIR spectroscopy in reflectance configuration on fresh and treated SAMs.

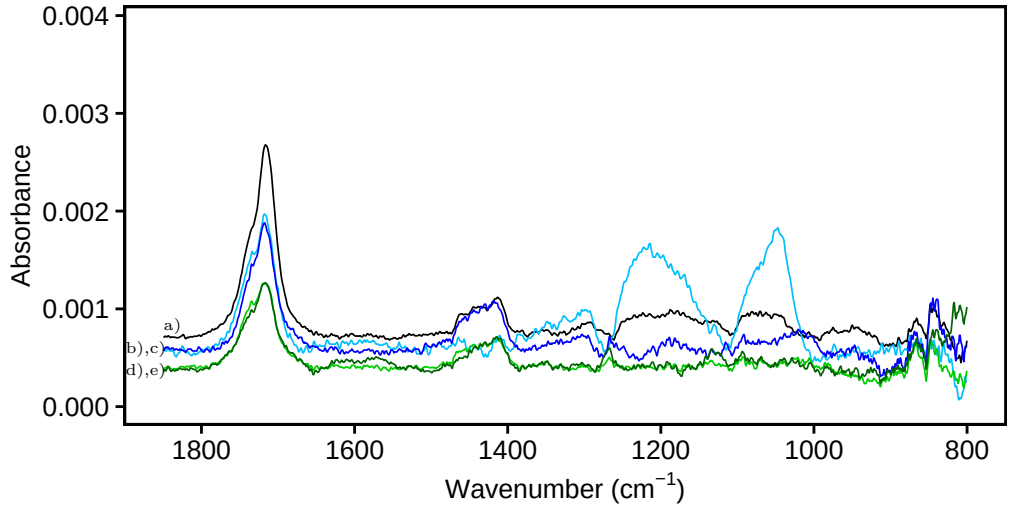

FIGURE 5.1: Infrared spectra of a) fresh **ALA SAM**, b) **ALA SAM** after UV irradiation for 1.5 h in IPA, c) **ALA SAM** after immersion for 1.5 h in 100 mM HCl in IPA in the dark, d) **ALA SAM** after UV irradiation for 1.5 h in 1 mM HCl in IPA, e) **ALA SAM** after UV irradiation for 1.5 h in 100 mM HCl in IPA, Exposure to UV light for 1.5 h is equivalent to 22 J cm^{-2} (4 mW cm^{-2}, 365 nm).

Comparison of IR spectra of **ALA SAM** and **lipoic acid** molecules dispersed in KBr pellet (figure 3.3c and 3.3d, respectively) as well as assignment of the strong double peak to carbonyl C=O bond in acyclic dimers (peak 1715 cm^{-1})[3,7,10] and in monomers (peak 1740 cm^{-1}),[2–4,7,10,11] have already been discussed in chapter 3. This section focusses on the stability of **ALA SAM**. Figure 5.1 shows stacked IR spectra, which indicate that both UV treatment in pure IPA (figure 5.1b) and an immersion into 100 mM HCl in IPA in the dark for 1.5 h (figure 5.1c) yield almost the same IR spectrum, showing a drop of ∼25 % in intensity of the double peak at 1715-1740 cm^{-1}. This could be indicative of (i) a loss of COOH groups; (ii) the

removal of any fractions of a double layer; or (iii) conformational changes within the SAM. UV treatments in 1 mM HCl in IPA (figure 5.1d) and 100 mM HCl in IPA (figure 5.1e) for 1.5 h also yield almost identical spectra, but show ∼55 % drop in intensity of the double peak. Such a strong decrease is indicative of loss of COOH groups.

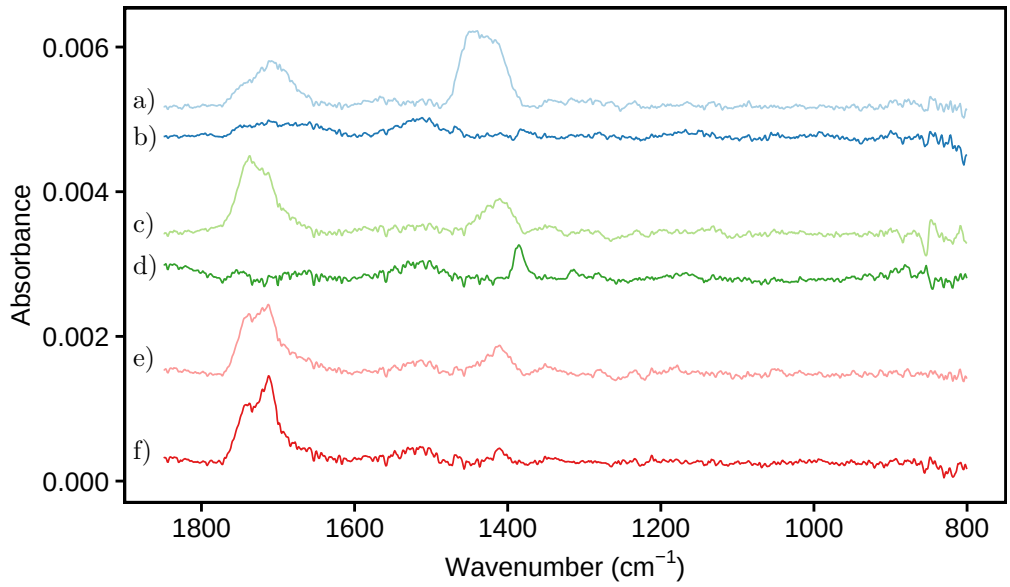

FIGURE 5.2: Infrared spectra of a) fresh **DTBA SAM**, b) **DTBA SAM** after UV irradiation for 1.5 h in 100 mM HCl in IPA, c) fresh **MHA SAM**, d) **MHA SAM** after UV irradiation for 1.5 h in 100 mM HCl in IPA, e) fresh **MOA SAM**, and f) **MOA SAM** after UV irradiation for 1.5 h in 100 mM HCl in IPA. Exposure to UV light for 1.5 h is equivalent to 22 J cm^{-2} (4 mW cm^{-2}, 365 nm).

Figure 5.2 compares the IR spectra of fresh and UV treated in 100 mM HCl in IPA for 1.5 h **DTBA SAM**, **MHA SAM** and **MOA SAM**. Fresh SAMs yield similar spectra to that of fresh **ALA SAM**, with the main difference being the shape and intensity of the double peak in the 1715-1740 cm^{-1} region. The IR spectra of **MHA SAM** and **MOA SAM** are almost identical, differing only by a small change in the proportions of the peaks in 1715-1740 cm^{-1} region assigned to C=O in acyclic dimers and monomers. On the other hand, fresh **DTBA SAM** yields a weaker and broader double peak in the same region, which could be indicative of substantially lower quantity of COOH groups, originating from the loss of molecules, that in turn

leads to lower packing and order, conformational changes and loss of signal due to stronger effect of the surface selection rule.

An exposure to soft UV for (365 nm, 4 mW cm^{-2}, 1.5 h) in the acidic catalyst (100 mM HCl in IPA) leads to a complete loss of the double peak (1715-1740 cm^{-1}) in IR spectra of **DTBA SAM** and **MHA SAM** (see figure 5.2b and 5.2d) The disappearance of the peaks in IR spectra of SAMs usually is indicative of a severe, but not necessarily total loss of molecules from the surface. At lower coverage molecules might be lying flat on the surface with the axis of bond vibrations parallel to the gold surface and therefore 'invisible' to IR spectra due to the surface selection rule. On the other hand, the UV treatment has only a subtle effect on the double peak in IR spectra of **MOA SAM** (figure 5.2f), i.e. the peak at 1712 cm^{-1} show an increase, while the peak 1740 cm^{-1} show a drop in intensity suggesting that the treatment has a minimal effect on **MOA SAM** structure.

5.1.3 XPS

X-ray Photoelectron Spectroscopy (XPS) measurements were carried out to obtain additional chemical information of fresh and treated SAMs terminated with carboxylic acid group, and to quantify effects of the UV treatment under acid. Unless stated otherwise, binding energies are referenced to alkyl carbon in C 1s at 284.5 eV and spectra are scaled so that intensity of Au $4f_{7/2}$ peak in each set of measurements would reach the same (arbitrary chosen[b]) value.

Figure 5.3 shows XPS spectra with fitted components of fresh and UV treated **ALA SAM**. In terms of positions of the fitted components and their relative peak areas, Fresh **ALA SAM** yields similar spectra to fresh **DTBA SAM** (figure C.1), **MHA SAM** (figure C.2), **MOA SAM** (figure C.3) and **MUA SAM** (figure C.4), except for the amount of alkyl/aryl carbon due to varying chain length, and high quantity (∼50 %) of unbound sulfur in fresh **ALA SAM** due to cross-linking of the molecules (see section 3.2.3 in chapter 3). As discussed in section 3.2.3.1, components in C 1s region are assigned to alkyl/aryl carbon (284.5 eV),[12–16] C-S carbon (∼286.0 eV)[15,16] and C=O carbon (∼289.1 eV)[2,10,15,17–20]; components in O 1s region are attributed to C=O oxygen (∼532.0 eV)[10,16,21,22] and C-O oxygen (∼533.5 eV)[10,16,21,22]; spin-orbit doublets in S 2p associated with bound thiols (S $2p_{3/2}$ at ∼161.9 eV)[1,12,23,24] and unbound thiol or disulfide (S $2p_{3/2}$ at ∼163.1 eV).[25–27]

Figure 5.3 allows for a direct comparison of the spectra of fresh and UV treated in acid **ALA SAM**. It visually shows that the chemical composition does not change, because positions of the peaks do not shift and their relative ratios do not change,

[b]The arbitrary value, in fact, corresponds to the initial Au $4f_{7/2}$ peak intensity in one of the samples.

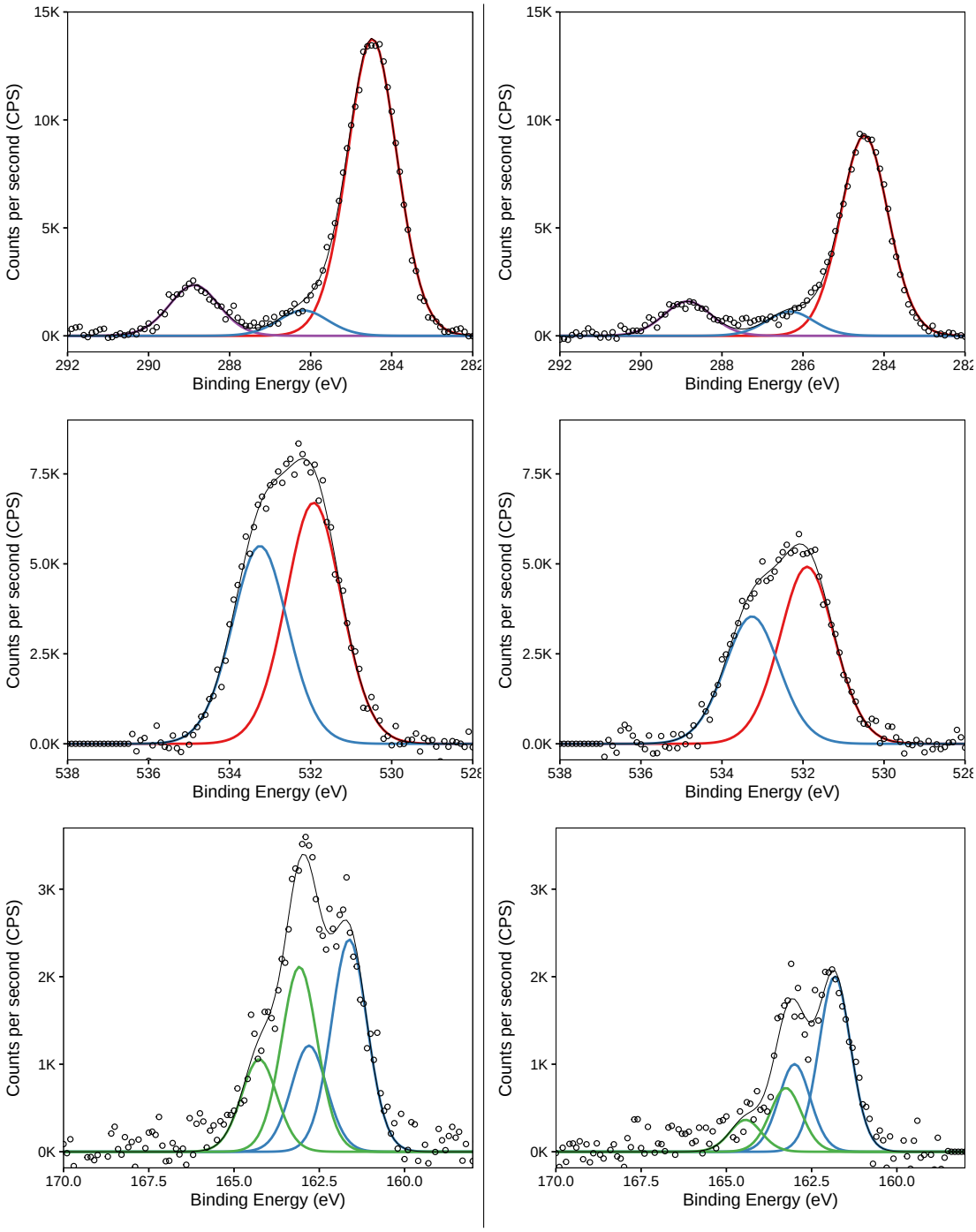

FIGURE 5.3: XPS spectra with fitted components of fresh (on the left) and UV-treated (on the right) **ALA SAM**. Spectra correspond to C 1s (top row), O 1s (middle row) and S 2p (bottom row). UV-treated samples were exposed to soft UV (365 nm, 4 mW cm^{-2}) for 1.5 h in the acidic catalyst (100 mM HCl in IPA).

however, intensities of the peaks decrease by a similar fraction (except the disproportionately high loss of unbound sulfur, see sections 3.2.3 and 3.2.4 for the explanation), which is indicative of a partial SAM loss from the surface.

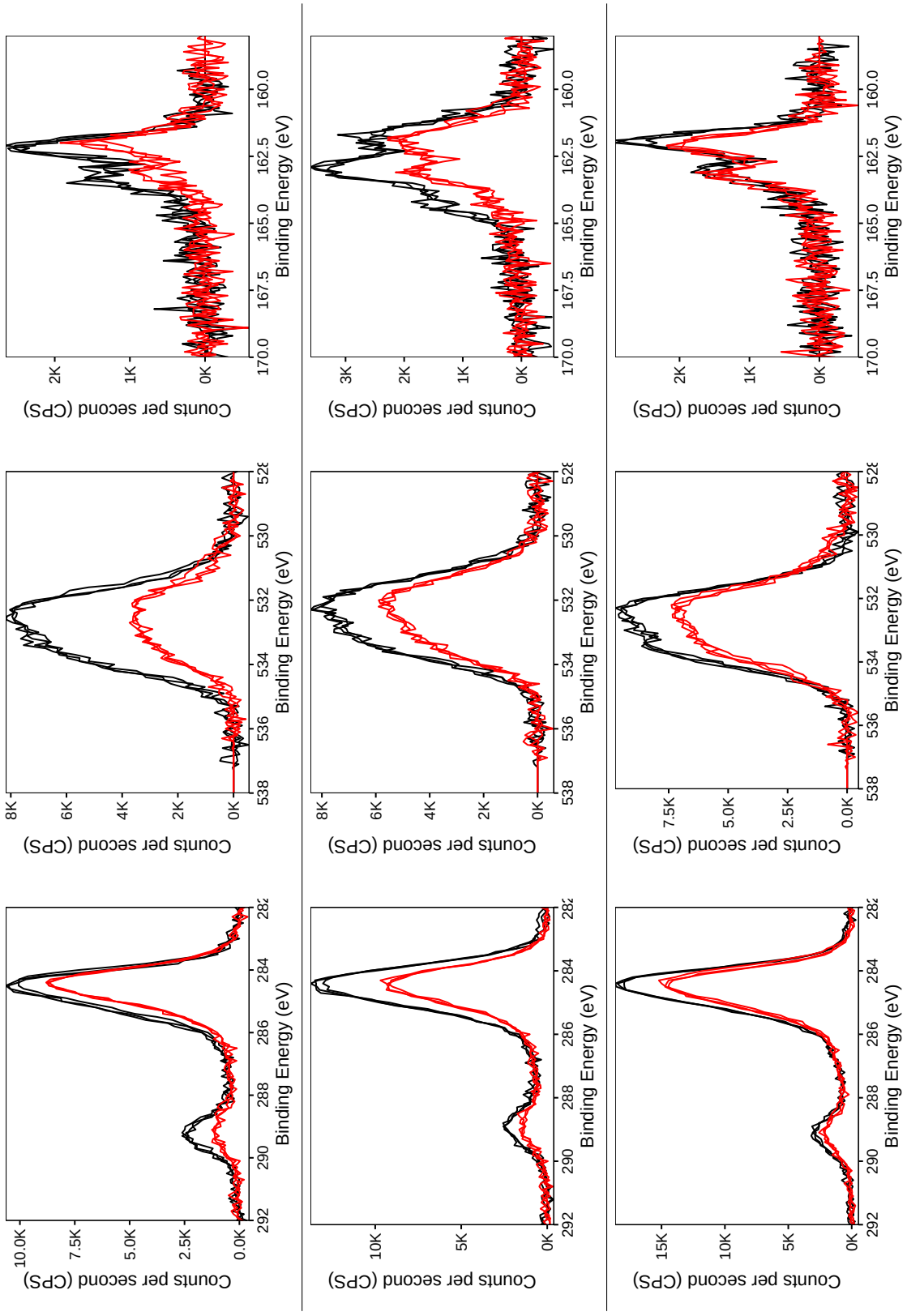

FIGURE 5.4: XPS spectra of fresh (in black) and UV treated in acid (in red) SAMs. Spectra correspond to S 2p (top row), O 1s (middle row) and C 1s (bottom row) of **MHA SAM** (left column), **ALA SAM** (middle column) and **MOA SAM** (right column). Multiple spectra were recoded for each state of each SAMs.

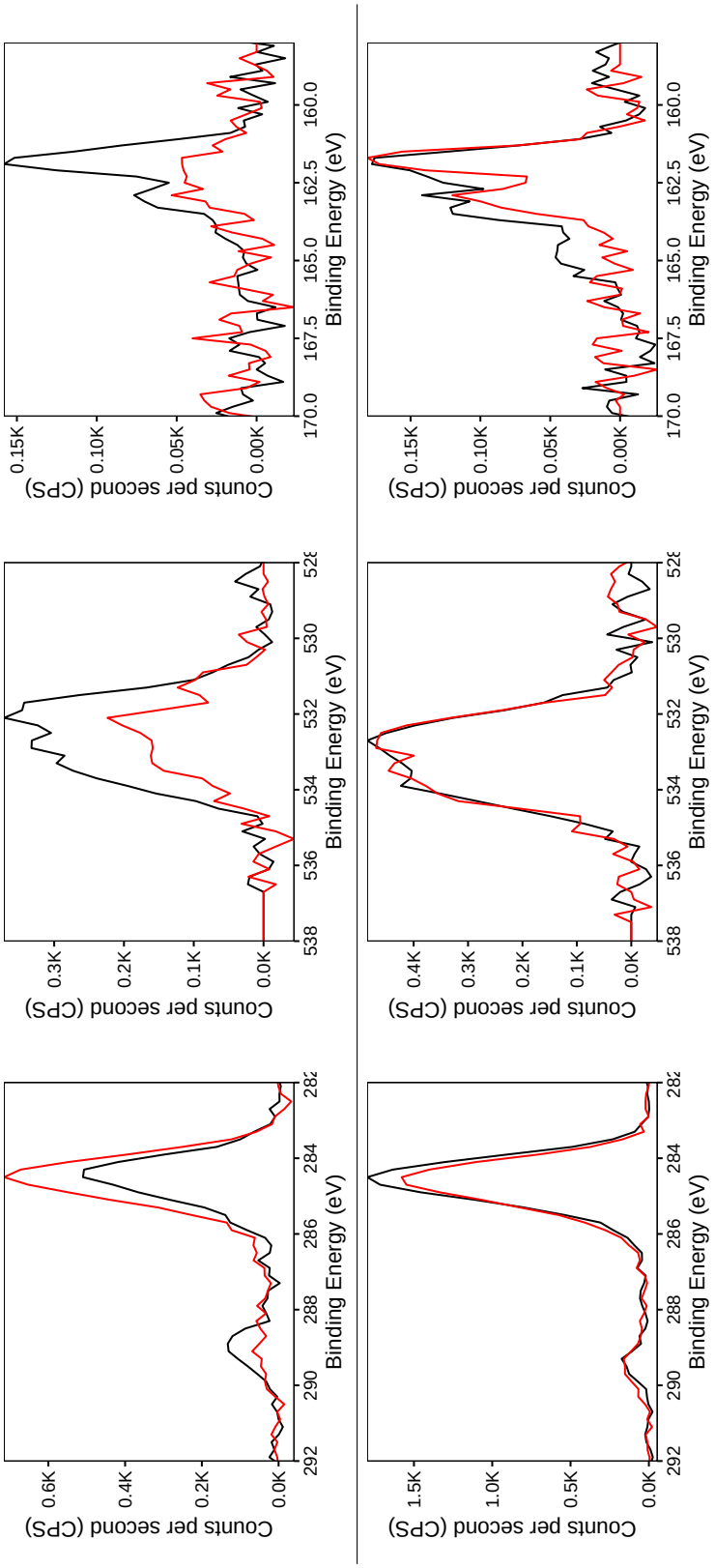

FIGURE 5.5: XPS spectra of fresh (in black) and UV treated in acid (in red) SAMs. Spectra correspond to S 2p (top row), O 1s (middle row) and C 1s (bottom row) of **DTBA SAM** (left column) and **MUA SAM** (right column).

XPS spectra in figures 5.4 and 5.5 reveal that instability of molecules under soft UV (365 nm) irradiation in acid is a common issue among COOH SAMs, but only affects thin monolayers. For example, figure 5.5 shows no substantial change in **MUA SAM**, but a diminishing of the peaks, especially those related to carboxylic acid and thiolate groups, in **DTBA SAM**. Moreover, treated **DTBA SAM** also yields a relative increase of alkyl carbon, usually associated with adventitious hydrocarbons, and the appearance of oxidised sulfur species. Figure 5.4 clearly indicates that the severity of fractional loss gradually increases with decreasing SAM thickness, i.e. **MHA SAM** is affected more (∼50 % left) than **MOA SAM** (∼80 % left), while **ALA SAM**, which yields intermediate thickness, shows an average stability of the two (∼65 % left).

Quantitative analysis of stability of the SAMs, based on integrated peak areas, is summarised in table 5.2. It shows that alkyl carbon does not decrease as much as other chemical species in **MHA SAM**, i.e. its relative amount increases, which is an indication of increasing levels of adventitious hydrocarbons, but not as much as in **DTBA SAM**. Although visual differences in spectra in figures 5.4 and 5.5 suggest that **MHA SAM** is more stable than **DTBA SAM**, the tabulated data suggest that **DTBA SAM** and **MHA SAM** have a similar stability. However, this quantitative analysis could overestimate the stability of **DTBA SAM** due to weaker peaks and lower signal-to-noise ratio in spectra of fresh **DTBA SAM** than **MHA SAM**, all of which limit accuracy of the fitted components. Nevertheless, the rest of the data in tabulated and plotted forms (figures 5.6a and 5.6b) show the same trend as spectra in figures 5.4 and 5.5.

TABLE 5.2: Fraction of chemical elements and their species left in **DTBA SAM**, **MHA SAM**, **ALA SAM**, **MOA SAM** and **MUA SAM** after the soft UV treatment in the acidic catalyst. *Analysis is based on XPS spectra normalised to have equal Au $4f_{7/2}$ peak areas before and after the treatment, therefore, amount of gold stays at 100 %.*

	Carbon			Oxygen			Gold	Sulfur
SAM	C=O	C-C C=C	Total	C=O	C-O	Total	Total	Total
DTBA SAM+UV$^{HCl}_{1.5\,h}$	50%	153%	118%	41%	61%	48%	100%	47%
MHA SAM+UV$^{HCl}_{1.5\,h}$	51%	88%	74%	41%	51%	45%	100%	50%
ALA SAM+UV$^{HCl}_{1.5\,h}$	63%	66%	68%	72%	64%	69%	100%	58%
MOA SAM+UV$^{HCl}_{1.5\,h}$	76%	82%	80%	80%	77%	79%	100%	76%
MUA SAM+UV$^{HCl}_{1.5\,h}$	103%	87%	94%	101%	101%	104%	100%	92%

UV refers to soft UV (365 nm, 4 mW cm^{-2}).

HCl (superscript) refers to acid catalyst 100 mM HCl in IPA.

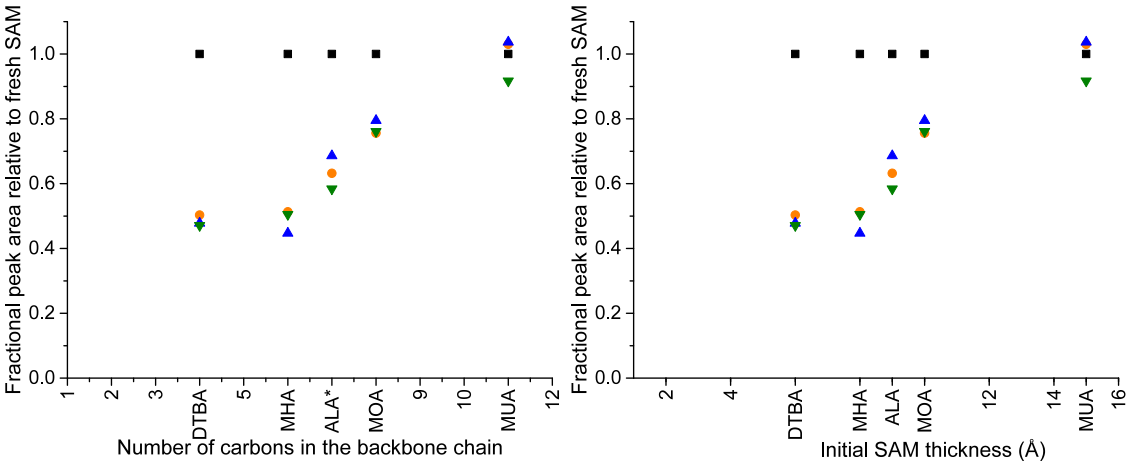

(A) Based on number of carbons (B) Based on initial SAM thickness

FIGURE 5.6: Fractions of carbonyl (C=O) carbon (yellow circles), total oxygen (blue triangles pointing up) and total sulfur (green triangles pointing down) left in **ALA SAM**, **DTBA SAM**, **MHA SAM**, **MOA SAM**, and **MUA SAM** after exposure to soft UV (365 nm, 4 mW cm^{-2}, 1.5 h) in the acidic catalyst (100 mM HCl in IPA) are plotted against a) number of carbons in the chain and b) initial SAM thickness. ALA is assigned an average chain length of 7 carbons. Analysis is based on XPS spectra normalised to have equal Au $4f_{7/2}$ peak areas before and after the treatment, therefore, amount of gold (black squares) stays at 100 %, which also visually indicates the expected level of chemical elements and their species for the SAMs that do not exhibit loss of surface coverage.

5.1.4 Photo-patterning and selective metallisation

Following the photo-sensitivity study, the suitability of short chain COOH-terminated SAMs for photo-patterning and selective metallisation with copper were investigated. All samples were photo-patterned in the same way as **SAM1** discussed in section 3.3 in chapter 3, i.e. samples were irradiated through a chromium mask under an optical microscope with soft UV (365 nm, 22 J cm^{-2}, 36 mW cm^{-2}, 10 min), unless stated otherwise. A chromium mask was separated from a sample using organic spacers with thicknesses varying from a few to tens of microns, in order to prevent mechanical damage and to accommodate the acidic catalyst (100 mM HCl in IPA). Electrochemical deposition (ECD) was used to deposit copper on the samples at constant or sweeping (10 mV s^{-1} scan rate) potentials in the range of 0.0 to −0.3 V in 10 mM $CuSO_4$ in 10 mM H_2SO_4 electrolyte. All potentials stated in this section are referenced to Ag/AgCl.

Optical images in figure 5.7 indicate that only **ALA SAM** yield a reasonable pattern for selective copper deposition at constant (−0.1 V) or sweeping (0.4 to −0.3 to 0.0)V potential. None of the other SAMs show any sign of selective metallisation by sweeping potential, while **DTBA SAM** and **MHA SAM** yield copper on photo-patterned regions after deposition at a constant potential (−0.1 V), but metallisation is not uniform across the whole sample or selectivity is poor.

Although, each (photo-patterned) SAM yield slightly different peak potential (E_p) values, optical images in figure 5.7 are representative of the findings: (i) **DTBA SAM** samples yield similarly poor selectivity at −0.02 V, −0.04 V and −0.08 V, (ii) **MHA SAM** sample showed little copper at −0.02 V and −0.04 V, some partial metallisation at −0.08 V and progressively less selective metallisation at −0.12 V and −0.15 V than at −0.10 V, finally (iii) **MOA SAM** samples showed small quantities of copper on the surface after deposition negative potentials of −0.04 V, −0.08 V, −0.10 V, −0.12 V, −0.15 V and −0.20 V, while −0.25 V and −0.30 V potentials led

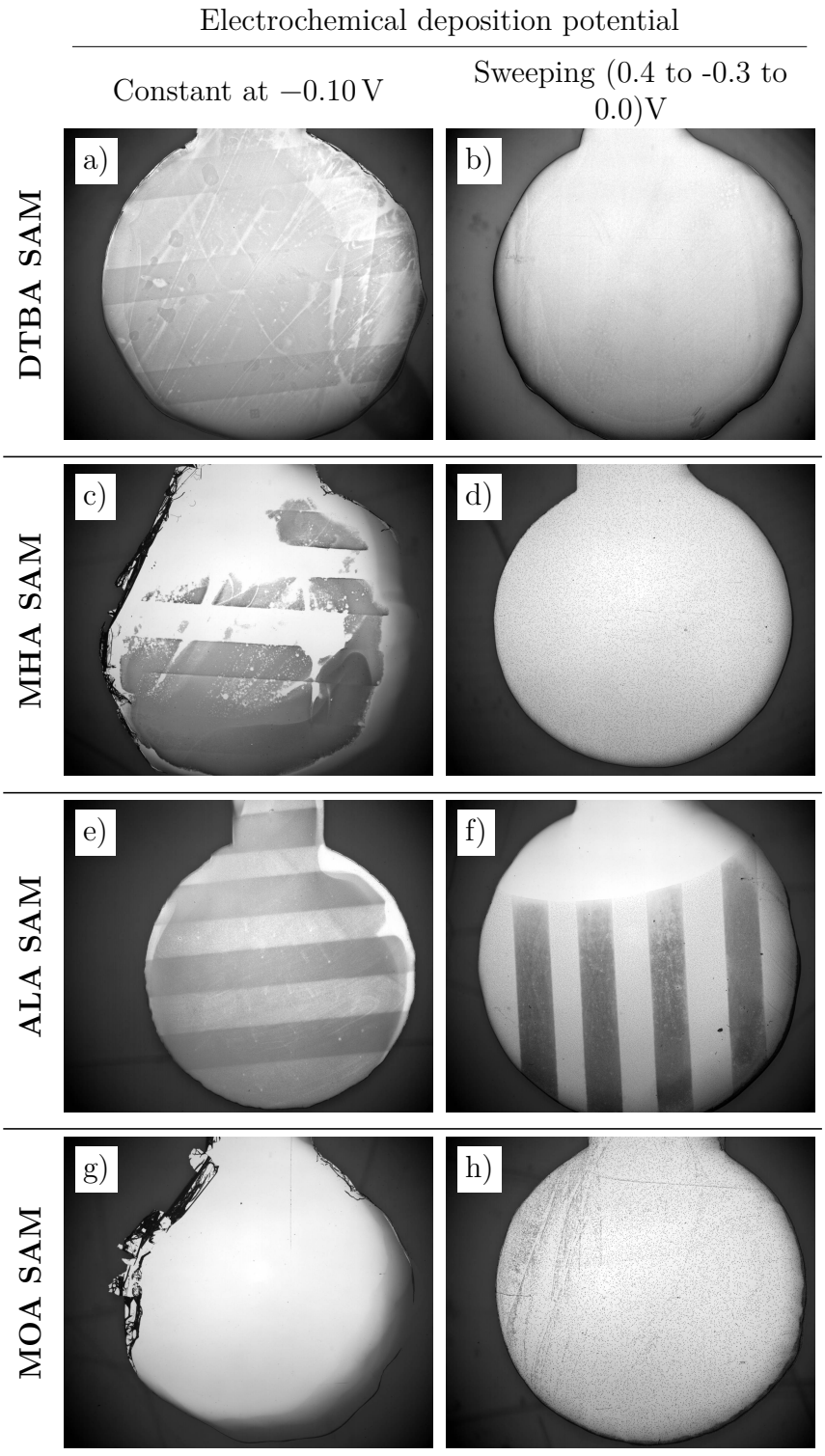

FIGURE 5.7: Optical images of photo-patterned (365 nm, 22 J cm^{-2}, 36 mW cm^{-2}, 10 min) and metallised a)-b)**DTBA SAM**, c)-d) **MHA SAM**, e)-f) **ALA SAM** and g)-h) **MOA SAM**. Copper was electrochemically deposited from 10 mM $CuSO_4$ in 10 mM H_2SO_4 electrolyte at a constant (−0.10 V, 20 s) (left column) or sweeping (0.4 to -0.3 to 0.0)V (right column) potential. Darker areas correspond to UV-treated regions and higher quantities of reduced copper.

to partial metallisation that did not resemble in any way the shape of the expected pattern. This contrasts with the highly selective metallisation of photopatterned **SAM1** in the range of −0.15 to −0.20 V.

Poor selectivity of metallisation is indicative of a small difference between E_p values of treated and non-treated regions, i.e. similarly low values in **DTBA SAM** and **MHA SAM**, but high in **MOA SAM**. High selectivity on **ALA SAM** could be indicative of the transition between high stability and packing of **MOA**-like SAM and low stability and packing of **MHA**-like SAM

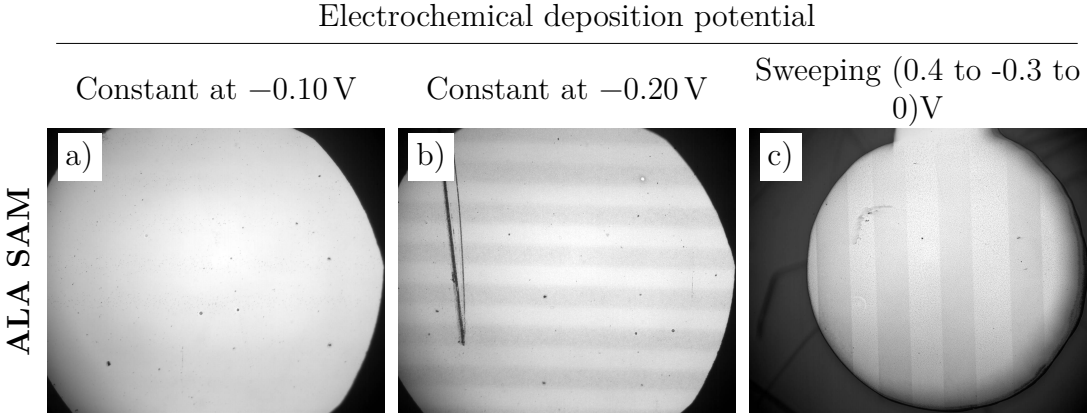

FIGURE 5.8: Optical images patterned **ALA SAM** samples. Despite identical procedures of photo-patterning (365 nm, 22 J cm^{-2}, 36 mW cm^{-2}, 10 min) and copper electrodeposition, figures a) and c) show significantly lower selectivity than figures 5.7e and 5.7f, respectively. Optical image of patterned **ALA SAM** after Cu deposition at constant potential of b) −0.20 V show slightly higher quality, but still much lower than in 5.7e.

However, photo-patterning of **ALA SAM** yields low reproducibility. A number of patterned **ALA SAM** samples led to poor copper selectivity following deposition at constant −0.10 V (figure 5.8a) and at sweeping (figure 5.8c) potentials. Slight improvements were obtained at more negative potentials of −0.20 V (figure 5.8b) and −0.25 V, but the overall quality of such patterns is much lower than shown in figure 5.7e or 5.7f. This could be indicative of the variation in SAM quality, for example, packing or cross-linking of the molecules, induced by slight variation of SAM formation conditions (i.e. SAM formation time, temperature).

5.1.5 Discussion

Fresh SAMs yield expected characteristics, except the advancing water contact angles (table 5.1). High advancing angle (45°) on **DTBA SAM** is an indication of substantially disordered SAM, which is also supported by the large hysteresis (∼40°) loop, and by the broad and weak double peak in IR spectra assigned to carbonyl (C=O) bond (1715-1740 cm^{-1} in figure 5.2). **MHA SAM**, **ALA SAM** and **MUA SAM** show slightly lower (∼30°), but still not the wetting angles reported for carboxylic acid (COOH) terminated SAMs. Since the SAMs do yield wetting angles for a receding water droplet, this is attributed to a slightly lower than optimum quality of COOH SAMs. It has been reported that COOH SAMs are highly sensitive to their formation conditions,[3–9] which were purposely not optimised in this study (i.e. formed from DCM rather than EtOH solution and without any additional acids) for the following two reasons: (i) to maintain consistency with **SAM1** formation conditions; and (ii) to form slightly disordered and less densely packed SAMs in order to have more accurate controls for the expected slightly disordered monolayer of lipoic acid resulting from photocleavage of bulky pyrene groups in **SAM1** (see chapter 3). Higher advancing (39°) and especially the receding (19°) angles on **MOA SAM** than **MHA SAM**, **ALA SAM** and **MUA SAM** are assigned to originate from adventitious hydrocarbon contamination, that COOH SAMs are prone to. Indeed, reproducibility of COOH SAMs with appropriate contact angles and ellipsometric thicknesses was low, and a number of samples were excluded as unreliable.

Exposure of **DTBA SAM** and **MHA SAM** to soft UV (365 nm, 4 mW cm^{-2}) for 1.5 h in acidic catalyst 100 mM HCl in IPA dramatically reduces thickness (to 2-3 Å) and turns surfaces from hydrophilic (typical for COOH groups) into hydrophobic (typical for adventitious hydrocarbons), as shown in table 5.1. Moreover, peaks associated with carbonyl C=O bond disappear in IR spectra (1715-1740 cm^{-1} in figure 5.2). All of the above suggest at least a partial loss of molecules in each

SAM. That is confirmed by XPS, which also indicates that molecules still present on the gold surfaces are intact and do not disintegrate, except for a weak signal in S 2p region associated with oxidised sulfur in treated **DTBA SAM**. Surprisingly, quantitative analysis of XPS data suggests that as much as ∼50 % of the molecules are still present in both SAMs (table 5.2). This suggests that the partial loss of the monolayers leads to a high disorder and an increases in tilt angle from the surface normal, which results in a more parallel alignment of the C=O bonds with the gold surface. Therefore, the stronger impact of the surface selection rule could lead to strongly suppressed and most likely undetectable signal in FT-IRRAS spectra, despite the presence of a fraction of molecules on the surface. XPS data also show a relative increase in alkyl carbon in both SAMs (table 5.2) indicating an increase of adventitious hydrocarbons, which are likely to cover the top of the disordered and poorly packed SAMs. That would prevent water droplets from interacting with hydrophilic COOH groups, and would explain the hydrophobic nature of the treated SAMs. This explanation is also in line with the fact that **DTBA SAM** shows higher increase of adventitious hydrocarbons and higher contact angles than **MHA SAM**. While for **DTBA SAM** ellipsometry also indicates that ∼50 % of molecules are left on the surface, for **MHA SAM** ellipsometry suggests that only ∼25 % of the initial monolayer is still present, which does not agree with the XPS data. However, ellipsometric thickness measurements are subject to limited accuracy and precision for values below 10 Å, and even more so for values below 5 Å, due to sample-to-sample variation and instrumental uncertainty of at least 1-2 Å, contamination layer of hydrocarbons few angstroms thick being always present on reference samples (freshly cleaned gold) that are exposed to ambient conditions,[1,2] and the fact that increasing adventitious contamination (as indicated by XPS) also contributes to the ellipsometry measurements. Therefore the actual thickness (or fraction of molecules on the surface) might be lower in **DTBA SAM** and higher in **MHA SAM** than indicated in table 5.1. On the other hand, visual comparison of XPS spectra of

fresh and treated **DTBA SAM** in figures 5.5 and C.1 indicate that less than 50 % of carbonyl carbon and sulfur is left on the surface, which suggests that quantitative analysis of **DTBA SAM** might overestimate the amount of molecules left in the SAM due to weak and broaden peaks, in addition to low signal-to-noise ratio. Finally sample-to-sample variation was observed and attributed to slight changes in SAM formation conditions (e.g. immersion time and ambient temperature) and photo-deprotection conditions (e.g. UV intensity at the sample) that might affect SAM stability and severity of the SAM removal, respectively.

In contrast to thin **DTBA SAM** and **MHA SAM**, the thick **MUA SAM** does not yield any substantial change in ellipsometric thickness (table 5.1) or XPS spectra (figures 5.5 and C.4) following the analogous UV treatment. Nevertheless, receding and advancing contact angles increase (table 5.1) and reach similar values to those of treated **ALA SAM** and **MOA SAM**. The increase in advancing angle in **ALA SAM**, **MOA SAM** and **MUA SAM** is mainly associated with esterification of small fraction of COOH by the HCl acid, which has been reported to take place on a comparable time scale.[3,4] On the other hand, low receding angles indicate presence of the COOH groups, and the resulting high hysteresis (∼45°) confirms chemical heterogeneity at the surface of the SAMs.

XPS data of slightly thinner **MOA SAM** indicate that ∼80 % of intact molecules stay in the SAM upon the UV treatment. This is in agreement with slight changes of the double peak in IR spectra (1715-1740 cm^{-1} in figure 5.2), however, the fact that no changes are detected by the ellipsometry is attributed to a combination of the instrumental uncertainty and sample-to-sample variation. Lower loss of molecules in **MOA SAM** than in **DTBA SAM** and **MHA SAM** is attributed to suppressed penetration of the catalyst to the gold-SAM interface by the higher thickness and better packing in **MOA SAM** due to stronger van der Waals interaction originating from longer alkyl chains. The fact that **MOA SAM** preserves most of its properties,

despite the 20 % loss of molecules, could be indicative that van der Waals interaction is strong enough to keep the resulting monolayer together.

Some of the effects of the treatment on **ALA SAM** are intermediate of those observed for **MHA SAM** and **MOA SAM**: (i) intensity of carbonyl (C=O) double peak in IR spectra (1715-1740 cm^{-1} in figure 5.1) drops to ∼45 % of its initial value, which is around the midpoint between the observed small changes in **MOA SAM**, but complete disappearance in **MHA SAM**; (ii) XPS data suggest that ∼65 % of the monolayer stays on the surface, which again is the mid-point between ∼50 % and ∼80 %. On the other hand, in contrast to **MHA SAM**, XPS data of **ALA SAM** do not show any substantial increase in adventitious hydrocarbons (table 5.1), and yield contact angles similar to those of hydrophilic **MOA SAM** and **MUA SAM** rather than those of **MHA SAM** (table 5.1). Although the dramatic drop in thickness (to 3 Å) is similar to that of **MHA SAM** and **DTBA SAM**, as discussed earlier, ellipsometry measurements in this range requires cautious interpretation due to limited accuracy and low fractional precision. Overall, **ALA SAM** retains most of its properties, despite the fact that its stability is intermediate when compared to **MHA SAM** and **MOA SAM**.

The fact that FTIR and XPS indicate a gradual increase in stability with increasing ellipsometric thickness of the fresh SAMs, and that the trend is linear (figure 5.4) in the range of **MHA SAM**, **ALA SAM** and **MOA SAM**, suggest that the primary reason for the loss of molecules in **ALA SAM** is its thin thickness rather than its unconventional dithiolane head group. Nevertheless, XPS does indicate that dithiolane head group lowers the stability, because S 2p regions clearly show higher fractional loss of unbound sulfur (or disulfide) than bound to gold sulfur (figure 5.3).

It is not surprising that fresh **ALA SAM** shows intermediate thickness (table 5.1) when compared to fresh **MHA SAM** and **MOA SAM**. **Lipoic acid** can bind to

gold through just one sulfur atom, that leads to **MHA**-like or **MOA**-like configuration depending on which sulfur atom does bind to the surface. Assuming near equal proportions of the two, the resulting monolayer could be treated as an equimolar SAM of **MHA** and **MOA**. Of course, fresh **ALA SAM** is likely to have a complexity similar to that proposed for **SAM1** in figure 3.12, which includes both molecules that are cross-linked (figure 3.10) and molecules that are bound to gold surface via both sulfur atoms.

Selective metallisation following photo-patterning of **DTBA SAM**, **MHA SAM**, **ALA SAM**, **MOA SAM** and **MUA SAM** under the same conditions as **SAM1** (see section 3.3) revealed that only **ALA SAM** can produce copper patterns (figures 5.7e and 5.7f) of comparable quality to **SAM1** (figures 3.15b, 3.16c and 3.18c). Although deposited copper on **DTBA SAM** and **MHA SAM** does show a pattern, selectivity on the former is low (figure 5.7a), while surface coverage on the latter is poor (figure 5.7c). Moreover, only electrochemical deposition at constant potentials lead to appearance of the patterns, while sweeping potential method leads to a uniform copper coverage (figures 5.7b and 5.7d). Metallised pattern on **MOA SAM** has not been observed at all, despite ECD at sweeping potential or at constant potentials of up to $-0.30\,\mathrm{V}$, which is significantly more negative than optimum potentials for patterned **ALA SAM** (-0.10 to $-0.20\,\mathrm{V}$) or **SAM1** (-0.16 to $-0.20\,\mathrm{V}$). In contrast to **SAM1**, reproducibility of metallised patterns on **ALA SAM** is low (figure 5.8), while optimum deposition parameters vary from sample to sample. Poor quality of copper deposition on photo-patterned **DTBA SAM** and **MHA SAM** most likely results from small difference in E_p values between the treated and non-treated regions, which are attributed to relatively high disorder in non-treated regions anyway. On the other hand, little copper is observed on **MOA SAM** due to its higher E_p value, that indicates higher order in the SAM, which does not decrease significantly upon the UV treatment. The possibility to produce selective metallisation on patterned **ALA SAM** is attributed to the fact that the SAM can

accommodate both **MHA**-like disordered and **MOA**-like ordered state, but also to the loss of cross-linked molecules due to UV exposure in acid. However, slight changes in **ALA SAM** formation condition (e.g. immersion time, ambient temperature) could lead to stronger **MHA**-like or **MOA**-like character and also affect the extent of cross-linking, all of which affect the stability of the SAM and therefore the level of disorder induced by the UV irradiation in acid.

Overall, this study revealed that thin COOH-terminated SAMs (i.e. **DTBA SAM**, **MHA SAM**, **ALA SAM** and **MOA SAM**) have limited stability, while thick **MUA SAM** is not affected under UV irradiation in the acidic conditions. Instability of **ALA SAM** is attributed mostly to its short chain length, and partially to the cross-linking of its dithiolane head groups. Consequently, acidic catalysts for the photo-deprotection of such SAMs should be used with caution. On the other hand, this study suggests that reducing density of molecules and increasing disorder in a SAM might be equally, or even more, beneficial than reducing SAM thickness, in order to achieve high selective metallisation by electrochemical deposition, as demonstrated on photo-patterned **SAM1** in chapter 3.

5.1.6 Conclusions

The stability of carboxylic acid (COOH) terminated SAMs under irradiation of soft UV in an acidic catalyst was investigated. A range of COOH SAMs with varying thickness were exposed to UV light (365 nm, 4 mW cm^{-2}) for 1.5 h in 100 mM HCl in IPA, and characterised with ellipsometry, wetting measurements, FTIR and XPS. It was found that thin SAMs show limited stability under such condition. The instability of the SAMs results in the removal of intact molecules from the gold surface rather than their partial disintegration on the surface. It was observed that the severity of a loss of molecules increases gradually, as the thickness of COOH SAMs decreases, i.e. **DTBA SAM** and **MHA SAM** yield at least 50 % loss, while **MUA SAM** does not show any detectable signs of instability. Furthermore, FTIR and XPS data suggest a linear trend between fractional loss of molecules and initial SAM thickness in the range of **MHA SAM**, **ALA SAM** and **MOA SAM**. Consequently, the instability of **ALA SAM** is primarily assigned to its low thickness, and also partially attributed to the detected cross-linking of dithiolane head groups. Therefore, acidic catalyst should be used with caution in photo-deprotections of thin (i.e. alkyl chain consists of fewer than 10 -CH_2- units) COOH-terminated monolayers.

Subsequently, the suitability of the unstable COOH-terminated SAMs for photo–patterning and metallisation was investigated. It was observed that only **ALA SAM** yield patterns of selective metallisation with comparable quality to **SAM1**. However, the sample-to-sample reproducibility is poor and not even remotely comparable to **SAM1** system. Nevertheless, this study has revealed that reducing the packing and ordering of molecules within a SAM might be equally, or maybe even more, beneficial than reducing SAM thickness by photocleavage, in order to achieve high selectivity of metallisation, as demonstrated on **SAM1** in chapter 3.

5.2 Azide-terminated SAMs for click chemistry on a surface

Self-assembled monolayers (SAMs) of functionalised long-chain alkanethiolates (LCATs) on metals[28] is a versatile platform for selective immobilisation of molecules, biological species or nanoparticles. SAMs used for biological applications usually require incorporation of oligoethylene glycol (OEG) units to reduce non-specific protein adsorption.[29] Furthermore, SAM-based studies usually investigate more than just one-type SAM system, while some applications require more than just a single functional group within a SAM.[30–32] Thus, if it is required to fine-tune surface chemistry for the control of immobilisation, density and orientation of the active sites, it is essential to have an easy access to a variety of functional groups. However, commercial availability of long-chain alkanethiolates incorporating oligoethylene glycol units (LCAT-OEGs) with various functional groups is severely limited, while their synthesis tends to be strenuous.

This chapter presents the characterisation of SAMs formed using molecules synthesised[c] by a new versatile solid phase synthesis approach that gives access to a range of functionalised LCAT-OEGs. This is achieved through a minimised intermediate purification and a flexible late-stage functionalisation, which is ideal for applications requiring quick and iterative fine-tuning of SAM properties.

To demonstrate the available versatility, three molecules **reagent 2**[c] (figure 5.9a), **LCAT-OEG-4**[c] (figure 5.9c) and **LCAT-OEG-1**[c] (figure 5.9e) containing a number of functionalities are investigated. Firstly, all three molecules contain amide as linker, which has been reported to improve the stability of a SAM due to formation

[c] Synthesised by J. Murray at R. S. Bon research group, School of Chemistry, University of Leeds, UK. Procedure described in the reference[33].

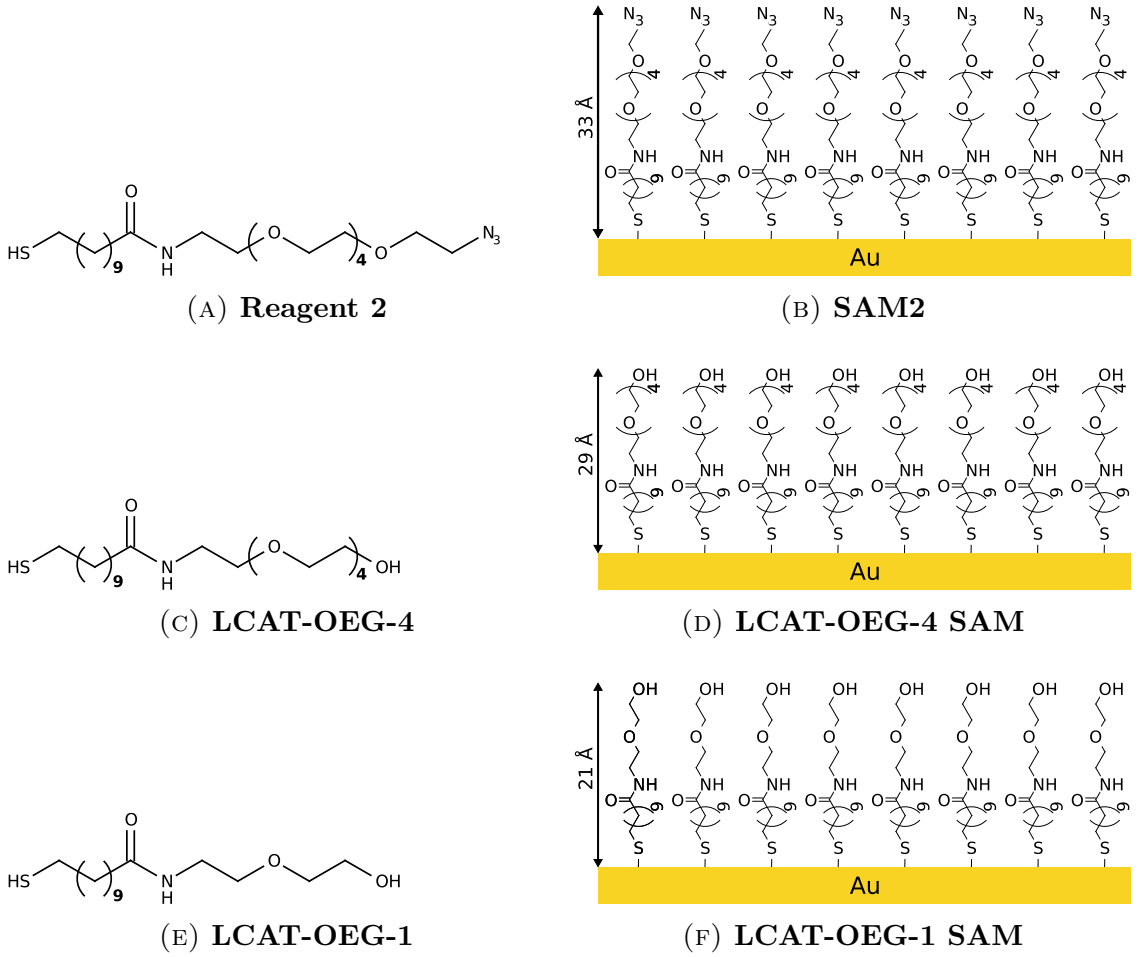

(A) **Reagent 2** (B) **SAM2**

(C) **LCAT-OEG-4** (D) **LCAT-OEG-4 SAM**

(E) **LCAT-OEG-1** (F) **LCAT-OEG-1 SAM**

FIGURE 5.9: Molecular structures of reagent molecules[c] and their corresponding SAMs.

of hydrogen bonds between the chains.[34,35] Secondly, molecules incorporate different number of ethylene glycol units, that are used to prevent non-specific binding of biological macromolecules such as proteins.[29] Finally, **LCAT-OEG-4** and **LCAT-OEG-1** contain alcohol end group, while **reagent 2** contains azide functional group to facilitate click chemistry[36] on the surface. As discussed in the 'Introduction' chapter, click chemistry[36] is a quick, reliable, efficient, biocompatibile, highly selective and versatile method to join two units together,[36–40] which is applied in material science,[41–43] biosciences,[30,41,42,44–48] and drug developement.[41,42,44,48,49] Also, it has been shown to be particularly useful for performing reactions on a surface[50] and for SAM based applications[30–32,50–56] (see section 1.4 in the 'Introduction' chapter for more details).

The rest of this section is split into three parts. The first part shows that the above discussed molecules form dense, ordered and high quality **SAM2** (figure 5.9b), **LCAT-OEG-4 SAM** (figure 5.9d) and **LCAT-OEG-1 SAM** (figure 5.9f). The second part demonstrates that the amount of **reagent 2** in a SAM can be successfully reduced by the addition of diluent **LCAT-OEG-4** or **LCAT-OEG-1**. It is also shown that molar concentration of **reagent 2** in a SAM can be easily predicted. Finally, the third part demonstrates that **SAM2** successfully performs click chemistry to yield high surface coverage of amine terminated **strained cyclooctyne**[d] (figure 5.10a) in aqueous catalyst-free solution under ambient conditions.

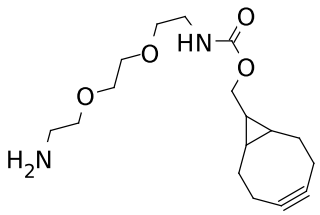

(A) **strained cyclooctyne**

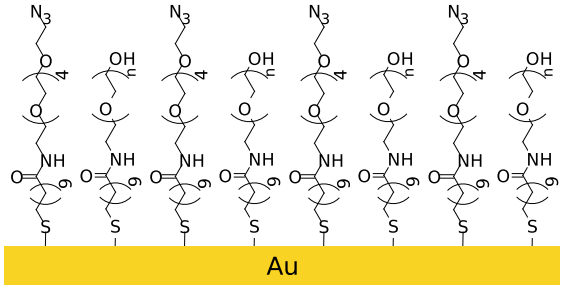

(B) Mixed SAM of **reagent 2** with **LCAT-OEG-4** (n=4) or **LCAT-OEG-1** (n=1)

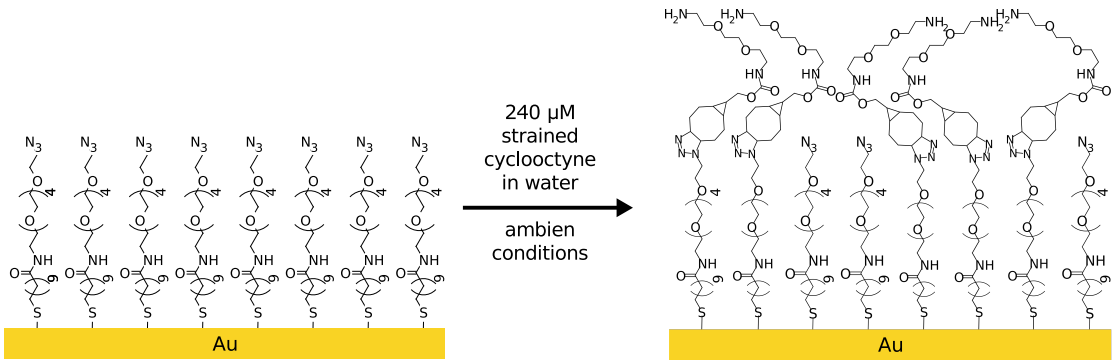

(C) Click reaction: catalyst-free strain-promoted azide-alkyne cycloaddition

FIGURE 5.10: Molecular structure of **strained cyclooctyne**[d] and schematic diagrams of mixed SAMs and click reaction on **SAM2**. The chain in **strained cyclooctyne** is bent for presentation purposes only.

[d] Synthesised by J. Murray at R. S. Bon research group, School of Chemistry, University of Leeds, UK.

5.2.1 Pure SAM2, LCAT-OEG-4 SAM and LCAT-OEG-1 SAM

This section discusses fabrication and characterisation of **SAM2** using ellipsometry, contact angle, FTIR and XPS measurements. Additionally SAMs formed by diluents **LCAT-OEG-4** and **LCAT-OEG-1** are investigated, in order to obtain reference spectra for the study of mixed SAMs discussed in section 5.2.2. **LCAT-OEG-4** was chosen due to its very similar molecular structure and composition to **reagent 2**, which should mix well, while the shorter **LCAT-OEG-1** was chosen because it is more distinguishable with spectroscopic techniques, even though it might not mix as well.

5.2.1.1 Ellipsometry and Wetting measurements

Wettability data and thickness obtained from ellipsometry measurements of pure **SAM2**, **LCAT-OEG-4 SAM** and **LCAT-OEG-1 SAM** are shown in table 5.3. Expected[e] thickness values of **SAM2** and **LCAT-OEG-1 SAM** agree with the ellipsometric thickness values within their uncertainty. **LCAT-OEG-4 SAM**, however, yields a 10 % higher value than expected, which can be indicative of 15° instead of 30° tilt angle from the surface normal, or the more likely case of some adventitious contamination attracted by the high energy of the alcohol (-OH) terminated surface. **LCAT-OEG-4 SAM** and **LCAT-OEG-1 SAM** yield similar hydrophilic contact angles that are comparable to those reported in the literature,[57] while **SAM2** shows lower angles than reported,[58] which is attributed to the hydrophilic OEG chain below the azide end group. Low contact angle hysteresis (∼11°) is comparable to that of **C18 SAM** (∼8°) and indicative of a high order and packing in the SAMs, which is in agreement with the ellipsometry data.

[e] See footnote [a] on page 166.

TABLE 5.3: Ellipsometric thickness and contact angles of pure (non-mixed) **SAM2**, **LCAT-OEG-4 SAM** and **LCAT-OEG-1 SAM**.

SAM	Ellipsometric thickness (Å)		Water contact angles (°)		
	Measured	Expected[e]	Advancing	Receding	Hysteresis
C18 SAM	22 ± 2	22	111 ± 1	103 ± 2	8
SAM2	34 ± 1	33	58 ± 3	46 ± 2	12
LCAT-OEG-4 SAM	32 ± 1	29	39 ± 2	30 ± 1	9
LCAT-OEG-1 SAM	23 ± 2	21	38 ± 1	25 ± 4	13

- Ellipsometric thickness was obtained using refractive index of 1.45 in Cauchy's equation.
- Uncertainties refer to whichever is the larger (i) standard deviation of sample-to-sample values or (ii) average of standard deviations from each sample (originating from variation in a single measurement or measurement-to-measurement).

5.2.1.2 XPS

X-ray Photoelectron Spectroscopy (XPS) measurements were carried out to obtain additional chemical information of the pure SAMs, and to characterise differences in chemical composition. The latter is important for quantifying the mixing of **reagent 2** with **LCAT-OEG-4** or **LCAT-OEG-1** in SAMs which is presented in the following sections. Binding energies are referenced to alkyl carbon in C 1s at 284.9 eV and spectra are scaled so that intensity of alkyl carbon component in C 1s in each set of measurements would reach the same (arbitrary chosen[f]) value.

Figure 5.11 shows the spectra of **SAM2** with fitted components, which are at the same positions in the spectra of **LCAT-OEG-4 SAM** and **LCAT-OEG-1 SAM**, except the peaks due to azide group in N 1s. The component at 400.1 eV in the N 1s region is attributed to the amide group.[20] Additional peaks at 401.7 eV and 405.2 eV are detected only in **SAM2** spectra and correspond to lateral and central (electron-deficient) nitrogen in azide group, respectively, with the latter peak

[f]The arbitrary value, in fact, corresponds to initial intensity of alkyl carbon component in C 1s in one of the samples.

being (2.1 ± 0.3) times smaller in area than the former, all in agreement with literature (once discrepancies due to different spectra referencing methods are taken into account).[20,21,58] A substantial drop in intensity of 401.7 eV and 405.2 eV peaks, indicating up to ∼60 % loss of azide group, was observed, while signal of other peaks (i.e. amide peak in N 1s, other peaks in C 1s and O 1s) did not change. However, acquisition parameters have been improved to limit degradation of azide group to ∼20 %, for more details please see section C.5. Spectra of C 1s can be fitted with three components corresponding to alkyl carbon at 284.9 eV,[12,20,59] carbon in OEG chain (C-O) and bound to nitrogen (C-N) at 286.9 eV,[20,22,59] and carbonyl carbon (C=O) in amide group at 288.3 eV.[20,22] Spectra of O 1s can be fitted with two components corresponding to carbonyl oxygen in amide group at 531.8 eV[20,22] and oxygen in OEG chain (C-O) at 533.4 eV.[16,20,22] Finally, S 2p region shows strong presence of the spin-orbit doublet at 161.8 eV (S $2p_{3/2}$) and 163.0 eV (S $2p_{1/2}$) assigned to thiols bound to gold (thiolates),[1,12,23,24] while the weak spin-orbit doublet at 163.4 eV (S $2p_{3/2}$) and 164.6 eV (S $2p_{1/2}$) are assigned to thiols not bound to gold.[25–27]

TABLE 5.4: Relative ratios of chemical elements and their species in pure **SAM2**, **LCAT-OEG-4 SAM** and **LCAT-OEG-1 SAM** based on integrated and normalised (using R.S.F.) peak areas in XPS spectra of C 1s, N 1s and Au 4f regions. *Alkyl carbon in C 1s is set to be equal to 10 in all of the spectra, because that is the amount of such atoms in all of the molecules. Uncertainties are presented in table C.1 in the appendix.*

	Carbon				Nitrogen	Gold
SAM	C=O	C-O C-N	C-C	Total	Total	Total
SAM2	1.7	12.8	**10**	24.6	3.5	15.7
*Expected**	*1*	*12*	*10*	*23*	*4*	
LCAT-OEG-4 SAM	1.5	11.0	**10**	22.6	1.1	15.9
*Expected**	*1*	*10*	*10*	*21*	*1*	
LCAT-OEG-1 SAM	1.6	4.1	**10**	15.7	1.2	14.9
*Expected**	*1*	*4*	*10*	*15*	*1*	

* Expected values based on the corresponding molecular structures shown in figures 5.9.

TABLE 5.5: Relative ratios of chemical elements and their species in pure **SAM2**, **LCAT-OEG-4 SAM** and **LCAT-OEG-1 SAM** based on integrated and normalised (using R.S.F.) peak areas in XPS spectra of O 1s and S 2p regions. *Alkyl carbon in C 1s is set to be equal to 10 in all of the spectra, because that is the amount of such atoms in all of the molecules. Uncertainties are presented in table C.1 in the appendix.*

	Oxygen			Sulfur
SAM	C=O	C-O	Total	Total
SAM2	1.0	5.1	6.1	0.7
*Expected**	*1*	*5*	*6*	*1*
LCAT-OEG-4 SAM	1.0	5.0	6.1	0.7
*Expected**	*1*	*5*	*6*	*1*
LCAT-OEG-1 SAM	1.0	1.9	2.9	0.7
*Expected**	*1*	*2*	*3*	*1*

* Expected values based on the corresponding molecular structures shown in figures 5.9.

Relative ratios (normalised to alkyl carbon component in C 1s) of chemical elements and their species in the SAMs are summarised in tables 5.4 and 5.5. As shown in the tables, the relative ratios are in a good agreement with the expected values based on molecular structure (figures 5.9), except the lack (∼30 %) of sulfur in all of the SAMs attributed to signal attenuation, and the excess (∼60 %) of carbonyl carbon in amide group. Almost identical ratios are obtained when XPS data are normalised to the carbonyl oxygen component in O 1s. The spectra in figure 5.12 visualise the differences between the pure SAMs, which are used to determine the fraction of **reagent 2** in the mixed SAMs in later sections. **SAM2** and **LCAT-OEG-4** yield substantially different N 1s spectra, but the difference in C 1s is rather subtle originating from a 9 % change in the amount of carbon, which is comparable to the deviation (see table C.1) between the spectra. On the other hand, **SAM2** and **LCAT-OEG-1 SAM** yield significantly different spectra in the N 1s, C 1s and O 1s regions.

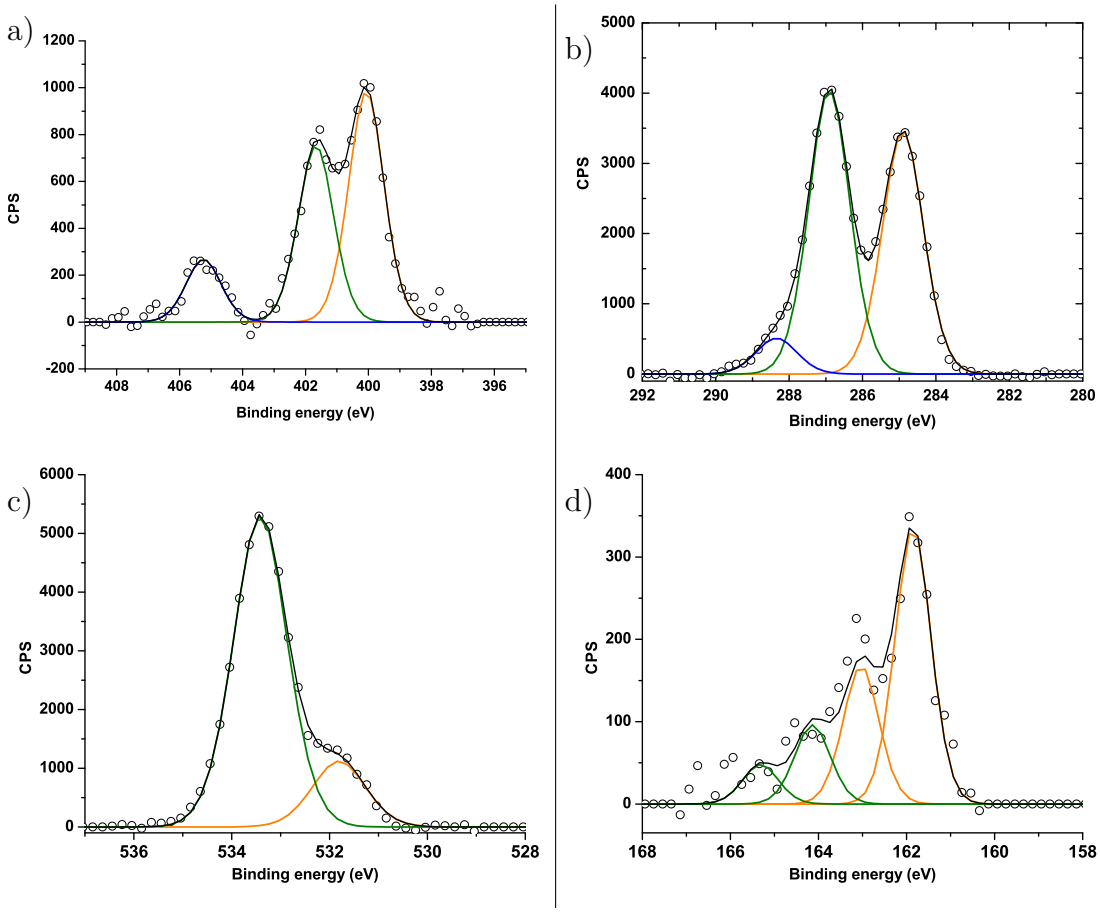

FIGURE 5.11: XPS spectra with fitted components of a) N 1s, b) C 1s, c) O 1s and d) S 2p regions of **SAM2**.

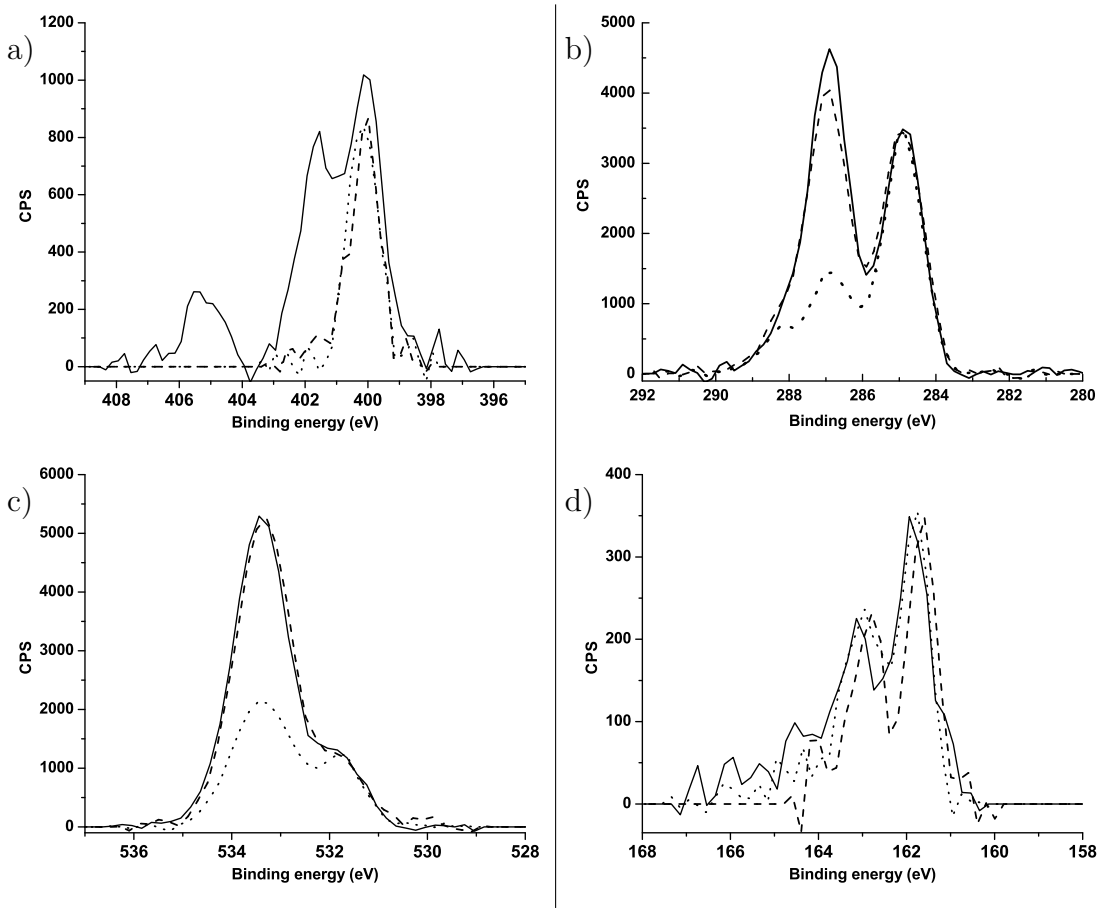

FIGURE 5.12: Overlaid XPS spectra of a) N 1s, b) C 1s, c) O 1s and d) S 2p regions of **SAM2** (solid line), **LCAT-OEG-4**(dashed line) and **LCAT-OEG-1** (dotted line).

5.2.2 Mixed SAM2

For certain applications, it is important to control the density of immobilised species. If immobilisation is based on specific chemical interactions, the density of bound species can be controlled by controlling the number of chemically active sites on the surface. In the case of click chemistry on **SAM2**, the active sites are the azide groups. Therefore, the ability to predict or fabricate surfaces with a desired concentration of azide groups is of great importance. Consequently, this section presents a study on mixing **reagent 2** with diluents **LCAT-OEG-4** and **LCAT-OEG-1** in the SAM environment. $\mathbf{SAM2}_{50\%}^{OEG4}$ and $\mathbf{SAM2}_{19\%}^{OEG4}$ were formed from EtOH solution of **LCAT-OEG-4** containing 50 % and 19 % molar fractions of **reagent 2** respectively. In the same manner $\mathbf{SAM2}_{50\%}^{OEG4}$ and $\mathbf{SAM2}_{19\%}^{OEG4}$ were formed, but **LCAT-OEG-1** was used instead of **LCAT-OEG-4**.

5.2.2.1 Ellipsometry and Wetting measurements

Wettability data and thickness obtained from ellipsometry measurements of pure **SAM2**, **LCAT-OEG-4 SAM** and **LCAT-OEG-1 SAM** are shown in table 5.6. Ellipsometry data do not show any clear trends of mixing (figure 5.13a), in fact $\mathbf{SAM2}_{50\%}^{OEG4}$ and $\mathbf{SAM2}_{19\%}^{OEG4}$ yield 6-26 % higher thickness values than pure **SAM2**. Similarly, thickness values of $\mathbf{SAM2}_{50\%}^{OEG1}$ and $\mathbf{SAM2}_{19\%}^{OEG1}$ are also significantly too high. Higher than expected SAM thickness is usually an indication of adventitious contamination, which was already discussed as the most probable reason for the smaller discrepancy between expected and measured thickness in pure SAMs. Higher levels of contamination could be caused by a combination of prolonged exposure to ambient conditions due to characterisation by other techniques and higher disorder in the SAMs, i.e. both SAMs formed from 19 % **reagent 2** solution show higher contact angle hysteresis and yield the highest thickness values.

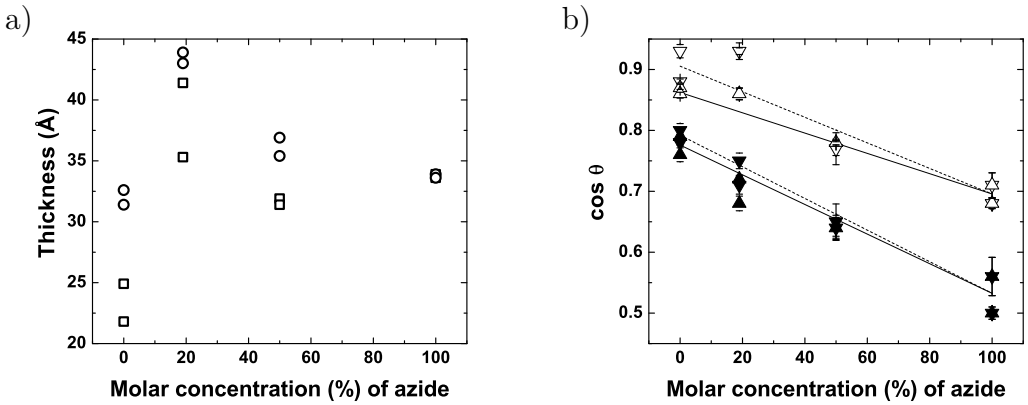

FIGURE 5.13: Plotted ellipsometry and wetting measurements data of pure and mixed SAMs against fractional molar concentration (%) of **reagent 2** in the SAM formation solution. Plotted a) thickness values of **SAM2** diluted with **LCAT-OEG-4** (open circles) and **LCAT-OEG-1** (open squares) do not show any linear trend. On the other hand, plotted b) cosine of the contact angles show a linear change in **SAM2** diluted with **LCAT-OEG-4** (triangles facing up) and **LCAT-OEG-1** (triangles facing down). Filled and open symbols correspond to advancing and receding angles, respectively. Solid and dotted lines represent the line of best fit for the Cassie equation for the contact angles (for the triangles facing up and down, respectively).

On the other hand, the fact that **SAM2** yields slightly lower surface energy than SAMs of the diluents **LCAT-OEG-4** and **LCAT-OEG-1**, and the fact that mixed SAMs yield intermediate contact angles compared to those of pure SAMs, provided an alternative way to study the mixing. The degree of mixing was estimated by analysis of the angles based on the Cassie equation.[60] Figure 5.13b shows plotted cosine values of the contact angles against the fractional molar concentration (%) of **reagent 2** in SAM formation solutions, which are in a good agreement with the plotted lines corresponding to the expected linear change in cosine of the contact angles with the change of fractional molar concentration (%) of **reagent 2** on the surface. This indicates that SAMs yield similar fractional molar concentration to that of the corresponding solutions.

TABLE 5.6: Ellipsometric thickness and contact angles of pure SAMs (**SAM2**, **LCAT-OEG-4 SAM** and **LCAT-OEG-1 SAM**) and mixed SAMs ($\mathbf{SAM2}_{50\%}^{OEG4}$, $\mathbf{SAM2}_{19\%}^{OEG4}$, $\mathbf{SAM2}_{50\%}^{OEG1}$ and $\mathbf{SAM2}_{19\%}^{OEG1}$).

SAM	Ellipsometric thickness (Å)		Water contact angles (°)		
	Measured	Expected[e]	Advancing	Receding	Hysteresis
C18 SAM	22 ± 2	22	111 ± 1	103 ± 2	8
SAM2	34 ± 1	33	58 ± 3	46 ± 2	12
$\mathbf{SAM2}_{50\%}^{OEG4}$	36 ± 1	33†	50 ± 2	39 ± 1	11
$\mathbf{SAM2}_{19\%}^{OEG4}$	43 ± 2	32†	46 ± 2	31 ± 2	15
LCAT-OEG-4 SAM	32 ± 1	29	39 ± 2	30 ± 1	9
$\mathbf{SAM2}_{50\%}^{OEG1}$	32 ± 1	29†	50 ± 2	40 ± 3	10
$\mathbf{SAM2}_{19\%}^{OEG1}$	38 ± 4	25†	43 ± 2	21 ± 2	22
LCAT-OEG-1 SAM	23 ± 2	21	38 ± 1	25 ± 4	13

† Expected value was calculated based on experimentally obtained values from pure **SAM2** and either **LCAT-OEG-4 SAM** or **LCAT-OEG-1**.

- Ellipsometric thickness was obtained using refractive index of 1.45 in Cauchy's equation.

- Uncertainties refer to whichever is the larger (i) standard deviation of sample-to-sample values or (ii) average of standard deviations from each sample (originating from variation in a single measurement or measurement-to-measurement).

5.2.2.2 XPS

X-ray Photoelectron Spectroscopy (XPS) measurements were carried out on mixed SAMs in order to provide another (independent) method of evaluating mixing on **reagent 2** and the diluents in a SAM environment. The amount of mixing was determined by evaluating the fractional difference in chemical composition of the mixed SAMs with respect to the obtained reference spectra of pure **SAM2**, **LCAT-OEG-4 SAM** and **LCAT-OEG-1 SAM**.

The spectra presented in this section were processed in the same manner as the spectra discussed in section 5.2.1.2. Although it was mentioned in the same section that normalisation to the carbonyl oxygen component in O 1s provides equally consistent data analysis of pure SAMs spectra, it was found, however, that normalisation of mixed SAMs spectra to the carbonyl oxygen component leads to slightly less satisfactory results, and in the case of $\mathbf{SAM2}_{19\%}^{OEG1}$ leads to abnormal results. Thus, only the data normalised to alkyl carbon in C 1s are presented in this section.

It is challenging to determine the mixing of **reagent 2** with the diluents by XPS, because the molecules have very similar chemical composition (see figures 5.9), therefore there is not much difference between their XPS spectra. As discussed in section 5.2.1.2, only the azide group leads to a significant difference between XPS spectra of **reagent 2** and **LCAT-OEG-4**. Although **LCAT-OEG-1** differs from **reagent 2** by additional changes in oxygen C-O peak in O 1s and carbon C-O (and C-N) peak in C 1s, both of them are subject to variations caused by adventitious contamination. Therefore, quantification of the amount of azide group on the surface is vital for determining the fractional molar concentration of **reagent 2** in the SAMs. However, due to X-ray induced reduction of azide group by up to 60 %, twenty XPS measurements were performed on each type of SAM to obtain statistically reliable values of integrated peak areas, as discussed in section C.5. Assuming the rate of

azide group reduction is independent of the molar concentration in the SAM, accurate mixing ratios can be determined by comparing peak areas in N 1s spectra of the mixed SAMs with those of the pure SAMs.

TABLE 5.7: Relative ratios of chemical elements and their species in mixed **SAM2**, **LCAT-OEG-4 SAM** and **LCAT-OEG-1 SAM** based on integrated and normalised (using R.S.F.) peak areas in XPS spectra of N 1s, O 1s, C 1s and Au 4f regions. *Alkyl carbon in C 1s is set to be equal to 10 in all of the spectra, because that is the amount of such atoms in all of the molecules. Uncertainties are presented in table C.1 in the appendix.*

	Carbon			Oxygen			Nitrogen	Gold
SAM	C=O	C-O C-N	Total	C=O	C-O	Total	Total	Total
$\mathbf{SAM2}_{50\%}^{OEG4}$	2.0	12.7	24.9	1.0	5.6	6.6	2.3	15.4
*Expected**	*1*	*11.9*†	*23.6*†	*1*	*5*	*6*	*2.3*†	
$\mathbf{SAM2}_{19\%}^{OEG4}$	1.7	12.4	24.2	1.0	5.5	6.6	1.6	13.8
*Expected**	*1*	*11.3*†	*23.0*†	*1*	*5*	*6*	*1.55*†	
$\mathbf{SAM2}_{50\%}^{OEG1}$	2.2	8.1	20.5	1.1	3.8	4.9	2.0	14.5
*Expected**	*1*	*8.5*†	*20.2*†	*1*	*3.5*	*4.5*	*2.4*†	
$\mathbf{SAM2}_{19\%}^{OEG1}$	1.9	5.8	17.8	1.4	2.5	4.0	1.8	12.1
*Expected**	*1*	*5.8*†	*17.4*†	*1*	*2.6*	*3.6*	*1.6*†	

* Expected values based on the corresponding molecular structures shown in figures 5.9.
† Expected value was calculated based on experimentally obtained values from pure **SAM2**, **LCAT-OEG-4 SAM** and **LCAT-OEG-1 SAM** presented in tables 5.4 and 5.5.

Tables C.2, C.3, C.4, C.5 and C.6 in the appendix detail integrated peak areas for each XPS measurement on each SAM type, while the summary is provided in table 5.7 (for uncertainties please refer to table C.1 in the appendix), whereas figures 5.14 and 5.15 visualise the differences by showing representative spectra of the pure and mixed SAMs. Quantitative analysis of integrated peak areas of total carbon, C-O (and C-N) carbon, total oxygen, oxygen in amide group (except for $\mathbf{SAM2}_{19\%}^{OEG1}$) and oxygen in OEG chain (C-O) yield relative ratios within 10 % of the expected values.

Based on the analysis, N 1s region suggests that $\mathbf{SAM2}_{50\%}^{OEG4}$ and $\mathbf{SAM2}_{19\%}^{OEG4}$ contain 50 % and 21 % of **reagent 2**, respectively, which are in a close agreement with

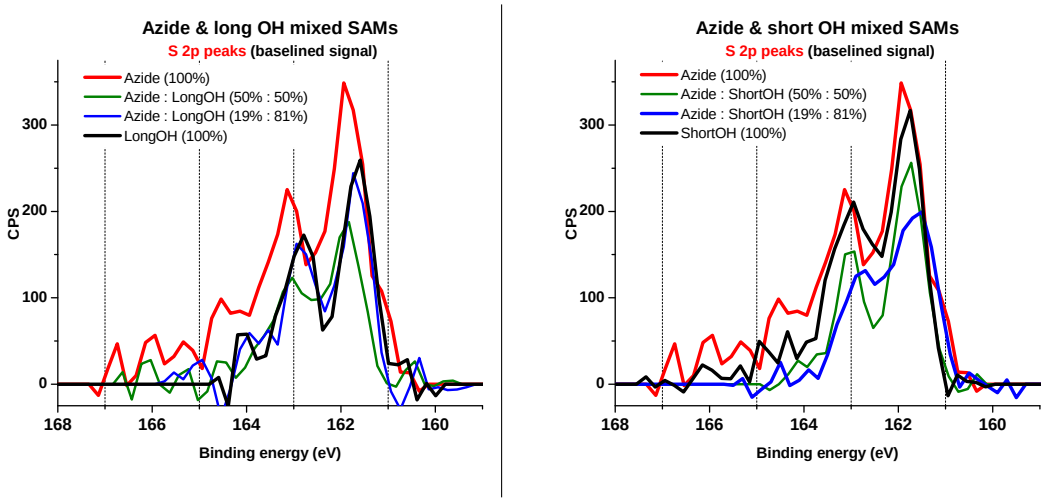

FIGURE 5.14: Overlaid XPS S 2p spectra of SAMs with 100 % (in red), 50 % (in green) 19 % (in blue) and 0 % (in black) molar fraction of **reagent 2** on the surface. Mixed SAMs contain **LCAT-OEG-4** (left column) and **LCAT-OEG-1** (right column), as the diluent. *Intensity of the spectra is not normalised.*

the fractional molar concentrations in the corresponding SAM formation solutions. Analysis of C-O (and C-N) peak in C 1s yields much higher percentages (94 % and 75 %, respectively), which are attributed to the effects of variation in adventitious contamination.

Mixing in $\mathbf{SAM2}^{OEG1}_{50\%}$ and $\mathbf{SAM2}^{OEG1}_{19\%}$ can be determined by evaluating N 1s region, the peak corresponding to oxygen in OEG chain (C-O), and the peak corresponding to carbon bound to oxygen (C-O) or nitrogen (C-N). The analysis suggests 36 %, 59 % and 46 % of **reagent 2** are in the former SAM. Although the percentages are spread out, their average of 47 % is ∼3 % lower than the concentration of the solution. The same regions suggest 25 %, 21 % and 20 % of **reagent 2** are in the latter SAM, giving an average of 22 %, which in this case is ∼3 % higher than the concentration of the solution.

Overall, XPS data indicate ∼20 % and ∼50 % fraction of **reagent 2** in the mixed SAMs formed from solutions containing 19 % and 50 % of fractional molar concentration of **reagent 2**.

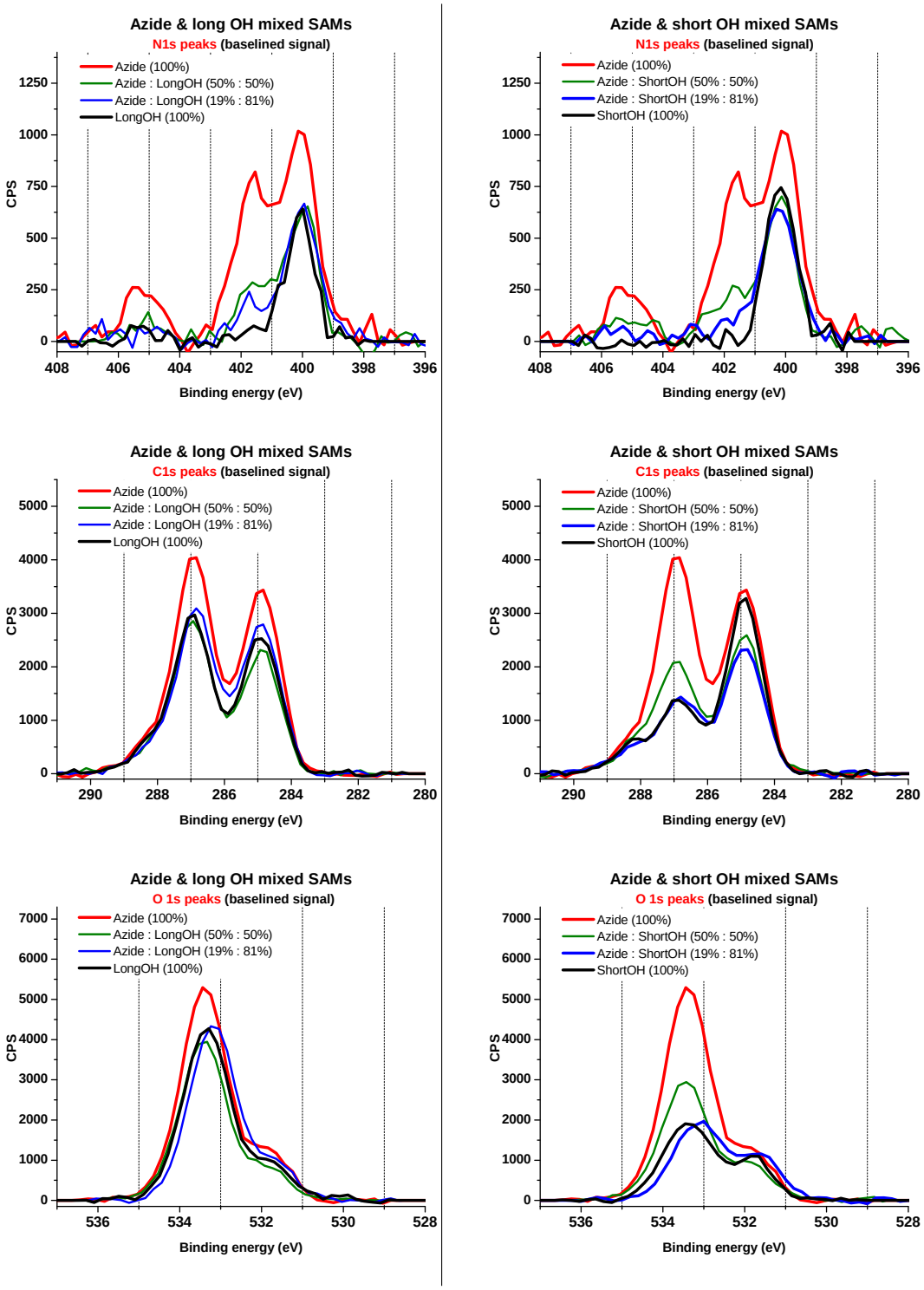

FIGURE 5.15: Overlaid XPS spectra of SAMs with 100 % (in red), 50 % (in green) 19 % (in blue) and 0 % (in black) molar fraction of **reagent 2** on the surface. Mixed SAMs contain **LCAT-OEG-4** (left column) and **LCAT-OEG-1** (right column), as the diluent. Spectra correspond to N 1s (top row), C 1s (middle row) and O 1s (bottom row). *Intensity of the spectra is not normalised.*

5.2.3 Click chemistry on the SAM surface

Following the successful fabrication, characterisation and mixing with the diluents, the intrinsic function of **SAM2** to facilitate click chemistry was investigated. This section presents a study, using ellipsometry and Quartz Crystal Microbalance with Dissipation (QCMD) techniques, of click reaction on the gold surface by performing cycloaddition between strained cycloalkyne and azide endgroup of **SAM2**, without the use of any catalyst.

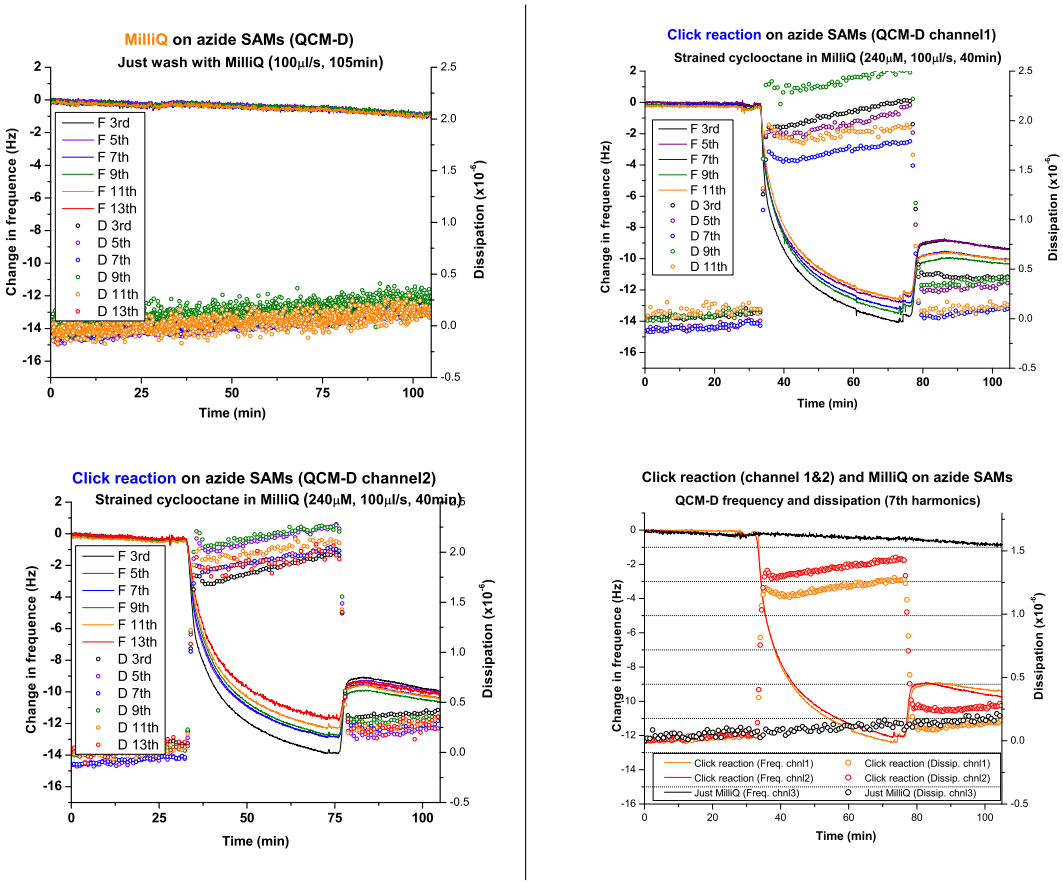

FIGURE 5.16: QCMD spectra of **SAM2** rinsed for 40 min with a) pure milliQ grade water, b)-c) 240 µM **strained cyclooctyne** solution in milliQ grade water. Figure d) overlays the 7th harmonics from figures a), b) and c). Solutions were rinsed at 100 µl s^{-1} rate.

Figure 5.16 shows the change in frequency and dissipation due to a 40 min rinse (at 100 µl s^{-1} rate) of **SAM2** with pure milliQ grade water (figure 5.16a) and 240 µM of **strained cyclooctyne** in milliQ grade water (figure 5.16b and 5.16c). There

are no evident changes, other than the drift, in figure 5.16a, but a clear difference in frequency appears in figures 5.16b and 5.16c after the rinse with the solution of **strained cyclooctyne**. Although it is difficult to see in the latter two figures that dissipation returns to drift level after the rinse with **strained cyclooctyne** solution, this is clearly shown in figure 5.16d, where the 7th harmonics from the other three figures are overlaid.

TABLE 5.8: Calculated mass of chemically bound **strained cyclooctyne** layer to **SAM2** using Sauerbrey equation and each harmonic from the acquired QCMD data

	Mass (ng/cm2)		Drift (ng/cm2/min)		Mass(ng/cm2) 20min later	
Harmonic	Chnl 1	Chnl 2	Chnl 1	Chnl 2	Chnl 1	Chnl 2
3rd	156	160	0.4	0.7	164	174
5th	155	163	0.5	0.6	164	176
7th	158	157	0.4	0.7	166	171
9th	165	163	0.3	0.6	170	175
11th	158	158	0.4	0.7	166	172
13th	158	153	0.5	0.7	168	168
Average	**158.3**	**159.1**	**0.40**	**0.67**		
STD	**3.3**	**3.6**	**0.07**	**0.04**		

QCMD does not measure properties of the adsorbed layers directly, but determines them by modelling the acquired data. Adsorbed films can be categorised into two main categories, rigid and viscoelastic, each of which requires different models. The former can be modelled using a simple Sauerbrey equation, while the latter requires complex Kelvin-Voigt or Maxwell models. It is important to choose the correct category, because modelling a rigid layer as viscoelastic yields underestimated mass of the film, while the reverse yields overestimated mass. Usually Sauerbrey equation is the correct choice for modelling a film, if (i) the change in dissipation is below 10×10^{-6}, while frequency changes by 10 Hz, (ii) signal of the overtones overlap, or (iii) Sauerbrey equation gives comparable values of the film mass calculated with the highest and lowest harmonics. Due to those criteria, Sauerbrey equation was chosen to model the adlayer of **strained cyclooctyne** on **SAM2**.

The calculated values of mass per area for each harmonic are presented in table 5.8. By taking into account the spread in the data and the drift in the QCMD system, mass density (mass per area) of the film is estimated to be in the range of 117-163 $\mathrm{ng\,cm^{-2}}$, which is equal to 33-46 $\mathrm{Å^2}$ area per molecule. Assuming that area per molecule in **SAM2** is similar to that of a simple alkanethiol SAM ($\sim$21 $\mathrm{Å^2}$), QCMD data suggest that the **strained cyclooctyne** layer is $\sim$1.5-2.0 times less densely packed, or in other word, the yield of the click reaction is in the range of $\sim$50-75 %. This is not surprising given that **strained cyclooctyne** is larger than azide group and that it can only bind through the alkyne group. Based on the bulk density (1.14 $\mathrm{g\,cm^{-3}}$) of **strained cyclooctyne**, the estimated thickness of the film is in the range of 10-14 Å, which is lower than the obtained value of (17 ± 2) Å using ellipsometry. Such discrepancy is not unexpected, because density of **strained cyclooctyne** in the layer chemically bound to **SAM2** is likely to be lower than that in bulk. The comparison of the thickness values obtained from QCMD and ellipsometry suggests that the density of **strained cyclooctyne** on the SAM is $\sim$40 % lower than in bulk.

Figure C.6 in the appendix shows that no changes are detected by QCMD upon further rinses with the **strained cyclooctyne** solution, indicating that reaction is fully completed within 40 min. The same figure also shows that chemical or physical adsorption occurs on **LCAT-OEG-4 SAM**. The same outcome was observed on **LCAT-OEG-1 SAM** and amine (NH_2) terminated SAM.

5.2.4 Discussion and conclusions

Ellipsometry and contact angle data (table 5.3) suggest that **reagent 2** forms a good quality SAM. This is also supported by the acquired XPS spectra, which show mainly sulfur species corresponding to thiols bound to gold surface (figure 5.11d). Furthermore, analysis of the XPS data yields relative ratios of chemical elements and their species that are comparable to the expected values (tables 5.4 and 5.5) determined from the molecular structure (figure 5.9). Although it was detected that X-ray induces up to 60 % reduction of azide group, it was limited to 20 % reduction by optimising acquisition parameters.

It was also shown that **SAM2** can successfully facilitate catalyst-free click chemistry by performing cycloaddition between strained cycloalkyne and azide endgroup of the SAM in aqueous solution under ambient conditions. Although it was not investigated in detail, it was observed that click chemistry on the surface was complete within a rinse phase (at $100\,\mu l\,s^{-1}$ rate, $240\,\mu M$ solution concentration) of 40 min and no additional changes were detected by QCMD due to repeated phases of rinsing. Analysis of QCMD data using Sauerbrey equation suggests that area per **strained cyclooctyne** molecule on **SAM2** is in the range of 33-46 $Å^2$, which suggests ∼1.5-2 times lower density than a conventional alkanethiol SAM. This suggests ∼50-75 % yield, assuming that **SAM2** has similar packing as conventional alkanethiol SAMs. This is not surprising, because **strained cyclooctyne** is larger than the azide group and can only bind through the alkyne group, which limits its packing on **SAM2**. QCMD data also suggest that film thickness of the **strained cyclooctyne** film is in the range of 10-14 Å, which is lower than (17 ± 2) Å measured by ellipsometry. The discrepancy, however, is likely to originate from the fact that the density of **strained cyclooctyne** is lower on **SAM2** than in bulk. For completeness, adsorption of **strained cyclooctyne** onto **LCAT-OEG-4 SAM**, **LCAT-OEG-1 SAM**

and amine (NH_2) terminated SAM was investigated, but no significant changes were detected.

It was also shown that the amount of **reagent 2** in a SAM can be diluted with **LCAT-OEG-4** or **LCAT-OEG-1**. Quantitative XPS data analysis (see tables 5.7, C.2, C.3, C.4, C.5 and C.6) of the pure and mixed SAMs suggests that fractional molar concentration of **reagent 2** in the SAMs is similar to that of the solutions the SAMs were formed in. This is also supported by the contact angle data. Measured contact angles on the pure and mixed SAMs are in the agreement with those predicted using Cassie equation[60] (see figure 5.13b and table 5.6).

5.3 Alkyl and aromatic SAMs in Raman spectroscopy and plasmonic systems

Organic electronics is emerging to become one of the most important technologies of the 21st century, due to the potential to produce flexible, transparent and cheap devices.[61,62] Developments in the field include organic transistors,[63] light emitting diodes[64,65] and solar cells.[66,67] The challenge, however, is to limit the number of molecules to just a few that are needed for the operation of a device, because molecular electronics offers desirable properties such as fast operation speeds, low switching energies, ultrahigh information densities, and cheap manufacturing. On the other hand, as the number of molecules in a group shrinks, the role of their conformation,[68] alignment and contact with an electrode[69] becomes increasingly more crucial, while probing the properties in small number of molecules is generally difficult to achieve.

Surface enhanced Raman spectroscopy offers a possible solution to easily probe a small number of molecules by combining molecular layers and plasmonic structures (metal structures that support light-driven coherent collective electron oscillation, also known as plasmons).[70–74] The strength of this method lies in the fact that plasmonic structures can confine light below the diffraction limit[75] and, in turn, used for sensing down to single molecule level.[70,71,76,77] Nanoparticle-on-mirror (NPoM) configuration is of particular interest, because in addition to the possibility of probing a small number of molecules of interest between the planar surface and a plasmonic structure, the orientation of electric field is fixed, while the coupling of the plasmons on a nanoparticle and its dipole image in the metal film enhances the sensitivity of the technique.[70,71,73,74]

SAMs offer unprecedented control of conformation, packing and orientation of the molecules in a monolayer as well as physical properties of the film, such as thickness

and conductivity. Therefore, **BPDT SAM** and **BPT SAM** provided an excellent platform for our collaborators to address one of the main outstanding questions of how molecular conductivity affects a surrounding plasmonic junction.[78] A covalent bond between thiol groups and gold atoms along with π-orbitals in phenyl rings turn **BPDT SAM** into a conductive spacer between gold nanoparticle and gold thin film,[79] in contrast to **BPT SAM** which covalently binds only to the gold thin film and, in turn, acts as an insulating layer. Compared to the latter SAM, the former yields a strong (50 nm) blue-shift of the plasmon resonance (of the coupled mode) in scattering spectra of gold nanoparticles. Although this blue-shift is in agreement with theoretical prediction[80–82] and the reported shift for direct quantum tunnelling between plasmonic structures,[83,84] it is necessary to exclude the possibility that the observed blue-shift could originate from the variation in SAM thickness of refractive index. Thus, my contribution to the published work is presented in this section.

My contribution of the performed ellipsometry measurements to the published work is summarised in table 5.9. Although ellipsometric **BPDT SAM** thickness of (1.1 ± 0.1) nm and **BPT SAM** thickness of (1.3 ± 0.1) nm do agree within their uncertainty values, the obtained averages show that the former SAM is 15 % thinner. This could result from a fraction of **BPDT** molecules lying flat on the gold surface due to bond formation of both thiols groups with the gold surface. The difference in thickness would account for up to 20 nm shift of the plasmon peak in the spectra, but it would shift to the opposite direction, as smaller separation between the plasmon structures lead to a red-shift. The presented thickness was obtained using refractive index of $n = 1.45$ in Cauchy's equation, and although there is some variation in the refractive index between organic molecules, an unrealistic shift to $n = 1.15$ would be required to account for the observed 50 nm blue-shift in the spectra.

Thus, it is concluded that the blue-shift is due to changes in molecular conductivity.

Furthermore, it is demonstrated that the system can be treated as a capacitor (gold nanoparticle separated from gold thin film) short-circuited by individual resistors (molecules in a SAM). Fitting of the model to the experimental data of the mixed **BPDT** and **BPT** SAMs suggests that fewer than 200 molecules are probed with an individual gold nanoparticle (60 nm in diameter). For more details, the reader is referred to the publication.[78]

Table 5.9: Ellipsometric thickness of **BPT SAM**, **BPDT SAM**, **C4 SAM**, **C5 SAM**, **C9 SAM**, **C12 SAM** and **C18 SAM**.

SAM	Ellipsometric thickness (nm) Measured
BPT SAM	1.3 ± 0.1
BPDT SAM	1.1 ± 0.1
C4 SAM	0.5 ± 0.1
C5 SAM	0.6 ± 0.1
C9 SAM	1.1 ± 0.1
C12 SAM	1.6 ± 0.1
C18 SAM	2.4 ± 0.1

Despite the substantial progress in both simulation[85–89] and chemical development of metal nanostructures[90] in recent years, only some pursuits to develop a comprehensive analytical model[91,92] capable of directly validating experimental results and producing parameters for the implementation of full electromagnetic simulations have been reported. However, most of them rely on approximation of Maxwell's equations and are limited to certain geometries, for example large separation of plasmonic structures.[93] Another approach is to treat a nanoplasmonic system as a high frequency circuit composed of capacitors, inductors and resistors,[94–97] which is a promising approach because a generalised equation that incorporates various contributions, for example geometry of the nanostructures, can be used to describe resonant conditions.

Surprisingly such model was not present, and further work by the collaborators on the similar systems to the one described above led to a development of an analytical

circuit model for coupled plasmonic dimers separated by small gaps, which provides a complete account of the optical resonance wavelength.[98] It is able to describe both insulating and conductive spacers (gaps), as well as provide quantitative agreement with full electromagnetic simulations.

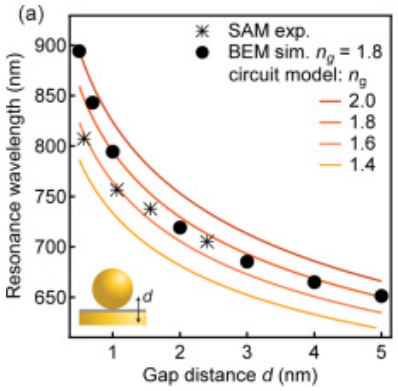

FIGURE 5.17: Values of ellipsometric thickness taken from table 5.9 are plotted against plasmon resonance wavelength. Taken from reference[98].

Comparison of the model with the experimental results has been evaluated as well. Again, ellipsometric measurements were performed on **C4 SAM**, **C5 SAM**, **C9 SAM**, **C12 SAM** and **C18 SAM** prepared in an identical manner to those used to gather scattering spectra of gold nanoparticles in NPoM configuration. This is done to evaluate the accuracy of our collaborators' model in determining the size and refractive index of the spacer (gap). The data are summarised in table 5.9 and plotted against the resonant wavelength (figure 5.17), which show a good agreement in trend with data generated by both the analytical model and full electromagnetic simulation. For more details, the reader is referred to the publication.[98]

Overall, it is shown that relatively simple aromatic and alkanethiol SAMs without an intrinsic active function can be used as an optimum platform to control properties of the spacer layer in surface enhanced Raman spectroscopy and nanoplasmonic systems.

5.4 References

[1]C. D. Bain, E. B. Troughton, Y. T. Tao, J. Evall, G. M. Whitesides and R. G. Nuzzo, J. Am. Chem. Soc. **111**, 321–335 (1989).

[2]E. B. Troughton, C. D. Bain, G. M. Whitesides, R. G. Nuzzo, D. L. Allara and M. D. Porter, Langmuir **4**, 365–385 (1988).

[3]R. Arnold, W. Azzam, A. Terfort and C. Wöll, Langmuir **18**, 3980–3992 (2002).

[4]A. Myrskog, H. Anderson, T. Aastrup, B. Ingemarsson and B. Liedberg, Langmuir **26**, 821–829 (2010).

[5]R. G. Nuzzo, L. H. Dubois and D. L. Allara, J. Am. Chem. Soc. **112**, 558–569 (1990).

[6]J. Li, K. S. Liang, G. Scoles and A. Ulman, Langmuir **11**, 4418–4427 (1995).

[7]E. L. Smith, C. a. Alves, J. W. Anderegg and M. D. Porter, Langmuir **8**, 2707–2714 (1992).

[8]O. Dannenberger, K. Weiss, H. J. Himmel, B. Jäger, M. Buck and C. Wöll, Thin Solid Films **307**, 183–191 (1997).

[9]H. J. Himmel, K. Weiss, B. Jäger, O. Dannenberger, M. Grunze and C. Wöll, Langmuir **13**, 4943–4947 (1997).

[10]M. Wells, D. L. Dermody, H. C. Yang, T. Kim, R. M. Crooks and a. J. Ricco, Langmuir **12**, 1989–1996 (1996).

[11]S. E. Creager and C. M. Steiger, Langmuir **11**, 1852–1854 (1995).

[12]P. E. Laibinis, G. M. Whitesides, D. L. Allara, Y. T. Tao, A. N. Parikh and R. G. Nuzzo, J. Am. Chem. Soc. **113**, 7152–7167 (1991).

[13]J. M. Tour, L. Jones, D. L. Pearson, J. J. S. Lamba, T. P. Burgin, G. M. Whitesides, D. L. Allara, A. N. Parikh and S. Atre, J. Am. Chem. Soc. **117**, 9529–9534 (1995).

[14]K. Heister, M. Zharnikov, M. Grunze and L. S. O. Johansson, J. Phys. Chem. B **105**, 4058–4061 (2001).

[15]S. D. Techane, L. J. Gamble and D. G. Castner, J. Phys. Chem. C **115**, 9432–9441 (2011).

[16]G. Beamson and D. Briggs, *High Resolution XPS of Organic Polymers: The Scienta ESCA300 Database* (Wiley, 1992), ISBN: 9780471935926.

[17]T. M. Willey, A. L. Vance, C. Bostedt, T. van Buuren, R. W. Meulenberg, L. J. Terminello and C. S. Fadley, Langmuir **20**, 4939–4944 (2004).

[18]S.-J. Xiao, S. Brunner and M. Wieland, J. Phys. Chem. B **108**, 16508–16517 (2004).

[19]R. V. Duevel and R. M. Corn, Anal. Chem. **64**, 337–342 (1992).

[20]A. C. Gouget-Laemmel, J. Yang, M. A. Lodhi, A. Siriwardena, D. Aureau, R. Boukherroub, J. N. Chazalviel, F. Ozanam and S. Szunerits, J. Phys. Chem. C **117**, 368–375 (2013).

[21]E. W. Wollman, D. Kang, C. D. Frisbie, I. M. Lorkovic and M. S. Wrighton, J. Am. Chem. Soc. **116**, 4395–4404 (1994).

[22]S. Engin, V. Trouillet, C. M. Franz, A. Welle, M. Bruns and D. Wedlich, Langmuir ACS J. Surfaces Colloids **26**, 6097–6101 (2010).

[23]P. Gupta, A. Ulman, S. Fanfan, A. Korniakov and K. Loos, J. Am. Chem. Soc. **127**, 4–5 (2005).

[24]F. Sun, D. G. Castner and D. W. Grainger, Langmuir **9**, 3200–3207 (1993).

[25]Y. Tai, M. Buck, M. Grunze, M. Zharnikov, A. Shaporenko, H.-T. Rong and W. Eck, J. Phys. Chem. B **108**, 16806–16810 (2004).

[26]T. Ishida, N. Choi, W. Mizutani, H. Tokumoto, I. Kojima, H. Azehara, H. Hokari, U. Akiba and M. Fujihira, Langmuir **15**, 6799–6806 (1999).

[27]H. Takiguchi, K. Sato, T. Ishida, K. Abe, K. Yase and K. Tamada, Langmuir **16**, 1703–1710 (2000).

[28]J. C. Love, L. A. Estroff, J. K. Kriebel, R. G. Nuzzo and G. M. Whitesides, Chem. Rev. **105**, 1103–1170 (2005).

[29]K. L. Prime and G. M. Whitesides, Science **252**, 1164 (1991).

[30]C. Nicosia and J. Huskens, Mater. Horizons **1**, 32 (2014).

[31]G. A. Hudalla and W. L. Murphy, Langmuir **25**, 5737–5746 (2009).

[32]R. a. Decréau, J. P. Collman and A. Hosseini, Chem. Soc. Rev. **39**, 1291–1301 (2010).

[33]J. Murray, D. Nowak, L. Pukenas, R. Azhar, M. Guillorit, C. Wälti, K. Critchley, S. Johnson and R. S. Bon, J. Mater. Chem. B **2**, 3741–3744 (2014).

[34]S.-W. Tam-Chang, H. A. Biebuyck, G. M. Whitesides, N. Jeon and R. G. Nuzzo, Langmuir **11**, 4371–4382 (1995).

[35]S. Svedhem, S. C. T. Svensson and B. Liedberg, J. Am. Chem. Soc., 3390–3394 (1999).

[36]H. C. Kolb, M. G. Finn and K. B. Sharpless, Angew. Chemie - Int. Ed. **40**, 2004–2021 (2001).

[37]E. M. Sletten and C. R. Bertozzi, Angew. Chemie - Int. Ed. **48**, 6974–6998 (2009).

[38]M. D. Best, Biochemistry **48**, 6571–6584 (2009).

[39]J. C. Jewett and C. R. Bertozzi, Chem. Soc. Rev. **39**, 1272–9 (2010).

[40]E. Lallana, R. Riguera and E. Fernandez-Megia, Angew. Chemie - Int. Ed. **50**, 8794–8804 (2011).

[41]J. E. Moses and A. D. Moorhouse, Chem. Soc. Rev. **36**, 1249–1262 (2007).

[42]K. Nwe and M. W. Brechbiel, Cancer Biother. Radiopharm. **24**, 289–302 (2009).

[43]R. A. Evans, Aust. J. Chem. **60**, 384–395 (2007).

[44]C. Hein, X.-M. Liu and D. Wang, Pharm Res **25**, 2216–2230 (2009).

[45]M. Grammel and H. C. Hang, Nat Chem Biol **9**, 475–484 (2013).

[46]R. Xie, S. Hong and X. Chen, Curr. Opin. Chem. Biol. **17**, 747–752 (2013).

[47]Y. Su, J. Ge, B. Zhu, Y. G. Zheng, Q. Zhu and S. Q. Yao, Curr. Opin. Chem. Biol. **17**, 768–775 (2013).

[48]P. Thirumurugan, D. Matosiuk and K. Jozwiak, Chem. Rev. **113**, 4905–4979 (2013).

[49]D. Zeng, B. M. Zeglis, J. S. Lewis and C. J. Anderson, J. Nucl. Med. **54**, 829–32 (2013).

[50]N. K. Devaraj and J. P. Collman, QSAR Comb. Sci. **26**, 1253–1260 (2007).

[51]J. Wang, F. Wu, M. Watkinson, J. Zhu and S. Krause, Langmuir **31**, 9646–9654 (2015).

[52]J. Mehlich and B. J. Ravoo, Org. Biomol. Chem. **9**, 4108 (2011).

[53]D. Samanta and A. Sarkar, Chem. Soc. Rev. **40**, 2567–2592 (2011).

[54]R. Chelmowski, D. Kafer, S. D. Köster, T. Klasen, T. Winkler, A. Terfort, N. Metzler-Nolte and C. Wöll, Langmuir **25**, 11480–11485 (2009).

[55]I. S. Choi and Y. S. Chi, Angew. Chemie - Int. Ed. **45**, 4894–4897 (2006).

[56]M. V. Gil, M. J. Arévalo and Ó. López, Synthesis **11**, 1589–1620 (2007).

[57]S. D. Evans, R. Sharma and a. Ulman, Langmuir **7**, 156–161 (1991).

[58]J. P. Collman, N. K. Devaraj, T. P. A. Eberspacher and C. E. D. Chidsey, Langmuir **22**, 2457–2464 (2006).

[59]P. Harder, M. Grunze, R. Dahint, G. M. Whitesides and P. E. Laibinis, J. Phys. Chem. B **102**, 426–436 (1998).

[60]B. D. Cassie and S. Baxter, Trans. Faraday Soc. **40**, 546–551 (1944).

[61]A. J. Heeger, S. Kivelson, J. R. Schrieffer and W. P. Su, Rev. Mod. Phys. **60**, 781–850 (1988).

[62]T. W. Kelley, P. F. Baude, C. Gerlach, D. E. Ender, D. Muyres, M. A. Haase, D. E. Vogel and S. D. Theiss, Chem. Mater. **16**, 4413–4422 (2004).

[63]A. Dodabalapur, L. Torsi and H. E. Katz, Science **268**, 270–271 (1995).

[64]J. H. Burroughes, D. D. C. Bradley, A. R. Brown, R. N. Marks, K. Mackay, R. Friend, P. L. Burns and A. B. Holmes, Nature **347**, 539–541 (1990).

[65]S. Reineke, F. Lindner, G. Schwartz, N. Seidler, K. Walzer, B. Lüssem and K. Leo, Nature **459**, 234–8 (2009).

[66]S. Günes, H. Neugebauer and N. S. Sariciftci, Chem. Rev. **107**, 1324–1338 (2007).

[67]L. Schmidt-Mende, A. Fechtenkötter, K. Müllen, E. Moons, R. H. Friend and J. D. MacKenzie, Science **293**, 1119–22 (2001).

[68]L. Venkataraman, J. E. Klare, C. Nuckolls, M. S. Hybertsen and M. L. Steigerwald, Nature **442**, 904–907 (2006).

[69]S. V. Aradhya and L. Venkataraman, Nat. Nanotechnol. **8**, 399 (2013).

[70]R. W. Taylor, F. Benz, D. O. Sigle, R. W. Bowman, P. Bao, J. S. Roth, G. R. Heath, S. D. Evans and J. J. Baumberg, Sci. Rep. **4**, 5940 (2014).

[71]L. Li, T. Hutter, U. Steiner and S. Mahajan, Analyst **138**, 4574–8 (2013).

[72]L. Cui, B. Liu, D. Vonlanthen, M. Mayor, Y. Fu, J. F. Li and T. Wandlowski, J. Am. Chem. Soc. **133**, 7332–7335 (2011).

[73]P. K. Aravind and H. Metiu, Surf. Sci. **124**, 506–528 (1983).

[74]P. Nordlander and E. Prodan, Nano Lett. **4**, 2209–2213 (2004).

[75]W. L. Barnes, A. Dereux and T. W. Ebbesen, Nature **424**, 824–30 (2003).

[76]H. X. Xu, E. J. Bjerneld, M. Käll and L. Börjesson, Phys. Rev. Lett. **83**, 4357–4360 (1999).

[77]R. Zhang, Y. Zhang, Z. C. Dong, S. Jiang, C. Zhang, L. G. Chen, L. Zhang, Y. Liao, J. Aizpurua, Y. Luo, J. L. Yang and J. G. Hou, Nature **498**, 82–86 (2013).

[78]F. Benz, C. Tserkezis, L. O. Herrmann, B. de Nijs, A. Sanders, D. O. Sigle, L. Pukenas, S. D. Evans, J. Aizpurua and J. J. Baumberg, Nano Lett. **15**, 669–74 (2015).

[79]M. Bürkle, J. K. Viljas, D. Vonlanthen, A. Mishchenko, G. Schön, M. Mayor, T. Wandlowski and F. Pauly, Phys. Rev. B **85**, 075417 (2012).

[80]O. Pérez-González, J. Aizpurua and N. Zabala, Opt. Express **21**, 15847–15858 (2013).

[81]O. Pérez-González, N. Zabala and J. Aizpurua, New J. Phys. **13**, 083013 (2011).

[82]L. Liu, Y. Wang, Z. Fang and K. Zhao, J. Chem. Phys. **139**, 064310 (2013).

[83]K. J. Savage, M. M. Hawkeye, R. Esteban, A. G. Borisov, J. Aizpurua and J. J. Baumberg, Nature **491**, 574–577 (2012).

[84]J. A. Scholl, A. García-Etxarri, A. L. Koh and J. A. Dionne, Nano Lett. **13**, 564–569 (2013).

[85]F. J. García de Abajo and J. Aizpurua, Phys. Rev. B **56**, 15873–15884 (1997).

[86]R. Esteban, A. G. Borisov, P. Nordlander and J. Aizpurua, Nat. Commun. **3**, 825 (2012).

[87]A. Salandrino and N. Engheta, Phys. Rev. B - Condens. Matter Mater. Phys. **74**, 1–5 (2006).

[88]M. Pelton, J. Aizpurua and G. Bryant, Laser Photonics Rev. **2**, 136–159 (2008).

[89]S. C. Hagness and A. Taflove, *Computational Electrodynamics: The Finite-Difference Time-Domain Method* (Artech House, 2005).

[90]H. Itoh, K. Naka and Y. Chujo, J. Am. Chem. Soc **126**, 3026–7 (2004).

[91]A. Dhawan, S. J. Norton, M. D. Gerhold and T. Vo-Dinh, Opt. Express **17**, 9688–9703 (2009).

[92]R. Trivedi, A. Thomas and A. Dhawan, Opt. Express **22**, 19970–19989 (2014).

[93]I. E. Mazets, Tech. Phys. **45**, 1238–1240 (2000).

[94]N. Engheta, A. Salandrino and A. Alù, Phys. Rev. Lett. **95**, 1–4 (2005).

[95]N. Engheta, Science **317**, 1698–1702 (2007).

[96]N. Liu, F. Wen, Y. Zhao, Y. Wang, P. Nordlander, N. J. Halas and A. Aluì, Nano Lett. **13**, 142–147 (2013).

[97]J. Shi, F. Monticone, S. Elias, Y. Wu, D. Ratchford, X. Li and A. Alù, Nat. Commun. **5**, 3896 (2014).

[98]F. Benz, B. de Nijs, C. Tserkezis, R. Chikkaraddy, D. O. Sigle, L. Pukenas, S. D. Evans, J. Aizpurua and J. J. Baumberg, Opt. Express **23**, 33255 (2015).

Chapter 6

Conclusions and Future work

This thesis explored SAMs of various complexity with a special focus on fabrication of surfaces that could exhibit an intrinsic active function. The complexity ranges from:

(i) simple alkanethiol and aromatic type SAMs which were shown to yield optimum precision over control of physical surface properties for optical spectroscopy such as surface-enhanced Raman spectroscopy, gaining a better understanding of plasmonic systems, and the development of a generalised circuit model for coupled plasmonic systems (discussed in chapter 5);

(ii) SAMs of azide terminated long-chain alkanethiololigoethyleneglycol (LCAT-OEG) type molecule that were shown to yield high quality monolayers, effective mixing with alcohol terminated LCAT-OEG molecules and successful facilitation of click chemistry in catalyst-free aqueous solution under ambient conditions (chapter 5);

(iii) a more complex SAM of larger molecules containing chromophore that turns it into a light sensitive (more specifically photocleavable) surface, that was shown to ultimately produce areas of low density instead of areas of functional groups upon

irradiation with UV, which is attributed to be the cause of the exceptionally high selectivity in electrochemical deposition of copper (chapter 3);

and finally to

(iv) fabrication of SAMs using bi-stable metal complexes (spin crossover compounds) (that show potential to exhibit spin crossover (SCO) behaviour in a thin film on gold surfaces), where SAMs of metal complexes were successfully fabricated using one of the ligands by forming SAMs from a solution of preformed Fe(II) complexes, and by Fe(II) coordination onto the successfully formed SAM of the ligand, but SCO behaviour was not 'unlocked' (chapter 4).

The following sections will conclude the results in more detail and will present future work.

6.1 Characterisation of Photocleavage of Acetylpyrene SAM

Reagent 1 successfully forms a SAM sensitive to soft UV light, which can be photopatterned for the use of highly selective copper deposition. Nevertheless, patterned **SAM1** yields regions with high and low packing of molecules rather than regions with different surface chemistry. For certain applications, it might be desirable to obtain a chemically patterned surface consisting of predefined areas containing high density of specific chemical groups. **SAM1** has a high potential to produce regions dense in carboxylic acid groups. This could be achieved by studying in detail and quantifying the impact of soft UV irradiation time and concentration of HCl acid in IPA on the rate of photo-deprotection in **SAM1** and loss of molecules in **ALA SAM**. Also, other acids that yield fewer side effects in carboxylic acid SAMs, for example acetic acid,[1,2] as well as other solvents, could be investigated. Otherwise,

a derivative of **reagent 1** could be synthesised that protects a carboxylic acid with a longer chain length, such as mercaptoundecanoic acid, to form a SAM that would lead to a stable carboxylic acid terminated monolayer after a UV treatment. Such SAM would also allow an easier study of the photo-deprotection of 1-acetylpyrene group.

This thesis presented only a brief study of **reagent 1** layer formation on silicon oxide and glass surface, and photo-patterning. Mechanisms of both phenomena are not well understood. The assumption that adsorption of the layers is driven by the pyrene group could be tested by exposing the surfaces to pyrene derivatives, for example 1-(Bromoacetyl)pyrene, and characterising them with UV/visible and fluorescence spectroscopies in reflection or transmission mode, as well as with XPS. However, in order to gain a better understanding of the mechanism behind the film formation on the surfaces, the role of adventitious contamination should be studied, which could also open possibilities of film formation on other surfaces. Attribution of thickness growth of the films to cross-linking (facilitated by opening of dithiolane ring and formation of new disulfide bonds) could be investigated by using a derivative of **reagent 1** that contains a thiol head group. It would also allow for the study of photocleavage rates and yields with and without catalysts in crystalline or gel-like states, while comparison of the results with identical treatments of SAMs on gold formed by such molecules would give a better understanding and quantification of gold quenching effect on the photocleavage reaction. On the other hand, investigation of control of **reagent 1** cross-linking would allow for the development of tools for reproducible fabrication of the films with desired thickness.

Because of the ability to photo-deprotect **reagent 1** layers on both sides of a glass and turn them hydrophilic without any rinsing steps, the applicability of the layers could be investigated for in-situ surface modification, for example, to control surface chemical composition, to immobilise biological species or nanoparticles through

binding to COOH or sulfur groups, to direct hydrophilic or hydrophobic species on a surface, or to act as a sensor due to reported sensitivity of fluorescence of pyrene derivatives to a local environment.[3–7]

6.2 SAMs for spin crossover (SCO) surfaces

Ligand $\mathbf{L_1}$ successfully forms a SAM, but it does not coordinate Fe(II) on gold surfaces. Furthermore, complex $\mathbf{C_1}$ demetallises during SAM formation. The precise mechanism that leads to the disintegration of complex $\mathbf{C_1}$ is unclear, however, thiomorpholine head group plays an important role. The instability is not intrinsic to the structure of ligand **bpp**, but attributed to thiomorpholine head group, because **bpp-SH** complex did show some presence of Fe iron (even though the complex was unstable on gold surfaces due to desulfurisation in the backbone).[8] Therefore, a new derivative of ligand **bpp** could be investigated, a derivative containing another remote head group that is stable on a metal surface and exhibits a strong affinity towards gold (e.g. thiophenol).

Both ligand $\mathbf{L_2}$ and complex $\mathbf{C_2}$ form SAMs, and the former successfully (with ∼100 % yield) coordinates Fe ions. However, it has not yet been demonstrated whether complexes in the SAMs do exhibit SCO behaviour, as a number of issues were encountered. Most importantly, the spectra of Fe 2p region did not indicate expected LS state in **SAM $\mathbf{C_2}$ [MeCN]** at room temperature. This could be down to various causes, however, it would be most promising to investigate:

- ***Improvement of surface coverage by using an alternative head group (e.g. thiol) or coordination of complex C_2 to (monodentate) ligand-terminated SAM.***

Both **SAM L_2** and **SAM C_2** yield low surface coverage, which decreases further upon ligand exchange or Fe coordination. Low coverage not only limits signal strength in XPS, FTIR and other techniques, it is also a likely reason for high excess of carbon and oxygen assigned to reversibly bound adventitious hydrocarbons. This complicates data analysis and development of the SAMs for a SCO surface.

As discussed in sections 4.3.1.2 and 4.4, low coverage could be assigned to a weak head group affinity towards gold and the bulky shape of the molecules. The former cause could be addressed by an alternative head group, for example a remote thiol group. This would certainly improve stability of the SAMs upon rinsing (ligand exchange) and Fe coordination, even if improvement in surface coverage in fresh SAMs would be limited.

On the other hand, low density due to the bulky shape of the molecules could be improved by coordinating complex **C_2** via the site for the SEL onto a low density (monodentate) ligand-terminated SAM, then backfilling the SAM with longer chain (monodentate) ligand-terminated thiols, and coordinating complex **C_2** again. This would allow the density to be increased by transposing complexes along the axis normal to the surface.

- ***Replacement of MeCN (and most likely MeOH) by H_2O as the SEL upon SAM C_2 exposure to ambient conditions.***

  Such possibility is not only supported by the data acquired in this study, but also by the report of the similar phenomena in a closely related ligand **Py_5**. In solution, H_2O, MeOH, MeCN, pyridine (Py) and other ligands replace each other at the SEL position in Fe(II) complex of **Py_5**.[9] On the contrary, the same study found that cyanide anion (CN^-) could not be replaced by prolonged exposure to excess of the other ligands, which was attributed to strong ligand field and even stronger electrostatic interaction of CN^- with the Fe ion. It is

highly likely that H_2O from moisture would not replace CN^- as the SEL in **SAM C_2**. Furthermore, CN^- should lead to LS state, which would allow a reference spectra for Fe 2p region to be obtained. Then coordination of weaker ligands could be studied in order to obtain SCO behaviour in the SAM.

- ***Dissociation of MeCN ligand from SAM C_2 under vacuum.***

  Again, in addition to such conclusions drawn from the data, it has been reported in Fe(II) complex of **Py_5** (see the experimental section on metal complex syntheses in the reference[10]). Although, XPS could not be operated under atmospheric pressure, FTIR measurements could be obtained before and after exposure of powder, dropcast and SAM samples to vacuum, while CN stretch should be easily detected in the range of 2050-2250 cm^{-1}.

- ***Suppression of SCO behaviour,[11–14] weakening of ligand field or pinning complex into one of the states (i.e. HS)[11–13,15,16] in monolayers and sub-monolayers by direct contact with gold surface.*** It has been reported that the second and further layers are usually not affected.[13,14,16–19] Therefore, it could be investigated whether the phenomena occur in **SAM C_2** by fabricating a bilayer of complex **C_2**. This could be easily achieved by coordinating a straight bridging bidentate ligand to **SAM C_2**, that would allow coordination of complex **C_2** on top. In principle, it could be expanded to multilayers of complex **C_2** by replacing bridging bidentate ligand with specific rigid polydentate ligand.

- ***Side reactions due to ambient conditions.*** SAM formation, Fe coordination and ligand exchange could be performed under inert nitrogen atmosphere, in order to eliminate possibility of side reactions or oxidation under ambient conditions.

- ***Coordination of different metal centres.*** Ions of other transition metals, for example cobalt(II), could be used to explore how their SCO behaviour is affected by their close proximity to gold surfaces, and whether unique properties of $\mathbf{Py_5}$ complexes[20–22] are preserved.

- ***Different characterisation methods.*** Cyclic voltammetry (CV) could be used to identify the oxidation state of Fe ions. Fourier Transform Infrared (FTIR), Enhanced Raman spectroscopy (NPoM configuration), near edge X-ray absorption fine structure (NEXAFS), X-ray magnetic circular dichroism (XMCD) could be used as alternatives to XPS to identify the spin state and molecular structure of complexes in the SAMs, while their packing or ordering could be studied with scanning tunneling microscopy (STM) and atomic-force microscopy (AFM).

6.3 Stability of COOH-terminated SAMs under soft UV in acidic conditions

It has been shown that **ALA SAM** and other COOH-terminated SAMs of similar thickness are unstable under soft UV irradiation in the acidic catalyst 100 mM HCl in IPA. It was also shown that the severity of the instability gradually increases with decreasing thickness, and this is the primary reason for the loss of molecules in **ALA SAM**. Nevertheless, the precise mechanism for the removal of the molecules is not known, because none of the compounds absorb strongly at 365 nm. However, it is clear that UV light and the presence of HCl is required.

A number of different aspects of the system could be investigated in order to gain a better understanding of the phenomenon. Firstly, different catalysts with lower concentrations of HCl or with alternative acids could be investigated. Secondly,

a photo-reaction study could be performed to determine a precise photo-reaction rate and photo-sensitivity to different wavelengths investigated. Finally, catalysts based on different solvents could be investigated. Additionally, SAMs with different functional groups could be studied. Hydrophobic SAMs with CH_3 functional group could be investigated to understand if polar end groups or disorder in the SAM play a more important role in the penetration of the catalyst to the gold surface. If end groups do play an important role, than alternative photo-deprotectable functional groups, such as amines, could be investigated for better SAM stability in photo-deprotectable systems. COOH SAMs presented in this chapter were purposely formed under the same conditions as **SAM1**, however, the stability of COOH SAMs formed under the optimum conditions,[1,2,23–27] could be investigated.

6.4 References

[1]R. Arnold, W. Azzam, A. Terfort and C. Wöll, Langmuir **18**, 3980–3992 (2002).

[2]A. Myrskog, H. Anderson, T. Aastrup, B. Ingemarsson and B. Liedberg, Langmuir **26**, 821–829 (2010).

[3]L. Gao, Y. Fang, X. Wen, Y. Li and D. Hu, J. Phys. Chem. B **108**, 1207–1213 (2004).

[4]L. Gao, Y. Fang, F. Lü, M. Cao and L. Ding, Appl. Surf. Sci. **252**, 3884–3893 (2006).

[5]S. Zhang, F. Lü, L. Gao, L. Ding and Y. Fang, Langmuir **23**, 1584–90 (2007).

[6]S. Zhang, L. Ding, F. Lü, T. Liu and Y. Fang, Spectrochim. Acta. A. Mol. Biomol. Spectrosc. **97**, 31–7 (2012).

[7]F. Lü, Y. Fang and G. Blanchard, Spectrochim. Acta Part A Mol. Biomol. Spectrosc. **74**, 991–999 (2009).

[8]L. Pukenas, F. Benn, E. Lovell, A. Santoro, L. J. Kershaw Cook, M. A. Halcrow and S. D. Evans, J. Mater. Chem. C **3**, 7890–7896 (2015).

[9]C. R. Goldsmith, R. T. Jonas, A. P. Cole and T. D. P. Stack, Inorg. Chem. **41**, 4642–4652 (2002).

[10]Christian R. Goldsmith, Robert T. Jonas and T. D. P. Stack, J. Am. Chem. Soc. **124**, 83–96 (2002).

[11]S. Beniwal, X. Zhang, S. Mu, A. Naim, P. Rosa, G. Chastanet, J.-F. Létard, J. Liu, G. E. Sterbinsky, D. A. Arena, P. A. Dowben and A. Enders, J. Phys. Condens. Matter **28**, 206002 (2016).

[12]B. Warner, J. C. Oberg, T. G. Gill, F. El Hallak, C. F. Hirjibehedin, M. Serri, S. Heutz, M. A. Arrio, P. Sainctavit, M. Mannini, G. Poneti, R. Sessoli and P. Rosa, J. Phys. Chem. Lett. **4**, 1546–1552 (2013).

[13]T. G. Gopakumar, M. Bernien, H. Naggert, F. Matino, C. F. Hermanns, A. Bannwarth, S. Mühlenberend, A. Krüger, D. Krüger, F. Nickel, W. Walter, R. Berndt, W. Kuch and F. Tuczek, Chem. - A Eur. J. **19**, 15702–15709 (2013).

[14]A. Pronschinske, R. C. Bruce, G. Lewis, Y. Chen, A. Calzolari, M. Buongiorno-Nardelli, D. A. Shultz, W. You and D. B. Dougherty, Chem. Commun. **49**, 10446–10452 (2013).

[15]M. Bernien, 'X-Ray Absorption Spectroscopy of Fe Complexes on Surfaces : Electronic Interactions and Tailoring of the Magnetic Coupling (Thesis)', PhD thesis (2009).

[16]T. G. Gopakumar, F. Matino, H. Naggert, A. Bannwarth, F. Tuczek and R. Berndt, Angew. Chemie - Int. Ed. **51**, 6262–6266 (2012).

[17]M. Bernien, H. Naggert, L. M. Arruda, L. Kipgen, F. Nickel, J. Miguel, C. F. Hermanns, A. Krüger, D. Krüger, E. Schierle, E. Weschke, F. Tuczek and W. Kuch, ACS Nano **9**, 8960–8966 (2015).

[18]M. Bernien, D. Wiedemann, C. F. Hermanns, A. Kruüger, D. Rolf, W. Kroener, P. Muüller, A. Grohmann and W. Kuch, J. Phys. Chem. Lett. **3**, 3431–3434 (2012).

[19]H. Naggert, A. Bannwarth, S. Chemnitz, T. von Hofe, E. Quandt and F. Tuczek, Dalton Trans. **40**, 6364–6366 (2011).

[20]C. Bachmann, M. Guttentag, B. Spingler and R. Alberto, Inorg. Chem. **52**, 6055–6061 (2013).

[21]J. R. Long, C. J. Chang and Y. Sun, **2**, 9212–9215 (2013).

[22]B. Das, A. Orthaber, S. Ott and A. Thapper, Chem. Commun. **51**, 13074–13077 (2015).

[23]R. G. Nuzzo, L. H. Dubois and D. L. Allara, J. Am. Chem. Soc. **112**, 558–569 (1990).

[24]J. Li, K. S. Liang, G. Scoles and A. Ulman, Langmuir **11**, 4418–4427 (1995).

[25]E. L. Smith, C. a. Alves, J. W. Anderegg and M. D. Porter, Langmuir **8**, 2707–2714 (1992).

[26]O. Dannenberger, K. Weiss, H. J. Himmel, B. Jäger, M. Buck and C. Wöll, Thin Solid Films **307**, 183–191 (1997).

[27]H. J. Himmel, K. Weiss, B. Jäger, O. Dannenberger, M. Grunze and C. Wöll, Langmuir **13**, 4943–4947 (1997).

Appendix A

Characterisation of Photocleavage of Acetylpyrene SAM

This appendix provides additional information related to the study of photolysis in **SAM1** and **reagent 1** layers presented in chapter 3.

A.1 Discrepancy between molecular structure of reagent 1 and XPS data

This section explains why XPS data presented in section 3.2.3.1 is normalised correctly to study surface coverage and change in its chemical composition, but it is not appropriate for the study of the precise molecular structure in **SAM1**. Chemical ratios determined from appropriately normalised (based on ether (C-O) oxygen) XPS data are presented in table A.1. There is a discrepancy between chemical ratios given in table A.1 and the expected values based on molecular structure of **reagent**

1 (figure 3.1a), which is associated with damaged induced by the acquisition of XPS data, because other techniques yield expected characteristics of the SAM, as discussed in section 3.2.4. After all, by a pure coincidence, normalised XPS data presented in section 3.2.3.1 and table 3.5 give a more accurate representation of non-damaged fresh **SAM1**, than correctly normalised data presented in this section and table A.1. Nevertheless, discussion presented in this section highlights the potential instability of aryl ketone under the XPS conditions, and highlights, that depending on which aspects of a system are under investigation, XPS data analysis and a choice of normalisation method may require a great caution.

XPS spectra in section 3.2.3.1 are normalised to Au $4f_{7/2}$ peak, while ratios of chemical elements in table 3.5 are relative to S 2p region. Such normalisation methods can result in overestimation of relative amount of chemical elements in a SAM due to attenuation of XPS signal, which increases with the thickness and packing of a SAM. The further away from the gold-SAM interface are the atoms, and the more densely packed is the SAM, the higher the overestimation is of their relative amounts. This is particularly useful in monitoring increase or decrease of SAM thickness or surface coverage, because changes in chemical ratios (determined by XPS) are enhanced by increase or decrease of this overestimation, in addition to increase or decrease of SAM thickness and its packing. Therefore, this method of data normalisation was preferred in the study of **SAM1** photolysis presented in section 3.2.3.1.

However, such normalisations can lead to incorrect interpretation of other aspects of a SAM. For example, while data in table 3.5 clearly show that chemical composition of the treated **SAM1** is completely different from the expected (and measured) values for fully (or at least partially) deprotected lipoic acid monolayer, data in the table can lead to wrong assumptions about molecular structure of **reagent 1** molecule in fresh **SAM1**. This can be illustrated by considering analysis of the

chemical ratios. Table 3.5 suggests 1.3 ether (C-O) and 1.8 (C=O) carbonyl **oxygens**, and 1.2 ether (C-O) and 1.8 (C=O) carbonyl **carbons** per molecule. It might seem to be acceptable to approximate the values to 1 and 2 atoms for each type of carbon and oxygen, and draw a conclusion that this confirms presence of one C-O group and two carbonyl groups, which agree with the molecular structure (figure 3.1a).

TABLE A.1: Peak areas and relative ratios of chemical species (presented in the brackets) in fresh **SAM1**, **ALA SAM**, **MHA SAM** and **MOA SAM** based on XPS spectra.

	Carbon			Oxygen			Gold	Sulfur
SAM	C=O	C-O	Total	C=O	C-O	Total		
SAM1	35 (1.4)	22 (0.9)	577 (23.0)	36 (1.4)	25 (**1.0**)	61 (2.5)	512 (20.4)	39 (1.5)
ALA SAM	39 (1.3)	-	285 (9.7)	36 (1.2)	29 (**1.0**)	66 (2.2)	644 (22.0)	62 (2.1)
MOA	43 (1.3)	-	356 (10.9)	40 (1.2)	33 (**1.0**)	73 (2.2)	621 (19.0)	29 (0.9)
MHA	37 (1.2)	-	233 (7.8)	39 (1.3)	30 (**1.0**)	69 (2.3)	687 (23.1)	31 (1.1)

Nevertheless, XPS data clearly show that there is only 40 % more carbonyl (C=O) oxygen and carbon than ether (C-O) oxygen and carbon, respectively, in fresh **SAM1**. That is evident in the O 1s spectra (figure 3.8a) and C 1s spectra (figure 3.7a) of fresh **SAM1**, which visually show that C=O peaks are not twice as large as C-O, and as indicated by the integrated peak areas of the spectra in tables 3.3 and 3.2; such comparison of chemical species is not affected by the spectra normalisation, and therefore stays the same, whether data is normalised to Au 4f, S 2p, O 1s or any other region or chemical species. It is also important to note that such values were repeatedly obtained on multiple samples from multiple batches. Chemical ratios determined from XPS data normalised to ether(C-O) carbon (table

A.1) correctly represent this trend, but also yield reasonable values for other regions in **SAM1**, **ALA SAM**, **MHA SAM** and **MOA SAM**.

If relative ratios of carbonyl to ether oxygen in fresh **ALA SAM**, **MHA SAM** and **MOA SAM** are used as a baseline, which show 20-30 % stronger signal from carbonyl oxygen, then fresh **SAM1** show only ∼15 % more carbonyl then ether oxygen per molecule.

Appendix B

SAMs for spin crossover (SCO) surfaces

B.1 SAM L_2 and SAM C_2 - effects of normalising spectra to N 1s

This section explains why XPS spectra (presented in section 4.3) were normalised (scaled) using N 1s region, and describes the expected changes in the spectra, which might not seem intuitive at first glance.

If XPS spectra of SAMs on gold do require intensity normalisation (scaling), it is normal practice to use the Au 4f region. However, a strong variation in Au 4f relative to other regions in **SAM L_2**, **SAM L_2+Fe** and **SAM C_2** suggests varying surface coverage, and therefore normalisation to gold is not an appropriate method to study molecular structure of those SAMs. The only element that does not change in quantity across the SAMs is sulfur. However, due to exceptionally weak peak and the fact that thiomorpholine-like sulfur appears as a mixture of two doublets, S 2p region is not appropriate for intensity normalisation either.

Depending on the sixth exogenous ligand (SEL), all the other elements, i.e. iron, oxygen, carbon and nitrogen do vary upon Fe(II) coordination to ligand $\mathbf{L_2}$ or ligand exchange in complex $\mathbf{C_2}$. The study presented in section 4.3 investigates MeCN, MeOH and H_2O as the SEL in **SAM $\mathbf{C_2}$**, therefore expected change in chemical composition can be predicted. Nevertheless, only N 1s region is appropriate for normalisation, because Fe 2p peaks are subject to a variation due to baseline correction of the complex background, while peaks in O 1s and C 1s regions vary between some samples and always show abnormally high excess.

Expected changes in peak areas are tabulated for (i) the perfect SAMs with no excess in carbon and oxygen (table B.1), and (ii) when the excess detected in **SAM $\mathbf{L_2}$** and **SAM $\mathbf{C_2}$** is used as a baseline (table B.2).

TABLE B.1: Expected relative ratios of chemical elements in **SAM $\mathbf{C_2}$** with different SELs (based on molecular structure), and expected change in peak areas, if the spectra are normalised to have equal integrated areas of thiomorpholine-like sulfur in S 2p,[c] or equal integrated areas in N 1s.[b]

	SAM $\mathbf{C_2}$ with exogenous ligand				Change in peak area	
Element	MeOH	H_2O	MeCN[a]	**MeCN scaled**[b]	MeCN[c] vs MeOH/H_2O[d]	**MeCN scaled**[b] vs MeOH/H_2O[d]
N	6	6	7[a]	**6.00**[b]	17 %[c]	**0 %**[b]
C	32	31	33	**28.29**	5 %[d]	**−10 %**[d]
O	3	3	2	**1.71**	−33 %	**−43 %**
S	1	1	1	**0.86**	0 %	**−14 %**
Fe	1	1	1	**0.86**	0 %	**−14 %**

[a] Based on molecular structure.

[b] Spectra are normalised to show equal integrated areas in region N 1s in **SAM $\mathbf{C_2}$** with exogenous MeCN ligand and with exogenous MeOH/H_2O ligand; the area is set to be equal to 6 for convenience. Thus, when compared former with the later spectra, it appears as if there are equal amount of N, but less S, Fe, O and C in **SAM $\mathbf{C_2}$** with MeCN ligand.

[c] If spectra of **SAM $\mathbf{C_2}$** with exogenous MeCN and MeOH/H_2O ligands are normalised to have equal peak areas of thiomorpholine-like sulfur in S 2p, then differences between the spectra directly correspond to differences between molecular structures of the SAMs. Thus, such spectra in the SAMs would show equal amounts of S and Fe, but increase in nitrogen and drop in oxygen in the SAM with MeCN as the SEL. Percentage values correspond to change in spectra of **SAM $\mathbf{C_2}$** with MeCN as the SEL w.r.t. to MeOH/H_2O as the SEL. However, in practise this method of normalisation was not useful due to weak and complex peaks in S 2p region.

TABLE B.2: Expected apparent drop in peak areas, when XPS spectra of **SAM C_2** with different SELs are normalised to have equal N 1s areas **(based on measured ratios)**.

Element	MeCN-MeOH[d]	MeCN-H_2O[d]
N	0 %	
C	−12 %	
O	−22 %	
S	−14 %	
Fe	−14 %	

[d] **SAM C_2** with MeOH and H_2O ligands only differ by one carbon atom (i.e. 3 % or, if excess of C is taken into account as a baseline, 2 %). The change is minute, given sample to sample deviation and signal-to-noise ratio. Furthermore, out of all the spectra that are expected to change, C region gives the smallest difference, when compared to **SAM C_2** with MeCN ligand. Therefore, **SAM C_2** with MeOH and H_2O ligands are treated as identical and referred to as MeOH/H_2O, while the change in C is averaged.

B.2 XPS spectra with fitted components

B.2.1 SAM L_2

Representative XPS spectra of **SAM L_2** with fitted components to supplement data presented in section 4.3.1.1. Associated chemical species, average peak positions, FWHM, integrated and fractional areas of fitted components are presented in tables 4.4 - 4.9.

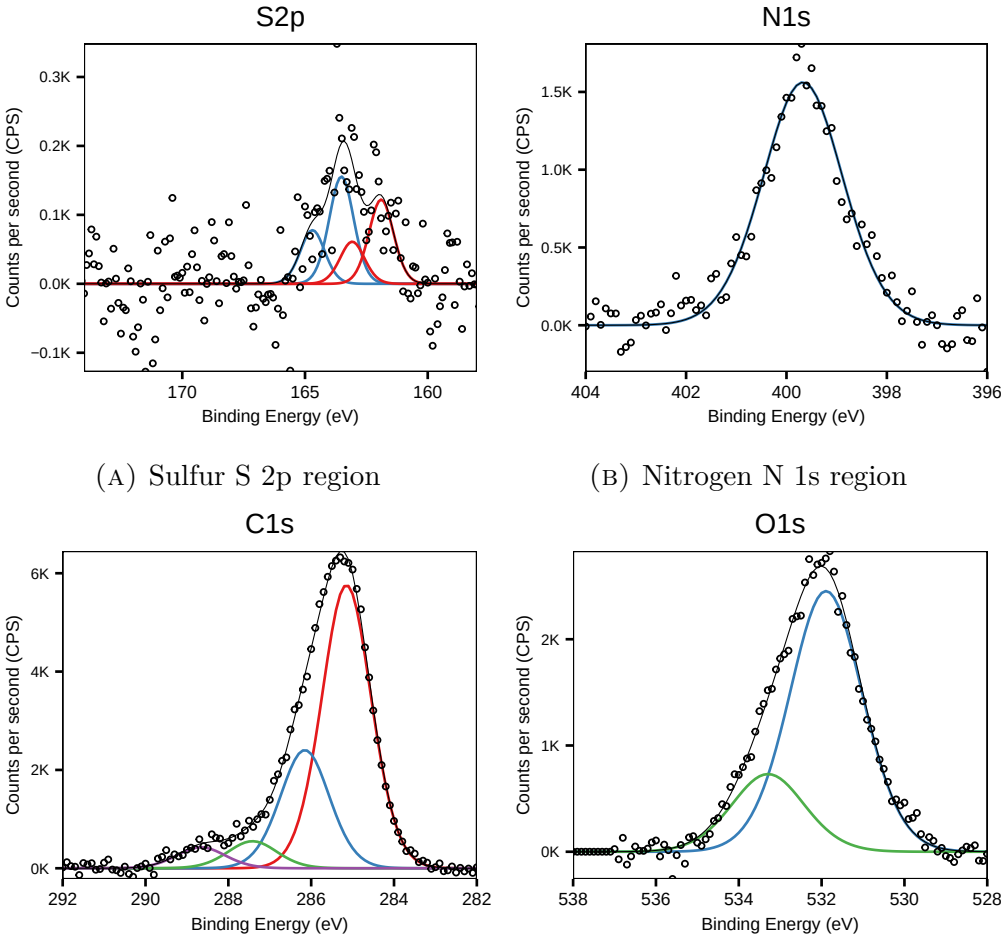

(A) Sulfur S 2p region

(B) Nitrogen N 1s region

(C) Carbon C 1s region

(D) Oxygen O 1s region

FIGURE B.1: High resolution XPS spectra with fitted components of **SAM L_2**.

B.2.2 SAM C_2

One of the representative XPS spectra of **SAM C_2** with fitted components to supplement data presented in section 4.3.1.1. Associated chemical species, average peak positions, FWHM, integrated and fractional areas of fitted components are presented in tables 4.4 - 4.9.

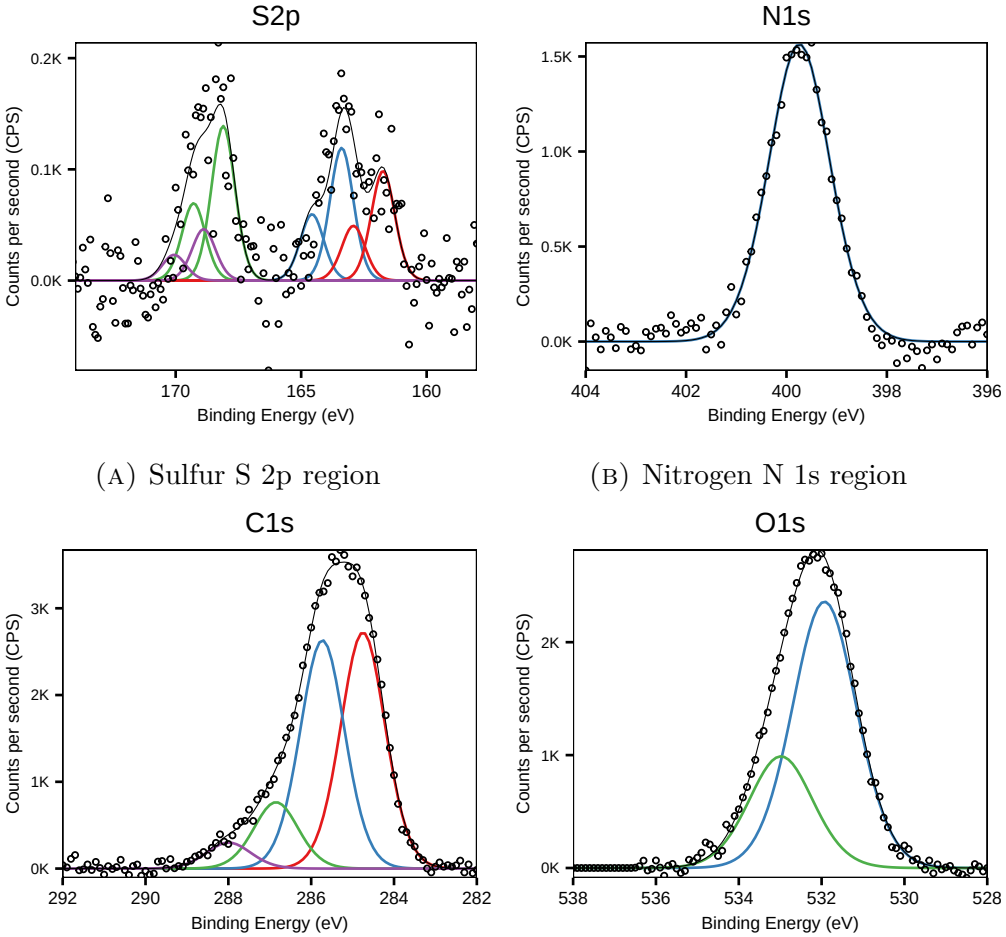

(A) Sulfur S 2p region

(B) Nitrogen N 1s region

(C) Carbon C 1s region

(D) Oxygen O 1s region

FIGURE B.2: High resolution XPS spectra with fitted components of **SAM C_2**.

B.2.3 SAM L_2+Fe(1m)

XPS spectra with fitted components of **SAM L_2+Fe(1m)** exposed to ∼5 mM $Fe(ClO_4)_2$ in MeCN to supplement data presented in section 4.3.3. A distinct peak at 530.3 eV in O 1s region is only present in **SAM L_1+Fe(1m)** exposed to ∼5 mM $Fe(ClO_4)_2$ in MeCN (and **SAM L_1** exposed to aqueous solution of ∼5 mM $Fe(ClO_4)_2$), but not detected in **SAM L_1+Fe(30m)**, **SAM L_1** or **SAM C_2**. The peak is associated with oxygen in iron oxides.[1–3] For further details, please see section 4.3.3.1.

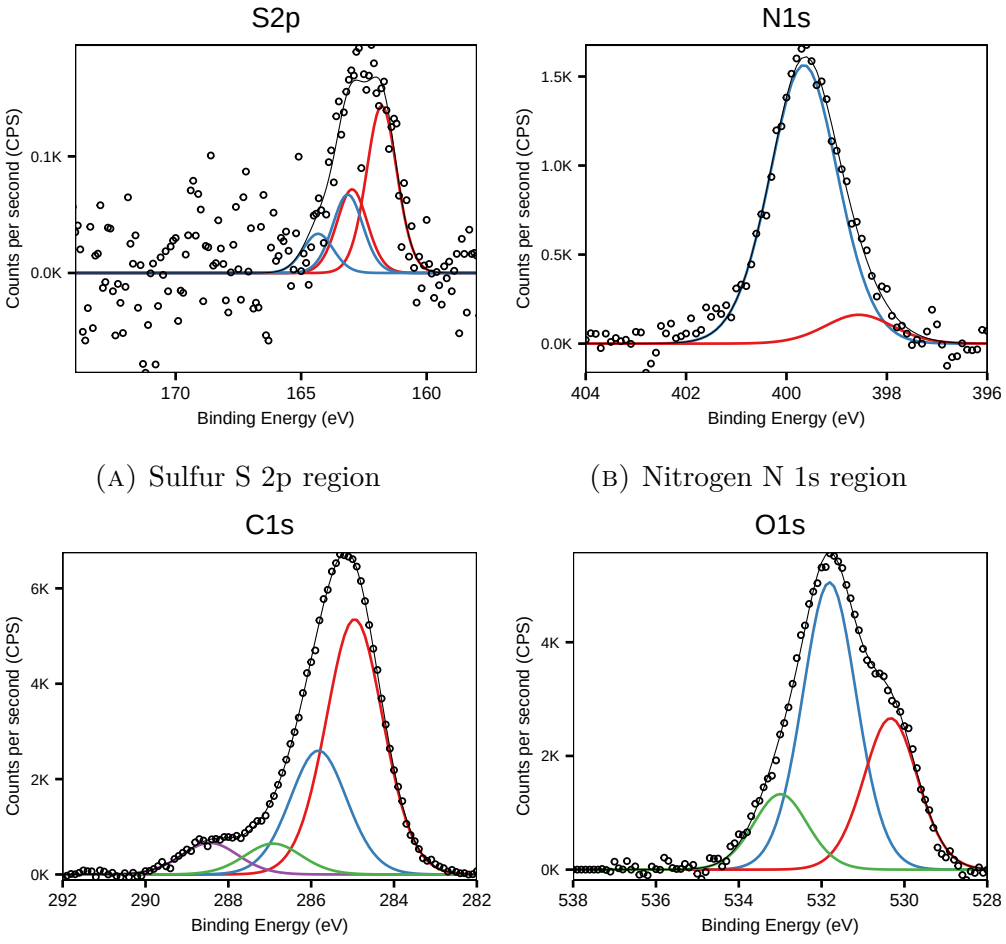

(A) Sulfur S 2p region

(B) Nitrogen N 1s region

(C) Carbon C 1s region

(D) Oxygen O 1s region

FIGURE B.3: High resolution XPS spectra with fitted components of **SAM L_2+Fe(1m)**.

B.3 Ligand exchange in SAM C_2 by rinsing - additional XPS spectra

B.3.1 Fe 2p region acquired at higher pass energies

Additional XPS spectra to supplement data and support discussions in section 4.3.2. Figures B.4 and B.5 show XPS spectra of Fe 2p region acquired at higher values of pass energy (PE) than spectra in figures 4.16b and 4.17b, respectively. Acquisition at higher pass energies increases intensity of a spectrum, which can help to distinguish some differences between the spectra of different samples or their states.

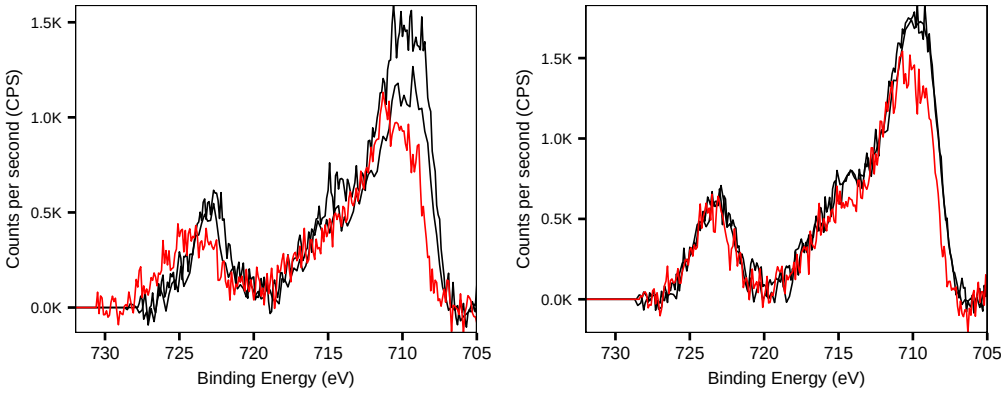

(A) Pass energy 30 eV (B) Pass energy 40 eV

FIGURE B.4: High resolution XPS spectra of Fe 2p region in **SAM C_2 [MeOH]** before (in **black**) and after (in **red**) rinsing with MeCN. Spectra of the same colour in figures a) and b) were acquired in consecutive order on the same sample. Multiple spectra of the same colour within figures a) and b) were acquired at the same pass energy, but at different spectral resolutions (i.e. 0.1 eV and 0.2 eV).

Figure B.4 shows spectra of Fe 2p region of **SAM C_2 [MeOH]** before and after the rinse with MeCN, however, no change in the peak shape is evident, that would be associated with switching between HS and LS states. The change in intensity in figures B.4a and B.4b is associated with baseline correction of the complex background, because (i) the change in intensity is evident between the spectra in black (figure B.4a), which correspond to two consecutive measurements on the same sample in the same state, and (ii) no differences in intensity are evident in figure 4.16b.

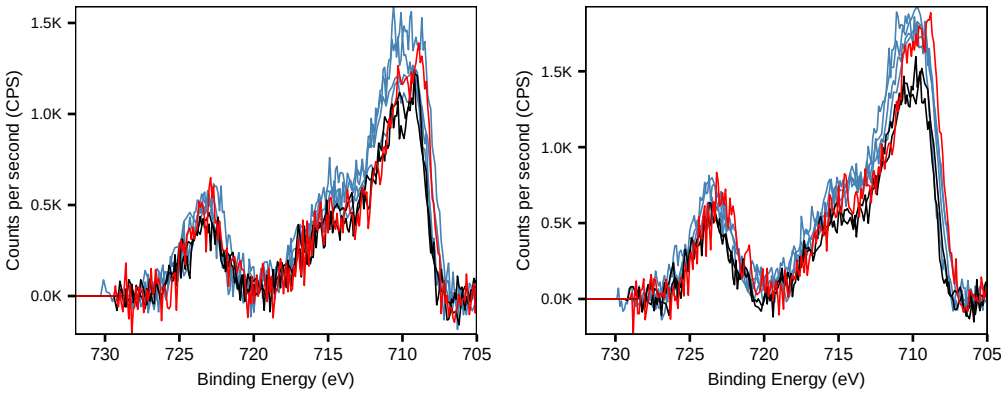

(A) Pass energy 30 eV (B) Pass energy 40 eV

FIGURE B.5: High resolution XPS spectra of Fe 2p region in **SAM C_2 [MeCN]** before (**in black**) and after (**in red**) rinsing with MeOH. For the comparison purposes, spectra of the first sample (**SAM C_2 [MeOH]** before the rinse with MeCN) and the second sample (**SAM C_2 [MeOH]** rinsed with MeCN immediately after SAM formation) are added (**in blue**). Spectra within red and black sets in figures a) and b) were acquired in consecutive order on the same sample. Multiple spectra in red and in black within figures a) and b) were acquired at the same pass energy, but at different spectral resolutions (i.e. 0.1 eV and 0.2 eV).

Figure B.5 shows spectra of Fe 2p region of **SAM C_2 [MeCN]** before and after the rinse with MeOH, but also includes spectra of the first sample (**SAM C_2 [MeOH]** before the rinse with MeCN) and the second sample (**SAM C_2 [MeOH]** rinsed with MeCN immediately after SAM formation) for comparative purposes. However, no change in the peak shape is evident, that would be associated with switching between HS and LS states.

As in the case of spectra in figure B.4, variation in intensity in figure B.5 is associated with baseline correction of the complex background. A distinct feature (i.e. sharp double peak) in Fe $2p_{3/2}$ peak in the red and black spectra in figure B.5a is attributed to an artefact due to combination of low intensity and low signal-to-noise ratio, because those features are not present in consecutively acquired spectra at pass energy of 40 eV(figure B.5b).

B.3.2 SAM C_2 [MeOH] - comparison of fresh (sample 1) and immediately rinsed with MeCN (sample 2)

Additional XPS spectra to supplement data and support discussions in section 4.3.2. Figures B.6 and B.7 compare spectra of sample 1 (**SAM C_2 [MeOH]** before it was rinsed with MeCN) and sample 2 (**SAM C_2 [MeOH]** taken out of the growth solution, rinsed with pure MeOH, dried under stream of nitrogen and immediately rinsed with MeCN). Regions N 1s, O 1s and S 2p yield no important differences, while shape of peaks in Fe 2p region is the same and variation in intensity is assigned to artefacts due to baseline correction of the complex background.

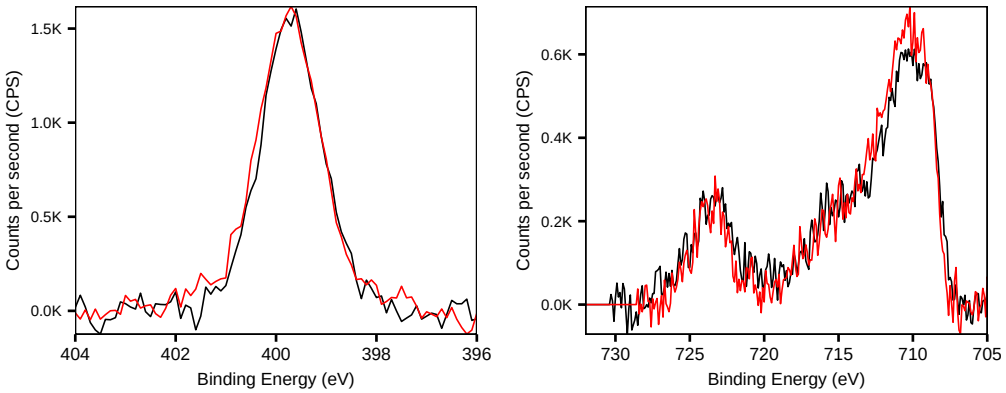

(A) Nitrogen N 1s region (B) Iron Fe 2p region

(C) Iron Fe 2p region (Pass energy 30 eV) (D) Iron Fe 2p region (Pass energy 40 eV)

FIGURE B.6: High resolution XPS spectra of sample 1 (**SAM C_2 [MeOH]** before the rinse with MeCN) in **black** and sample 2 (**SAM C_2 [MeOH]** rinsed with MeCN immediately after SAM formation) in **red**. Spectra of the same colour in figures b), c) and d) were acquired in consecutive order on the same sample. Multiple spectra of the same colour within figures c) and d) were acquired at the same pass energy, but at different spectral resolutions (i.e. 0.1 eV and 0.2 eV).

Difference in intensity in C 1s region in figure B.7b is small, and attributed to lower levels of adventitious hydrocarbons in sample 2.

A distinct feature (i.e. double peak) in Fe $2p_{3/2}$ peak in one of the black spectra in figure B.6c is attributed to an artefact due to combination of low intensity and low signal-to-noise ratio, as the feature is not present in other black spectra in figure B.6, which were acquired in consecutive order. Likewise the same cause is attributed to a similar feature in the red spectrum in figure B.6b.

Overall, spectra in B.6 and B.7 suggest almost identical chemical composition in both SAMs and do not indicate change of SEL and spin state in Fe ion.

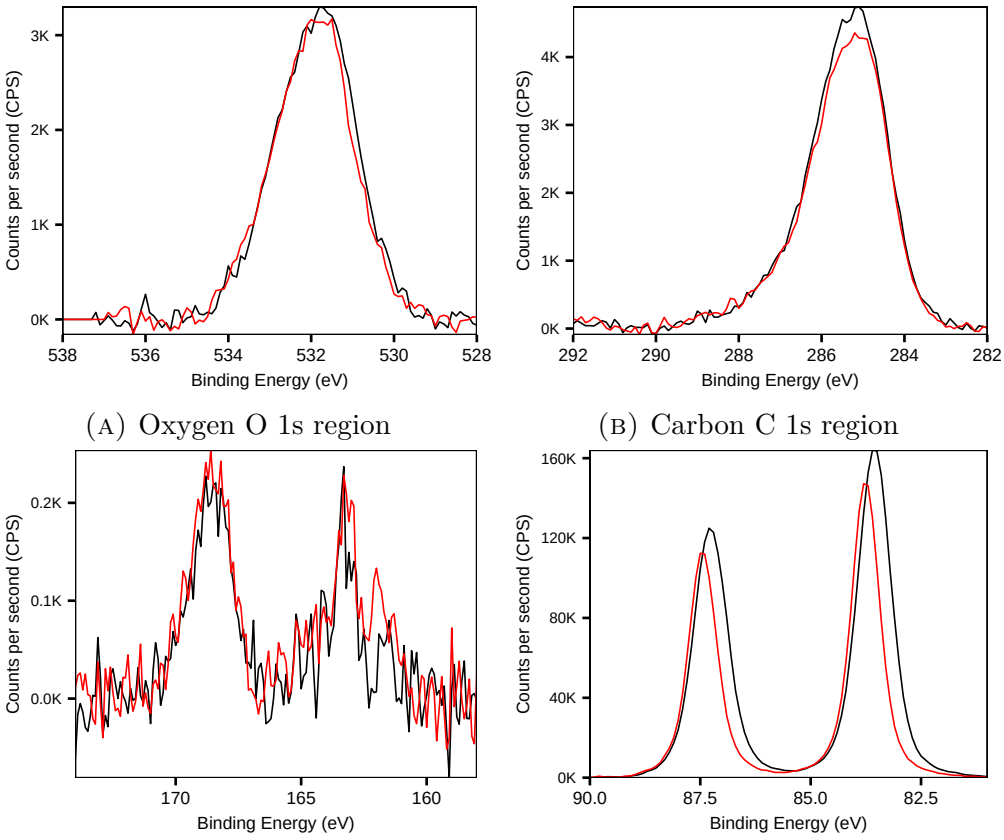

(A) Oxygen O 1s region

(B) Carbon C 1s region

(C) Sulfur S 2p region

(D) Gold Au 4f region

FIGURE B.7: High resolution XPS spectra of sample 1 (**SAM C_2 [MeOH]** before the rinse with MeCN) in **black** and sample 2 (**SAM C_2 [MeOH]** rinsed with MeCN immediately after SAM formation) in **red**.

B.3.3 Comparison of SAM C_2 [MeOH] (sample 2) rinsed once and twice with MeCN

Additional XPS spectra to supplement data and support discussions in section 4.3.2. Figures B.8 and B.9 compare spectra of **SAM C_2 [MeOH]** (sample 2) rinsed once and twice with MeCN.

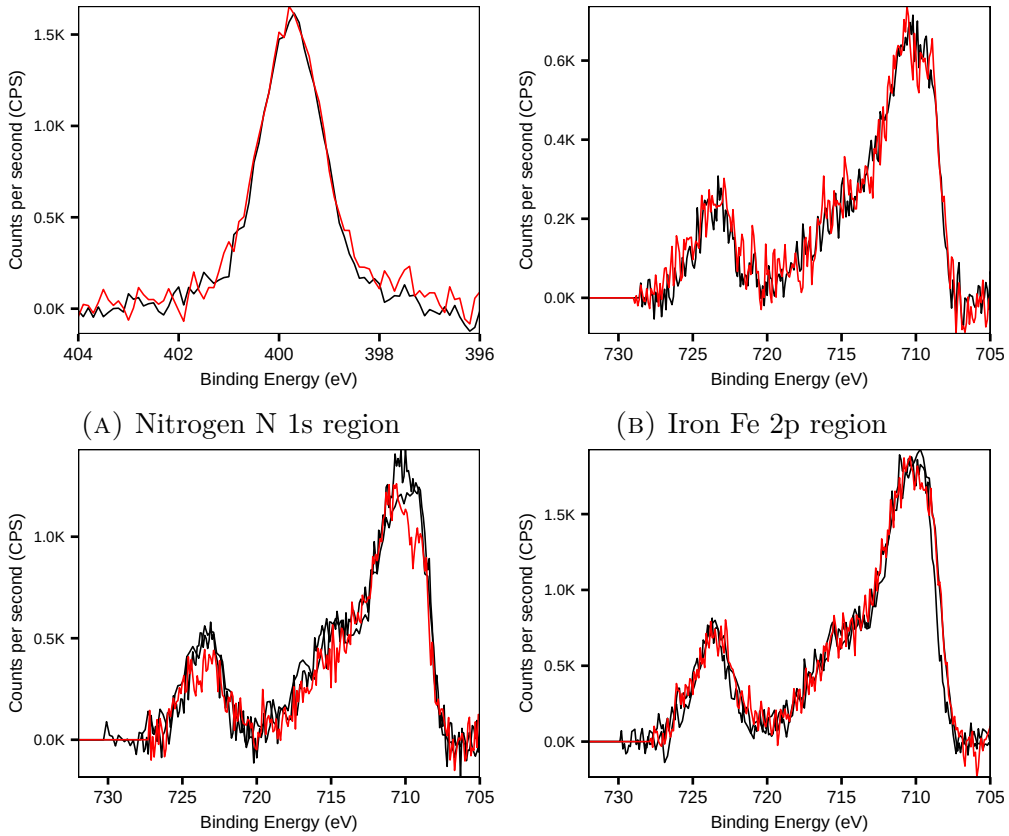

(A) Nitrogen N 1s region (B) Iron Fe 2p region

(C) Iron Fe 2p region (Pass energy 30 eV) (D) Iron Fe 2p region (Pass energy 40 eV)

FIGURE B.8: High resolution XPS spectra of **SAM C_2 [MeOH]** before (in **black**) and after (in **red**) the second rinse with MeCN. Spectra of the same colour in figures b), c) and d) were acquired in consecutive order on the same sample. Multiple spectra of the same colour within figures c) and d) were acquired at the same pass energy, but at different spectral resolutions (i.e. 0.1 eV and 0.2 eV).

Regions N 1s, Fe 2p, C 1s and O 1s yield no important differences, while a small drop in oxidised sulfur and a tiny increase in Au 4f signal could be indicative of removal of oxidised sulfur from the surface by the rinse or the artefacts due to the baseline correction of noisy background.

Again distinct features suggesting a separate sharp peak at $\sim$ 708 eV in Fe $2p_{3/2}$ peak in the red spectra in figures B.8b and B.8c are attributed to an artefact due to a combination of low intensity and low signal-to-noise ratio, as such features are not present in the red spectrum in figure B.8d, which was acquired in consecutive order on the same sample.

Overall, further rinse of **SAM C_2 [MeOH]** with MeCN does not affect its chemical composition, and does not suggest replacement of SEL or change in Fe spin state.

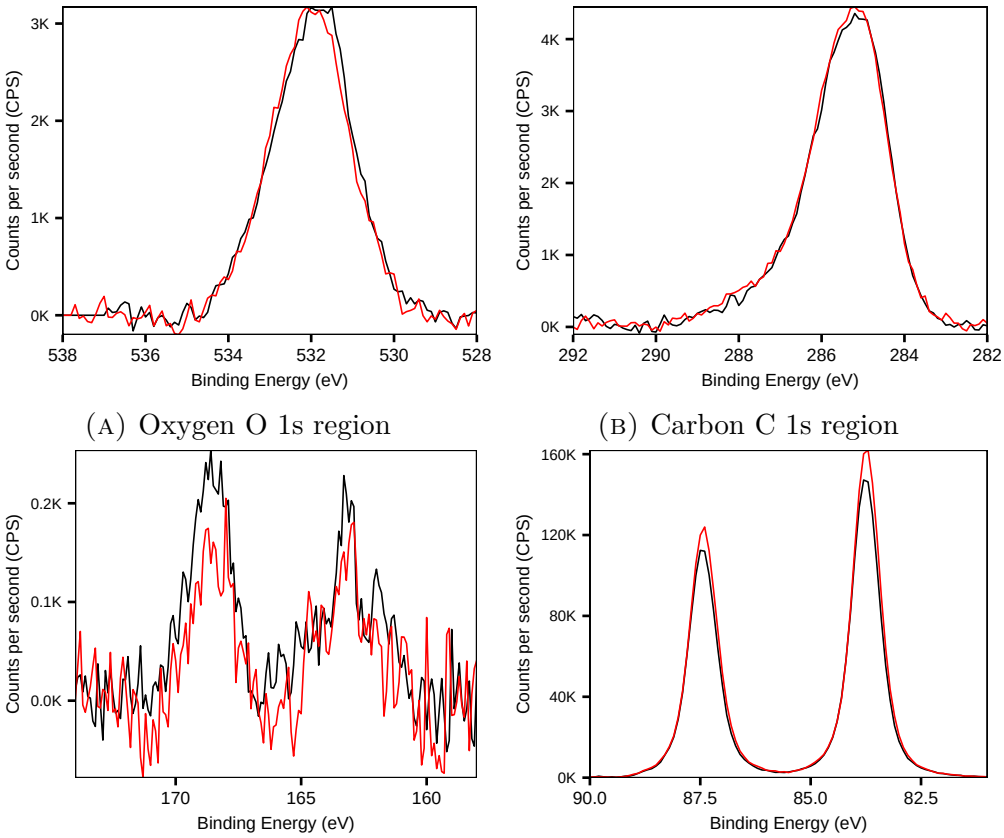

(A) Oxygen O 1s region

(B) Carbon C 1s region

(C) Sulfur S 2p region

(D) Gold Au 4f region

FIGURE B.9: High resolution XPS spectra of **SAM C_2 [MeOH]** before (in **black**) and after (in **red**) the second rinse with MeCN.

B.4 Fe(II) coordination to SAM L_2 in aqueous solution - additional XPS spectra

B.4.1 Rinsing with MeCN after 1 min of coordination

Additional XPS spectra to supplement data and support discussions in section 4.3.3. Figures B.10 and B.11 compare spectra of **SAM L_2+Fe(1m)** (produced by exposure to aqueous ~5 mM $Fe(ClO_4)_2$) before and after the rinse with MeCN. Increase in intensity of peaks in Fe 2p, O 1s, C 1s and Au 4f, is likely to be an artefact of using N 1s region to normalise intensities of the spectra, which suggest relative drop in integrated area of N 1s region. That could originate from an uncertainty induced by the weak signal or loss of nitrogen atoms. However, it is clear that rinsing with MeCN does not induce significant changes in chemical composition that could at least remotely be comparable to **SAM C_2**.

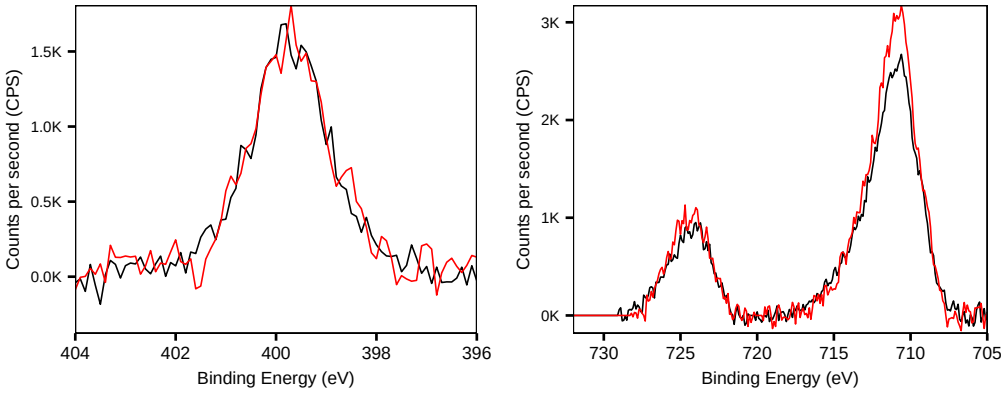

(A) Nitrogen N 1s region (B) Iron Fe 2p region

FIGURE B.10: High resolution XPS spectra of **SAM L_2+Fe(1m)** (produced by exposure to aqueous ~5 mM $Fe(ClO_4)_2$) before (in **black**) and after (in **red**) the rinse with MeCN.

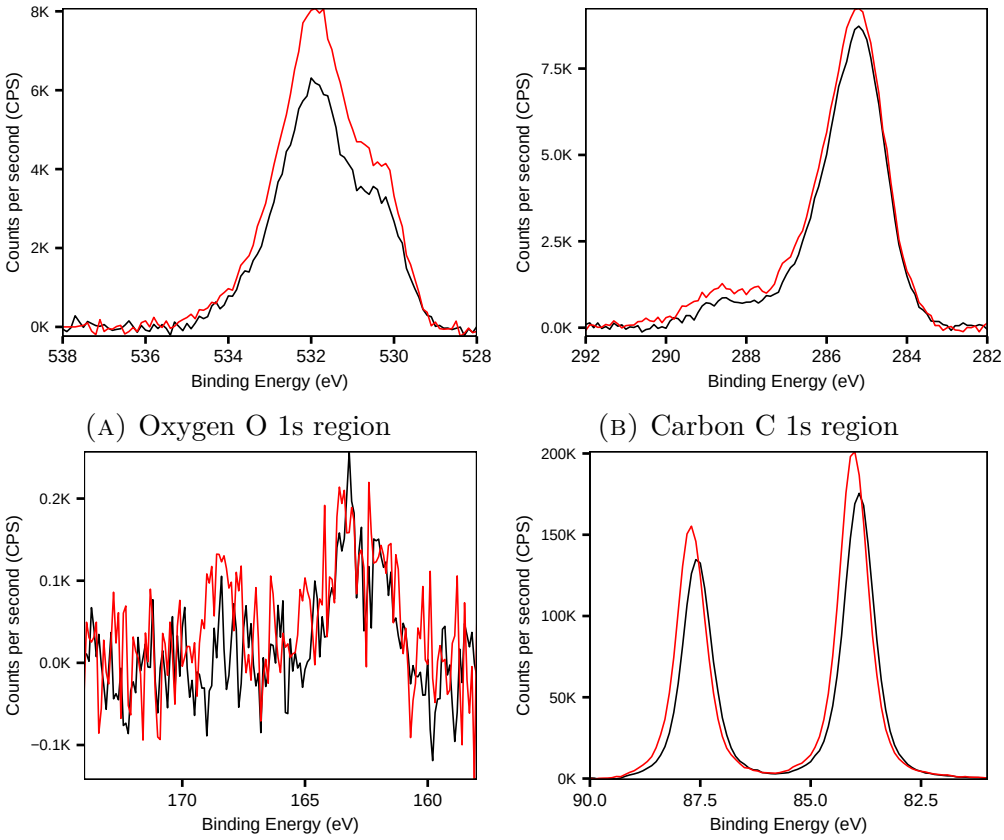

(A) Oxygen O 1s region

(B) Carbon C 1s region

(C) Sulfur S 2p region

(D) Gold Au 4f region

FIGURE B.11: High resolution XPS spectra of **SAM L_2+Fe(1m)** (produced by exposure to aqueous ∼5 mM $Fe(ClO_4)_2$) before (in **black**) and after (in **red**) the rinse with MeCN.

B.4.2 Rinsing with MeCN after 30 min of coordination

Additional XPS spectra to supplement data and support discussions in section 4.3.3. Figure B.12 compares spectra of **SAM L_2+Fe(30m)** (produced by exposure to aqueous ∼5 mM $Fe(ClO_4)_2$) before and after the rinse with MeCN. A drop in Fe 2p and C 1s, but increase in Au 4f peaks suggest small loss of material from the surface, which is also supported by the weaken intensity and signal-to-noise ratio in S 2p region. Despite some change in chemical composition in O 1s region, the SAM is not even remotely comparable to **SAM C_2**.

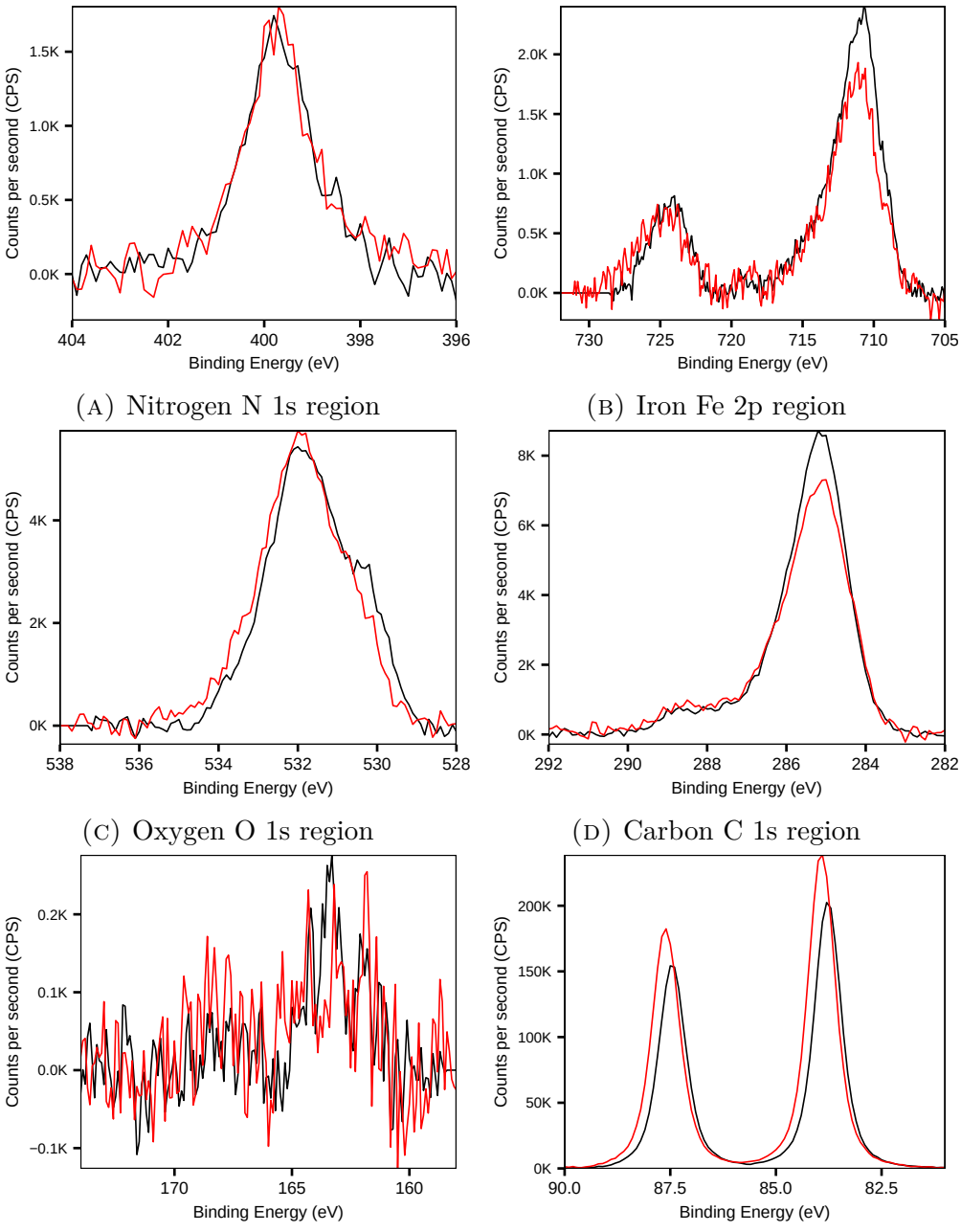

(A) Nitrogen N 1s region

(B) Iron Fe 2p region

(C) Oxygen O 1s region

(D) Carbon C 1s region

(E) Sulfur S 2p region

(F) Gold Au 4f region

FIGURE B.12: High resolution XPS spectra of **SAM L_2+Fe(30m)** (produced by exposure to aqueous ∼5 mM $Fe(ClO_4)_2$) before (in **black**) and after (in **red**) the rinse with MeCN.

B.5 Impurities in the SAMs - Cl, F and Br

XPS spectra of Cl, F and Br traces in **SAM L_2**, **SAM C_2 [MeOH]** and **SAM C_2 [MeCN]** to support discussions in sections 4.3.1.1 and 4.3.1.2

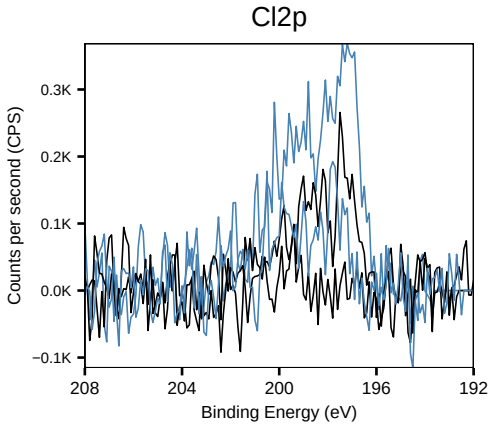

(A) Chloride Cl 2p region

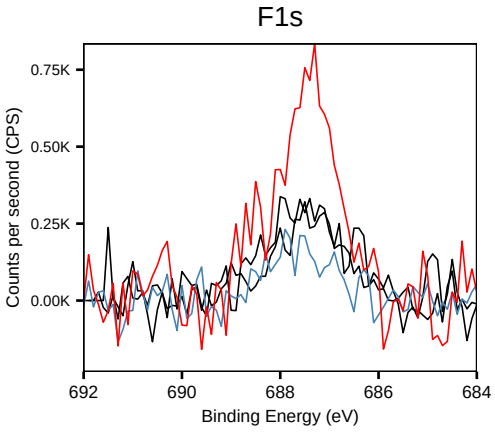

(B) Fluoride F 1s region

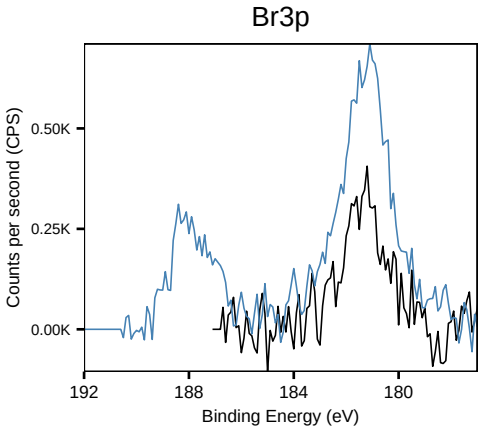

(C) Bromide Br 3p region

FIGURE B.13: High resolution XPS spectra (normalised and referenced to N 1s region) of **SAM L_2** (**in red**), **SAM C_2 [MeOH]** (**in black**) and **SAM C_2 [MeCN]** (**in blue**).

B.6 References

[1]M. C. Biesinger, B. P. Payne, A. P. Grosvenor, L. W. M. Lau, A. R. Gerson and R. S. S. Smart, Appl. Surf. Sci. **257**, 2717–2730 (2011).

[2]N. S. McIntyre and D. G. Zetaruk, Anal. Chem. (1977).

[3]A. P. Grosvenor, B. A. Kobe, M. C. Biesinger and N. S. McIntyre, Surf. Interface Anal. **36**, 1564–1574 (2004).

Appendix C

Characterisation of simple alkanethiol, aromatic, COOH- and azide-terminated SAMs

This appendix provides additional information related to the studies of (i) COOH–terminated SAMs stability under soft UV (365 nm) irradiation in acid, and (ii) azide terminated SAMs presented in chapter 5.

C.1 XPS spectra with fitted components of fresh and UV treated DTBA SAM

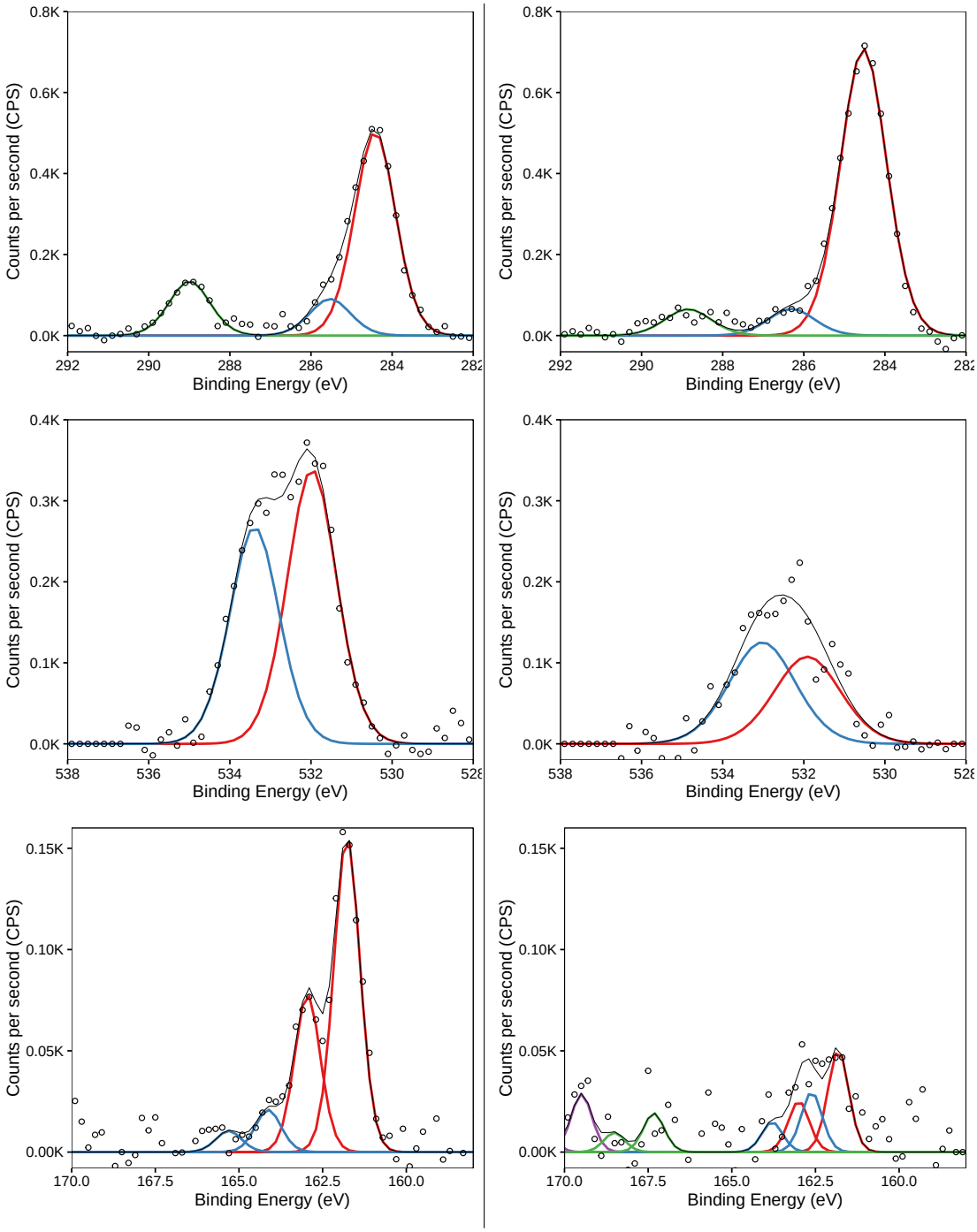

FIGURE C.1: XPS spectra with fitted components of fresh (on the left) and UV-treated (on the right) **DTBA SAM**. Spectra correspond to C 1s (top row), O 1s (middle row) and S 2p (bottom row). UV-treated samples were exposed to soft UV (365 nm, 4 mW cm^{-2}) for 1.5 h in the acidic catalyst (100 mM HCl in IPA).

C.2 XPS spectra with fitted components of fresh and UV treated MHA SAM

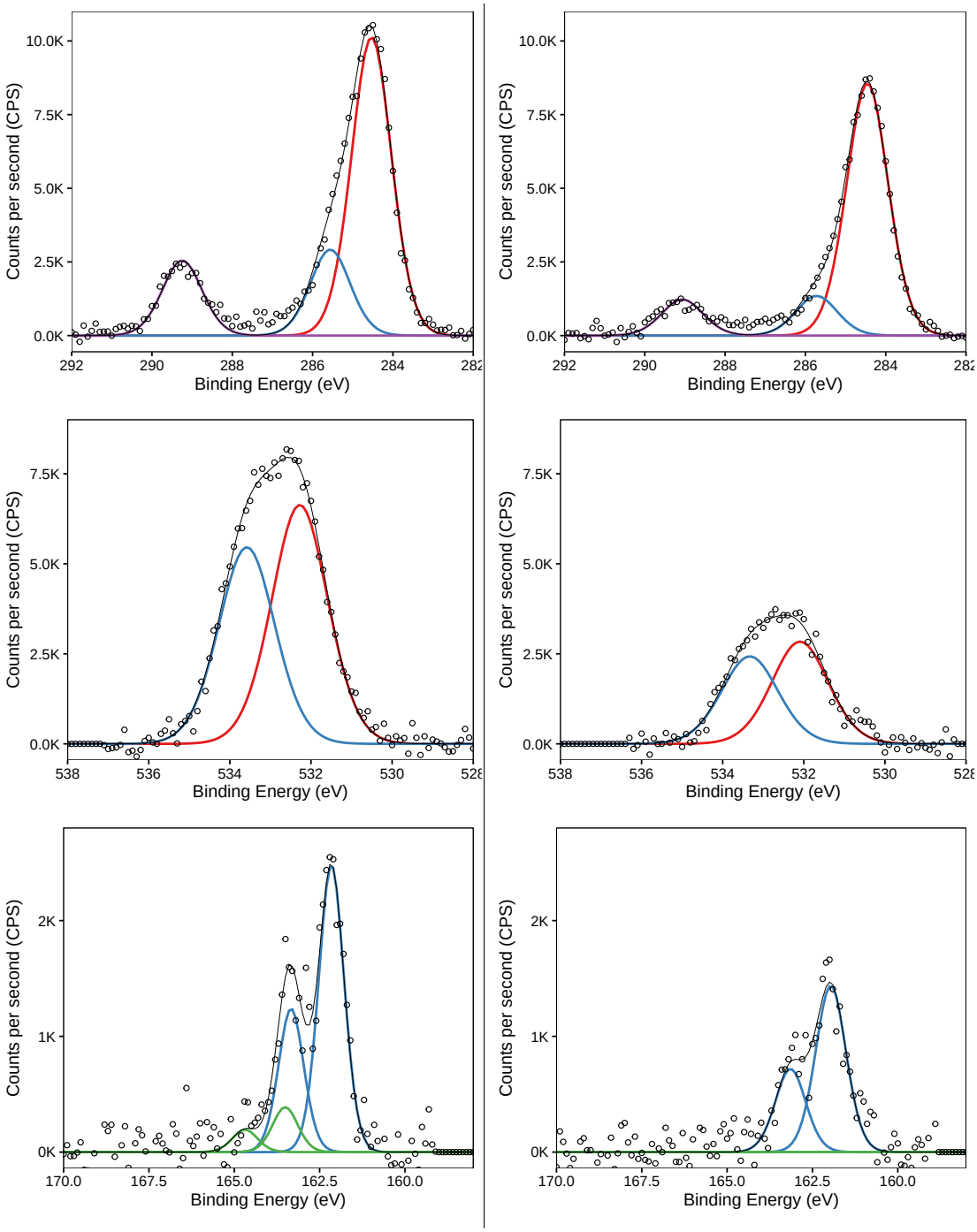

FIGURE C.2: XPS spectra with fitted components of fresh (on the left) and UV-treated (on the right) **MHA SAM**. Spectra correspond to C 1s (top row), O 1s (middle row) and S 2p (bottom row). UV-treated samples were exposed to soft UV (365 nm, 4 mW cm^{-2}) for 1.5 h in the acidic catalyst (100 mM HCl in IPA).

C.3 XPS spectra with fitted components of fresh and UV treated MOA SAM

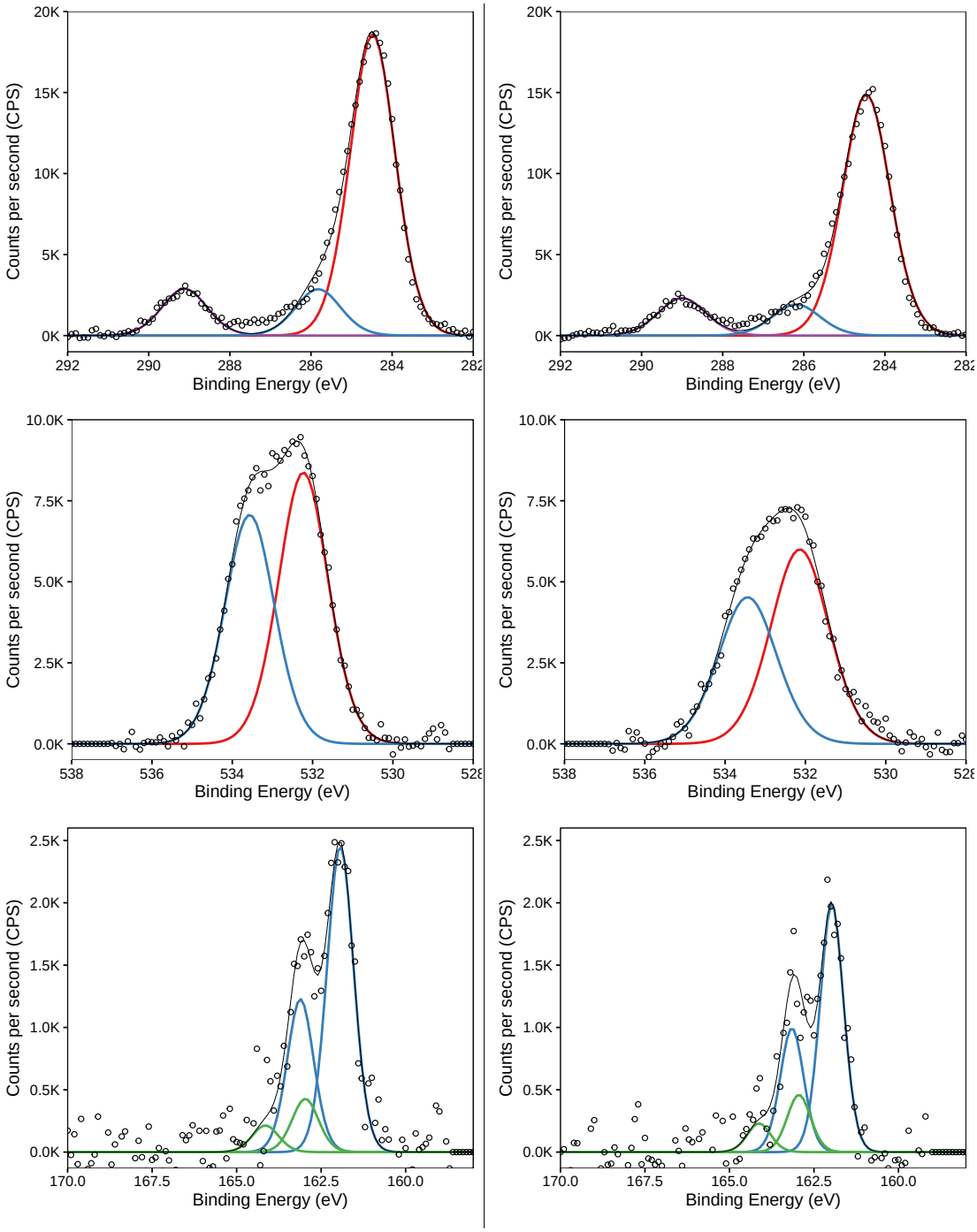

FIGURE C.3: XPS spectra with fitted components of fresh (on the left) and UV-treated (on the right) **MOA SAM**. Spectra correspond to C 1s (top row), O 1s (middle row) and S 2p (bottom row). UV-treated samples were exposed to soft UV (365 nm, 4 mW cm^{-2}) for 1.5 h in the acidic catalyst (100 mM HCl in IPA).

C.4 XPS spectra with fitted components of fresh and UV treated MUA SAM

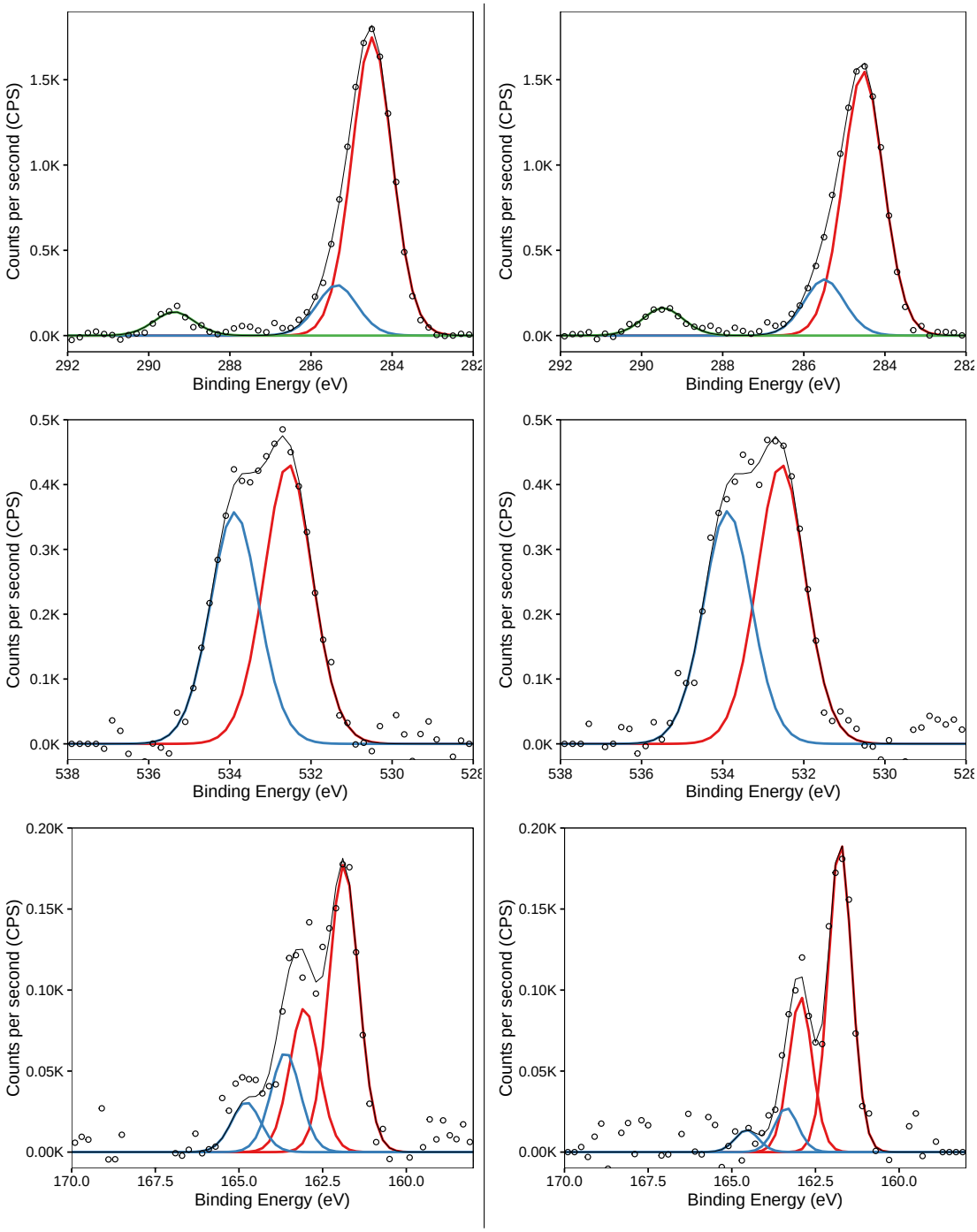

FIGURE C.4: XPS spectra with fitted components of fresh (on the left) and UV-treated (on the right) **MUA SAM**. Spectra correspond to C 1s (top row), O 1s (middle row) and S 2p (bottom row). UV-treated samples were exposed to soft UV (365 nm, 4 mW cm^{-2}) for 1.5 h in the acidic catalyst (100 mM HCl in IPA).

C.5 Azide-terminated SAMs - reduction of azide group under XPS conditions

Reduction of azide group was detected due to changes in N 1s spectra (see figure C.5) with increased exposure to to X-rays. Initially degradation of up to 60% was observed, but 20 different spots were analysed with XPS on two samples of pure azide SAM. Consequently, this reduction was decreased to 20% by optimising acquisition parameters. Quantitative analysis of the XPS spectra from all of the measurements, corresponding pass energy (PE) values, and spectral resolution values are detailed in the tables C.2, C.3, C.4, C.5 and C.6. The best results were obtained using the pass energies of 20 eV and 40 eV and with the spectral resolution of 0.2eV. All other samples were characterised with XPS using the same sets of parameters (these results are also presented in the tables mentioned above).

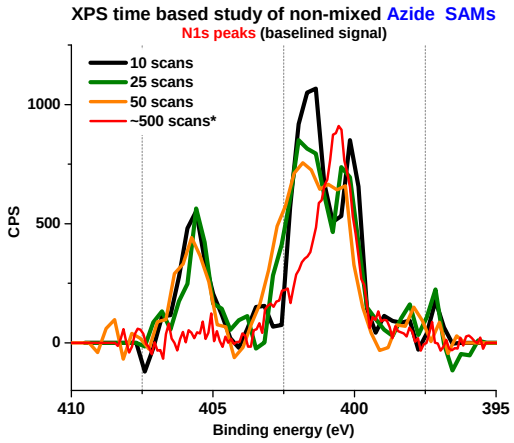

FIGURE C.5: XPS spectra of N1s region at different X-ray exposure times.

C.6 Azide-terminated SAMs - XPS peak areas including uncertainties

TABLE C.1: Relative ratios (with included uncertainties) of chemical elements and their species in pure and mixed **SAM2**, **LCAT-OEG-4 SAM** and **LCAT-OEG-1 SAM** based on integrated and normalised (using R.S.F.) peak areas in XPS spectra of N 1s, O 1s, C 1s and Au 4f regions. *Alkyl carbon in C 1s is set to be equal to 10 in all of the spectra, because that is the amount of such atoms in all of the molecules.*

	Carbon			Oxygen			Nitrogen	Gold
SAM	C=O	C-O C-N	Total	C=O	C-O	Total	Total	Total
SAM2	1.7 ± 0.2	12.8 ± 0.5	24.6 ± 0.8	1.0 ± 0.1	5.1 ± 0.3	6.1 ± 0.3	3.5 ± 0.7	15.7 ± 0.5
*Expcd**	*1*	*12*	*23*	*1*	*5*	*6*	*4*	
$\mathbf{SAM2}_{50\%}^{OEG4}$	2.0 ± 0.2	12.7 ± 0.3	24.9 ± 0.4	1.0 ± 0.1	5.6 ± 0.3	6.6 ± 0.3	2.3 ± 0.5	15.4 ± 0.5
*Expcd**	*1*	*11.9*†	*23.6*†	*1*	*5*	*6*	*2.3*†	
$\mathbf{SAM2}_{19\%}^{OEG4}$	1.7 ± 0.1	12.4 ± 0.6	24.2 ± 0.7	1.0 ± 0.1	5.5 ± 0.4	6.6 ± 0.4	1.6 ± 0.2	13.8 ± 0.4
*Expcd**	*1*	*11.3*†	*23.0*†	*1*	*5*	*6*	*1.55*†	
$\mathbf{SAM2}_{50\%}^{OEG1}$	2.2 ± 0.2	8.1 ± 0.3	20.5 ± 0.3	1.1 ± 0.1	3.8 ± 0.2	4.9 ± 0.2	2.0 ± 0.3	14.5 ± 0.3
*Expcd**	*1*	*8.5*†	*20.2*†	*1*	*3.5*	*4.5*	*2.4*†	
$\mathbf{SAM2}_{19\%}^{OEG1}$	1.9 ± 0.2	5.8 ± 0.2	17.8 ± 0.4	1.4 ± 0.1	2.5 ± 0.2	4.0 ± 0.3	1.8 ± 0.4	12.1 ± 0.6
*Expcd**	*1*	*5.8*†	*17.4*†	*1*	*2.6*	*3.6*	*1.6*†	
LCAT-OEG-4 SAM	1.5 ± 0.2	11.0 ± 0.6	22.6 ± 0.7	1.0 ± 0.1	5.0 ± 0.3	6.1 ± 0.4	1.1 ± 0.1	15.9 ± 0.4
*Expcd**	*1*	*10*	*21*	*1*	*5*	*6*	*1*	
LCAT-OEG-1 SAM	1.6 ± 0.1	4.1 ± 0.2	15.7 ± 0.4	1.0 ± 0.1	1.9 ± 0.1	2.9 ± 0.2	1.2 ± 0.1	14.9 ± 0.3
*Expcd**	*1*	*4*	*15*	*1*	*2*	*3*	*1*	

* Expected values based on the corresponding molecular structures shown in figures 5.9.

† Expected value was calculated based on experimentally obtained values from pure **SAM2**, **LCAT-OEG-4 SAM** and **LCAT-OEG-1 SAM** presented in tables 5.4 and 5.5.

C.7 Azide-terminated SAMs - XPS peak areas of all spectra

TABLE C.2: Relative ratios (calculated for each spectra) of chemical elements and their species in mixed **SAM2** and **LCAT-OEG-4 SAM** (50% and 50%, respectively) based on integrated and normalised (using R.S.F.) peak areas in XPS spectra of N 1s, O 1s, C 1s, S 2p and Au 4f regions. *Alkyl carbon in C 1s is set to be equal to 10 in all of the spectra, because that is the amount of such atoms in all of the molecules.*

XPS data on peak areas (normalised to alkyl C 1s) for mixed (50% : 50%) reagent 2 and LCAT-OEG-4 SAMs

			Au 4f	C 1s				N 1s	O1s			S 2p
			Region	Region	Alkyl	C-O & C-N	C=O	Region	Region	C=O	C-O	Region
Reagent 2 : LCAT-OEG-4 =50% : 50% SAMs	Smpl 1	PE=20, 0.1eV	16.4	24.1	10.0	12.5	1.7	1.4	6.1	0.9	5.2	0.7
		PE=20, 0.2eV	15.9	24.3		12.3	1.8	2.2	6.3	1.0	5.3	0.6
		PE=40, 0.3eV	15.9	25.3		13.2	2.0	1.7	6.6	1.0	5.6	1.1
		PE=20, 0.1eV	16.4	24.4		12.2	2.0	2.5	6.0	1.0	5.0	0.6
		Average	**16.1**	**24.5**		**12.5**	**1.9**	**1.9**	**6.2**	**1.0**	**5.3**	**0.7**
	Smpl 2	PE=20, 0.2eV										
		5 scans	14.7	24.7	10.0	12.7	1.8	2.9	6.6	1.0	5.6	0.8
		10 scans	14.8	25.7		12.9	2.3	2.8	7.3	1.1	6.0	0.7
		25 scans	15.3	25.0		12.9	1.8	2.3	6.7	1.0	5.7	0.8
		50 scans	15.3	24.9		12.8	1.9	2.0	6.9	1.0	5.8	1.0
		Average	**15.0**	**25.1**		**12.8**	**2.0**	**2.5**	**6.9**	**1.0**	**5.8**	**0.8**
		PE=20, 0.3eV										
		5 scans	14.8	24.9	10.0	12.4	2.3	1.7	6.6	0.9	5.8	0.8
		10 scans	15.2	25.0		12.9	2.1	3.1	6.9	1.0	5.8	0.8
		25 scans	15.0	25.3		12.4	2.1	3.2	6.7	0.9	5.8	0.7
		50 scans	15.2	25.0		12.7	2.0	2.6	6.5	0.9	5.6	0.8
		Average	**15.1**	**25.0**		**12.6**	**2.1**	**2.7**	**6.7**	**0.9**	**5.8**	**0.8**
		PE=40, 0.2eV										
		5 scans	15.2	25.1	10.0	12.8	2.0	2.5	6.8	0.9	5.8	0.7
		10 scans	15.5	25.1		13.2	1.8	1.8	6.7	0.9	5.8	0.8
		25 scans	15.1	25.1		12.9	2.0	2.3	6.9	1.0	5.8	0.7
		50 scans	15.4	25.0		12.7	2.1	2.0	6.6	0.9	5.6	0.8
		Average	**15.3**	**25.1**		**12.9**	**2.0**	**2.1**	**6.7**	**0.9**	**5.8**	**0.7**
		St. Dev. (%)	3%	2%	n/a	2%	9%	22%	5%	6%	5%	16%
		St. Dev.	0.5	0.4	n/a	0.3	0.2	0.5	0.3	0.1	0.3	0.1
		Average	**15.4**	**24.9**	**10**	**12.7**	**2.0**	**2.3**	**6.6**	**1.0**	**5.6**	**0.8**
Calc. fraction of reagent 2 (%)						**94%***		**50%***				
Expected for 50% : 50%				**23.6***	**10.0**	**11.9***	**1.0**	**2.3***	**6.0**	**1.0**	**5.0**	**1.0**

* Expected value was calculated based on experimentally obtained values from pure **SAM2**, **LCAT-OEG-4 SAM** and **LCAT-OEG-1 SAM** presented in tables 5.4 and 5.5.

TABLE C.3: Relative ratios (calculated for each spectra) of chemical elements and their species in mixed **SAM2** and **LCAT-OEG-4 SAM** (19% and 81%, respectively) based on integrated and normalised (using R.S.F.) peak areas in XPS spectra of N 1s, O 1s, C 1s, S 2p and Au 4f regions. *Alkyl carbon in C 1s is set to be equal to 10 in all of the spectra, because that is the amount of such atoms in all of the molecules.*

XPS data on peak areas (normalised to alkyl C 1s) for mixed (19% : 81%) reagent 2 and LCAT-OEG-4 SAMs

			Au 4f	C 1s				N 1s	O1s			S 2p
			Region	Region	Alkyl	C-O & C-N	C=O	Region	Region	C=O	C-O	Region
Reagent 2 : LCAT-OEG-4 =19% : 81% SAMs	Smpl 1	PE=20, 0.1eV	14.6	23.2	10	11.4	1.6	1.1	6.1	1.0	5.0	0.6
		PE=20, 0.2eV	14.3	22.3		10.8	1.6	1.5	5.6	0.9	4.7	0.6
		PE=40, 0.3eV	13.6	23.3		11.5	1.6	1.4	6.0	0.9	5.0	0.6
		PE=20, 0.1eV	14.7	23.7		11.7	1.7	1.4	6.1	1.1	5.0	0.7
		Average	**14.3**	**23.1**		**11.4**	**1.6**	**1.4**	**5.9**	**1.0**	**4.9**	**0.6**
	Smpl 2	PE=20, 0.2eV										
		5 scans	13.1	24.3	10	12.3	1.5	1.8	6.6	1.1	5.4	0.5
		10 scans	13.5	24.3		12.5	1.6	1.7	7.1	1.2	5.7	0.6
		25 scans	13.6	24.6		12.7	1.6	1.6	6.7	1.1	5.6	0.6
		50 scans	14.1	24.5		12.8	1.8	1.5	7.0	1.1	5.9	0.8
		Average	**13.6**	**24.4**		**12.6**	**1.6**	**1.7**	**6.8**	**1.1**	**5.6**	**0.6**
		PE=20, 0.3eV										
		5 scans	13.5	24.9	10	12.9	1.8	1.5	7.1	1.2	5.8	0.8
		10 scans	13.8	24.9		12.8	1.7	1.6	7.0	1.1	5.8	0.8
		25 scans	13.7	24.7		12.6	1.7	1.9	7.0	1.1	5.9	0.7
		50 scans	14.1	25.3		13.2	1.8	1.5	6.8	1.3	5.6	0.8
		Average	**13.8**	**25.0**		**12.9**	**1.8**	**1.6**	**7.0**	**1.2**	**5.8**	**0.8**
		PE=40, 0.2eV										
		5 scans	13.5	24.3	10	12.7	1.5	1.7	6.8	1.1	5.7	0.6
		10 scans	13.6	24.3		12.7	1.5	1.8	6.8	1.1	5.6	0.8
		25 scans	13.6	24.8		12.6	1.9	1.9	6.4	1.0	5.5	0.6
		50 scans	13.8	24.2		12.5	1.7	1.5	6.5	1.1	5.4	0.6
		Average	**13.6**	**24.4**		**12.6**	**1.6**	**1.7**	**6.6**	**1.1**	**5.5**	**0.7**
		St. Dev. (%)	3%	3%	n/a	5%	7%	12%	7%	9%	6%	15%
		St. Dev.	0.4	0.7	n/a	0.6	0.1	0.2	0.4	0.1	0.4	0.1
		Average	**13.8**	**24.2**	**10**	**12.4**	**1.7**	**1.6**	**6.6**	**1.0**	**5.5**	**0.7**
Calc. fraction of reagent 2 (%)						**75% ***		**21% ***				
Expected for 19% : 81%				**23***	**10.0**	**11.3***	**1.0**	**1.55***	**6.0**	**1.0**	**5.0**	**1.0**

* Expected value was calculated based on experimentally obtained values from pure **SAM2**, **LCAT-OEG-4 SAM** and **LCAT-OEG-1 SAM** presented in tables 5.4 and 5.5.

TABLE C.4: Relative ratios (calculated for each spectra) of chemical elements and their species in mixed **SAM2** and **LCAT-OEG-1 SAM** (50% and 50%, respectively) based on integrated and normalised (using R.S.F.) peak areas in XPS spectra of N 1s, O 1s, C 1s, S 2p and Au 4f regions. *Alkyl carbon in C 1s is set to be equal to 10 in all of the spectra, because that is the amount of such atoms in all of the molecules.*

XPS data on peak areas (normalised to alkyl C 1s) for mixed (50% : 50%) reagent 2 and LCAT-OEG-1 SAMs

			Au 4f	C 1s				N 1s	O1s			S 2p
			Region	Region	Alkyl	C-O & C-N	C=O	Region	Region	C=O	C-O	Region
Reagent 2 : LCAT-OEG-1 =50% : 50% SAMs	Smpl 1	PE=20, 0.1eV	14.9	20.4	10.0	8.3	1.9	2.0	4.7	1.1	3.6	0.7
		PE=20, 0.2eV	14.7	20.1		7.9	2.1	2.0	4.6	1.0	3.5	0.6
		PE=40, 0.3eV	15.0	20.8		8.4	2.1	2.1	4.6	1.0	3.6	0.5
		PE=20, 0.1eV	14.7	19.7		7.8	1.9	2.2	4.6	1.0	3.5	0.7
		Average	**14.8**	**20.3**		**8.1**	**2.0**	**2.1**	**4.6**	**1.0**	**3.5**	**0.6**
	Smpl 2	PE=20, 0.2eV			10.0							
		5 scans	14.2	20.2		7.6	2.5	2.5	5.2	1.1	3.9	0.8
		10 scans	14.6	20.7		8.2	2.3	1.7	5.0	1.1	3.9	0.7
		25 scans	14.8	21.0		8.5	2.2	1.6	5.0	1.2	3.8	1.0
		50 scans	14.3	20.6		7.9	2.3	1.9	4.9	1.1	3.9	0.6
		Average	**14.5**	**20.6**		**8.0**	**2.3**	**1.9**	**5.0**	**1.1**	**3.9**	**0.8**
		PE=20, 0.3eV			10.0							
		5 scans	14.2	20.7		7.8	2.7	1.6	4.9	1.0	3.8	0.7
		10 scans	14.5	20.2		7.6	2.5	2.7	5.2	1.1	4.2	0.8
		25 scans	13.7	20.5		8.2	1.9	2.1	4.7	1.0	3.8	0.8
		50 scans	14.3	20.8		8.4	2.3	2.1	5.0	1.0	3.9	0.8
		Average	**14.2**	**20.6**		**8.0**	**2.4**	**2.1**	**4.9**	**1.0**	**3.9**	**0.8**
		PE=40, 0.2eV			10.0							
		5 scans	13.9	20.3		8.1	2.1	2.3	4.7	1.1	3.6	0.6
		10 scans	14.9	21.0		8.5	2.3	2.1	4.9	1.1	3.8	0.8
		25 scans	14.5	20.6		8.3	2.1	1.9	5.0	1.1	3.8	0.6
		50 scans	14.2	20.4		8.3	2.0	1.7	4.8	1.1	3.6	0.6
		Average	**14.4**	**20.6**		**8.3**	**2.1**	**2.0**	**4.8**	**1.1**	**3.7**	**0.7**
		St. Dev. (%)	2%	2%	n/a	4%	10%	15%	4%	5%	5%	15%
		St. Dev.	0.3	0.3	n/a	0.3	0.2	0.3	0.2	0.0	0.2	0.1
		Average	**14.5**	**20.5**	**10**	**8.1**	**2.2**	**2.0**	**4.9**	**1.1**	**3.8**	**0.7**
		Calc. fraction of reagent 2 (%)				**46%***		**36%***			**59%**	
		Expected for 50% : 50%		**20.2***	**10.0**	**8.5***	**1.0**	**2.4***	**4.5**	**1.0**	**3.5**	**1.0**

* Expected value was calculated based on experimentally obtained values from pure **SAM2**, **LCAT-OEG-4 SAM** and **LCAT-OEG-1 SAM** presented in tables 5.4 and 5.5.

TABLE C.5: Relative ratios (calculated for each spectra) of chemical elements and their species in mixed **SAM2** and **LCAT-OEG-1 SAM** (19% and 81%, respectively) based on integrated and normalised (using R.S.F.) peak areas in XPS spectra of N 1s, O 1s, C 1s, S 2p and Au 4f regions. *Alkyl carbon in C 1s is set to be equal to 10 in all of the spectra, because that is the amount of such atoms in all of the molecules.*

XPS data on peak areas (normalised to alkyl C 1s) for mixed (19% : 81%) reagent 2 and LCAT-OEG-1 SAMs

			Au 4f	C 1s				N 1s	O1s			S 2p
			Region	Region	Alkyl	C-O & C-N	C=O	Region	Region	C=O	C-O	Region
Reagent 2 : LCAT-OEG-1 =19% : 81% SAMs	Smpl 1	PE=20, 0.1eV	13.2	17.8	10	5.8	1.8	1.5	3.9	1.4	2.5	0.5
		PE=20, 0.2eV	13.3	18.1		6.0	2.0	1.5	3.9	1.4	2.5	0.6
		PE=40, 0.3eV	12.9	17.7		5.9	1.8	1.6	3.8	1.4	2.5	0.4
		PE=20, 0.1eV	12.2	17.2		5.4	1.8	1.4	3.4	1.2	2.2	0.5
		Average	**12.9**	**17.7**		**5.8**	**1.9**	**1.5**	**3.8**	**1.3**	**2.4**	**0.5**
	Smpl 2	PE=20, 0.2eV										
		5 scans	11.5	17.8	10	5.5	1.9	1.7	3.7	1.2	2.5	0.6
		10 scans	11.3	17.8		5.9	1.6	2.3	3.9	1.5	2.4	0.5
		25 scans	12.0	17.9		5.9	2.0	1.1	4.2	1.5	2.8	0.9
		50 scans	12.3	18.5		6.2	2.1	1.8	4.2	1.5	2.7	0.6
		Average	**11.8**	**18.0**		**5.9**	**1.9**	**1.7**	**4.0**	**1.4**	**2.6**	**0.7**
		PE=20, 0.3eV										
		5 scans	11.2	17.3	10	5.7	1.6	2.6	3.8	1.3	2.5	0.6
		10 scans	11.8	17.7		5.7	2.1	2.0	4.1	1.5	2.5	0.7
		25 scans	12.5	17.6		6.1	1.7	2.6	4.7	1.6	2.9	0.7
		50 scans	12.1	18.6		6.0	2.2	1.4	4.0	1.4	2.6	0.8
		Average	**11.9**	**17.8**		**5.9**	**1.9**	**2.2**	**4.1**	**1.5**	**2.6**	**0.7**
		PE=40, 0.2eV										
		5 scans	11.2	17.3	10	5.6	1.6	2.2	3.8	1.3	2.5	0.5
		10 scans	11.9	17.7		5.9	1.8	1.8	3.9	1.4	2.5	0.7
		25 scans	12.1	18.1		5.8	2.1	1.6	4.0	1.4	2.5	0.5
		50 scans	12.3	17.9		5.8	1.9	1.4	3.9	1.3	2.5	0.6
		Average	**11.9**	**17.7**		**5.8**	**1.9**	**1.7**	**3.9**	**1.4**	**2.5**	**0.6**
		St. Dev. (%)	5%	2%	n/a	4%	10%	25%	6%	8%	6%	18%
		St. Dev.	0.6	0.4	n/a	0.2	0.2	0.4	0.3	0.1	0.2	0.1
		Average	**12.1**	**17.8**	**10**	**5.8**	**1.9**	**1.8**	**4.0**	**1.4**	**2.5**	**0.6**
Calc. fraction of reagent 2 (%)						**20% ***		**25% ***			**21%**	
Expected for 19% : 81%				**17.4***	**10.0**	**5.8***	**1.0**	**1.6***	**3.6**	**1.0**	**2.6**	**1.0**

* Expected value was calculated based on experimentally obtained values from pure **SAM2**, **LCAT-OEG-4 SAM** and **LCAT-OEG-1 SAM** presented in tables 5.4 and 5.5.

TABLE C.6: Relative ratios (calculated for each spectra) of chemical elements and their species in pure **SAM2**, **LCAT-OEG-4 SAM** and **LCAT-OEG-1 SAM** based on integrated and normalised (using R.S.F.) peak areas in XPS spectra of N 1s, O 1s, C 1s, S 2p and Au 4f regions. *Alkyl carbon in C 1s is set to be equal to 10 in all of the spectra, because that is the amount of such atoms in all of the molecules.*

XPS data on peak areas (normalised to alkyl C 1s) for non-mixed (100%) reagent 2, LCAT-OEG-4 and LCAT-OEG-1 SAMs

			Au 4f	C 1s				N 1s	O1s			S 2p
			Region	Region	Alkyl	C-O & C-N	C=O	Region	Region	C=O	C-O	Region
LCAT-OEG-1 SAM	Smpl 1	PE=20, 0.1eV	15.4	15.6		3.9	1.7	1.1	2.8	1.0	1.7	0.7
		PE=20, 0.2eV	14.7	15.1		3.8	1.4	1.3	2.8	1.0	1.8	0.7
		PE=40, 0.3eV	14.9	15.8	10	4.1	1.6	1.2	2.7	0.9	1.7	0.6
	Smpl 2	PE=20, 0.1eV	15.0	15.8		4.1	1.6	1.1	3.0	1.1	1.9	0.8
		PE=20, 0.2eV	14.6	16.0		4.2	1.7	1.2	2.9	1.0	1.9	0.8
		PE=20, 0.2eV	14.8	16.1		4.4	1.6	1.3	3.2	1.1	2.1	0.8
	Std. Dev.		2%	2%		6%	6%	6%	7%	6%	8%	8%
			0.3	0.4		0.2	0.1	0.1	0.2	0.1	0.1	0.1
	Average		**14.9**	**15.7**	**10.0**	**4.1**	**1.6**	**1.2**	**2.9**	**1.0**	**1.9**	**0.7**
	Expected			15	10	4	1	1	3	1	2	1
LCAT-OEG-4 SAM	Smpl 1	PE=20, 0.1eV	15.3	22.9		11.2	1.5	1.1	6.5	1.1	5.3	0.7
		PE=20, 0.2eV	16.0	23.0		11.2	1.8	1.2	6.1	1.0	5.0	0.7
		PE=40, 0.3eV	15.8	23.5	10	11.8	1.6	1.1	6.4	1.0	5.4	0.7
	Smpl 2	PE=20, 0.1eV	16.5	21.6		10.2	1.4	1.3	5.5	1.0	4.4	0.8
		PE=20, 0.2eV	16.0	22.4		10.8	1.6	0.9	6.0	1.0	4.9	0.8
		PE=20, 0.2eV	15.8	22.2		10.7	1.4	1.0	6.0	1.0	5.0	0.7
	Std. Dev.		3%	3%		5%	10%	12%	6%	4%	7%	10%
			0.4	0.7		0.6	0.2	0.1	0.4	0.0	0.3	0.1
	Average		**15.9**	**22.6**	**10.0**	**11.0**	**1.5**	**1.1**	**6.1**	**1.0**	**5.0**	**0.7**
	Expected			21	10	10	1	1	6	1	5	1
SAM 2	Smpl 1	PE=20, 0.1eV	16.4	23.8		12.2	1.7	1.8	5.6	0.9	4.6	0.7
		PE=20, 0.2eV	15.8	22.9	10	11.7	1.5	3.2	5.6	1.0	4.6	0.9
		PE=40, 0.3eV	15.7	24.3		12.7	1.5	3.3	6.1	1.0	5.0	0.8
		PE=20, 0.1eV	16.8	23.5		12.2	1.5	4.4	5.5	0.9	4.6	0.6
	Smpl 2	PE=20, 0.2eV										
		5 scans	15.4	24.4		12.6	1.6	4.9	6.1	0.9	5.1	0.9
		10 scans	16.2	24.8	10	13.0	2.0	3.8	6.7	1.0	5.5	0.7
		25 scans	15.1	24.6		12.7	1.5	3.2	6.0	0.9	5.0	0.5
		50 scans	15.5	24.7		12.4	2.0	3.6	6.4	1.1	5.2	0.8
		PE=20, 0.3eV										
		5 scans	15.5	25.4		13.3	1.9	3.6	6.1	1.0	5.1	0.7
		10 scans	15.6	25.1	10	13.3	1.6	3.9	6.6	1.0	5.6	0.8
		25 scans	15.3	25.7		13.4	1.6	3.6	6.2	1.1	5.2	0.6
		50 scans	15.9	25.8		13.6	2.0	3.8	6.4	1.0	5.4	0.8
		PE=40, 0.2eV										
		5 scans	15.1	25.5		13.3	1.8	3.7	6.0	0.9	5.2	0.8
		10 scans	15.4	24.6	10	13.0	1.6	3.4	6.1	1.0	5.1	0.8
		25 scans	15.3	24.8		13.1	1.6	3.7	6.2	1.0	5.2	0.8
		50 scans	15.5	24.3		12.6	1.7	3.2	6.0	0.9	5.0	0.7
		PE=60, 0.2eV										
		5 scans	15.5	24.7		13.2	1.4	3.3	6.0	0.9	5.1	0.5
		10 scans	15.5	24.4	10	13.0	1.3	3.3	5.9	0.9	5.0	0.7
		25 scans	15.3	24.6		13.3	1.3	2.7	6.0	0.9	5.1	0.7
		50 scans	15.3	23.9		12.6	1.3	3.0	5.8	0.9	4.9	0.7
	Std. Dev.		3%	3%		4%	11%	19%	6%	6%	6%	15%
			0.5	0.8		0.5	0.2	0.7	0.3	0.1	0.3	0.1
	Average		**15.7**	**24.6**	**10.0**	**12.8**	**1.7**	**3.5**	**6.1**	**1.0**	**5.1**	**0.7**
	Expected			23	10	12	1	4	6	1	5	1

C.8 Azide-terminated SAMs - QCMD data of prolonged measurements on SAM2 and -OH terminated SAM

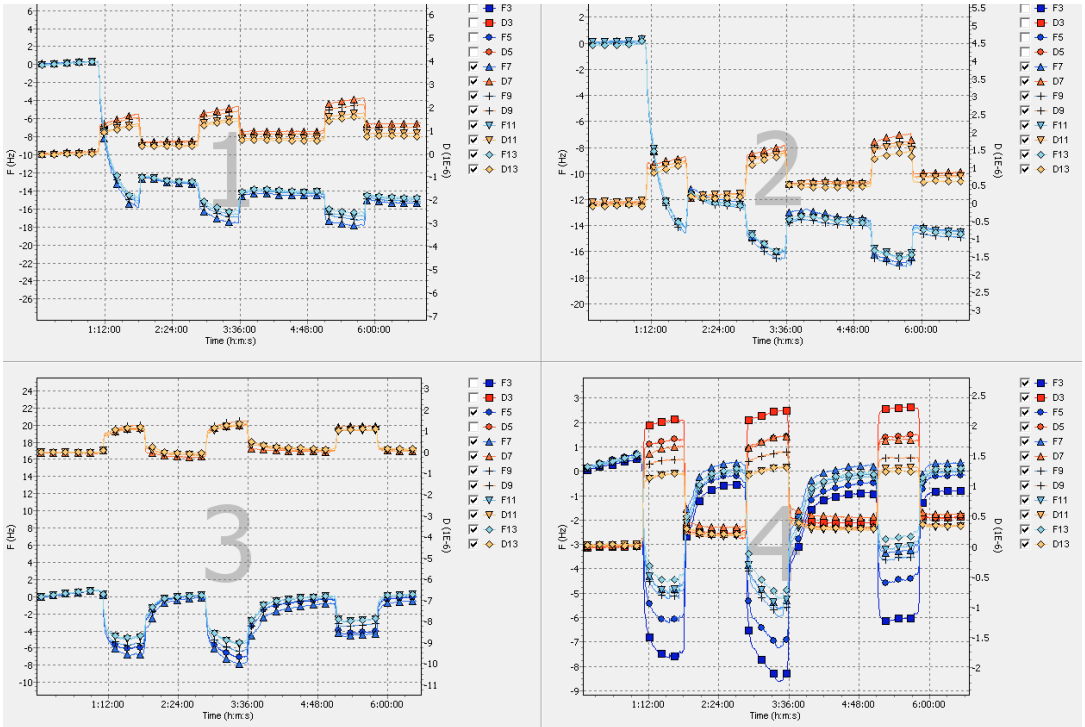

FIGURE C.6: A snapshot of prolonged QCMD measurements of rinsing **SAM2** (top row) and **LCAT-OEG-4 SAM** (bottom row) with 240 µM **strained cyclooctyne** aqueous solution. Two samples (one on the left and one on the right side) of each type of SAM were investigated. Graphs in blue correspond to the change in frequency, while graphs in yellow, orange and red correspond to the change in dissipation.